#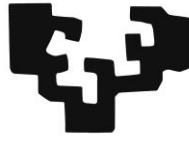 *Ultrasmall Glyco-Gold Nanoparticles: Synthesis Optimization, Characterization and Applications in Immune-Cell Targeting*

Doctoral Thesis presented by:

## Valentin Laurent Cognet

Leioa, 2020

eman ta zabal zazu

Universidad del País Vasco
Euskal Herriko Unibertsitatea

# Ultrasmall Glyco-Gold Nanoparticles: Synthesis Optimization, Characterization and Applications in Immune-Cell Targeting

**Valentin Laurent Cognet**

**Doctoral Thesis**

**2020**

**Midatech Pharma España**

**H2020 European Training Network Immunoshape**

*To my family*

# Acknowledgments

# Contents

# Abbreviations

**$^{13}$C NMR** Carbon-13 Nuclear Magnetic Resonance

**$^{1}$H NMR** Proton Nuclear Magnetic Resonance

**AAL** *Aleuria aurantia* Lectin

**Ac** Acetate

**α-Galactose-C$_2$** 2'-Thioethyl α-D-galactopyranoside

**α-Mannose1,2-α-Mannose** 2-*O*-(α-D-Mannopyranosyl)-D-mannopyranose

**APC** Antigen Presenting Cell

**BF$_3$.OEt$_2$** Boron trifluoride diethyl etherate

**β-Glucose-C$_2$** 2'-Thioethyl β-D-glucopyranoside

**BLI** Biolayer Interferometry

**β-*N*-Acetyl-Glucosamine-EG$_2$** 2'-[2-(2-Thiooethoxy)ethyl]-2-acetamido-2-deoxy-β-D-glucopyranoside

**Boc** Tert-butyloxycarbonyl

**BSS** Brust-Schiffrin Synthesis

**CAD** Charged Aerosol Detector

**CD** Cluster of Differentiation

**CDCl$_3$** Deuterated Chloroform

**CH$_2$Cl$_2$** Dichloromethane

**CLR** C-type Lectin = C-type Lectin Receptor

**ConA** Concanavalin A

**CRD** Carbohydrate Recognition Domain

**CS$_2$** Carbon disulfide

**CTL** Cytotoxic T Lymphocyte = Killer T Cell

**CuAAC** Cu(I)-Promoted Azide-Alkyne [3 +2] Cycloaddition

**CuSO$_4$** Copper sulfate

**δ** Chemical Shift

**D$_2$O** Deuterium Oxide

**d$_3$-αMan** Dendron$_3$-α-Mannose

**d$_9$-αMan** Dendron$_9$-α-Mannose

**DAD** Diode Array Detector

**DB$_{18}$C$_6$** Dibenzo-18-crown-6

**DC** Dendritic Cell

**DCS** Differential Centrifugation Sedimentation

**DC-SIGN** Dendritic Cell-Specific Intercellular adhesion molecule-3-Grabbing Non-integrin

**DF** Degree of Functionalization

**DLS** Dynamic Light Scattering

**DMSO** Dimethyl Sulfoxide

**DTT** Dithiothreitol

**ECA** *Erythrina cristagalli* lectin

**EDC** Ethyl-3-(3-dimethylaminopropyl)carbodiimide

**EG** Ethylene Glycol

**ESI** Electrospray Ionization

**FPLC** Fast Protein Liquid Chromatography

**Fuc** Fucose

**Gal** Galactose

**Glc** Glucose

**GlcNAc** *N*-Acetylglucosamine

**GMP** Good Manufacturing Practice

**GNP** Gold Nanoparticle

**H$_2$SO$_4$** Sulfuric acid

**HAuCl$_4$** Tetrachloroauric acid

**HHL** *Hippeastrum hybrid* Lectin

**HPLC** High-Performance Liquid Chromatography

**ICP-AES** Inductively Coupled Plasma - Atomic Emission Spectroscopy

**ICP-MS** Inductively Coupled Plasma - Mass Spectrometry

**ID** Identification

**IL-4** Interleukin 4

**KCN** Potassium cyanide

**K$_D$** Equilibrium Dissociation Constant

**KOH** Potassium hydroxide

**LC** Liquid Chromatography

**LC-CAD-MS** Liquid Chromatography - Charged Aerosol Detection - Mass Spectrometry

**LDI** Laser Desorption Ionization

**MALDI** Matrix Assisted Laser Desorption Ionization

**Man** Mannose

**MeOH** Methanol

**MeONa** Sodium methoxide

**MMR** Mannose Receptor

**MP-AES** Microwave Plasma - Atomic Emission Spectrometry

**mrCLR** mannose-recognizing C-type Lectin Receptor

**MS** Mass Spectrometry

**MW** Molecular Weight

**MWCO** Molecular Weight Cut-Off

**NaBH$_4$** Sodium borohydride

**NaHCO$_3$** Sodium bicarbonate

**NaN$_3$** Sodium azide

**NaOH** Sodium hydroxide

**NHS** N-Hydroxysuccinimide

**NMR** Nuclear Magnetic Resonance

**NP** Nanoparticle

**NPA/NPL** *Narcissus pseudonarcissus* Lectin

**PA-IL** *Pseudomonas aeruginosa* agglutinin

**PBS** Phosphate-Buffered Saline

**PEG** Polyethylene Glycol

**PEG(5)NH$_2$** α-Thio-ω-aminoethyl penta(ethylene glycol)

**PEG(8)COOH** α-Thio-ω-(propionic acid) octa(ethylene glycol)

**PKBD** Pharmacokinetics and Biodistribution

**PMA** Phorbol 12-Myristate 13-Acetate

**PPh$_3$** Triphenylphosphine

**RPLC** Reverse Phase Liquid Chromatography

**RT** Room Temperature or Retention Time

**SEC** Size Exclusion Chromatography

**SPB** Surface Plasmon Band

**SPR** Surface Plasmon Resonance

**Sulfo-NHS** N-hydroxysulfosuccinimide

**TBAI** Tetra-n-butylammonium iodide

**TCEP** Tris(2-carboxyethyl)phosphine

**TCEP=O** Oxidized Tris(2-carboxyethyl)phosphine

**TEM** Transmission Electron Microscopy

**TFF** Tangential Flow Filtration

**THPTA** Tris(3-hydroxypropyltriazolylmethyl)amine

**TLC** Thin-Layer Chromatography

**TMAH** Tetramethylammonium hydroxide

**UF** Ultrafiltration

**UHPLC** Ultra-High-Performance Liquid Chromatography

**UV-Vis** Ultraviolet–Visible

**XPS** X-ray Photoelectron Spectrometry

**ZP** Zeta Potential

**λ** Wavelength

x

# Abstract

Gold nanoparticles (GNP) are hybrid materials, with excellent physicochemical characteristics, made of a gold core and a corona of organic molecules, amongst them carbohydrates. Ultrasmall GNP (nanoclusters) are usually obtained through a modified Brust-Schiffrin synthesis. The combination of glycoscience and ultrasmall GNP enables wide biotechnological and clinical applications. Using GNP multivalency or multifunctionality properties, carbohydrates can, for instance, trigger the cluster glycoside effect required for the targeting of lectin receptors.

To deliver reliable and reproducible GNP material, a tight control of the synthesis and a broad spectrum of analytical techniques are essential. To this end, the passivation step of the aqueous Brust-Schiffrin synthesis was thoroughly studied using different bifunctional platforms made of either positive or negative oligo-PEG and a monosaccharide with a short alkyl side chain with narrow one-parameter variations (pH, temperature). An increased passivation time led, for all the models studied, to an increase of the core and the overall size of the particles, as well as to a gradual decrease of the ligand density. Attributing these changes to the presence of sodium borohydride, the reducing agent that forms the particles, scavenging ion exchange resins were tested. IRA-400 was able to remove most of sodium borohydride from the crude solution and prevent the passivation effects previously observed. Moreover, an extensive characterization was performed to optimize the analytical techniques, compare the data and obtain the most accurate description of the synthesized material. This work demonstrated the sensitivity of techniques such as UV-Vis spectrophotometry and size exclusion chromatography for GNP size evolution monitoring.

A novel chromatographic method of corona characterization for weak or non-UV absorbent ligands was developed using charged aerosol detection coupled with mass spectrometry (LC-CAD-MS), accompanied by a new particle etching protocol using tris(2-carboxyethyl)phosphine (TCEP) (to enable complete release of the ligands in the reduced, thiol form). The results were compared to those obtained by ^{1}H NMR. Taking advantage of the mass dependent property of the CAD, the degree of functionalization after post-functionalization reactions was also determined. Results obtained with both techniques were similar and validated the complementarity of the methods.

A library of α-mannose derivatives together with oligosaccharides were used to decorate GNP through post-functionalization reactions. The different routes to design the α-mannose library and functionalize GNP were compared to find the most efficient method considering parameters such as the yield of the final α-mannose derivative, the degree of functionalization of the GNP and challenges of characterization. α-Mannose derivatives were synthesized with different functional groups: amine, carboxylic acid, azide, alkyne, isothiocyanate. GNP bearing the complementary moieties were then coupled to the carbohydrates, with the goal of achieving the highest degree of functionalization. Non-derivatized oligosaccharides were also bound to an amino-oxy GNP through an oxime link. The success of the non-modified carbohydrate oxime route created a straightforward method for GNP decoration.

Biochemical (microarray, biolayer interferometry) and biological (cell uptake) assays were performed to achieve and optimize the targeting of lectins such as DC-SIGN by Glyco-GNP. Biolayer interferometry demonstrated that α-mannose and, more significantly, the dimer α-mannose1,2α-mannose (and two chemically enhanced mimetics ISh045 and ISh046) were able to effectively bind to DC-SIGN when presented on particles with a 4 nm core (plasmonic), but not when incubated with 2 nm core GNP. These results were in line with the cell uptake assay performed with a dendritic cell (THP-1) model expressing DC-SIGN. Specific uptake was only observed with 4 nm core GNP functionalized with α-mannose1,2α-mannose and its mimetics (30-fold increase) and α-mannose (6-fold increase). The ability of GNP to quench fluorescence was used to screen a library of lectins with different carbohydrate affinities. A microarray of fluorescent lectins was printed, and the GNP were able to quench the fluorescence by selectively binding to the lectins, discriminating them depending on their spatial orientation and sugar specificity.

# Resumen

- **Introducción**

Las nanopartículas de oro o *gold nanoparticles* (GNP) son materiales híbridos compuestos por un núcleo de oro y una corona de moléculas orgánicas (ligandos) y tienen excelentes características fisicoquímicas: una relación superficie/volumen alta, versatilidad, estabilidad, facilidad de síntesis, biocompatibilidad y baja toxicidad. Dependiendo del método de síntesis utilizado, se pueden obtener partículas de varios tamaños y formas. Las GNP ultra pequeñas (nanoclusters) se obtienen generalmente a través del método de síntesis Brust-Schiffrin, publicado por primera vez en 1994. Las partículas obtenidas tienen un tamaño de núcleo inferior a 5 nm y una forma esférica. La principal forma de unión entre el núcleo de oro y los ligandos de la corona es el enlace azufre-oro (S-Au) formado por ligandos tiol o disulfuro.

Las GNP tienen dos características esenciales: multivalencia y multifuncionalidad y por ello permiten la presentación, en gran cantidad, de prácticamente cualquier tipo de molécula orgánica. Los ligandos orgánicos que forman la corona pueden ser materiales tales como péptidos, proteínas, carbohidratos, ácidos nucleicos, fármacos, sondas o polímeros (por ejemplo, polietilenglicoles). El tipo de ligando impacta fuertemente en las propiedades biológicas *in vivo* de las GNP, como, por ejemplo, en la capacidad de sigilo, la vida media, la distribución o el *targeting* (activo o pasivo) de órganos o células.

Las aplicaciones de las GNP en áreas de diagnóstico y terapéuticas son múltiples: agentes de contraste, sensores, tratamiento de infecciones por microorganismos, cáncer (a través de antibióticos, medicamentos antitumorales o terapia fototérmica) o vacunas (adyuvante o sistema de administración).

La gliconanotecnología es la combinación de la glicociencia y la nanotecnología, de manera que los carbohidratos y las nanopartículas funcionen de forma sinérgica. Los carbohidratos, a menudo denominados azúcares o sacáridos, pueden mejorar la estabilidad, solubilidad, biocompatibilidad, biodegradabilidad y conferir propiedades de sigilo a las GNP. También se pueden usar como agentes de *targeting* usando la multivalencia conferida por las GNP para mejorar la avidez del carbohidrato para su receptor a través del efecto clúster glicosídico (*cluster glycoside effect*). Los receptores de carbohidratos generalmente pertenecen a la familia de las lectinas y su interacción con los carbohidratos es débil, aunque altamente específica.

Las aplicaciones de las gliconanopartículas son numerosas y han sido ampliamente documentadas en bioensayos, diagnósticos y terapias. Las gliconanopartículas de oro ultra pequeñas fueron publicadas por primera vez por Penadés et al. en 2001.

Midatech Pharma posee la plataforma de GNP ultra pequeñas Midacore$^{TM}$. Gracias a su versatilidad, se han desarrollado varias líneas de investigación con diferentes clases de moléculas: inmunoterapias para diabetes, quimioterapias (carcinoma hepatocelular) o tratamientos para la psoriasis. Algunos de estos proyectos han llegado a fases clínicas.

- **Capítulo I**

La síntesis de Brust-Schiffrin utiliza borohidruro de sodio como agente reductor. Tras su adición a una mezcla de ácido tetracloroaúrico y ligandos con tiol o disulfuro, las GNP se forman de manera instantánea. Al contrario de la primera síntesis de Brust-Schiffrin que se hacía en dos fases con un disolvente orgánico, las GNP Midacore$^{TM}$ se obtienen usando agua para la síntesis y para la purificación. Aunque el principio general de la reacción y su ejecución parece ser sencillo, su control y comprensión siguen siendo todo un desafío. Las GNP son productos complejos, y son muchos los factores que pueden influir en sus características fisicoquímicas. Por lo tanto, la calidad, reproducibilidad y escalado solo se pueden lograr a través de un proceso de fabricación totalmente controlado, que incluya síntesis, purificación y un *array* analítico completo.

Una vez hecha la adición del borohidruro de sodio, las partículas nuclean y entran en una etapa de pasivación.

El objetivo de la investigación es doble: entender los fenómenos que actúan durante la pasivación y poner a punto un *array* analítico con técnicas sensitivas y robustas.

Con estos fines, la etapa de pasivación se estudió a fondo con varias plataformas bifuncionalizadas con dos ligandos: un espaciador derivado de polietilenglicol positivo (PEG(5)NH$_2$) o negativo (PEG(8)COOH) y un monosacárido con una cadena lateral corta (α-Galactose-C$_2$ o β-Glucose-C$_2$). En primer lugar, fueron sometidas a variaciones ajustadas de un parámetro (pH o temperatura) y analizadas a lo largo de un día. En segundo lugar, se investigó el efecto del borohidruro sódico en la etapa de pasivación, utilizando resinas de intercambio iónico que permiten la eliminación de éste durante el proceso.

La caracterización fue exhaustiva y se dividió en tres partes:

- La corona: por espectroscopía de resonancia magnética nuclear de protones ($^1$H NMR), cromatografía de fase inversa: cromatografía líquida de ultra alto rendimiento utilizando un detector de aerosol cargado y espectrometría de masas (LC-CAD-MS) y cromatografía líquida de alto rendimiento utilizando detector de matriz de diodos (HPLC-DAD) junto con los análisis elementales: espectroscopía de emisión atómica de plasma acoplada inductivamente (ICP-AES), y espectrometría de fotoelectrones de rayos X (XPS).
- El tamaño de partícula y la distribución: por dispersión dinámica de la luz (DLS), sedimentación, centrifugación diferencial (DCS) y cromatografía de exclusión por tamaño (SEC).
- El tamaño y la forma del núcleo: por microscopía electrónica de transmisión (TEM) y espectrofotometría ultravioleta-visible (UV-Vis).

Los diferentes experimentos realizados demostraron la importancia de la fase de pasivación durante la síntesis acuosa de Brust-Schiffrin. Se observaron dos tendencias principales: el crecimiento de tamaño de las GNP, tanto a nivel de núcleo como de partículas completas, y la disminución de densidad de ligandos con el aumento del tiempo de pasivación. Las técnicas UV-Vis (aumento de la banda de plasmón de superficie) y SEC (desplazamiento del tiempo de elución) demostraron que el crecimiento era gradual y comenzaba tan pronto como terminaba la nucleación. Se demostró que otras técnicas de medición de tamaño, como TEM, DLS y DCS, son menos sensibles, aunque tienen la ventaja de dar un valor absoluto de tamaño. $^1$H NMR y LC-CAD-MS mostraron que la proporción entre los ligandos permanece estable durante el tiempo de pasivación. Por otro lado, la densidad del ligando exhibió una disminución gradual después de la nucleación. Esta disminución se observó para ambos ligandos usando LC-CAD-MS, XPS e ICP-AES.

La caída en la densidad del material orgánico en el núcleo se puede atribuir al decapado de ligandos por la acción del borohidruro de sodio. Para lograr su eliminación e investigar las consecuencias en el proceso de pasivación, se compararon dos resinas, IRA-400 e IRA-743. IRA-400 pudo eliminar casi el 90 % del borohidruro de sodio e impedir los efectos relacionados incluso hasta después de cuatro días. Un análisis exhaustivo mostró la ausencia de un aumento significativo del tamaño tanto del núcleo como del tamaño total de la partícula. Además, la densidad de ligando permaneció estable durante ese tiempo.

### ▪ Capítulo II

Debido a su complejidad inherente, las GNP requieren técnicas analíticas de vanguardia para caracterizarse completamente. Hoy en día, se ha desarrollado y publicado una amplia gama de técnicas. Sin embargo, a pesar de que las GNP compartan características comunes, los análisis deben adaptarse a cada molécula. Una caracterización adecuada es esencial desde la I+D hasta la producción comercial y debe fortalecerse a medida que el producto avanza hacia el uso humano/comercial. Tradicionalmente, el tamaño de las nanopartículas se determina mediante técnicas de dispersión (DLS), centrifugación analítica (DCS) y microscopía (TEM), mientras que la química de superficie se caracteriza por espectroscopía (UV-Vis, NMR, MS, XPS) usando a veces cromatografía (LC, GC) y análisis térmico (TGA).

La resonancia magnética nuclear de protones ($^1$H NMR) permite la identificación y la cuantificación de los ligandos de la corona. Tiene la ventaja de poder detectar todas las especies orgánicas sin derivatización. La integración relativa de picos de ligando bien resueltos permite la obtención de la ratio entre ellos. Sin embargo, puede ser difícil obtener información fiable debido a que los espectros de $^1$H NMR de nanopartículas funcionalizadas muestran un ensanchamiento significativo de las bandas correspondientes a los ligandos, como resultado de su unión a la superficie de la nanopartícula. Una estrategia para lograr resultados sensibles, específicos y reproducibles es decapar los ligandos del núcleo de las GNP utilizando un reactivo específico. Llamamos a ese paso pretratamiento. Para permitir mediciones fiables, los ligandos deben escindirse por completo tras la reacción con un reactivo de ataque químico, pero no degradarse a través de reacciones secundarias. En el caso de $^1$H NMR, los laboratorios de análisis de Midatech Pharma usan de manera rutinaria una solución de cianuro de potasio en hidróxido de potasio (KCN/KOH).

La cromatografía líquida de alto rendimiento utilizando un detector de aerosol cargado y espectrometría de masas (LC-CAD-MS) combina en un sistema HPLC o UHPLC tres tipos de detectores: un UV-Vis (DAD), un detector de aerosol cargado (CAD) y un espectrómetro de masas (MS). El CAD puede detectar compuestos que no absorben en UV. La detección depende de la masa y la respuesta no depende de las propiedades espectrales o fisicoquímicas de los analitos. Esta característica significa que, en teoría, genera una respuesta idéntica para cantidades idénticas de diferentes analitos, lo que es muy útil en ausencia de materiales estándar.

Ese es, por ejemplo, el caso de los ligandos obtenidos a través de la post-funcionalización de GNP, donde se realiza una reacción química directamente en la partícula, entre un ligando en la superficie de GNP y una molécula que lleva un grupo funcional compatible. El CAD es, por tanto, apropiado para las GNP con ligandos que no absorben en UV: PEG y carbohidratos.

No obstante, el método KCN/KOH no es adecuado para el LC-CAD-MS porque el pH alcalino de la solución conduce a la formación rápida de disulfuros, tanto homodímeros como heterodímeros, después de su liberación del núcleo, lo que hace que la preparación no sea apropiada para métodos cromatográficos.

El objetivo principal de este capítulo es mejorar la caracterización de los ligandos de la corona en GNP ultra pequeñas. Usando una serie de nanopartículas de oro, se han seleccionado diferentes reactivos de *etching* para encontrar una alternativa superior a KCN/KOH. De esta forma, usando la mejor molécula: tris(2-carboxyethyl)phosphine (TCEP), se desarrolló un método cromatográfico de LC-CAD-MS, usando $^1$H NMR como herramienta de confirmación.

El *etching* completo y limpio de las GNP tal como se obtiene con KCN/KOH solo se logró usando TCEP. La prueba de equivalencia de TCEP y KCN/KOH para la proporción de ligando realizada por $^1$H NMR mostró datos similares. Se logró una buena reproducibilidad entre lotes y una buena sensibilidad.

El tratamiento con TCEP se usó con LC-CAD-MS y se comparó con $^1$H NMR después del tratamiento con KCN/KOH. Al igual que con la $^1$H NMR, los picos relacionados con el TCEP se identificaron, el CAD determinó la proporción y las estructuras se confirmaron por espectrometría de masas. Se realizaron diferentes reacciones de post funcionalización utilizando PEG con amina terminal o ácido carboxílico. Las proporciones de ligando calculados por CAD, realizadas sin estándares de calibración, demostraron la validez de la respuesta dependiente de la masa con los compuestos estudiados (monosacáridos, oligo-PEG y oligo-PEG funcionalizado). Además, LC-CAD-MS mostró su superioridad cuando se realizaron reacciones de múltiples pasos con ligandos de peso molecular más alto y que la complejidad de los espectros de $^1$H NMR impidió su interpretación.

- **Capítulo III**

La funcionalización "covalente" de las GNP ultra pequeñas se puede obtener a través de diferentes métodos:

- *One-Pot Synthesis*: síntesis Brust-Schiffrin modificada utilizando borohidruro de sodio como agente reductor en presencia de una sal de oro y ligandos de tiol o disulfuro.
- Post-funcionalización: se realizan reacciones a través de rutas de síntesis orgánicas comunes entre los ligandos unidos a las GNP y moléculas con grupos funcionales complementarios.
- Intercambio de ligando: incorporación a las GNP de nuevos ligandos a través de grupos con tiol o disulfuro reemplazando los previamente unidos o llenando sitios vacíos en el núcleo.

La post-funcionalización consiste en usar reacciones orgánicas específicas simples que pueden definirse como química bioortogonal. Desde el punto de vista de la síntesis, tiene la ventaja de permitir el control estequiométrico de manera simple. Además, los puntos de unión de la molécula suelen estar en el extremo terminal de las GNP, lo que permite una presentación adecuada en la parte externa de la plataforma. La otra ventaja principal es la purificación que se realiza comúnmente por ultrafiltración o diálisis.

Se necesitan reacciones fáciles, rápidas, selectivas y reproducibles con altos rendimientos para post-funcionalizar las GNP. Las reacciones de bioconjugación que utilizan principios de química orgánica se han optimizado y documentado ampliamente, lo que llevó a la creación de una biblioteca de enlaces formados por grupos funcionales compatibles, junto con sus agentes de activación y catalizadores. Estos principios se han aplicado ampliamente a las GNP.

Para este trabajo, se eligieron cuatro tipos de reacciones: condensación de isotiourea, condensación de amida (amina con ácido o anhídrido carboxílico), cicloadición de azida-alquino Huisgen (química clic) y reacciones *Schiff base-like*.

Como molécula principal para el diseño y la optimización de estas rutas sintéticas se utilizó una biblioteca de derivados de α-manosa junto con oligosacáridos. Los derivados de α-manosa se sintetizaron con diferentes grupos funcionales: amina, ácido carboxílico, azida, alquino e isotiocianato.

Se sintetizaron GNP con grupos complementarios para realizar la post-funcionalización con el objetivo de lograr el mayor grado de funcionalización, usando plataformas bifuncionalizadas hechas con oligo-PEG positivo (PEG(5)NH$_2$) o negativo (PEG(8)COOH) y un monosacárido con una cadena lateral corta ($\alpha$-Galactose-C$_2$ o $\beta$-Glucose-C$_2$). También se unieron oligosacáridos a una amino-oxi-GNP a través de un enlace oxima.

La adaptación de la química bioortogonal a las plataformas de GNP ultra pequeñas se logró con éxito. La modificación del grupo funcional terminal del PEG se alcanzó en rendimientos cuantitativos, dando como resultado la presentación de nuevas funciones. Esto valida la post-funcionalización como un método directo para modificar el grupo terminal de oligo-PEG en GNP utilizando moléculas de bajo peso molecular disponibles comercialmente. La posterior funcionalización con derivados de $\alpha$-manosa dio como resultado diferentes rendimientos dependiendo de la ruta elegida. La conclusión principal es que las vías más simples proporcionan los mejores rendimientos. Una cadena de alquino más larga con la $\alpha$-manosa también tuvo efectos positivos en los rendimientos. Con ambos PEG amino y carboxílico, las reacciones de acoplamiento de amida proporcionaron rendimientos relativamente altos, haciendo de esta ruta la más adecuada para experimentos adicionales.

La vía amino-oxi con los enlaces oxima dio buenos resultados, a pesar del alto número de pasos y la complejidad de los carbohidratos utilizados (2-$O$-($\alpha$-D-mannopiranosil)-D-manopiranosa, 1,3-$\alpha$-1,6-$\alpha$-D-manotriosa y maltotriosa). Una vez superados los desafíos de la síntesis y caracterización, se demostró que la ruta de la oxima era una vía sencilla para la funcionalización de las GNP. La ausencia de la necesidad de funcionalización de los carbohidratos lo convierte en un excelente método para unir carbohidratos complicados a bajo coste y esfuerzo.

- **Capítulo IV**

Los receptores de lectinas de tipo C (CLR) son una amplia familia de proteínas de origen no inmune, sin actividad catalítica, capaces de unirse inversamente a carbohidratos exógenos o endógenos. Poseen uno o varios dominios de reconocimiento de carbohidratos (CRD) que determinan la especificidad del ligando.

Los CLR transmembrana están presentes en las células presentadoras de antígenos (APC), como las células dendríticas (DC) y los macrófagos. Reconocen glicoepítopos propios y ajenos. Al reconocer sus ligandos a través de CLR, los APC tienen la capacidad de capturarlos, internalizarlos, procesarlos y presentarlos en su superficie. A diferencia de los macrófagos, las DC son APC profesionales con capacidad para inducir una fuerte respuesta inmune adaptativa con un bajo nivel de antígeno. Están ampliamente distribuidos y tienen una movilidad importante que los convierte en los centinelas del cuerpo.

Las APC poseen una gran variedad de CLR para reconocer a los patógenos, entre ellos, los CLR que reconocen manosa (mrCLR), como DC-SIGN (molécula de adhesión intercelular específica de células dendríticas-3-Grabing no integrina). DC-SIGN es un mrCLR que reconoce el ligando *High Mannose* y sus derivados. Está implicado en el reconocimiento y la captación de numerosos patógenos como el VIH. La estructura truncada de *High Mannose* α-manosa1,2α-manosa ha mostrado una buena eficiencia y tiene la ventaja de ser más fácil de obtener sintéticamente.

Se pueden usar carbohidratos para hacer *targeting* de los CLR, pero tienen el inconveniente de interactuar con varias lectinas y tener una interacción muy débil. Para mejorar el *targeting* de un ligando tipo glicano a un CLR, se puede usar un sistema multivalente y potenciar la interacción mediante el efecto cluster glicosídico. El fenómeno se logra mediante la oligomerización o agrupamiento de CLR y la presentación multivalente de los glicanos.

Las GNP son una de las plataformas multivalentes que pueden hacer *targeting* de los CLR, gracias al acoplamiento de varias copias de carbohidratos en la misma GNP. Su versatilidad permite el ajuste para adaptarse a los CRD de las CLR y obtener una afinidad óptima. El objetivo principal del *targeting* de APC es el diseño de vacunas en dos campos principales: patógenos y cáncer. Esas vacunas dependerían de las células T (inmunidad adaptativa celular).

Reconociendo el potencial de las GNP para hacer *targeting* a los CLR y particularmente DC-SIGN, se han utilizado GNP ultra pequeñas con dos tamaños de núcleo diferente: 2 y 4 nanómetros unidas a α-manosa o unos derivados a través de reacciones de post-funcionalización.

Se han intentado dos estrategias:
- Usando el monómero α-manosa y multiplicando el número de moléculas por partícula usando dendrones (tridentes de 3 o 9 ramas).
- Usando el α-manosa1,2α-manosa, el dímero de la estructura *High Mannose* y glicomiméticos desarrollados para mejorar sus características: ISh045 e ISh046.

Para seleccionar las GNP, se han utilizado dos técnicas bioquímicas: *microarrays* de lectina con detección fluorescente y *biolayer interferometry* (BLI). El *microarray* de lectina se realizó con una amplia biblioteca de lectinas para optimizar el ensayo. El BLI se realizó utilizando DC-SIGN. Además, un ensayo de internalización celular *in vitro* se realizó en células que expresan DC-SIGN (THP-1). También se ha realizado un ensayo *in vivo* de farmacocinética y biodistribución en ratas con GNP funcionalizados con α-manosa.

Los experimentos de *microarrays* de lectina demostraron con éxito la capacidad de las GNP de 2 y 4 nm para apagar la fluorescencia emitida por las lectinas inmovilizadas en un chip. El experimento demostró la importancia del tamaño del núcleo y por lo tanto la presentación del azúcar en la GNP: las GNP de 2 nm con derivados de α-manosa solo se unieron a una de las tres lectinas vegetales específicas de manosa: ConA, mientras que las GNP de 4 nm se unieron a ConA, HHL y NPL. Por otra parte, GNP decoradas con β-galactosa se unieron a lectinas que reconocen el epítopo β-galactosa (PA-IL), indicando la especificidad de este ensayo. En general y a pesar de que mostraron cierta interacción inespecífica, las GNP de 4 nm fueron claramente superiores en comparación con las de 2 nm. El dímero α-manosa1,2α-manosa y sus miméticos también tuvieron una interacción superior al monómero α-manosa, incluso aunque éste estuviese presentado en un dendrón.

La *biolayer interferometry,* usando la lectina DC-SIGN, confirmó las diferencias entre las plataformas de 2 nm y 4 nm. Sólo las GNP de 4 nm pudieron unirse a DC-SIGN. La $\alpha$-manosa1,2$\alpha$-manosa y sus miméticos demostraron una interacción superior a la del monómero $\alpha$-manosa. GNP de 4 nm con $\alpha$-manosa1,2$\alpha$-manosa y los miméticos ISh046 e ISh045 dieron unos valores de $K_D$: 0,99, 0,38 y 1,15 nM respectivamente mientras que en el caso de la $\alpha$-manosa se obtuvo un valor de 6.80 nM.

La captación celular con células THP-1 que expresan DC-SIGN (mimética de células dendríticas) fue en línea con el ensayo BLI con DC-SIGN. Solo los derivados de $\alpha$-manosa funcionalizados con GNP de 4 nm mostraron un aumento significativo en la internalización. La internalización cuantificada en términos de cantidad de oro fue mejorada por $\alpha$-manosa1,2$\alpha$-manosa y los miméticos alrededor de 30 veces mientras $\alpha$-manosa solo 6 veces. Las GNP no funcionalizadas mostraron una absorción basal muy baja. La baja absorción inespecífica y la alta absorción específica de las GNP de 4 nm con derivados de $\alpha$-manosa los convierten en excelentes candidatos para el *targeting* específico de células inmunes como las células dendríticas.

El ensayo de biodistribución mostró resultados interesantes sobre el destino *in vivo* de GNP con $\alpha$-manosa. Con una inyección sistemática estaban presentes después de 24 horas en la sangre y la piel. No se detectó toxicidad aguda.

# Introduction


# Gold and Glyco Nanoparticles

# I.    Gold Nanoparticles

Gold Nanoparticles, also referred to as AuNP or GNP, are among the most stable metal nanoparticles. They have excellent characteristics for biotechnological/clinical use: optoelectronic properties, large surface to volume ratio, versatility, stability, ease of synthesis, biocompatibility and low toxicity[1]. Their physicochemical properties are dependent on their size, shape, organic shell and the interparticle distance. GNP can be divided between clusters and colloids/crystals with regard to their size (1-100 nm)[2] and can present various shapes: spherical (nanosphere) or anisotropic (e.g. nanorods, nanotubes, nanostars)[3].

For their synthesis, two approaches are possible, top-down or bottom-up, with three types of methods: chemical, physical or biological[4].

The chemical bottom-up *in situ* synthesis is the oldest one and remains the most used for spherical GNP[5]. *In situ* refers to a one-step synthesis for the core formation, as opposed to multi-step methods such as seed growth. Briefly, larger GNP are synthesized through citrate reduction of tetrachloroauric acid ($HAuCl_4$) in water by a method first defined by Turkevich et al. in 1951[6] and optimized by Frens et al. in 1973[7]. Ultrasmall GNP, or nanoclusters (< 5 nm), are obtained by Brust-Schiffrin synthesis[8] (BSS) using sodium borohydride ($NaBH_4$) as a reducing agent.

In this thesis, the focus will be on the ultrasmall GNP obtained through a modified Brust-Schiffrin method to produce a spherical core of 1-5 nm. It was first published in 1994, and, since then, has been optimized by various groups to a single-phase method to obtain water-soluble GNP[9,10].

Ultrasmall GNP are characterized by the absence (for the 1 nm core) or the low (up to 5 nm core) surface plasmon resonance (SPR) and light scattering. For spherical GNP, the surface plasmon band (SPB) is located around 520 nm but is very sensitive not only to the GNP itself, but also its environment[11]. Two other distinctive properties of GNP are the ability to quench fluorescence and the redox activity[12].

GNP are hybrid inorganic/organic platforms that can be divided in two parts: the core made of gold ($Au^0$), governing the physical behavior, and the shell or corona, consisting of organic material that dictates the chemical behavior[13]. Two interfaces can also be defined: the gold core-organic shell and the organic shell-medium (*Figure 1*). The combination of the four parameters determines the GNP efficacy, toxicity and PKBD (pharmacokinetics and biodistribution).



Organic Corona-Medium Interface

Organic Corona/Shell

Gold Core-Organic Corona Interface
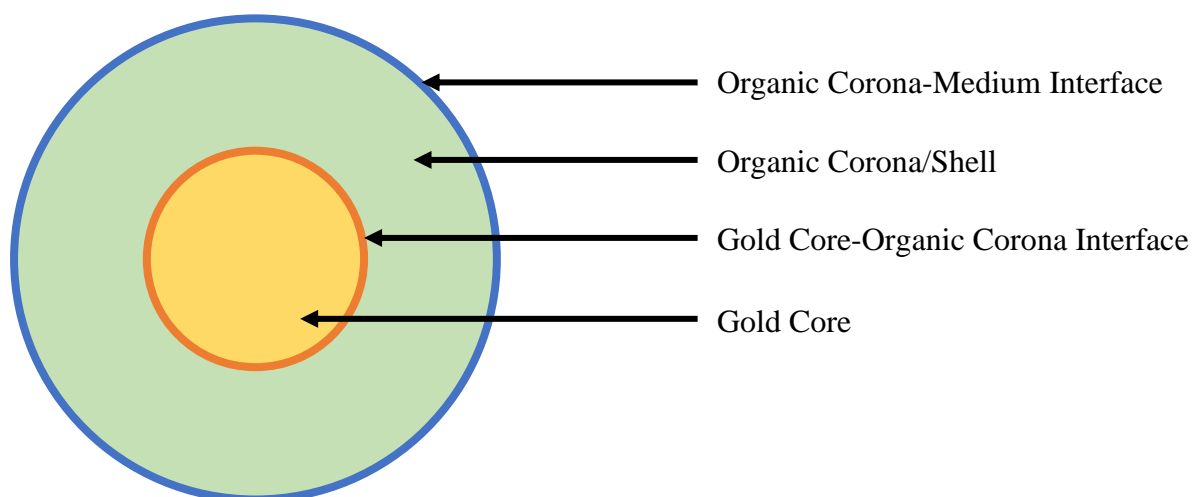
Gold Core

*Figure 1: General configuration of GNP. Spherical model.*

The organic corona can be made of various molecules referred to as ligands or linkers, which are bound either to the gold core or to another ligand. They act as a shell, interacting with the environment (solvents or biological media) and provide stability by preventing aggregation (e.g. by electrostatic repulsion, hydration of the surface and steric exclusion)[14]. As a multifunctional system, particles can be made of more than one type of ligand and four chemical strategies can be used to add ligands to the nanoparticle: physical adsorption, electrostatic binding, specific affinity recognition and covalent coupling[12].

The binding between the gold core and the ligands can be achieved through various chemical functionalities such as carboxylic acid, amine, phosphine or thiol. The main form of covalently binding to nanoparticulate gold is the is the sulfur to gold (S-Au) bond formed by thiol or disulfide ligands. Sulfurs atoms have the strongest interaction with gold (200 kJ/mol)[14]. The S-Au bond can only be displaced by another thiol, such as intracellular glutathione[15], and is mildly affected by oxidation.

The strength of the binding can be modulated by changing the interface. For example, bidentate groups, such as 1,2-dithiane or dithiocarbonate (e.g. lipoic acid), increase the strength of the ligand-gold bond, whereas amine or carboxylate groups bind less strongly[2,16]. This is an important factor, since a stronger binding, together with a denser ligand shell, improves the stability of the whole construct.

GNP allow the presentation in high quantity of virtually any type of organic molecule. The organic ligands forming the corona can be materials such as lipids, peptides, proteins, carbohydrates, nucleic acids, drugs, probes (e.g. fluorescent dyes) or polymers (e.g. polyethylene glycols)[17]. The type of ligand strongly impacts the biological properties of the GNP, for example functions such as the stealth ability (depending on the ligand length and bulk), targeting or payload delivery. Moreover, the outermost functional group and its charge are of utmost importance, since it is in direct contact with the environment and, therefore, influences the interactions with media, cells and amongst particles[18,19].

GNP in diagnostic and therapeutic areas have a wide range of applications. For diagnostic purposes, GNP can be used as contrast agents in biomedical imaging or as sensors[20,21]. For therapeutic approaches, GNP are mainly used in research programs to treat microorganism infections (antibiotics), cancer (antitumoral drugs) or as vaccines (adjuvant or delivery system)[22].

The use of GNP for cancer therapy relies on various principles and mechanisms, which can also be applied to other areas, namely[1]:
- Multivalency: several copies of antigens or drugs can be delivered in a single construct.
- Multifunctionality: different payloads can be bound to the GNP.
- Solubility: enable hydrophobic molecule solubilization in water.
- Stealth: hiding the GNP and attached drugs from potential clearance by the Reticulo-Endothelial System (RES), thereby improving half-life.
- Passive targeting: through Enhanced Permeability and Retention (EPR) effect due to leaky vasculature of the tumors.
- Active delivery: using a targeting agent to improve cell uptake (e.g. endocytosis)[13].
- Photothermal therapy (PTT) using a laser to generate heat or photodynamic therapy (PDT) using photosensitizers and oxygen[23].

## II. Glycoscience and Nanoparticles

Glyconanotechnology is the combination of glycoscience and nanotechnology, in which carbohydrates and nanoparticles work in a synergistic way[24].

Carbohydrates, often referred to as sugars or saccharides, are one of the four classes of biomolecules (alongside proteins, lipids and nucleic acids). They are often conjugated with other biopolymers and are involved in many biological and pathological processes[25]. The diversity of the monomers, linkage points, anomeric configurations and substitutions with different chemical groups form a complex glyco-code[26].

There are two ways carbohydrates can be used with nanoparticles[25]:
- To improve stability (avoid aggregation), solubility, biocompatibility, biodegradability and confer stealth (protein-repellant) properties[27].
- As a targeting agent, using multivalency to improve the avidity of the carbohydrate for its receptor through the cluster glycoside effect[28]. Carbohydrate receptors usually belong to the lectin family and their interaction with carbohydrates, although highly specific, is weak.

Applications of glyconanoparticles are broad and have been extensively documented[26,29,30,31]:
- Bioassays: receptor interaction studies (carbohydrate-carbohydrate and carbohydrate-protein interactions).
- Diagnostic and detection (biosensors, molecular imaging).
- Therapy through inhibition or antagonism (anti-adhesive therapy against pathogens), drug delivery or vaccines (cancer or microorganisms).

Among glyconanoparticles, the high valency and the versatility of GNP make them an ideal synthetic scaffold which can be easily designed/adjusted to offer proper orientation and spacing for the desired application[32]. Other scaffolds include silver particles, magnetic particles, quantum dots, dendrimers, polymers, neoglycoproteins, liposomes or micelles[30,33].

Ultrasmall Glyco-GNP were first synthesized in 2001 by Penadés et al., following a modified Brust-Schiffrin synthesis to take advantage of the globular shape with glycocalyx-like surface form of GNP[10]. The ultrasmall Glyco-GNP versatility was later demonstrated with various carbohydrates and other types of molecules (peptides, probes) in multimodal systems[33,34].

# III.   Midatech Pharma's Midacore<sup>TM</sup> Platform

Midatech Pharma's Midacore<sup>TM</sup> GNP platform has been extensively developed and is protected by a family of more than 20 patents (*Figure 2*).

The GNP are obtained through a modified Brust-Schiffrin synthesis to get ultrasmall non-plasmonic (2 nm core) and plasmonic (4 nm core) particles. The reaction consists in the one-step *in situ* reduction of a gold salt in the presence of ligands which are bound to the gold core through S-Au bonds.

Midacore<sup>TM</sup> GNP are usually bifunctional with two types of ligands: a non-immunogenic monosaccharide with short alkyl side chain and an oligo-ethylene glycol with a functional terminal unit[35,36,37]. The monosaccharides are essentially 2'-Thioethyl α-D-galactopyranoside (α-Galactose-$C_2$) or 2'-Thioethyl β-D-glucopyranoside (β-Glucose-$C_2$). The PEG are mainly α-Thio-ω-(propionic acid) octa(ethylene glycol) (PEG(8)COOH, 1-mercapto-3,6,9,12,15,18,21,24-octaoxaheptacosan-27-oic acid) or α-Thio-ω-aminoethyl penta(ethylene glycol) (PEG(5)$NH_2$, 1-amino-17-mercapto-3,6,9,12,15-pentaoxa-heptadecanol).

The platform is versatile since it permits the modulation of the ligand ratio or the removal of one of the compounds.

Polyethylene glycols (PEG) are flexible molecules (composed of repeating -$CH_2$-$CH_2$-O- units) forming heavily hydrated coils on the surface of particles. They are relatively inert (non-immunogenic) and soluble in water, as well as most polar organic solvents (e.g. DMSO, methanol). They possess a strong ability to stabilize particles by preventing nanoparticle aggregation at high ionic concentration and non-specific interactions with proteins (e.g. protein corona)[38] or cells[39]. They also improve the characteristics of the nanoparticles *in vitro* and *in vivo*, such as half-life or oral bioavailability[40]. This is partly due to the capacity to evade the Mononuclear Phagocyte System (MPS), a macrophage mediated uptake after protein adsorption on the nanoparticle surface. The PEG terminal group is critical, as it impacts the stability and biological behavior of the particles[41] (e.g. PEG(5)$NH_2$ if protonated can lead to aggregation). The functional group of the PEG can additionally be used to bind to molecules presenting a complementary moiety to achieve active targeting, drug delivery or to obtain PKBD improvement[17]. The PEG may also be branched (rather than linear), longer or present a different terminal group.

Once the particle is obtained, two strategies can be applied to add new ligands: post-functionalization[42] and ligand place exchange[43]. Ligand place exchange refers to a reaction in which a thiol or disulfide ligand is added to the GNP solution and binds directly to the core (either to a free binding site or by replacing another ligand on the surface). Post-functionalization is a reaction where ligands on the GNP (e.g. functional PEG) react with molecules added to the solution. It involves functional groups and traditional bioorthogonal organic chemistry. Using these two approaches, a wide range of compounds can be added to the particle shell.

Midacore™ has been used in different pipelines of research employing a wide range of molecules.

In the field of diabetes, GNP were used as a carrier for the loading of peptides such as insulin and its analogues[44], glucagon and glucagon-like peptide[45,46] and amylin[47]. Insulin-GNP combined with a buccal drug delivery system were tested up to clinical stages[48]. An immunotherapy strategy using the autoantigen peptide proinsulin (C19A3) for the treatment of type-1 diabetes also went through clinical trials[49,50,51].

Peptide-based immunotherapies were largely developed for cancer[52,53]. For instance, H3.3K27M (histone H3.3 with amino acid substitution mutation lysine 27 to methionine)[54] was used to treat diffuse intrinsic pontine glioma (DIPG). Moreover, peptides such as the cyclic Arginylglycylaspartic acid (cRGD) or SIKVAV[55] were used for the targeting of cancer cells expressing integrin receptors. A wide range of antitumoral molecules were also loaded onto Midacore™ GNP (e.g. doxorubicin, irinotecan, platins, temozolomide, docetaxel, sorafenib)[56,57]. For example, the antitubulinic drug mertansine (DM1) was used to create a hepatocellular carcinoma (HCC) therapy[58].

Auto-immune diseases were also an area of interest, with the development of a methotrexate-GNP gel for psoriasis treatment[59].

Other Midacore™ applications include conjugation to antibacterial drugs (e.g. amoxicillin, ciprofloxacin, rifampicin, vancomycin)[60] or peptides for prophylactic treatment against infectious agents[61], GNP use for intracellular delivery of peptides to obtain a Cytotoxic T Lymphocyte (CTL) response[62], treatment of osteoporosis with teriparatide[63] or binding to nucleic acids[64].
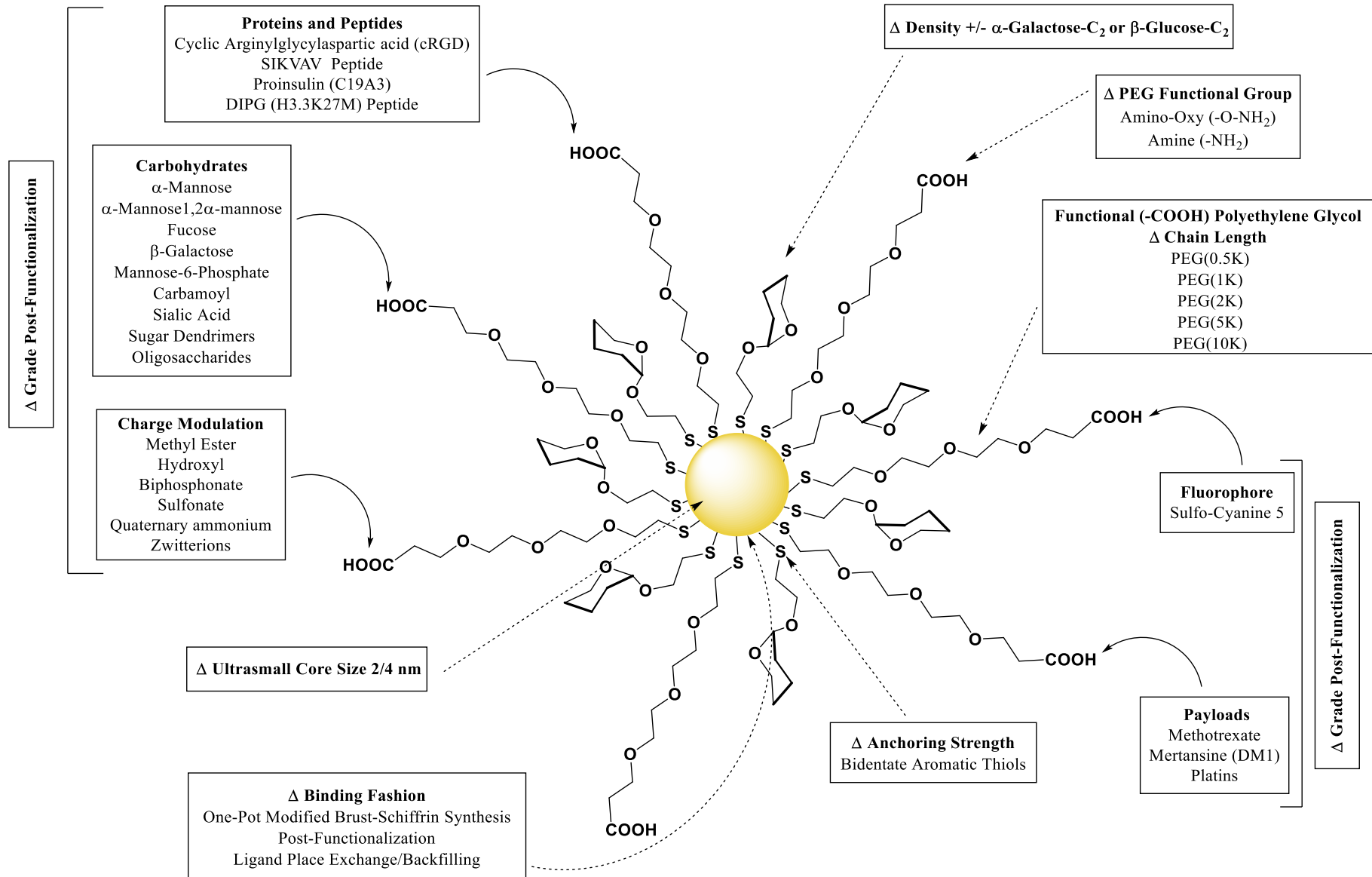
*Figure 2: Summary of Midatech Pharma Midacore$^{TM}$ gold nanoparticle platform.*

# IV. Immunoshape - Thesis Objectives

The objective of the work described in this thesis was to improve and broaden the Midacore™ ultrasmall GNP platform and to use it with carbohydrates of immunological interest. The chemistry can be divided into two parts: GNP and carbohydrates. The GNP part was performed within Midatech Pharma, while the carbohydrates were either made in house or obtained through partners of the H2020 European network Immunoshape (Grant agreement ID: 642870)[65]. Immunoshape is a Marie Sklodowska Curie European Training Network composed of 14 European public and private research groups "providing multidisciplinary and multisectoral training in biomedical glycoscience and its industrial applications to a new generation of young scientists". The biochemical and biological parts were performed within Midatech facilities and during secondments in other Immunoshape research groups.

Using the platform mentioned previously, special focus was put on the post-functionalization of GNP using carbohydrates involved in immune mechanisms. $\alpha$-Mannose and its derivatives were the molecules of choice for the chemical development of the platform, but other carbohydrates (e.g. $\beta$-galactose and oligosaccharides) were also included in the research.

To deliver reliable and reproducible material, a strong process control and a broad array of analytical techniques are necessary. This is particularly relevant for complex systems such as GNP. An investigation of the factors affecting the particle quality during a one-pot aqueous Brust-Schiffrin synthesis was conducted using 2 nm bifunctional GNP made of $\alpha$-Galactose-$C_2$ or $\beta$-Glucose-$C_2$ and PEG(8)COOH or PEG(5)NH$_2$. The syntheses were performed using a benchtop reactor at medium scale to ensure the most controlled environment.

Brust-Schiffrin synthesis can be divided into three steps: first, pre-nucleation of the gold salt and mixing with ligands, second, nucleation with sodium borohydride addition, which leads to an immediate formation of the particle, and, last, passivation, which corresponds to the interaction of the newly formed GNP with an excess of ligands and sodium borohydride.

Of the three steps, the passivation step was explored. Using one-parameter modifications, several batches were synthesized. The influence of time of passivation (before purification), pH, temperature and nature of the ligands were monitored. Two GNP characteristics, size and ligand shell, were thoroughly investigated.

The parameters were tightly controlled, (e.g. pH 12 or > 12.5 and temperature 18 or 25 °C) aiming at the delivery of material in quantities to supply clinical trials with methods transferable to GMP (Good Manufacturing Practice) production. The capacity of ion exchange resins (IRA-400) to scavenge sodium borohydride during the passivation and its impact on the GNP were also evaluated. Finally, no process can be developed without the analytical feedback. Therefore, the products obtained were analyzed with several analytical techniques to characterize the core and the particle size, as well as the corona ligand ratio and density. Each technique was optimized and tailored for ultrasmall GNP. The information obtained was then cross analyzed to obtain the most accurate picture of the material.

As previously mentioned, GNP require a comprehensive array of techniques to fully characterize them. The ligand corona plays an extremely important role and should be thoroughly described. To do so, novel analytical techniques are required. A Liquid Chromatography methodology using with Charged Aerosol Detection coupled with Mass Spectrometry (LC-CAD-MS) was developed to characterize multivalent 2 nm GNP. The ligand ratios after Brust-Schiffrin synthesis and post-functionalization were determined by LC-CAD-MS and compared to Proton Nuclear Magnetic Resonance (^{1}H NMR), a widely used technique for the determination of ligand ratios. For both techniques, an etching pre-treatment is necessary to dissolve the core and release the ligands. While potassium cyanide (KCN), a common gold oxidizing agent works well for ^{1}H NMR, chromatographic techniques, such as LC-CAD-MS require an etching molecule that maintains all the ligands in their reduced thiol form (no ligand disulfide recombination), and, at the same time, completely dissolves the core. For this reason, a pre-treatment using tris(2-carboxyethyl)phosphine (TCEP) was developed.

The main feature of CAD is its capacity to detect weak or non-UV absorbent species and its mass-dependent response. For those reasons, it was suited to the analysis of Glyco-GNP to detect molecules such as carbohydrates or oligo-PEG. Moreover, the mass-dependent response allowed the semi-quantification of analytes without standards for ratio determination after post-functionalization reactions. The mass spectrometer completed the analysis with identification of the ligands through their m/z values.

To add new ligands to the GNP platform, post-functionalization was used. Different bioorthogonal chemical reactions were performed to achieve the most efficient ligand loading[66].

A library of α-mannose derivatives was synthesized by derivatization of α-mannose pentaacetate. The monosaccharide was chemical modified to present a rigid side chain with a terminal functional moiety. A diverse range of terminal groups was studied, including carboxylic acid, amine, alkyne, azide or isothiocyanate. To bind the α-mannose derivatives to the bifunctional 2 nm GNP, the oligo-PEG were used. Terminal carboxylic acid PEG or pegamine were linked to the complementary α-mannose derivative. Also, modification of the terminal PEG function was performed to present other binding groups (such as azide, alkyne or amino-oxy) or protecting groups (for example acetyl, methyl ester or hydroxyl). Finally, GNP bearing amino-oxy PEG functionality were reacted with non-modified oligosaccharides to attach to the carbohydrates through an oxime bond.

The main purpose of the Immunoshape consortium was the "Development of selective carbohydrate immunomodulators targeting C-type lectin receptors on antigen presenting cells". Within that framework, Midacore[TM] GNP were used as a multivalent system for the targeting of C-type lectins using carbohydrate conjugates[67,68].

α-Mannose and related ligands were coupled to the GNP to take advantage of the cluster-glycoside effect. In fact, oligosaccharides containing α-mannose are implicated in many physiological or pathological mechanisms through their interaction with mannose-recognizing C-type lectin receptors (mrCLR), such as Dendritic Cell-Specific Intercellular adhesion molecule-3-Grabbing Non-integrin (DC-SIGN).

Biochemical assays, as well as *in vitro* and *in vivo* biological experiments, were performed to obtain and optimize the affinity between Glyco-GNP and lectins and use these receptors to improve cell targeting. A GNP library composed of linear and ramified (dendrons) α-mannose as well as α-mannose1,2α-mannose and two synthetically enhanced mimetics (ISh045 and ISh046) was designed. Two sizes of GNP, non-plasmonic (2 nm core) and plasmonic (4 nm core), were employed to assess the importance of the particle size, curvature and multivalency. Apart from the α-mannose derivatives, controls such as β-galactose functionalized GNP completed the library.

A lectin microarray using ultrasmall GNP fluorescence quenching properties was developed. It consisted in widely used and well characterized lectins of different origin (plants, microorganisms and humans) with different structures and carbohydrate affinity. Fluorescent lectins were printed on a chip and incubated with the GNP. The goal was to validate the capacity of GNP to specifically bind to the lectins through their carbohydrate corona and obtain a quenching of fluorescence.

Biolayer interferometry (BLI), a label-free technology for measuring biomolecular interactions, was used to screen and select the best constructs for the targeting of DC-SIGN. DC-SIGN is a tetravalent α-mannose specific lectin present on macrophages and dendritic cells (DC) and is implicated in the immune adaptive response. *In vitro* experiments were then performed to determine if the binding affinity measured by BLI correlated with an effective uptake with DC-SIGN expressing cells (differentiated THP-1 cells).

*In vivo* experiments were also performed with rats to get insights about the fate of α-mannose decorated ultrasmall GNP after systemic administration.

To summarize, the research was divided into the following chapters:
- *Chapter I* was dedicated to the study of the passivation phase of the aqueous Brust-Schiffrin synthesis.
- *Chapter II* to the development of a new analytical technique, LC-CAD-MS with an improved pre-treatment, TCEP, to characterize the ligand shell.
- *Chapter III* to the synthesis of α-mannose derivatives and the optimization of post-functionalization pathways with those derivatives as well as non-modified oligosaccharides.
- *Chapter IV* to the use of a GNP library to study the interaction with C-type lectins and improve the uptake in immune cells through DC-SIGN binding.

# V. References

1.      Singh, P. *et al.* Gold Nanoparticles in Diagnostics and Therapeutics for Human Cancer. *Int. J. Mol. Sci.* **19**, 1979 (2018).

2.      Daniel, M.-C. & Astruc, D. Gold nanoparticles: assembly, supramolecular chemistry, quantum-size-related properties, and applications toward biology, catalysis, and nanotechnology. *Chem. Rev.* **104**, 293–346 (2004).

3.      EUSMI / European Soft Matter Infrastructure. https://eusmi-h2020.eu/access/wp4/NSL-BIOMA.

4.      Elahi, N., Kamali, M. & Baghersad, M. H. Recent biomedical applications of gold nanoparticles: A review. *Talanta* **184**, 537–556 (2018).

5.      Zhao, P., Li, N. & Astruc, D. State of the art in gold nanoparticle synthesis. *Coord. Chem. Rev.* **257**, 638–665 (2013).

6.      Turkevich, J., Stevenson, P. C. & Hillier, J. A study of the nucleation and growth processes in the synthesis of colloidal gold. *Discuss. Faraday Soc.* **11**, 55–75 (1951).

7.      Frens, G. Controlled Nucleation for the Regulation of the Particle Size in Monodisperse Gold Suspensions. *Nat. Phys. Sci.* **241**, 20–22 (1973).

8.      Brust, M., Walker, M., Bethell, D., Schiffrin, D. J. & Whyman, R. Synthesis of thiol-derivatised gold nanoparticles in a two-phase Liquid–Liquid system. *J. Chem. Soc. Chem. Commun.* 801–802 (1994).

9.      Brust, M., Fink, J., Bethell, D., Schiffrin, D. J. & Kiely, C. Synthesis and reactions of functionalised gold nanoparticles. *J. Chem. Soc. Chem. Commun.* 1655–1656 (1995).

10.     Fuente, J. M. de la *et al.* Gold Glyconanoparticles as Water-Soluble Polyvalent Models To Study Carbohydrate Interactions. *Angew. Chem. Int. Ed.* **40**, 2257–2261 (2001).

11.     Boisselier, E. & Astruc, D. Gold nanoparticles in nanomedicine: preparations, imaging, diagnostics, therapies and toxicity. *Chem. Soc. Rev.* **38**, 1759–1782 (2009).

12.     Yeh, Y.-C., Creran, B. & Rotello, V. M. Gold nanoparticles: preparation, properties, and applications in bionanotechnology. *Nanoscale* **4**, 1871–1880 (2012).

13. Arvizo, R., Bhattacharya, R. & Mukherjee, P. Gold nanoparticles: opportunities and challenges in nanomedicine. *Expert Opin. Drug Deliv.* **7**, 753–763 (2010).

14. Sperling, R. A. & Parak, W. J. Surface modification, functionalization and bioconjugation of colloidal inorganic nanoparticles. *Philos. Trans. R. Soc. Lond. Math. Phys. Eng. Sci.* **368**, 1333–1383 (2010).

15. Hong, R. *et al.* Glutathione-mediated delivery and release using monolayer protected nanoparticle carriers. *J. Am. Chem. Soc.* **128**, 1078–1079 (2006).

16. Vigderman, L. & Zubarev, E. R. Therapeutic platforms based on gold nanoparticles and their covalent conjugates with drug molecules. *Adv. Drug Deliv. Rev.* **65**, 663–676 (2013).

17. Conde, J. *et al.* Revisiting 30 years of biofunctionalization and surface chemistry of inorganic nanoparticles for nanomedicine. *Front. Chem.* **2**, (2014).

18. Jia, Y.-P., Ma, B.-Y., Wei, X.-W. & Qian, Z.-Y. The in vitro and in vivo toxicity of gold nanoparticles. *Chin. Chem. Lett.* **28**, 691–702 (2017).

19. Guerrini, L., Alvarez-Puebla, R. A. & Pazos-Perez, N. Surface Modifications of Nanoparticles for Stability in Biological Fluids. *Materials* **11**, 1154 (2018).

20. Peixoto de Almeida, M. *et al.* Chapter 13 - Gold Nanoparticles as (Bio)Chemical Sensors. in *Comprehensive Analytical Chemistry* vol. 66 529–567 (Elsevier, 2014).

21. Nune, S. K. *et al.* Nanoparticles for biomedical imaging. *Expert Opin. Drug Deliv.* **6**, 1175–1194 (2009).

22. Carabineiro, S. A. C. Applications of Gold Nanoparticles in Nanomedicine: Recent Advances in Vaccines. *Molecules* **22**, 857 (2017).

23. Dykman, L. A. & Khlebtsov, N. G. Gold Nanoparticles in Biology and Medicine: Recent Advances and Prospects. *Acta Naturae* **3**, 34–55 (2011).

24. Reichardt, N. C., Martín-Lomas, M. & Penadés, S. Glyconanotechnology. *Chem. Soc. Rev.* **42**, 4358–4376 (2013).

25. de la Fuente, J. M. & Penadés, S. Glyconanoparticles: types, synthesis and applications in glycoscience, biomedicine and material science. *Biochim. Biophys. Acta* **1760**, 636–651 (2006).

26.     Marradi, M., Chiodo, F. & García, I. Glyconanotechnology and Disease: Gold Nanoparticles Coated with Glycosides as Multivalent Systems for Potential Applications in Diagnostics and Therapy. in *Carbohydrates in Drug Design and Discovery* 89–131 (The Royal Society of Chemistry, 2015).

27.     Kang, B., Opatz, T., Landfester, K. & R. Wurm, F. Carbohydrate nanocarriers in biomedical applications: functionalization and construction. *Chem. Soc. Rev.* **44**, 8301–8325 (2015).

28.     Lundquist, J. J. & Toone, E. J. The Cluster Glycoside Effect. *Chem. Rev.* **102**, 555–578 (2002).

29.     Adak, A. K., Li, B.-Y. & Lin, C.-C. Advances in multifunctional glycosylated nanomaterials: preparation and applications in glycoscience. *Carbohydr. Res.* **405**, 2–12 (2015).

30.     Marradi, M., Martín-Lomas, M. & Penadés, S. Glyconanoparticles: Polyvalent Tools to Study Carbohydrate-Based Interactions. in *Advances in Carbohydrate Chemistry and Biochemistry* vol. 64 211–290 (Academic Press, 2010).

31.     García, I., Marradi, M. & Penadés, S. Glyconanoparticles: multifunctional nanomaterials for biomedical applications. *Nanomed.* **5**, 777–792 (2010).

32.     Compostella, F., Pitirollo, O., Silvestri, A. & Polito, L. Glyco-gold nanoparticles: synthesis and applications. *Beilstein J. Org. Chem.* **13**, 1008–1021 (2017).

33.     Marradi, M., Chiodo, F., García, I. & Penadés, S. Glyconanoparticles as multifunctional and multimodal carbohydrate systems. *Chem. Soc. Rev.* **42**, 4728–4745 (2013).

34.     Barrientos, Á. G., Fuente, J. M. de la, Rojas, T. C., Fernández, A. & Penadés, S. Gold Glyconanoparticles: Synthetic Polyvalent Ligands Mimicking Glycocalyx-Like Surfaces as Tools for Glycobiological Studies. *Chem. – Eur. J.* **9**, 1909–1921 (2003).

35.     Penades, S., Rojo, J. & Martin-Lomas, M. Nanoparticles - US8790934B2. (2014).

36.     Golding, J., Williams, P. & Roskamp, M. Nanoparticles and their use in cancer therapy - US20170340665A1. (2017).

37.     Lund, T. *et al.* The influence of ligand organization on the rate of uptake of gold nanoparticles by colorectal cancer cells. *Biomaterials* **32**, 9776–9784 (2011).

38.     Charbgoo, F. *et al.* Gold nanoparticle should understand protein corona for being a clinical nanomaterial. *J. Controlled Release* **272**, 39–53 (2018).

39.     Manson, J., Kumar, D., Meenan, B. J. & Dixon, D. Polyethylene glycol functionalized gold nanoparticles: the influence of capping density on stability in various media. *Gold Bull.* **44**, 99–105 (2011).

40.     Alalaiwe, A., Roberts, G., Carpinone, P., Munson, J. & Roberts, S. Influence of PEG coating on the oral bioavailability of gold nanoparticles in rats. *Drug Deliv.* **24**, 591–598 (2017).

41.     Arvizo, R. R. *et al.* Modulating Pharmacokinetics, Tumor Uptake and Biodistribution by Engineered Nanoparticles. *Plos One* **6**, 1–6 (2011).

42.     Algar, W. R. *et al.* The Controlled Display of Biomolecules on Nanoparticles: A Challenge Suited to Bioorthogonal Chemistry. *Bioconjug. Chem.* **22**, 825–858 (2011).

43.     Hostetler, M. J., Templeton, A. C. & Murray, R. W. Dynamics of Place-Exchange Reactions on Monolayer-Protected Gold Cluster Molecules. *Langmuir* **15**, 3782–3789 (1999).

44.     Rademacher, T. & Mous, J. Nanoparticle-insulin and insulin analogue compositions - US20150216942A1. (2015).

45.     Williams, P., Rademacher, T., Schobel, A. M. & Dadey, E. Combination peptide-nanoparticles and delivery systems incorporating same - US9474687B2. (2016).

46.     Rademacher, T. Nanoparticle glucagon compositions - US20150216940A1. (2015).

47.     Rademacher, T. & Williams, P. Nanoparticle peptide compositions - US9114082B2. (2015).

48.     Sheridan, C. Proof of concept for next-generation nanoparticle drugs in humans. *Nat. Biotechnol.* **30**, 471–472 (2012).

49.     McAteer, M., Dayan, C. M. & Birchall, J. C. Nanoparticle-Based Antigen Specific Immunotherapy - US20180177891A1. (2018).

50.     Dul, M. *et al.* Conjugation of a peptide autoantigen to gold nanoparticles for intradermally administered antigen specific immunotherapy. *Int. J. Pharm.* **562**, 303–312 (2019).

51.     Enhanced Epidermal Antigen Specific Immunotherapy Trial - ClinicalTrials.gov. https://clinicaltrials.gov/ct2/show/NCT02837094.

52.     Rademacher, T. & Philip, R. Nanoparticle tumour vaccines - US20140248360A1. (2014).

53.     Himmler, G. *et al.* Nanoparticles comprising antigens and adjuvants, and immunogenic structures - US9079765B2. (2015).

54.     H3.3K27M-specific Peptide Vaccine (Code C132684). https://ncit.nci.nih.gov/ncitbrowser/pages/concept_details.jsf?dictionary=NCI_Thesaurus&version=20.02d&code=C132684&ns=ncit&type=properties&key=null&b=1&n=0&vse=null.

55.     Roskamp, M. *et al.* SIKVAV peptide functionalized ultra-small gold nanoparticles for selective targeting of α6β1 integrin in hepatocellular carcinoma. *J. Phys. Conf. Ser.* **829**, 012017 (2017).

56.     Garcia Barrientos, A. & de Torres Domínguez, E. Nanoparticle-based liver-targeting therapy and imaging - GB2541166A. (2017).

57.     Ma, P. *et al.* Inorganic nanocarriers for platinum drug delivery. *Mater. Today* **18**, 554–564 (2015).

58.     Hale, S. J. M. *et al.* DM1 Loaded Ultrasmall Gold Nanoparticles Display Significant Efficacy and Improved Tolerability in Murine Models of Hepatocellular Carcinoma. *Bioconjug. Chem.* **30**, 703–713 (2019).

59.     Özcan, A. *et al.* Nanoparticle-Coupled Topical Methotrexate Can Normalize Immune Responses and Induce Tissue Remodeling in Psoriasis. *J. Invest. Dermatol.* **140**, 1003–10140 (2020).

60.     Rademacher, T. W., Bradman, G., Ullate, S. P. & Castilla, R. O. M. D. Nanoparticles comprising antibacterial ligands - US9034380B2. (2015).

61.     Rademacher, T. W. & Williams, P. Nanoparticles for providing immune responses against infectious agents - US8895023B2. (2014).

62.     Rademacher, T. & Williams, P. Nanoparticle-peptide compositions - US9598479B2. (2017).

63.    Rademacher, T. & Williams, P. Nanoparticle peptide compositions - US20140248365A1. (2014).

64.    Rademacher, T. W. *et al.* Nanoparticles Comprising Rna Ligands - US20080213177A1. (2008).

65.    Development of Selective Carbohydrate Immunomodulators Targeting C-type Lectin Receptors on Antigen Presenting Cells | IMMUNOSHAPE Project | H2020 | CORDIS | European Commission. https://cordis.europa.eu/project/id/642870.

66.    Hermanson, G. T. Chapter 3 - The Reactions of Bioconjugation. in *Bioconjugate Techniques (Third edition)* 229–258 (Academic Press, 2013).

67.    Cummings, R. D. & McEver, R. P. C-type Lectins. in *Essentials of Glycobiology* (Cold Spring Harbor Laboratory Press, 2009).

68.    Brown, G. D., Willment, J. A. & Whitehead, L. C-type lectins in immunity and homeostasis. *Nat. Rev. Immunol.* **18**, 374–389 (2018).

# Chapter I

# Aqueous Brust-Schiffrin Synthesis of Ultrasmall Gold Nanoparticles: Study of the Passivation Effect

# I. Introduction

Ultrasmall gold nanoparticle synthesis using sodium borohydride as reducing agent is also known as Brust-Schiffrin synthesis[1]. Since its publication in 1994, the recipe has been widely used and modified, yet the basic principles remain the same[2]. Thiol or disulfide ligands in presence of a gold salt (tetrachloroauric acid: $HAuCl_4$) are quickly reduced with an excess of a reducing agent: sodium borohydride ($NaBH_4$). As the gold reduces to form the core of the particles, the ligands create a corona, limiting the core growth by the formation of sulfur-gold bonds.

Even though the general principle of the reaction and its execution appear to be straightforward, its complete control and understanding remains very challenging. GNP are complex products, and many factors can influence their physicochemical characteristics. The desired quality, scalability and reproducibility between batches can therefore only be achieved through a fully controlled manufacturing process, including synthesis, purification and a comprehensive array of analytical techniques[3]. Indeed, slight changes in material characteristics can have a profound impact on the particle *in vitro* and *in vivo* behavior, affecting efficacy, PKBD or toxicity[4].

To thoroughly control the Brust-Schiffrin synthesis, the critical parameters should be meticulously defined and individualized. For that purpose, they are divided in two categories: organic and process chemistry.

Organic chemistry parameters must be carefully chosen:
- Solvent: mostly influenced by the ligand nature (solubility and stability). For hydrophilic ligands, a single-phase reaction can be performed. Water, ethanol, methanol and dimethyl sulfoxide (DMSO) either pure or as a mixture are solvents of choice[2]. For more hydrophobic ligands, organic solvents can be used (e.g. toluene) in a biphasic reaction[1].
- Concentration: the viscosity of the ligands and the GNP should be taken in account when fixing the optimal concentrations.
- Stoichiometry: using Au as a standard, the number of equivalents of ligands and reducing agent can be tuned. Generally, they are both used in excess. The core size decreases with increasing ligand/Au ratio[5].

- Ligands: two main types of ligands with a similar ability to cap the particles can be used: thiols and disulfides[6]. When more than one ligand is used, they will compete to form the particle corona, leading to a ratio on the GNP surface that can be different from the ligand ratio added to the mixture[7]. The overall physicochemical nature of the ligands: solubility, steric hindrance, chemical groups (e.g. amine, carboxylic acid, hydroxyl) should be considered, as it impacts the capping and, *in fine,* the particle[8]. For instance, bulky ligands such as high molecular weight PEG result in GNP with a smaller and more monodisperse core[9,10].

The process of synthesis should be tightly controlled and monitored:
- Temperature: elevated temperatures resulted in bigger particles when tested with a wide thermal range from -20 °C to 90 °C[11].
- pH: in aqueous solution, adjustment can be performed using a strong base. Variation around neutral pH (5.5 - 8) showed that a higher pH led to smaller GNP[12].
- Timing: since the reaction requires sequential addition of the reagents, timing is critical: addition of the gold, the ligands, eventual pH adjustment and addition of the reducing agent. Time of purification should also be considered. Longer equilibration of the ligand with gold at alkaline pH generated more monodisperse GNP[13].
- Mixing: the stirring and the vessel type affect the homogenization time. Faster addition of NaBH$_4$ produced more monodisperse material[5], but slow stirring was also used to obtain ultrasmall nanoclusters[14].
- Volumes: the devices (e.g. reactor vessel) should be adapted to the scale. Challenges of scale-up (e.g. purification, exothermic process, gas release) should be considered[15].

To achieve the optimal synthesis on a non-industrial scale, pilot scale benchtop reactors must be used to control the reaction through software monitoring of the parameters (e.g. pH, temperature, stirring, steps).

Downstream purification of the GNP can be performed by various techniques, such as precipitation, extraction, chromatography, dialysis and ultrafiltration (UF). UF, the most common, is a size-based separation technique using a membrane with a nominal molecular weight cut-off (MWCO). The membrane is usually made of polysulfone, (modified) polyethersulfone or regenerated cellulose[16]. A pressure is applied between the crude solution and the membrane, causing the contaminants (e.g. excess ligands, salts) smaller than the MWCO to go through the membrane while the GNP are retained. The GNP retention depends on the particle size (core and ligand shell) and the solution nature (pH and ionic strength). UF can take various forms: while centrifugal ultrafiltration (dead-end filtration) is the reference for R&D, when advancing toward clinical stages, automation and high-throughput using Tangential Flow Filtration (TFF) systems performing diafiltration are required (*Figure 1*)[17]. The purification efficiency to obtain high-end concentration of pure and non-degraded material in short process times depends on several parameters, such as the solvent, the volume of solution, the viscosity, the GNP concentration and the protocol of filtration (e.g. membrane pore size)[18].
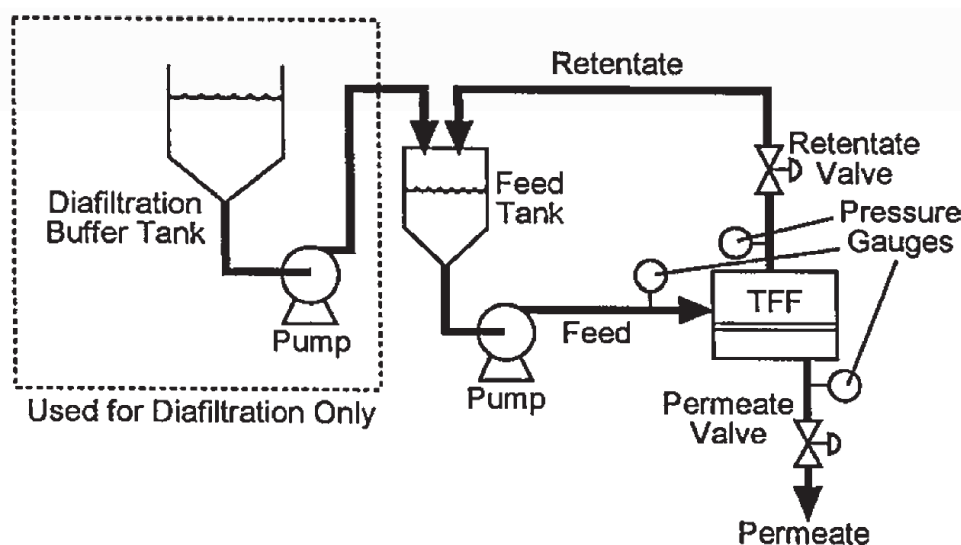


*Figure 1: Principle of Tangential Flow Filtration with a diafiltration setup. The feed tank contains the crude solution, which is pumped into the feed tubing and passes through the "TFF" membrane unit (cassette or column) in a tangential fashion. Contaminants with a size under the MWCO go through the membrane to the permeate. The GNP go back to the feed tank through the retentate tubing, the solution gets gradually more concentrated and the contaminants are removed. To maintain the volume or exchange the solvent, diafiltration can be used. In this case, another pump refills the feed tank from the diafiltration buffer tank. The system is automatized using weighing balances to know the volume in the tanks, and pressure gauges (sensors) to know the pressure before, after and across the membrane (transmembrane pressure: TMP). The pressure can be tuned by modulating the feed pump speed and the backpressure applied by the retentate valve[19].*

For pilot scale syntheses, Midatech Pharma uses, under GMP-like conditions, a Syrris Atlas Potassium benchtop reactor, and for the purification a Repligen KR2i TFF system (*Figure 2*).

Brust-Schiffrin synthesis can be divided in three parts:

- Pre-Nucleation: mixture of ligands with the gold salt and eventual pH adjustment.
- Nucleation: addition of the reducing agent: sodium borohydride, and instantaneous formation of the particles.
- Passivation: particle evolution in presence of sodium borohydride and excess ligands (since the contaminants are gradually removed from the GNP solution, part of the purification should be considered as passivation time).
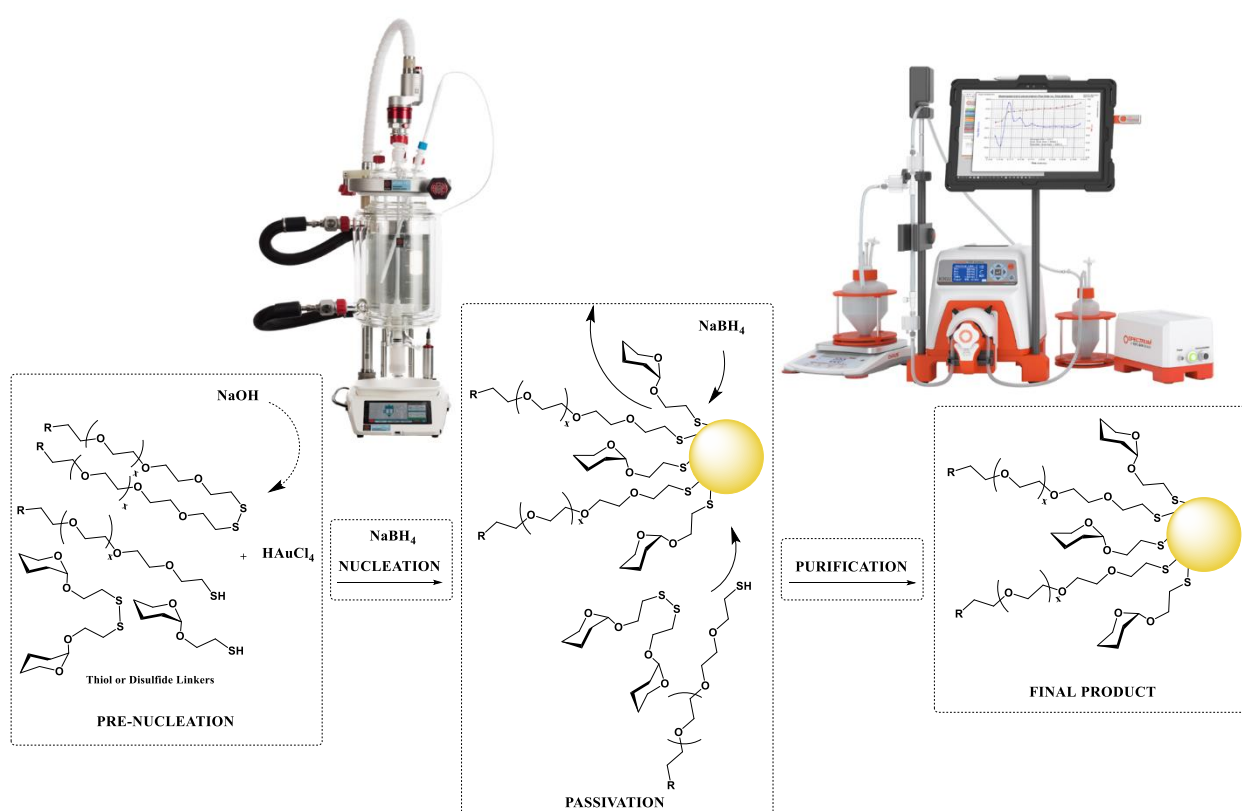


*Figure 2: General Principle of Midatech Pharma´s ultrasmall GNP Brust-Schiffrin synthesis and purification on a pilot scale using a Syrris Atlas reactor and a Repligen KR2i tangential flow filtration system.*

Ligands and $NaBH_4$, depending on the conditions, have both demonstrated their dual capacity in forming/stabilizing the GNP or etching it[20,21]. In optimized conditions, thiol groups have been used to etch GNP and obtain a more monodisperse population with a method called size focusing (survival of the more robust clusters)[22]. On the other hand, GNP growth during passivation has also been demonstrated[8,23,24].

Most of the aforementioned observations come from peer-reviewed, published research that, in some instances, dates from more than 25 years ago. Moreover, the syntheses were performed with R&D methods, meaning less well controlled parameters, and analyses that were occasionally incomplete, potentially leading to errors in data interpretation.

On top of that, GNP characterization requires a broad array of analytical techniques. In fact, it is critical to obtain the most accurate picture of the material and detect minute differences[25]. Techniques such as Transmission Electron Microscopy (TEM) and Ultraviolet–Visible (UV-Vis) spectrophotometry inform about the core size and shape, while Dynamic Light Scattering (DLS), Differential Centrifugation Sedimentation (DCS) and Size Exclusion Chromatography (SEC) are used to characterize the whole particle. As for the shell, techniques including Liquid Chromatography (LC), Mass Spectrometry (MS) and Nuclear Magnetic Resonance (NMR) spectroscopy are used to identify and quantify the ligands. The analytical pipeline can be completed with elemental analyses such as Microwave Plasma - Atomic Emission Spectrometry (MP-AES), Inductively Coupled Plasma - Atomic Emission Spectroscopy (ICP-AES) and X-ray Photoelectron Spectrometry (XPS)[26,27,28]. For each technique, parameters such as sensitivity, limit of detection or versatility should be known and the information they bring individually analyzed and compared for appropriate data interpretation. For example, TEM is an essential technique for particle shape and size determination but lacks sensitivity for ultrasmall GNP[29].

Finally, GNP being a diverse family, observations and conclusions drawn for a particle do not necessarily translate to another. For instance, the original biphasic BSS preparation differs greatly from Midatech´s aqueous synthesis, and each GNP can potentially exhibit different properties depending on its ligands.

## II.  Objectives

The intended goal is to investigate and better understand the process of passivation during ultrasmall gold nanoparticle synthesis. To achieve that, the study of ultrasmall GNP with GMP-like control of synthesis and a state of art analytical characterization will be discussed in this chapter.

The platforms consisted of water-soluble GNP, that were synthesized using $H_2O$ as a solvent, and sodium hydroxide (NaOH) to adjust the solution to an alkaline pH. The GNP were capped with two ligand species : an oligo-PEG, PEG(5)$NH_2$ or PEG(8)COOH, and a monosaccharide, $\alpha$-Galactose-$C_2$ or $\beta$-Glucose-$C_2$. All ligands are disulfides and water-soluble. The theoretical size of the particle gold core is 2 nm, postulating that they are composed of 44 ligands and 102 Au atoms: (Ligand A)$_x$(Ligand B)$_y$@$Au_{102}$, with $x + y = 44$[30,31].

The density of the PEG strongly impacts the covering of the core. It can take different conformations: mushroom/random-coiled (deformable) at low density or rigid brush orientation at high density[32]. Not only do PEG density and conformation affect the GNP stealth properties by shielding the core, with *in vitro* and *in vivo* consequences[4,33], but also influence the stability of the material during its storage[25]. Using a monosaccharide with a short alkyl side chain to modulate the amount of PEG on the GNP has, for instance, an impact on the uptake of GNP by cancer cells[34]. For these reasons, both ligand ratios and density were extensively studied.

The core and the whole particle size evolution were also measured, paying attention to distribution and aggregation, since both can have a significant impact on cell uptake and toxicity[35].

Three GNP models were used:
- (PEG(5)$NH_2$)$_x$($\alpha$-Galactose-$C_2$)$_y$@$Au_{102}$
- (PEG(8)COOH)$_x$($\alpha$-Galactose-$C_2$)$_y$@$Au_{102}$
- (PEG(8)COOH)$_x$($\beta$-Glucose-$C_2$)$_y$@$Au_{102}$.

Having cationic (pegamine) and anionic (PEG carboxylic acid) particles offers two relevant opposite models, cationic particles being moderately toxic with a pore-forming capacity on cell membranes[36] and anionic being non-toxic[37].

Four parameters were monitored to evaluate their influence on the passivation process: the ligand species (PEG with either terminal carboxylic acid or amine), the temperature, the pH and the time. Temperature and pH were modified within a short range to evaluate whether small differences impact the GNP. pH was maintained within the alkaline window since the stability of $NaBH_4$ in water is greatly affected by it. In fact, even though concentration and temperature affect the rate of hydrolysis of sodium borohydride, pH is the most critical parameter[38]. The half-life of $NaBH_4$ rises from 61.4 minutes at pH 10 to 4.3 days at pH 12[39]. Time of passivation was also comprehensively studied, with several time points between 0 and 24 hours. This parameter is critical since the GNP synthesis scale-up can result in a longer purification and, therefore, a longer passivation.

The main experiment was the synthesis of four different batches in a benchtop reactor. For the two PEG(5)NH$_2$/α-Galactose-C$_2$ batches, the pH was fixed to 12 and the temperature to either 18 °C or 25 °C. As for the two PEG(8)COOH/α-Galactose-C$_2$ batches, the pH was fixed to either 12 or > 12.5 and the temperature to 18 °C. Once the $NaBH_4$ was added, the particles formed immediately. Aliquots were taken from the reactor at different relevant time points and purified by centrifugal ultrafiltration to stop the passivation.

A following experiment consisted in the removal of $NaBH_4$ during passivation using ion exchange resins. These have the advantages of being affordable, scalable and easy to remove by filtration. After the addition of the sodium borohydride and the nucleation, two resins were used: Amberlite IRA-743[40] and Amberlite IRA-400[41]. Their capacity in scavenging the boron and the effect it has on GNP size was studied with (PEG(8)COOH)$_x$(α-Galactose-C$_2$)$_y$@Au$_{102}$ and (PEG(5)NH$_2$)$_x$(α-Galactose-C$_2$)$_y$@Au$_{102}$. In a more comprehensive experiment with optimized conditions, the evolution of the (PEG(8)COOH)$_x$(β-Glucose-C$_2$)$_y$@Au$_{102}$ gold nanoparticles after removal of $NaBH_4$ using various amounts of IRA-400 was studied.

To follow the evolution of GNP during all the passivation experiments, an extensive range of analytical techniques was employed.

The characterization can be split in three parts (*Figure 3*):

- The shell/corona by Proton Nuclear Magnetic Resonance Spectroscopy ($^1$H NMR), Reverse Phase chromatography: Ultra-High-Performance Liquid Chromatography using a Charged Aerosol Detector and a Mass Spectrometer (LC-CAD-MS) and High-Performance Liquid Chromatography using a Diode Array Detector (HPLC-DAD) together with the elemental analyses ICP-AES and XPS.

- The overall particle size and distribution by DLS, DCS and SEC using Fast Protein Liquid Chromatography (FPLC).

- The core size and shape by TEM and UV-Vis.

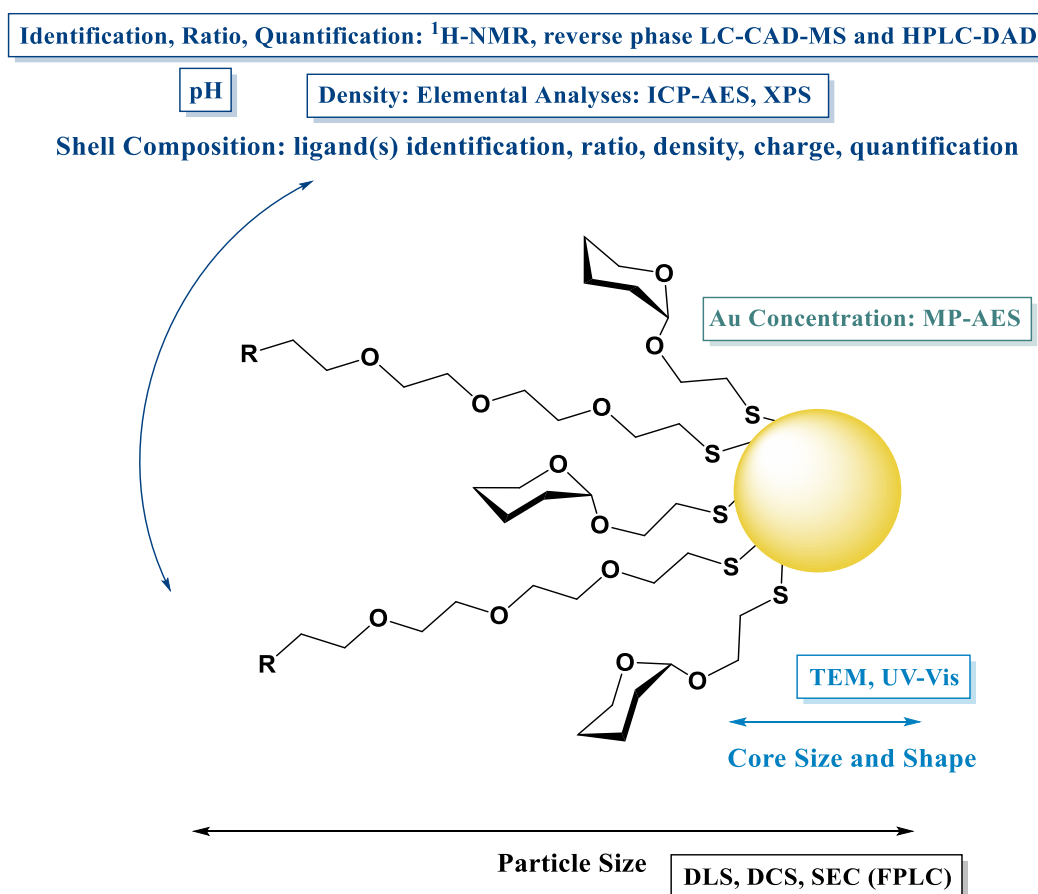Gold concentration (MP-AES) and pH were also monitored.



*Figure 3: Critical Parameters of the GNP: core size and shape, particle size and shell composition with the respective analytical techniques used for the passivation study.*

# III.   Results and Discussion

## 1. GNP evolution over time of passivation

Four different batches were synthesized by a modified Brust-Schiffrin synthesis using a benchtop reactor. Within minutes, excess homo-disulfide ligands and $HAuCl_4$ (500 mg) were dissolved in water and added to the reactor. The solution was adjusted to alkaline pH and a fresh aqueous solution of $NaBH_4$ was quickly added. The mixture was allowed to incubate, then aliquots were taken at different times and purified by centrifugal ultrafiltration. Starting immediately after the nucleation (t = 0), a total of seven aliquots were taken: 0, 0.5, 1, 2, 5, 9 and 24 hours.

The ligand ratio on the GNP was modulated by the amount of each of the disulfide ligands added to the solution. The targeted ligand ratio on the GNP was 50:50. **GNP-1** and **GNP-2** were produced with molar ratios of α-Galactose-$C_2$/PEG(5)$NH_2$ 50:50. **GNP-3** and **GNP-4** were made with α-Galactose-$C_2$/PEG(8)COOH 40:60. The syntheses were performed at two different temperatures: 18 °C and 25 °C. The temperature was allowed to equilibrate before the addition of the ligands and controlled throughout the whole reaction using the reactor cooler. pH was modulated ranging from ~ 12.0 (adjustment to basic pH) to > 12.5 (large excess of base, ~ 10-fold compared to pH ~ 12.0) a few minutes before the nucleation (*Table 1*).

*Table 1: Batches synthesized and different key parameters.*

| Batch | Ligand I | Ligand II | Charge and Shortened Ligand ID | Ligand Addition Ratio (%) | Temperature (°C) | pH |
|---|---|---|---|---|---|---|
| GNP-1 | α-Galactose-$C_2$ | PEG(5)$NH_2$ | Positive PEGNH$_2$ | 50:50 | 18 | ~ 12 |
| GNP-2 | | | | | 25 | |
| GNP-3 | | PEG(8)COOH | Negative PEGCOOH | 40:60 | 18 | |
| GNP-4 | | | | | | > 12.5 |

The rest of parameters were the same for the four batches, and process reproducibility was ensured using the automated benchtop reactor. Aliquots of identical volumes were sampled and purified by centrifugal ultrafiltration using Amicon 10 kDa filters (*Figure 4*). The GNP were resuspended in water with identical volumes. Analyses were performed immediately after the syntheses.
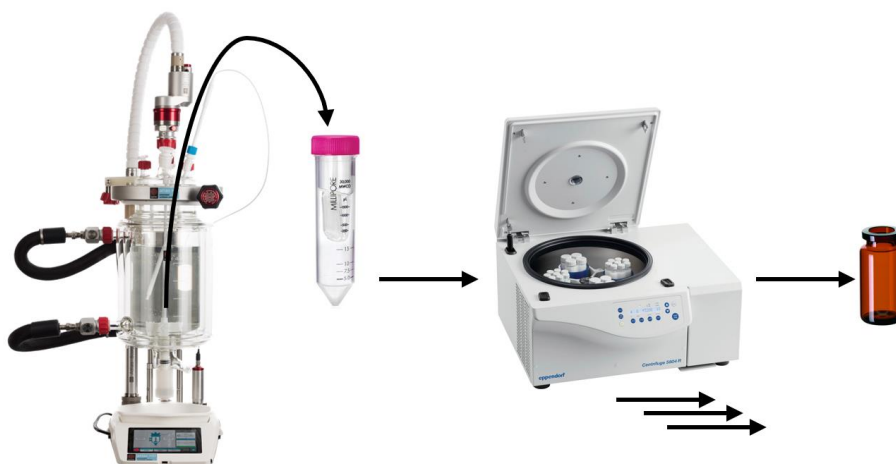
*Figure 4: Process of aliquot sampling during the passivation study. Crude GNP solution was taken directly from the reactor and sampled in Amicon filters. Several centrifugal ultrafiltration cycles were performed. Final product was resuspended in water and stored in amber glass vials.*

The gold content (MP-AES analysis) and the pH were monitored (*Figure 5*). The gold concentration defines the yield of the reaction and should ideally be steady as the volume of resuspension was the same for all the aliquots. The gold concentration was stable for all the samples and the yields were quantitative for GNP-3 and GNP-4 (PEG(8)COOH). GNP-1 and GNP-2 (PEG(5)NH$_2$) had a lower yield, which can be explained by the loss of material during the purification process: particles that have shorter PEG are more likely to pass through the membrane, resulting in a bigger loss of material. Moreover, positive particles are stickier, causing material loss during the different steps of the synthesis.

pH was stable and alkaline. GNP-1 and GNP-2 with their amine function showed higher pH than GNP-3 and GNP-4 with the carboxylic acid (the alkaline pH is explained by the presence of the carboxylate salt -COONa that was confirmed by MP-AES, *data not shown*).
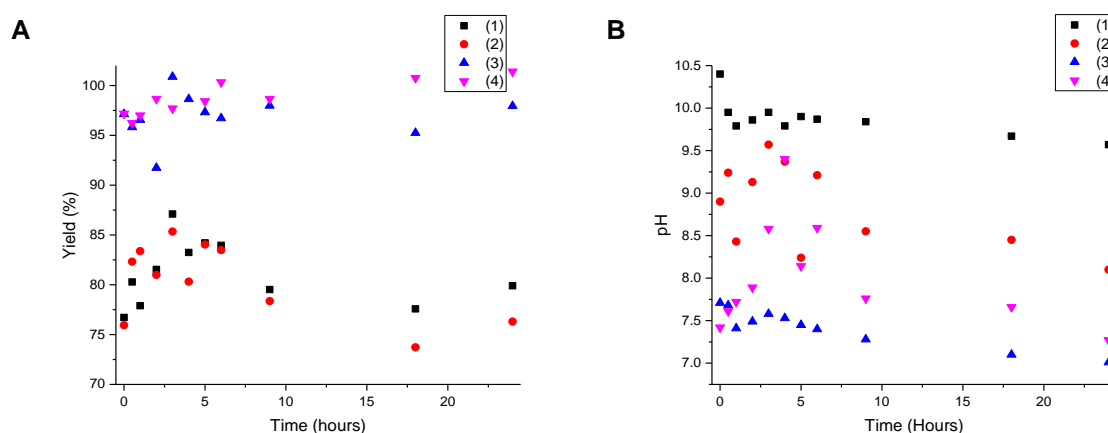


*Figure 5: Evolution of (A) the yield (percentage of theoretical maximum Au content by MP-AES) and (B) the pH of (1) GNP-1 (PEGNH$_2$, 18 °C, pH 12), (2) GNP-2 (PEGNH$_2$, 25 °C, pH 12), (3) GNP-3 (PEGCOOH, 18 °C, pH 12) and (4) GNP-4 (PEGCOOH, 18 °C, pH > 12.5).*

The core size of GNP was measured using two analytical techniques: UV-Vis spectrophotometry and TEM.

UV-Vis spectrophotometric measurement was used to monitor the surface plasmon band intensity (*Figure 6*). A plasmon at 520 nm is characteristic of spherical GNP[42]. For ultrasmall particles, SPB rises as the size increases. Since this technique is not quantitative, the absolute size of the core cannot be determined. However, it allows the comparison among the different samples. There was a clear increase of the plasmon over time of passivation. At the nucleation time, no plasmon was observed for any of the batches. The intensity gradually increased to reach its maximum after 24 hours. The increase was higher for positive particles, GNP-1 and GNP-2, than the negative, GNP-3 and GNP-4. Between the positive GNP, the highest temperature (25 °C) exhibited more plasmon increase. Comparing negative particles, the highest pH (> 12.5) presented more plasmon. Interestingly, the negative particle at pH 12, GNP-3, did not show any clear plasmon.
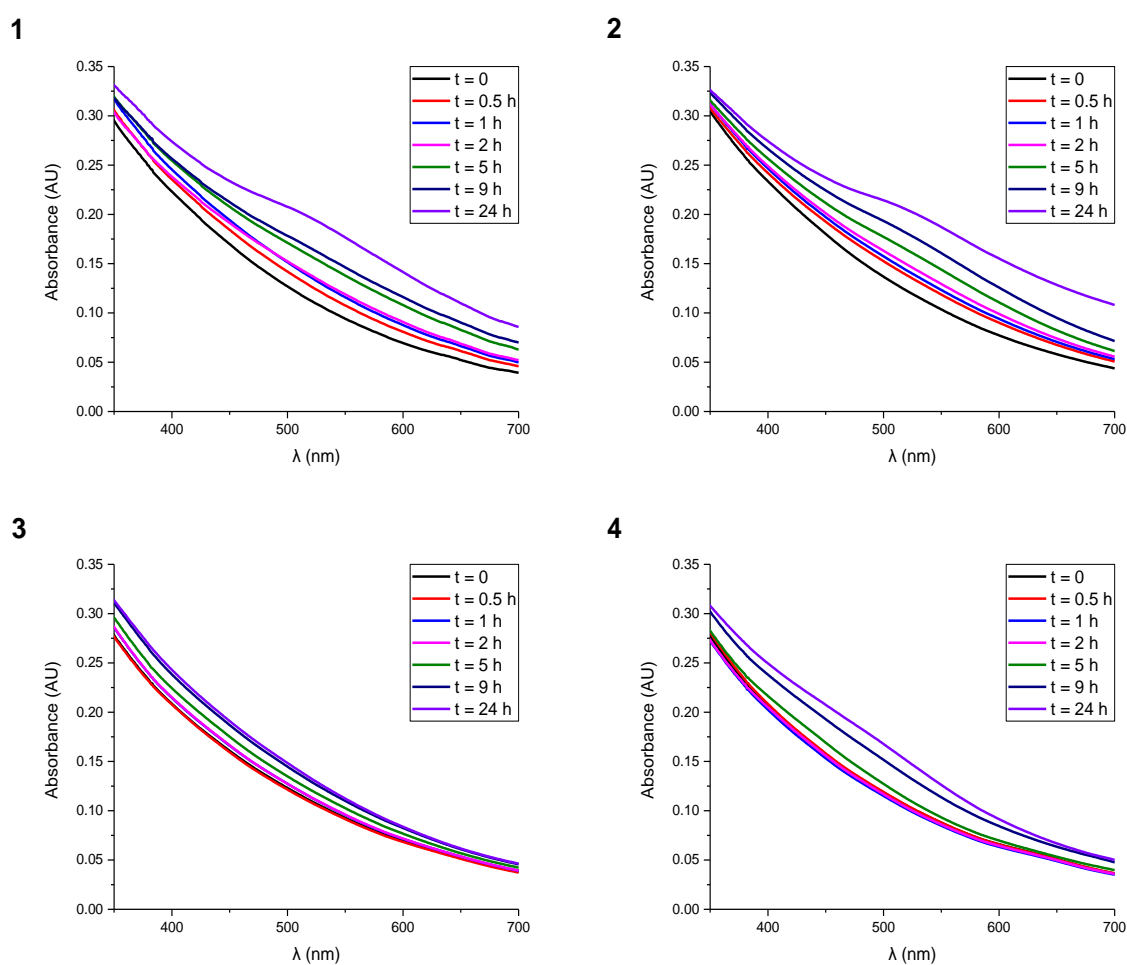


*Figure 6: UV-Vis spectra (λ 350-700 nm) of (1) GNP-1 (PEGNH₂, 18 °C, pH 12), (2) GNP-2 (PEGNH₂, 25 °C, pH 12), (3) GNP-3 (PEGCOOH, 18 °C, pH 12) and (4) GNP-4 (PEGCOOH, 18 °C, pH > 12.5).*

TEM pictures of the GNP were taken (*Figure 7*) and processed to obtain the mean and median diameter (*Figure 8*). Although TEM gives direct measurement of the size, it did not show the same gradual trend of size increase as the UV-Vis spectra. Only positive GNP (GNP-1 and GNP-2) at the latest time points (24 hours) showed a significant increase of core size. The rest of the values oscillated within the analytical error of the technique. TEM, despite not being precise enough, was able to confirm the increase in size seen by UV-Vis: the samples with the strongest plasmonic bands also showed a significant size increase by TEM.



*Figure 7: TEM pictures of (1) GNP-1 (PEGNH$_2$, 18 °C, pH 12), (2) GNP-2 (PEGNH$_2$, 25 °C, pH 12), (3) GNP-3 (PEGCOOH, 18 °C, pH 12) and (4) GNP-4 (PEGCOOH, 18 °C, pH > 12.5) at t = 0 (top) and after 24 hours (bottom).*
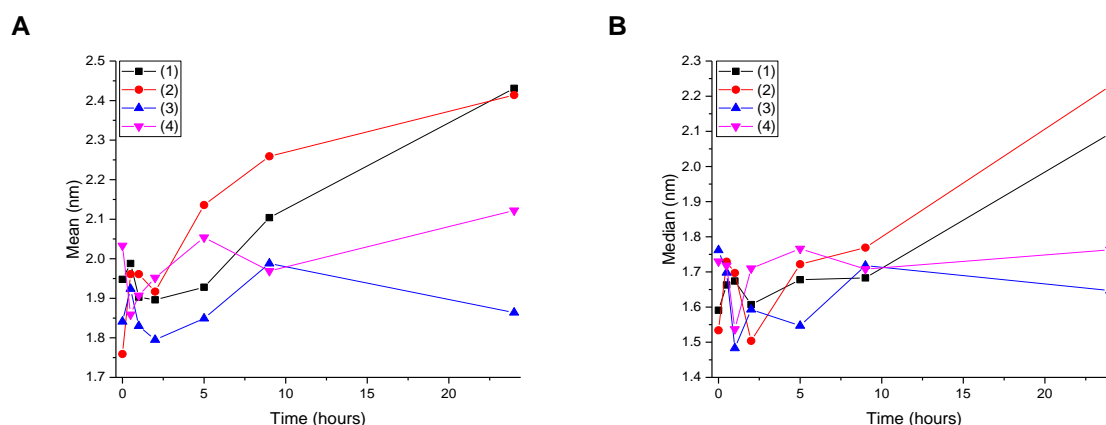


*Figure 8: TEM (A) Mean and (B) Median size of (1) GNP-1 (PEGNH$_2$, 18 °C, pH 12), (2) GNP-2 (PEGNH$_2$, 25 °C, pH 12), (3) GNP-3 (PEGCOOH, 18 °C, pH 12) and (4) GNP-4 (PEGCOOH, 18 °C, pH > 12.5).*

To characterize the overall size of the GNP, three analytical techniques were used: DLS, DCS, and SEC. They all exhibited the same trend regarding particle size increase over passivation time, although with different sensitivity.

DLS distributions (*Figure 9*) and mean hydrodynamic ratio by volume (*Figure 10*) showed an increase of size over time of passivation for the positive particles GNP-1 and GNP-2. Rather than keeping a gaussian shape and display a regular displacement of the peak and its maximum, the 24-hour peaks of positive GNP showed broadening (tailing). GNP-2 (25 °C) tailing was bigger than GNP-1 (18 °C). Negative GNP did not show any significant increase of the size over time.

DCS distributions (*Figure 11*) and median diameter by surface (*Figure 12*) revealed an increase of size over time of passivation for the all the particles. It was more pronounced for positive particles. For negative particles, it was almost undetectable at pH 12 but visible at pH > 12.5. Looking at the distributions, the positive particles after 24 hours had lost their gaussian shape and presented a tail. GNP-2 even displayed a second population.

SEC was performed on a FLPC chromatographic system and the wavelength of 400 nm was used to detect the GNP. The chromatograms (*Figure 13*) and the volume at maximum peak height (*Figure 14*) demonstrated, for all particles, a gradual increase of size, as evidenced by the decrease of the elution volume, with increasing time of passivation. However, the growth was not the same for all the batches. GNP-2 (PEGNH$_2$, 25 °C, pH 12) displayed the most substantial growth, followed by GNP-1 (PEGNH$_2$, 18 °C, pH 12), GNP-4 (PEGCOOH, 18 °C, pH > 12.5) and GNP-3 (PEGCOOH, 18 °C, pH 12). It appears that positive particles were more affected than negative ones, while higher temperature and excess of NaOH (pH > 12.5) increased the growth. GNP-2 presented a second population

10 mM PBS (pH 7) was used as a mobile phase and to dilute PEGCOOH GNP during SEC experiments. A solution of Borax/NaOH (pH 10-10.5) was required to dilute and disaggregate PEGNH$_2$ GNP before analysis. This issue is probably related to the amine binding to the core during storage and was reversed at high pH[43]. The reversible aggregation related to the storage, as well as the higher growth during the passivation compared to carboxylic acid-PEG particles, indicates that the pegamine plays an active role in the particle evolution (*Figure 15*).

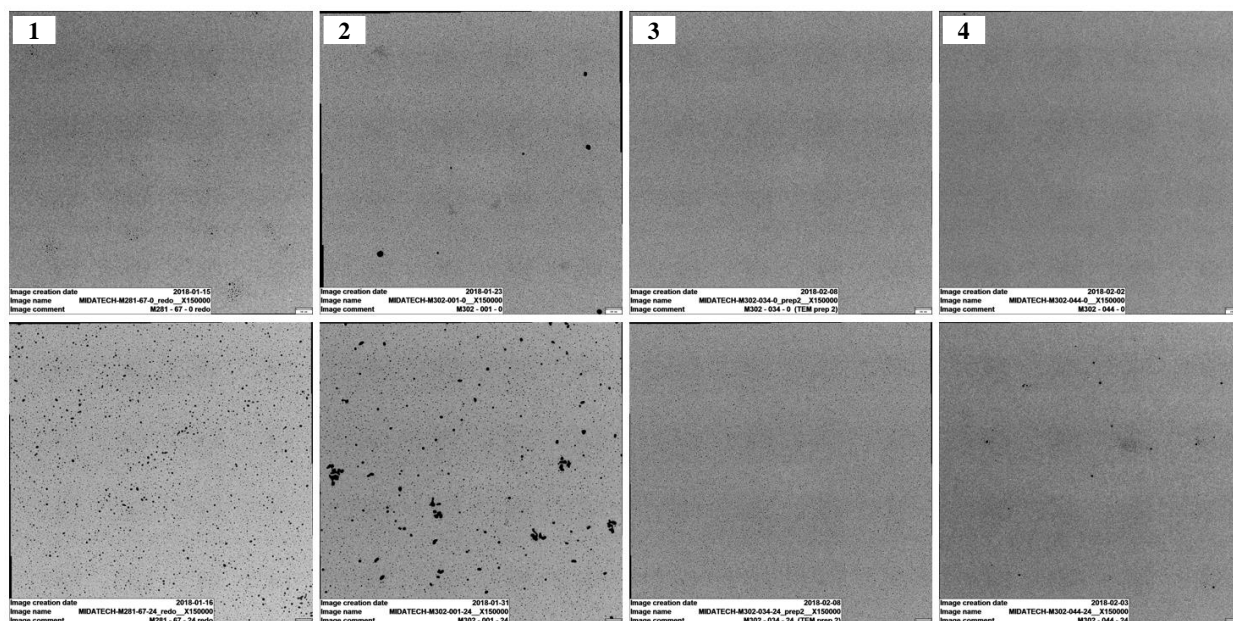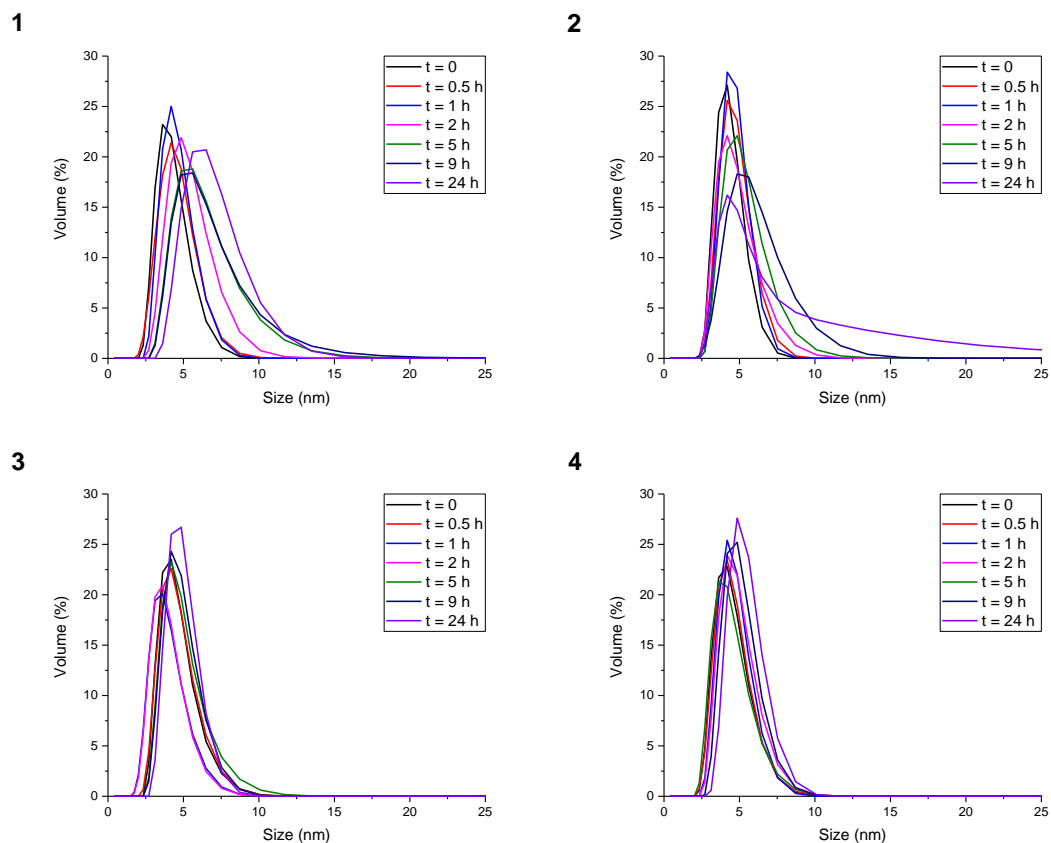*Figure 9: DLS hydrodynamic size distribution by volume of (1) GNP-1 (PEGNH₂, 18 •C, pH 12), (2) GNP-2 (PEGNH₂, 25 •C, pH 12), (3) GNP-3 (PEGCOOH, 18 •C, pH 12) and (4) GNP-4 (PEGCOOH, 18 •C, pH > 12.5).*
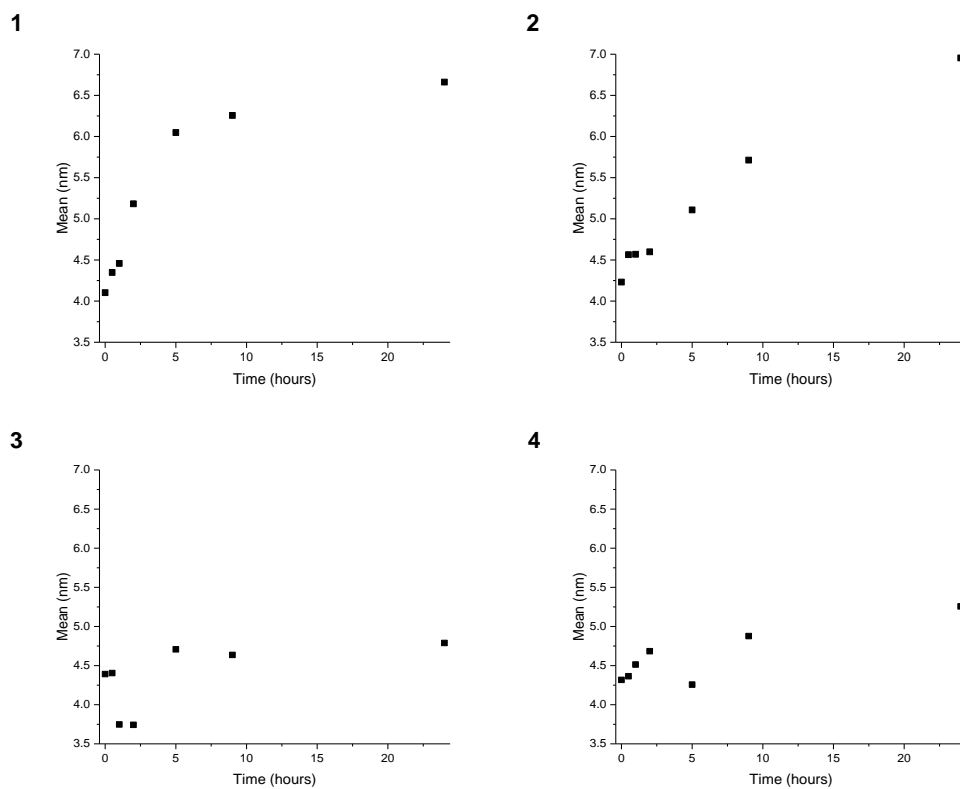


*Figure 10: DLS hydrodynamic size mean by volume of (1) GNP-1 (PEGNH₂, 18 •C, pH 12), (2) GNP-2 (PEGNH₂, 25 •C, pH 12), (3) GNP-3 (PEGCOOH, 18 •C, pH 12) and (4) GNP-4 (PEGCOOH, 18 •C, pH > 12.5).*
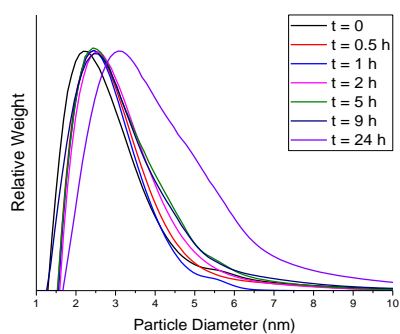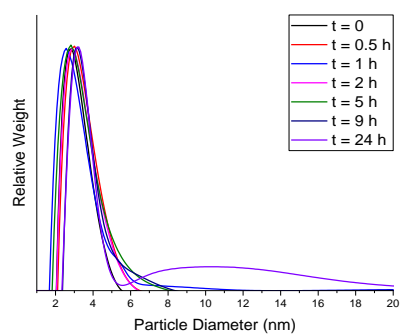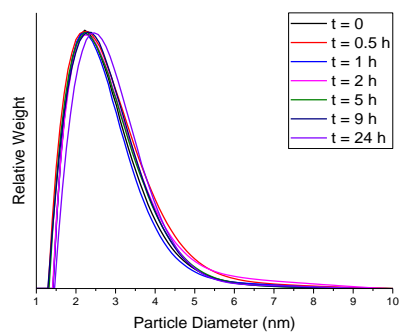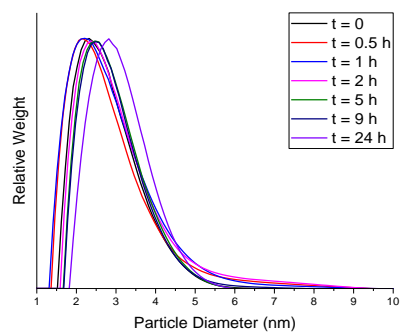
*Figure 11: DCS diameter distribution of (1) GNP-1 (PEGNH$_2$, 18 °C, pH 12), (2) GNP-2 (PEGNH$_2$, 25 °C, pH 12), (3) GNP-3 (PEGCOOH, 18 °C, pH 12) and (4) GNP-4 (PEGCOOH, 18 °C, pH > 12.5).*
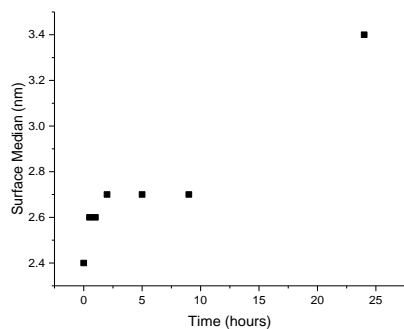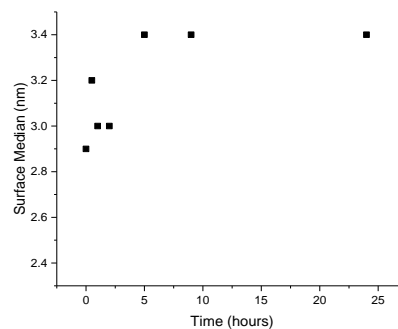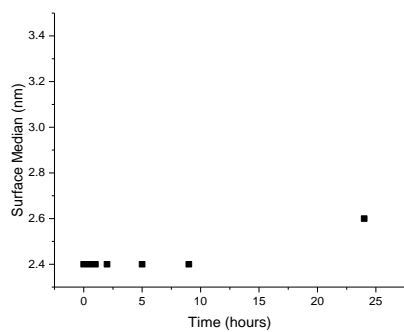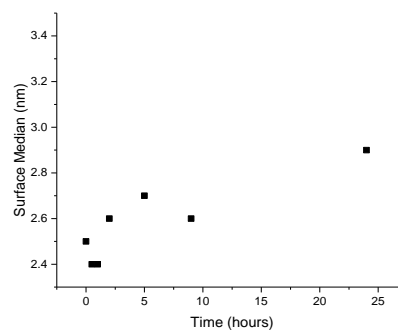


*Figure 12: DCS size median by surface of (1) GNP-1 (PEGNH$_2$, 18 °C, pH 12), (2) GNP-2 (PEGNH$_2$, 25 °C, pH 12), (3) GNP-3 (PEGCOOH, 18 °C, pH 12) and (4) GNP-4 (PEGCOOH, 18 °C, pH > 12.5).*

*Figure 13: FPLC size exclusion chromatograms of (1) GNP-1 (PEGNH₂, 18 °C, pH 12), (2) GNP-2 (PEGNH₂, 25 °C, pH 12), (3) GNP-3 (PEGCOOH, 18 °C, pH 12) and (4) GNP-4 (PEGCOOH, 18 °C, pH > 12.5) (λ = 400 nm).*



*Figure 14: Volume at maximum peak height of FPLC size exclusion chromatograms of (1) GNP-1 (PEGNH₂, 18 °C, pH 12), (2) GNP-2 (PEGNH₂, 25 °C, pH 12), (3) GNP-3 (PEGCOOH, 18 °C, pH 12) and (4) GNP-4 (PEGCOOH, 18 °C, pH > 12.5). (λ = 400 nm).*

38
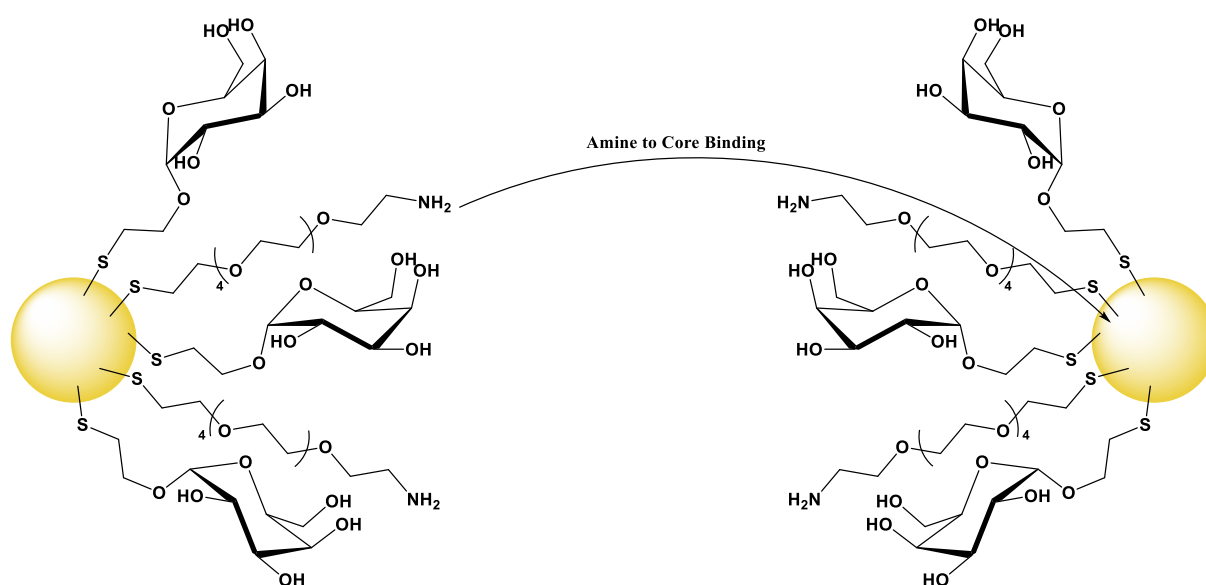
*Figure 15: Possible mechanism of enhancement of aggregation for pegamine particles during the passivation (and storage).*

Compared to DLS and DCS, SEC demonstrated better sensitivity and was able to identify the gradual increase of particle size over time of passivation for all the batches. It was also able to show the impact of the different conditions. Although DLS and DCS are less sensitive, they have the advantage of providing an absolute size value. Interestingly, SEC chromatograms also revealed the loss of gaussian shape for the positive particles after 24 hours, as observed with the two other techniques (bigger tail at 25 °C than 18 °C).

Ligand identification, ratio (relative amounts of the different ligands) and density (number of ligands per GNP) were determined through a wide array of analytical techniques.

^{1}H NMR and reverse phase liquid chromatography LC-CAD-MS allowed the determination of the oligo-PEG/monosaccharide ratio on the particle. CAD and MS were used because of the lack of chromophore in the ligands. Both analyses were performed after the GNP were subjected to an etching treatment to release the ligands (*see details in Chapter II*). Apart from the ligand ratio, LC-CAD-MS was also used to determine the ligand density.

Two methods of elemental analysis, XPS and ICP-AES, were employed to measure the ligand density through the sulfur to gold (S/Au) ratio. Since there was only one atom of sulfur per ligand for the GNP studied, it is possible, in terms of molarity, to assume that [S] = [Ligand] to obtain an approximation of the ligand density.

Another reverse phase liquid chromatography analysis was performed to understand how the time of passivation affected the polarity of the GNP. Unlike the previously mentioned LC-CAD-MS analysis, the particles were injected without any digestion, and the detection was performed with a UV-Vis detector ($\lambda$ = 400 nm) using a HPLC-DAD device.

The ratios of $\alpha$-Galactose-$C_2$/PEG obtained by ^{1}H NMR and LC-CAD-MS were compared for all the samples (*Figure 16*). As expected, the ratios for all the batches were close to 50:50: with ^{1}H NMR, all ratios were roughly falling between 45:55 and 55:45, while with LC-CAD-MS, that range went from 45:55 to 60:40. This illustrated the reliability of the two techniques to measure the ligand ratio. Over time of passivation, the ratio was stable, except for the 24 hours points for the negative particles (GNP-3 and GNP-4).
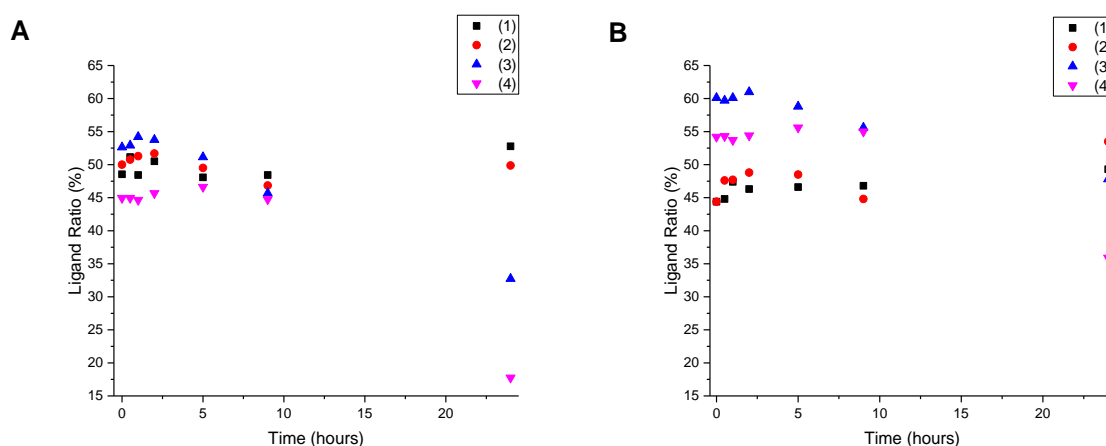


*Figure 16: Ratios of $\alpha$-Galactose-$C_2$/PEG by (A) ^{1}H NMR and (B) LC-CAD of (1) GNP-1 (PEGNH$_2$, 18 °C, pH 12), (2) GNP 2 (PEGNH$_2$, 25 °C, pH 12), (3) GNP-3 (PEGCOOH, 18 °C, pH 12) and (4) GNP-4 (PEGCOOH, 18 °C, pH > 12.5).*

The decrease in the amount of α-Galactose-$C_2$ relative to the PEG for the negative particles after 24 hours of passivation can be explained by the degradation of the carbohydrate. In fact, both LC-CAD-MS and ^{1}H NMR reveal the presence of a new compound related to α-galactose, which remains bound to the particle (*Figure 18 and Figure 39 in the annex*). The degradation was more pronounced at pH > 12.5 (GNP-4) than at pH ~ 12 (GNP-3). The new compound is believed to be galacturonic acid as GNP can oxidize monosaccharides (*Figure 17*). The mechanism depends not only on the GNP characteristics such as the ligand shell, but also on the solution pH[44]. This would explain the absence of degradation with the positively charged particles (PEGNH$_2$) and the difference between the two batches of negatively charged particles (PEGCOOH). It should be noted that the rest of the negatively charged particle aliquots (t = 0 to t = 9 hours) presented the α-galactose degradation over long storage, as well as a decrease of pH, while pegamine particles did not show any significant degradation of the carbohydrate or change of pH (*data not shown*).
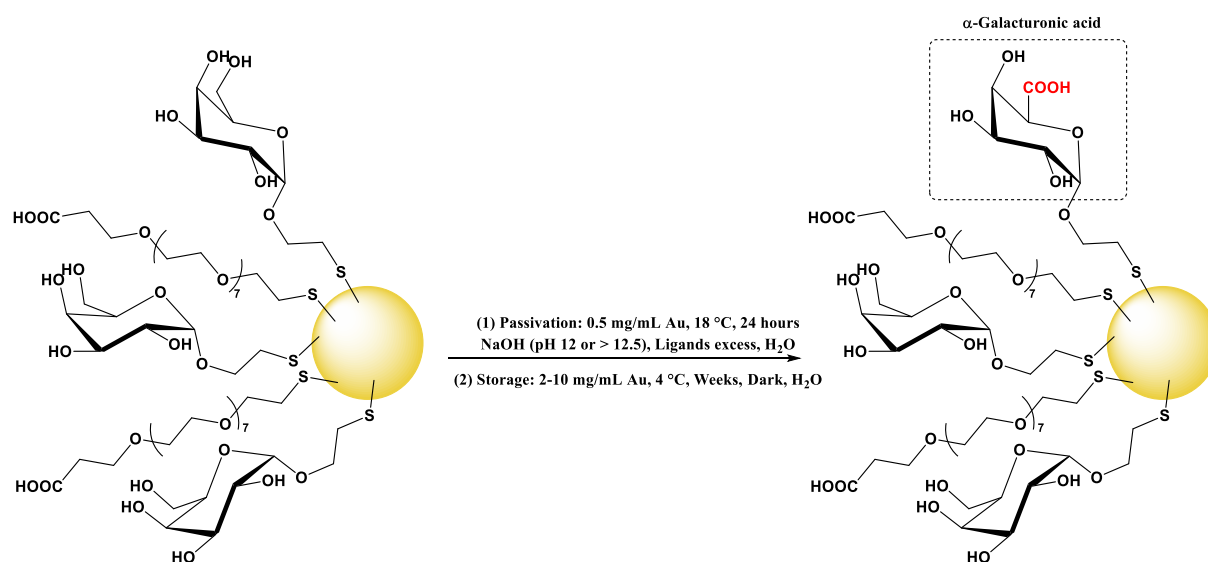


*Figure 17: Possible mechanisms of α-Galactose-$C_2$ degradation into α-Galacturonic acid during (1) passivation and (2) storage on (PEG(8)COOH)$_x$(α-Galactose-$C_2$)$_y$@Au$_{102}$.*

LC-CAD-MS was also used to follow the evolution of ligand density by comparing the ligand areas (*Figure 18*). All the batches showed a significant and gradual decrease of the α-Galactose-$C_2$ and oligo-PEG areas over time of passivation (*Figure 19*). The effect was the least intense with GNP-3 (PEGCOOH, 18 °C, pH 12), meaning a lower drop of ligand density. It should be noted that GNP-3 is also the particle least affected by the size increase over time. The α-Galactose-$C_2$ degradation product is visible on the chromatograms of GNP-3 and GNP-4 after 24 hours.
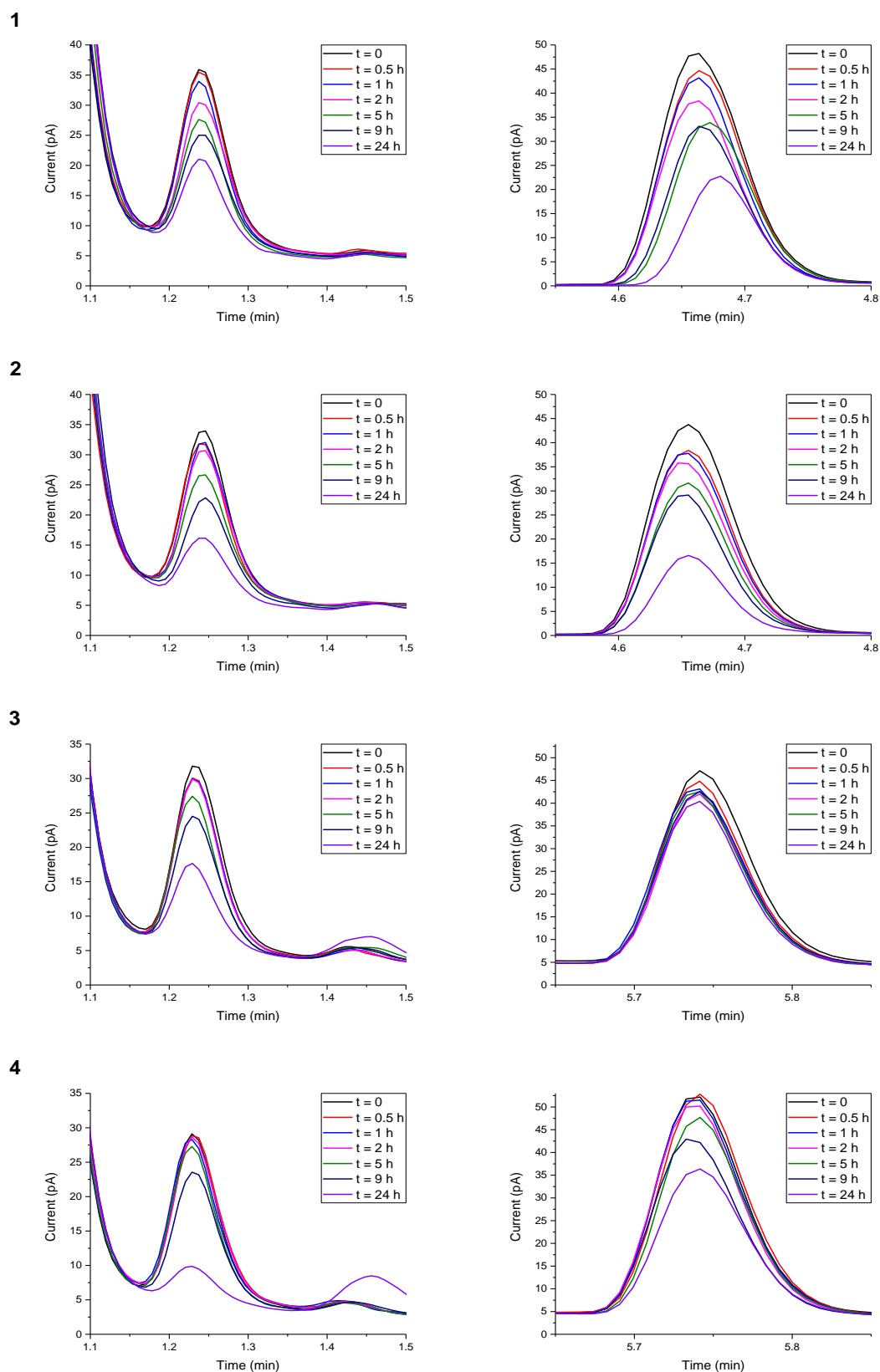
*Figure 18: Zoomed sections of different segments of LC-CAD chromatograms. On the left: α-Galactose-$C_2$ (RT 1.23 min), α-Galactose-$C_2$ degradation product (RT 1.42 min). On the right: PEG(5)NH$_2$ (RT 4.47 min) and PEG(8)COOH (RT 5.74 min). (1) GNP-1 (PEGNH$_2$, 18 °C, pH 12), (2) GNP-2 (PEGNH$_2$, 25 °C, pH 12), (3) GNP-3 (PEGCOOH, 18 °C, pH 12) and (4) GNP-4 (PEGCOOH, 18 °C, pH > 12.5).*
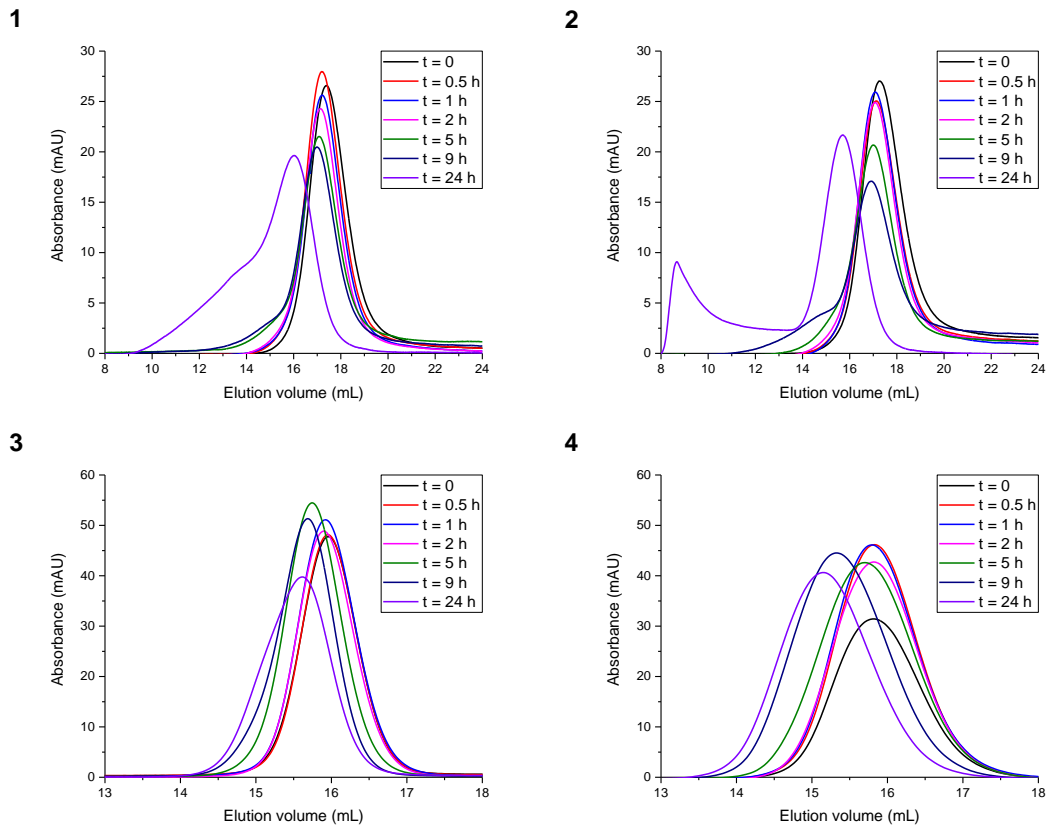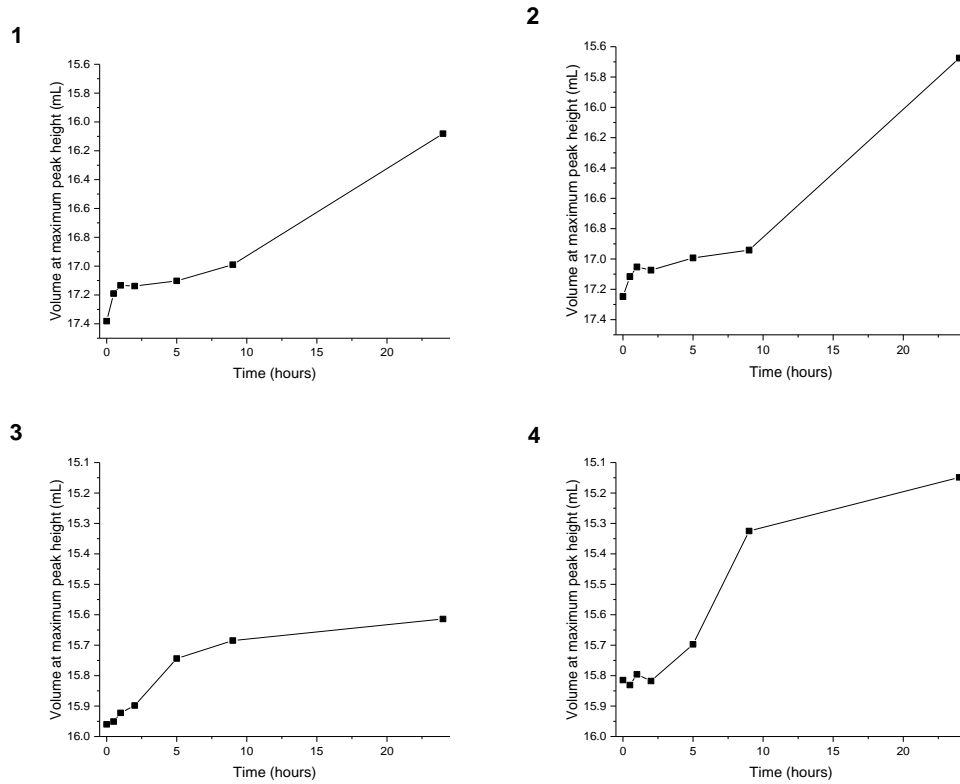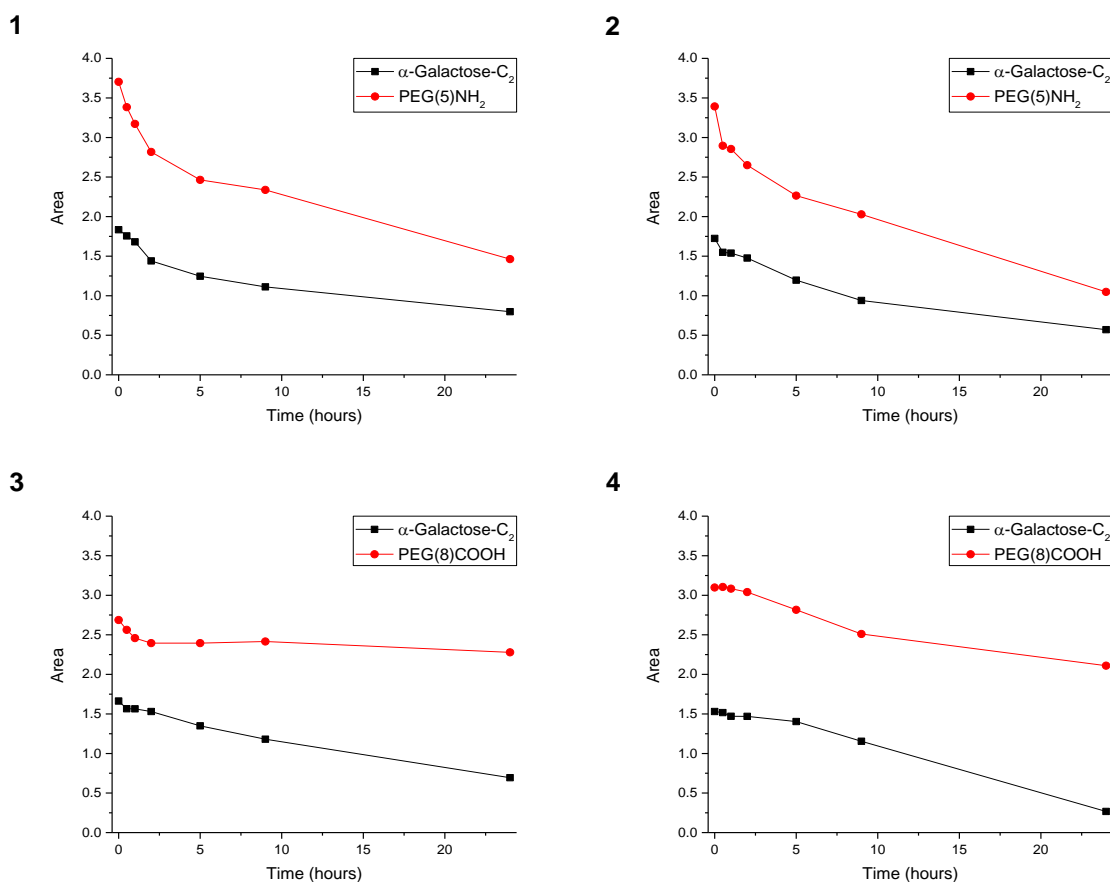
*Figure 19: Ligand area measured by LC-CAD of (1) GNP-1 (PEGNH₂, 18 •C, pH 12), (2) GNP-2 (PEGNH₂, 25 •C, pH 12), (3) GNP-3 (PEGCOOH, 18 •C, pH 12) and (4) GNP-4 (PEGCOOH, 18 •C, pH > 12.5).*

A reverse phase HPLC-DAD procedure with a wavelength of 400 nm to detect the gold core was used to study the GNP polarity (*Figure 20*). While a decrease of ligand density is the factor that would impact the retention time the most, other aspects, such as gold core size growth, should not be underestimated.

Thus, it is not possible to attribute all the changes observed in the following graphs to alterations in the ligand corona. Nevertheless, the clear tendency of retention time increase over time of passivation for all the GNP batches, appears to indicate a change in the properties of the particles. This change, together with the relative stability of the ligand ratio observed by ^{1}H NMR and LC-CAD-MS, indicates that the decrease of the GNP polarity could be linked to a loss of organic material and, therefore, a drop of ligand density. The increase of retention time was more pronounced for GNP-2 than GNP-1, and, GNP-4 than GNP-3.
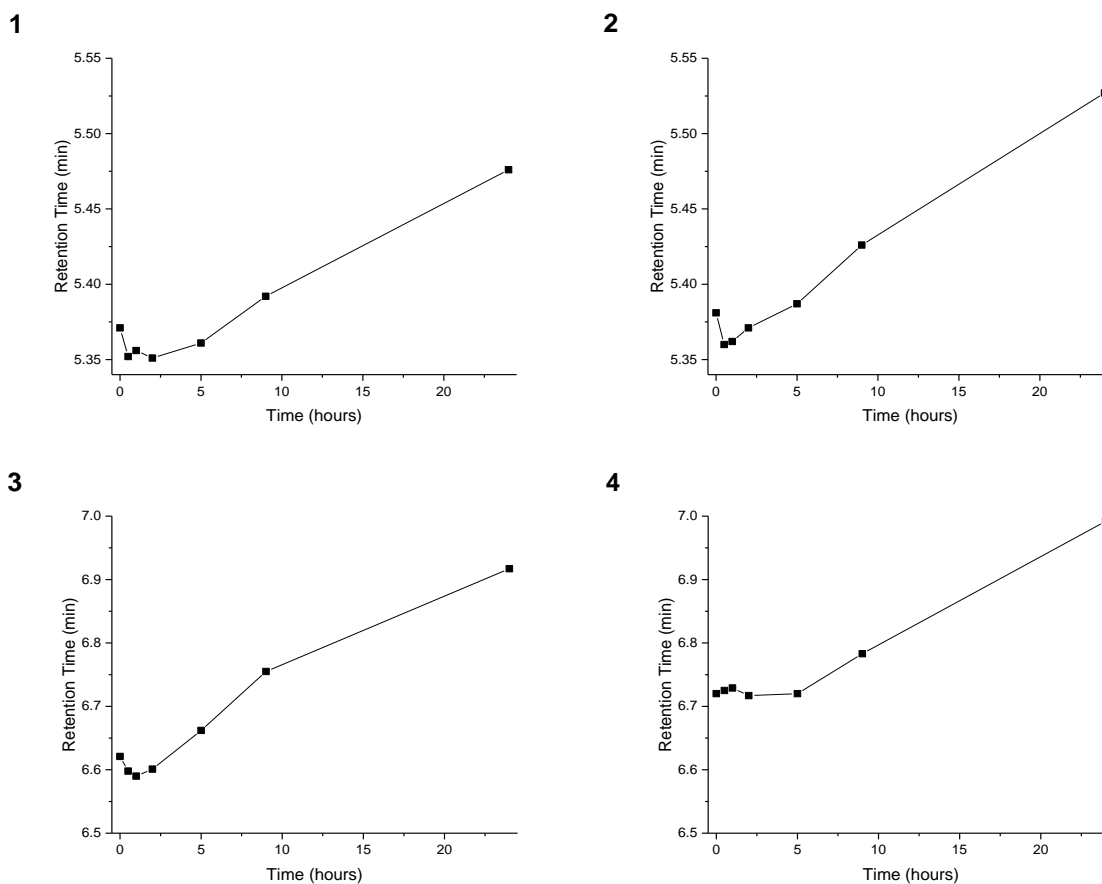
*Figure 20: Reverse phase HPLC-DAD retention time of (1) GNP-1 (PEGNH$_2$, 18 °C, pH 12), (2) GNP-2 (PEGNH$_2$, 25 °C, pH 12), (3) GNP-3 (PEGCOOH, 18 °C, pH 12) and (4) GNP-4 (PEGCOOH, 18 °C, pH > 12.5). (λ = 400 nm).*

To confirm the trend of decrease of ligand density during the passivation process, XPS and ICP-AES analyses were performed. The samples were digested to the atomic level using an *aqua regia* treatment. The concentration of sulfur and gold were obtained, and the molar ratio was calculated. A decrease of ligand density was observed by both XPS (*Figure 21*) and ICP-AES (*Figure 22*).

The values showed that the theoretical ratio: 0.43 (44 ligands and 102 Au atoms per particle) was underestimated for the pegamine batches (GNP-1 and GNP-2) up to 5-9 hours of passivation and after that time, it was overestimated. Regarding the PEGCOOH GNP (GNP-3 and GNP-4), the theoretical ratio was only overestimated after 24 hours of passivation.

None of the techniques were accurate enough to give an exact S/Au ratio and compare the batches, but the trend of ligand density decrease seen by LC-CAD-MS was confirmed.
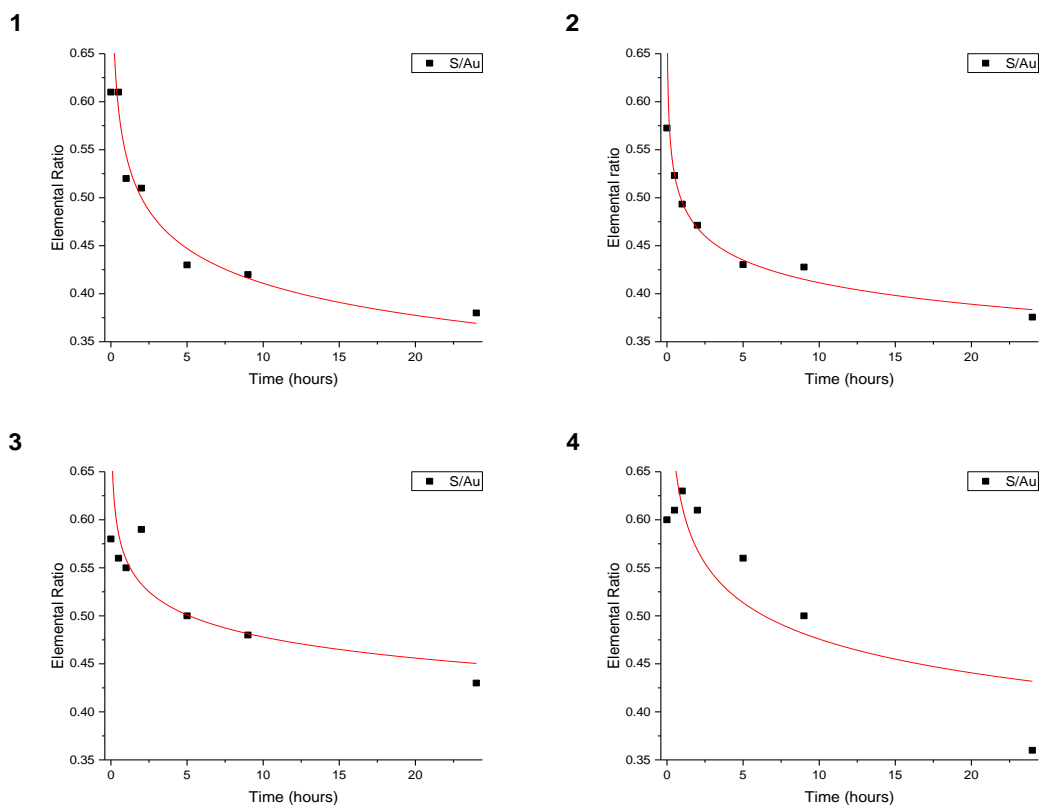
*Figure 21: Sulfur to gold molar ratio measured by XPS of (1) GNP-1 (PEGNH₂, 18 °C, pH 12), (2) GNP-2 (PEGNH₂, 25 °C, pH 12), (3) GNP-3 (PEGCOOH, 18 °C, pH 12) and (4) GNP-4 (PEGCOOH, 18 °C, pH > 12.5).*
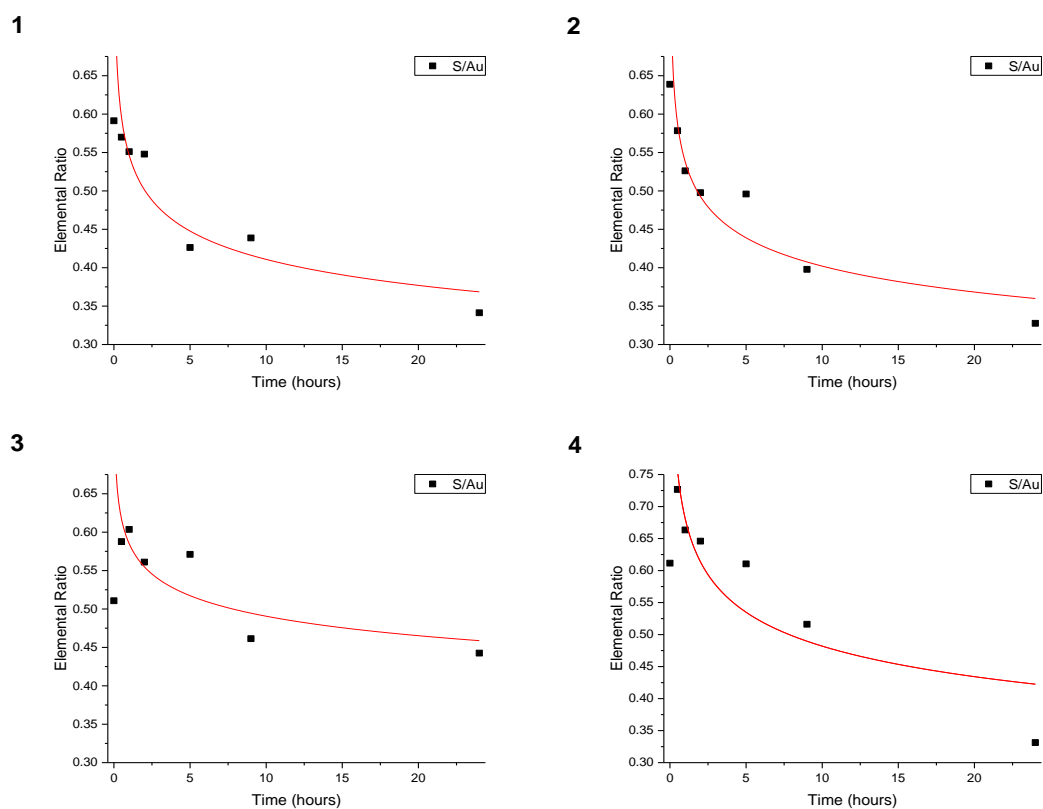


*Figure 22: Sulfur to gold molar ratio measured by ICP-AES of (1) GNP-1 (PEGNH₂, 18 °C, pH 12), (2) GNP-2 (PEGNH₂, 25 °C, pH 12), (3) GNP-3 (PEGCOOH, 18 °C, pH 12) and (4) GNP-4 (PEGCOOH, 18 °C, pH > 12.5).*

## 2. Sodium borohydride scavenging by ion exchange resins: proof of concept

The first set of experiments with GNP-1 to GNP-4 showed that the particles evolve during passivation, with two main phenomena occurring: size increase and ligand density decrease. As mentioned previously, the purification by ultrafiltration is dependent on several factors, one of them being the amount of material. Essentially, the greater the amount of material, the longer the purification takes, and therefore, the longer the time of passivation. To decrease the impact of passivation mechanisms, two anion exchange resins to scavenge the sodium borohydride were evaluated: IRA-400 (strong) and IRA-743 (weak)[45]. Moreover, the two models previously used: positive (PEG(5)NH$_2$) and negative (PEG(8)COOH) GNP were tested to see the impact of the particle charge on NaBH$_4$ scavenging efficacy.

Two batches, **GNP-5** and **GNP-6** were synthesized at 18 °C with the BSS protocol previously described (*Table 2*).

*Table 2: Different Batches synthesized for the proof of concept of scavenging experiments.*

| Batch | Ligand I | Ligand II | Charge and Shortened Ligand ID | Ligand Addition Ratio (%) |
|-------|----------|-----------|-------------------------------|---------------------------|
| GNP-5 | α-Galactose-C$_2$ | PEG(5)NH$_2$ | Positive PEGNH$_2$ | 50:50 |
| GNP-6 | | PEG(8)COOH | Negative PEGCOOH | 40:60 |

The mixture was incubated for 3 minutes after nucleation and then recovered from the reactor vessel. An aliquot (t = 0) was taken and purified by centrifugal ultrafiltration.

The rest of the solution was transferred to four Erlenmeyer flasks in equal volumes. The Erlenmeyer flasks contained: (1) 450 mg of IRA-400 per mg of gold, (2) 450 mg of IRA-400 per mg of gold, (3) 450 mg of IRA-743 per mg of gold and (4) no resin. After 30 minutes at room temperature with mild agitation, (1), (2) and (3) were filtered, using a Büchner funnel to remove the resin, and transferred to another Erlenmeyer flask with no resin for (1) and (3) or with 450 mg of IRA-743 per mg of gold for (2). 30 minutes later, (2) was filtered using a Büchner funnel and transferred to another Erlenmeyer flask with no resin. Essentially, (2) was exposed to the two resins sequentially, while (1) and (3) were exposed to only one of the resins. Aliquots of the four final Erlenmeyer flasks were taken at 6 and 18 hours, purified by centrifugal ultrafiltration, and then resuspended with identical volumes (*Figure 23*). Unpurified aliquots of the different samples were kept, to compare the crude gold and boron concentrations. Analyses were performed immediately after the syntheses.
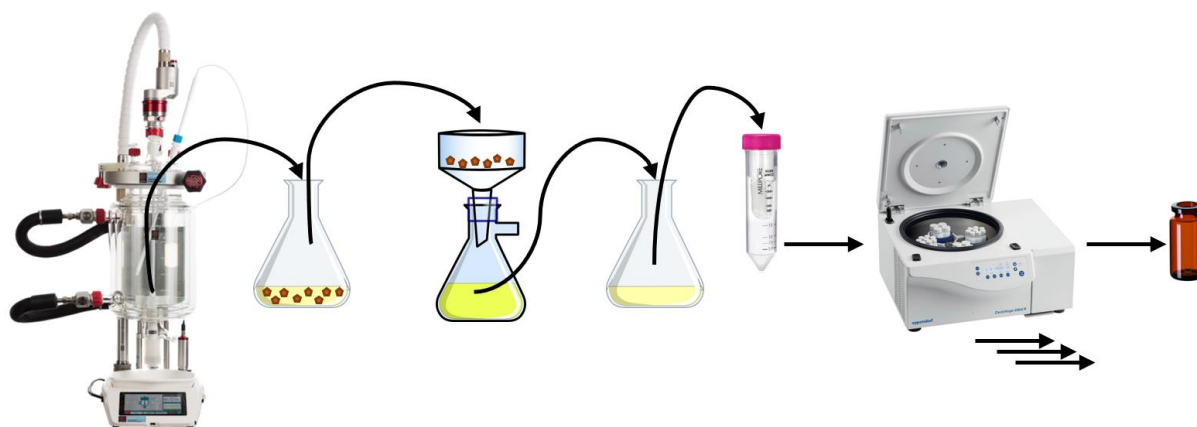
*Figure 23: Schematic overview of the purification process using IRA-400 and IRA-743 resins. The crude GNP solution was taken from the reactor after nucleation and incubated in Erlenmeyer flasks with the resins. The resins were removed by filtration using a Büchner funnel and the different treated GNP solutions were transferred to other Erlenmeyer flasks and further incubated. Aliquots were taken at 6 and 18 hours and purified by centrifugal ultrafiltration.*

The gold and boron content of the unpurified samples (MP-AES analysis) were measured (*Figure 24*). Samples treated with the different resins were compared with the untreated samples to quantify the relative drop in [Au] and [B] caused by the resins. A [B] drop was sought as a proof of the sodium borohydride scavenging by the resins. IRA-400 significantly outperformed IRA-743, with the former removing over 90 % of the boron, against less than 50 % with the latter. Using the two resins led to an increase of the scavenging, achieving a final [B] below 2 %.

However, [Au] loss should be considered, as it affects the final yield of the reaction. In the conditions studied, this loss was below 20 % with IRA-400 alone, and around 30 % with the two resins. This probably results from an adsorption of the GNP onto the resins. It should be noted that no washing of the resins was applied, which, theoretically, could lead to higher yields.
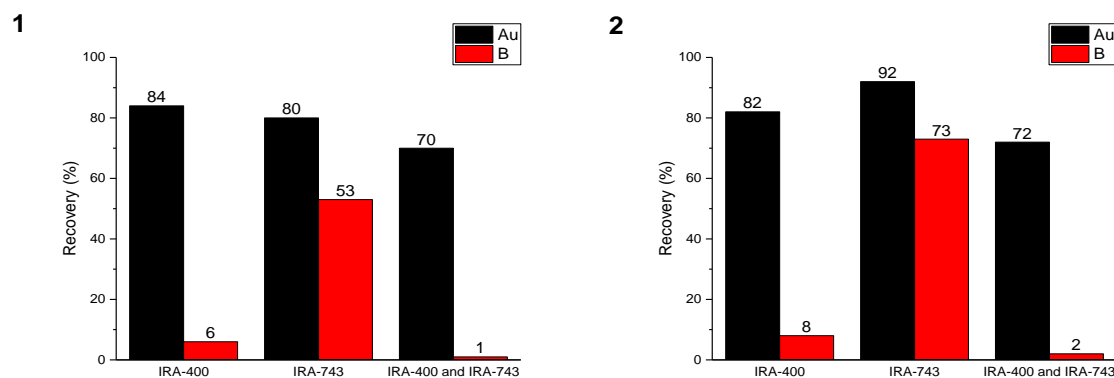


*Figure 24: Percentages of remaining gold and boron with the different resins compared to the untreated sample by MP-AES of (1) GNP-5 (PEGNH₂) and (2) GNP-6 (PEGCOOH).*

47

The UV-Vis spectra of the untreated samples confirmed the SPB increase with time of passivation for both positive and negative particles (*Figure 25*). When compared to the sample purified immediately after nucleation (t = 0), IRA-400 (alone or in combination with IRA-743) almost completely prevented plasmon increase, while IRA-743 did so only partially. This shows that resins are an effective way to remove the $NaBH_4$ from the crude nanoparticle solution and confirms the link between the scavenging of sodium borohydride and the prevention of plasmon increase.
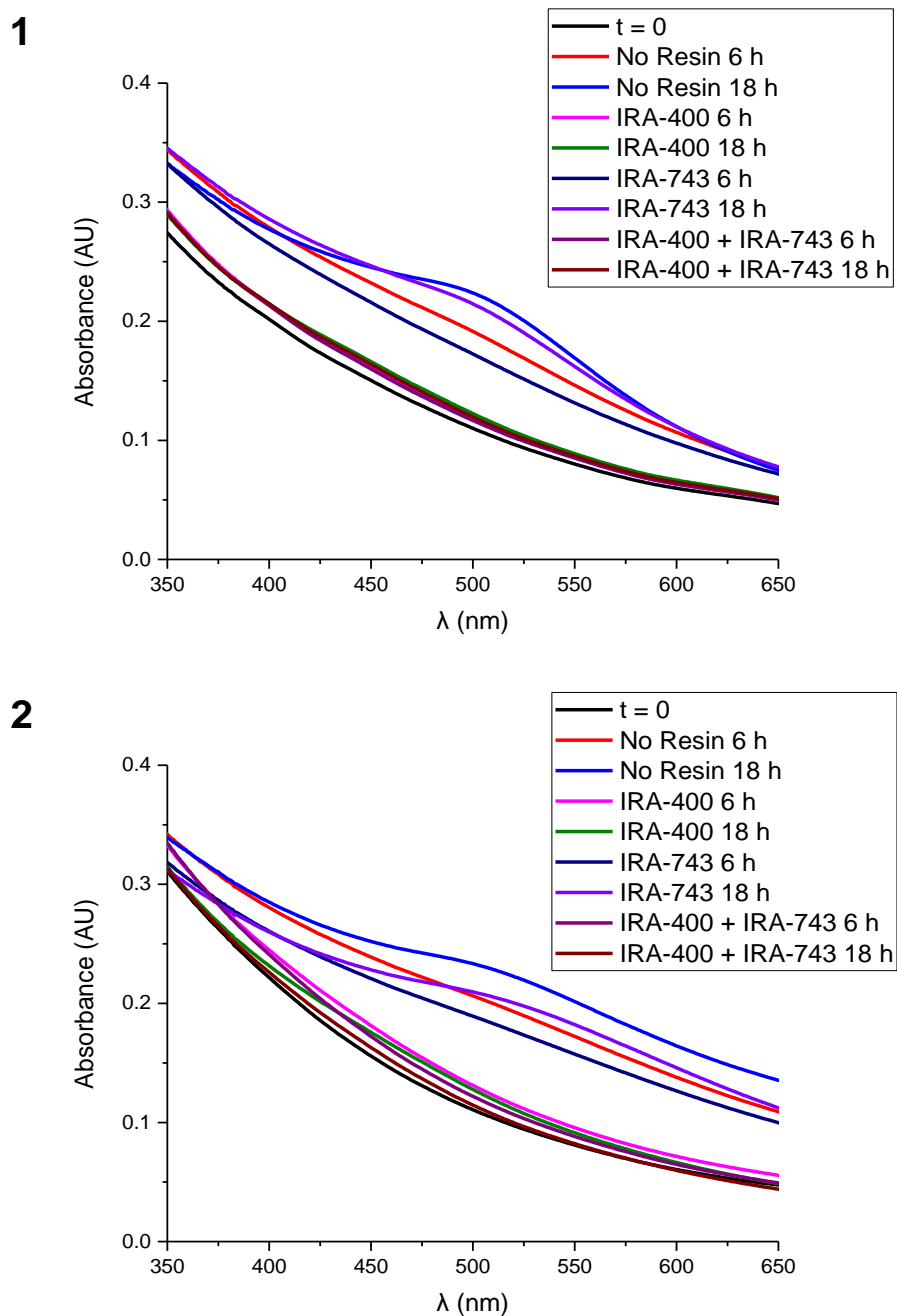


*Figure 25: UV-Vis spectra (λ 350-650 nm) of (1) GNP-5 (PEGNH₂) and (2) GNP-6 (PEGCOOH).*

## 3. Impact of IRA-400 treatment on GNP passivation

Following the experiment with the resins that demonstrated the capacity of IRA-400 to scavenge sodium borohydride and prevent plasmon increase from occurring over the time of passivation, a further experiment was performed to focus on lowering the IRA-400 quantity (from 450 mg of IRA-400 per mg of gold to 100 mg of IRA-400 per mg of gold) and evaluating the effect of the resin in a longer passivation time (up to four days). Also, the analytical characterization, in terms of changes in core size, was expanded to include also TEM analysis, in addition to UV-Vis. The overall size of the particles was measured by DLS, DCS and SEC. The ligand ratio was determined by $^1$H NMR and LC-CAD-MS. HPLC-DAD, XPS and ICP-AES were used to estimate the ligand density.

One batch, **GNP-7**, was produced with a molar ratio β-Glucose-C$_2$/PEG(8)COOH 45:55 (*Table 3*). The experimental design and the synthesis conditions were identical to GNP-5 and GNP-6 (*Figure 23*) except from to the resin treatment and the time points of aliquot sampling.

In the case of GNP-7, Erlenmeyer flasks contained: (1) 300 mg of IRA-400 per mg of gold, (2) 200 mg of IRA-400 per mg of gold, (3) 100 mg of IRA-400 per mg of gold and (4) no resin. After 30 minutes at room temperature with mild agitation, (1), (2) and (3) were filtered using a Büchner funnel to remove the resin and transfer to another Erlenmeyer flask with no resin. Aliquots of the four final Erlenmeyer flasks were taken at 6, 18 and 96 hours, purified by centrifugal ultrafiltration, then resuspended with identical volumes. Unpurified aliquots of the different samples were also kept.

*Table 3: Batch synthesized for the IRA-400 optimization experiment.*

| Batch | Ligand I | Ligand II | Charge and Shortened Ligand ID | Ligand Addition Ratio (%) |
|-------|----------|-----------|-------------------------------|---------------------------|
| GNP-7 | β-Glucose-C$_2$ | PEG(8)COOH | Negative PEGCOOH | 40:60 |

Gold and boron content of unpurified samples (MP-AES analysis) were measured (*Figure 26*). Samples treated with the different amounts of IRA-400 were compared with the untreated sample, to quantify the relative drop of [Au] and [B] caused by the different resin quantities. A greater amount of resin resulted in lower [Au] and [B]. Roughly, by increasing the concentration of resin from 100 mg/mg Au to 300 mg/mg Au, [Au] dropped from 90 % to 80 %, substantially affecting the final yield of the reaction. [B] was the same for 200 and 300 mg/mg Au, reaching a plateau of approximately 10%.

Looking at the elemental concentrations only, the intermediate amount of resin, 200 mg/mg Au appears to be the best compromise to scavenge the maximum quantity of sodium borohydride while maintaining high yields, with above 80 % [Au] and only 11 % [B] remaining.
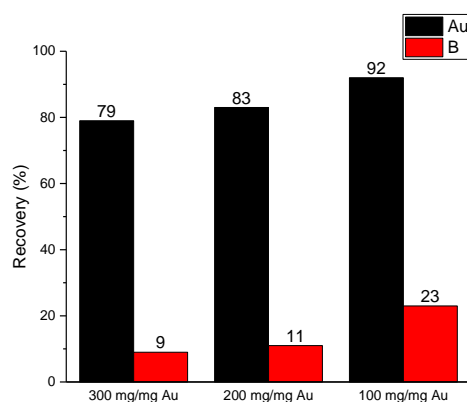


*Figure 26: Percentages of remaining gold and boron compared to the untreated sample with different amounts of IRA-400 by MP-AES for GNP-7 (PEGCOOH).*

UV-Vis spectrophotometric measurements were used to monitor the relative SPB intensity (*Figure 27*). Comparing to t = 0, for the samples incubated with 200 and 300 mg/mg Au of resin, the plasmon increase was minimal (within analytical uncertainty), even after 96 hours. GNP incubated with resin at the lowest concentration, 100 mg/mg Au, showed a minor increase of plasmon. Without resin, a significant plasmon band appeared. Interestingly, it did not increase any further after 18 hours.
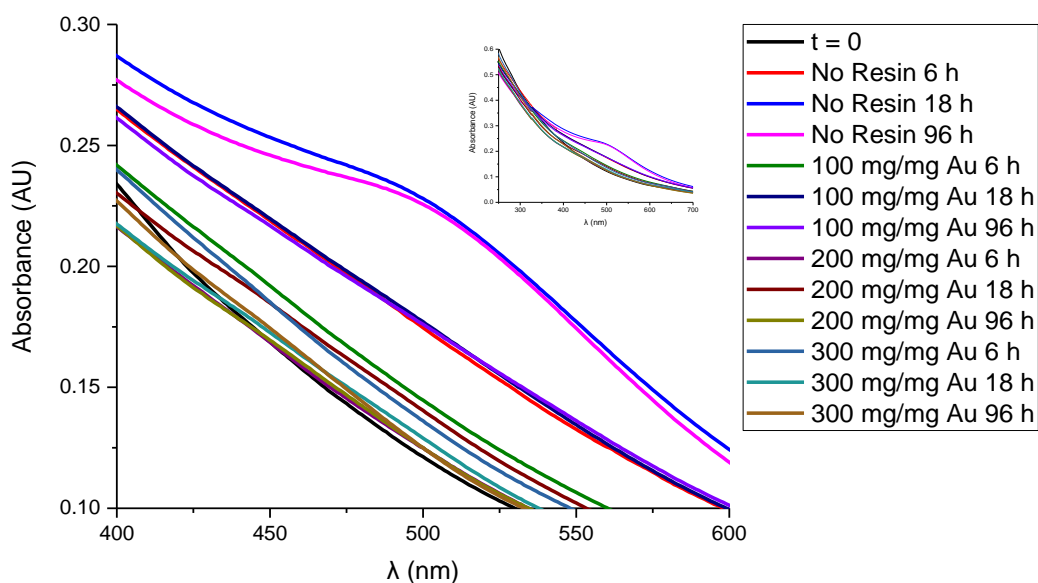


*Figure 27: UV-Vis spectra zoom (λ 400-600 nm) of GNP-7 (PEGCOOH).*

TEM pictures of the GNP were taken and processed to obtain the mean and median diameter (*Figure 28*). Only the samples without resin showed a significant size increase.
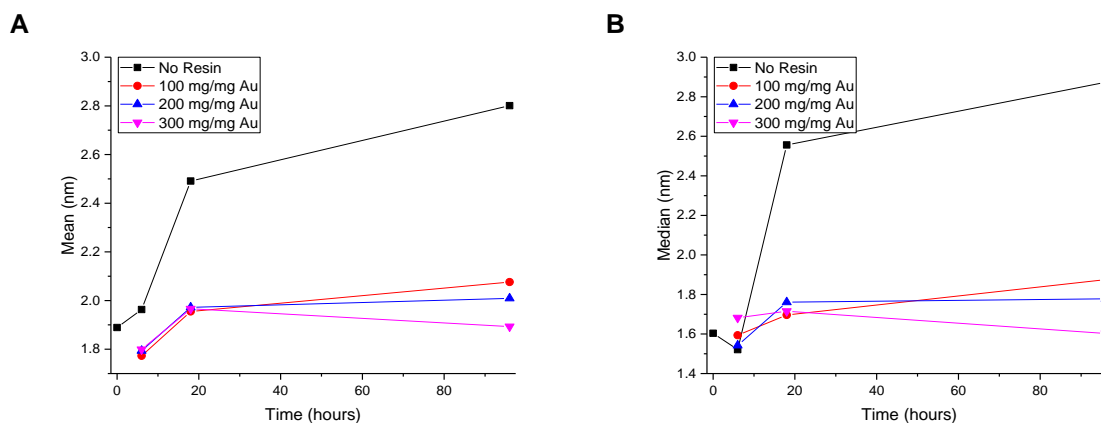


*Figure 28: TEM (A) Mean and (B) Median size of GNP-7 (PEGCOOH).*

To characterize the overall size of the GNP, three analytical techniques were used: DLS, DCS and SEC.

By DLS it was not possible to see any significant difference between the samples (*Figure 29*).

On the other hand, DCS showed an increase of size over time of passivation, although only for samples without resin after 18 hours (*Figure 30*).

SEC demonstrated, for all the samples, a gradual increase of particle size (Figure *31*), that was inversely correlated with the concentration of resin. Samples treated with resin only showed a moderate size increase, while without resin the growth was greater, leading to a loss of gaussian aspect after 18 hours.

Compared to DLS and DCS, SEC demonstrated again a greater sensitivity, since it was able to identify the gradual increase of particle size over time of passivation for all the samples, illustrating the impact of the resin concentration.
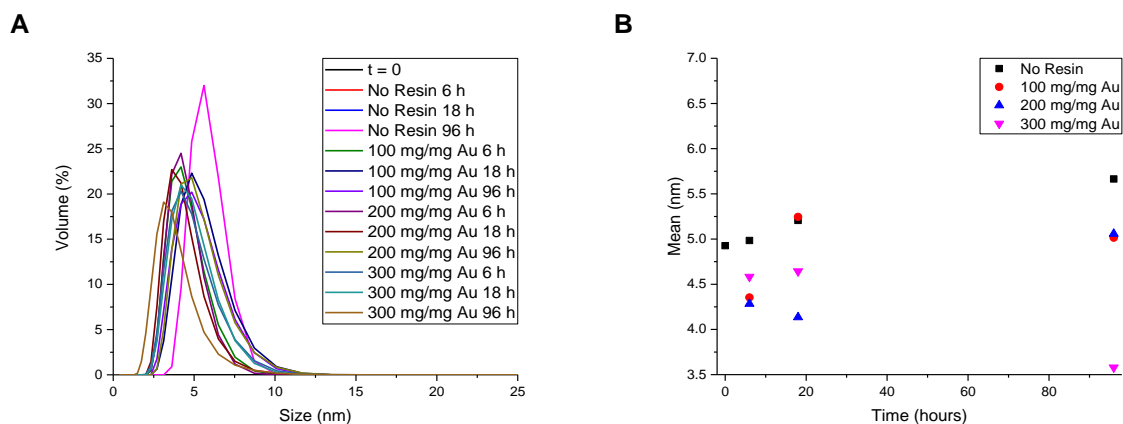
*Figure 29: DLS (A) hydrodynamic size distribution and (B) size mean by volume of GNP-7 (PEGCOOH).*
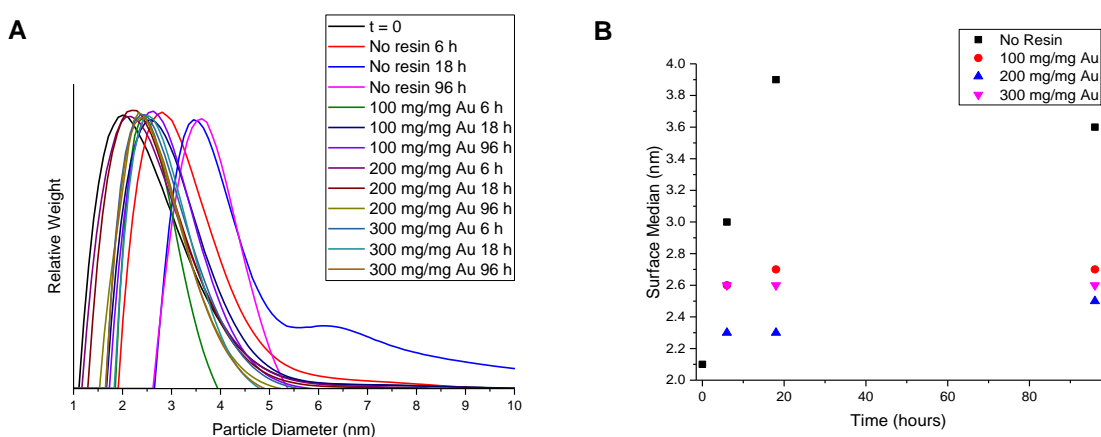


*Figure 30: DCS (A) diameter distribution and (B) median size by surface of GNP-7 (PEGCOOH).*
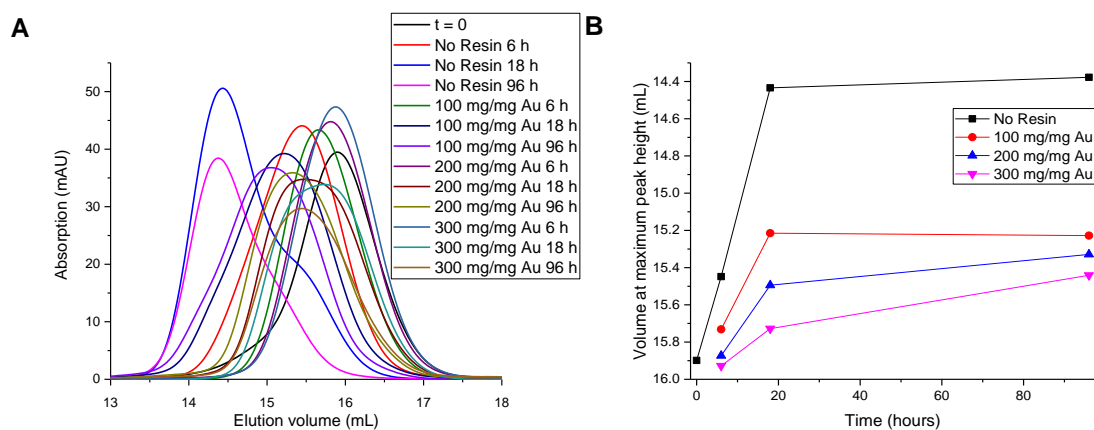


*Figure 31: FPLC (A) size exclusion chromatograms and (B) volume at maximum peak height of GNP-7 (PEGCOOH) (λ = 400 nm).*

^{1}H NMR and LC-CAD-MS allowed the identification and ratio determination of the ligands β-Glucose-C$_2$ and PEG(8)COOH (*Figure 32*). As expected, the molar ratios for all the samples were close to 50:50 at t = 0 and after 6 hours However, for untreated samples, after 18 hours, a relative drop in β-Glucose-C$_2$ was observed down to 20 % by ^{1}H NMR (*Figure 40 in the annex),* and < 35 % by LC-CAD-MS. This could be explained by the degradation of the carbohydrate and the formation of related compounds such as gluconic acid, by the previously explained mechanism with α-Galactose-C$_2$.
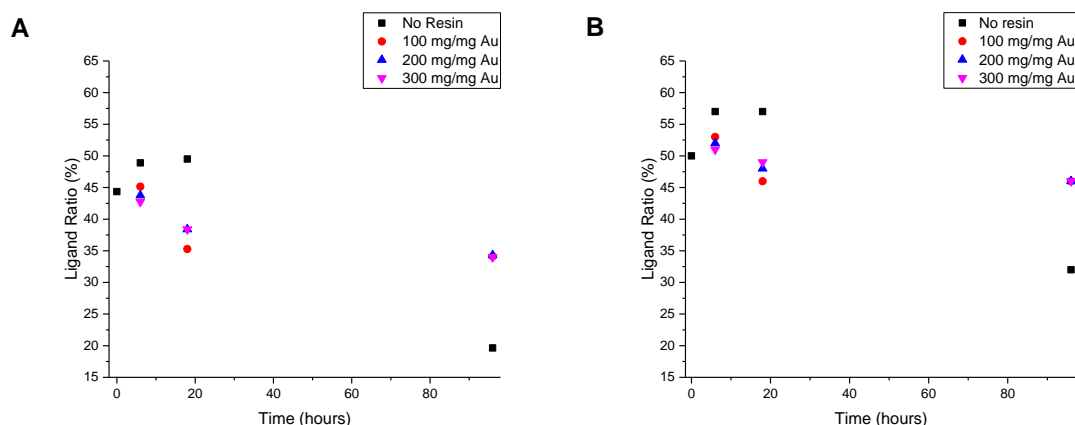


*Figure 32: Ratios of β-Glucose-C₂/PEGCOOH by (A) ¹H NMR and (B) LC-CAD of GNP-7 (PEGCOOH).*

LC-CAD-MS was also used to follow the evolution of the ligand density by comparing the ligand areas (*Figure 33*). The samples without resin showed a significant and gradual decrease of β-Glucose-C$_2$ and PEG(8)COOH. A more limited ligand density drop was also observed for the lowest IRA-400 concentration, 100 mg/mg Au. For the highest concentrations of resin, the density remained stable, observing even a slight increase of density for the PEG(8)COOH, correlated with the drop of the β-Glucose-C$_2$/PEG(8)COOH ratio in presence of the resins.
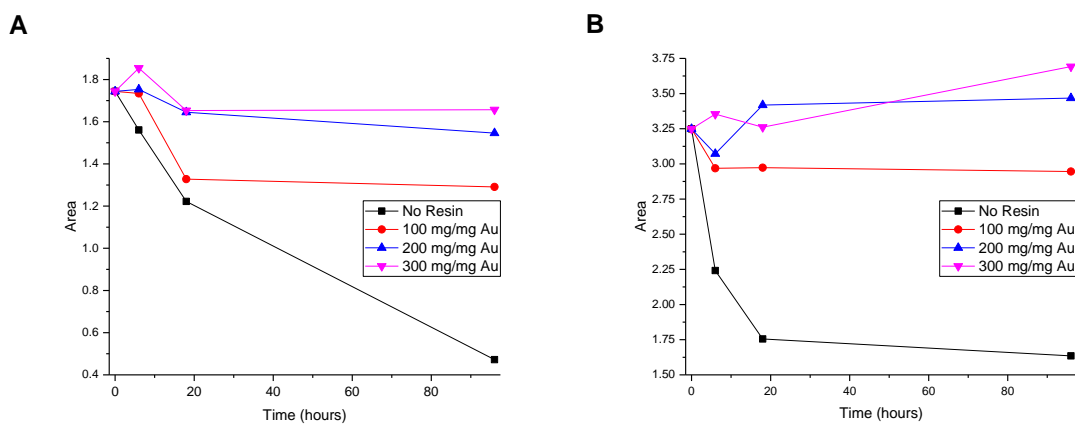


*Figure 33: Ligand area of GNP-7 (PEGCOOH) measured by LC-CAD. (A) β-Glucose-C₂. (B) PEG(8)COOH.*

HPLC-DAD analyses showed an increase of the retention time for the batches without resin treatment. The retention time of the samples treated with the resin remained relatively more stable (*Figure 34*).
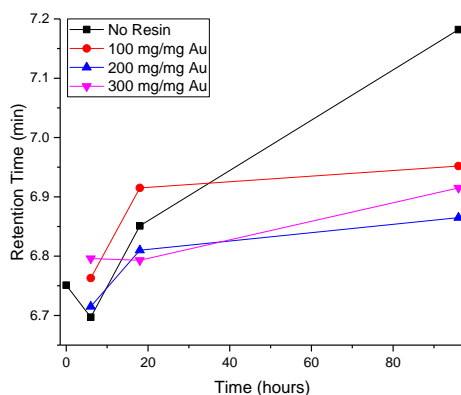


*Figure 34: Reverse phase HPLC-DAD retention times of GNP-7 (PEGCOOH) with the different concentrations of IRA-400 (λ = 400 nm).*

XPS (*Figure 35 A*) and ICP-AES (*Figure 35 B*) analyses were performed and the S/Au molar ratio was calculated. This confirmed the data obtained by LC-CAD-MS: a sharp drop of the density for untreated samples: below 0.25 after 96 hours and a lower decrease for IRA-400, 100 mg/mg Au. For IRA-400 200 and 300 mg/mg Au, the ligand density remained stable over time of passivation, with values between 0.50 and 0.65 (above the theoretical model of 0.43).
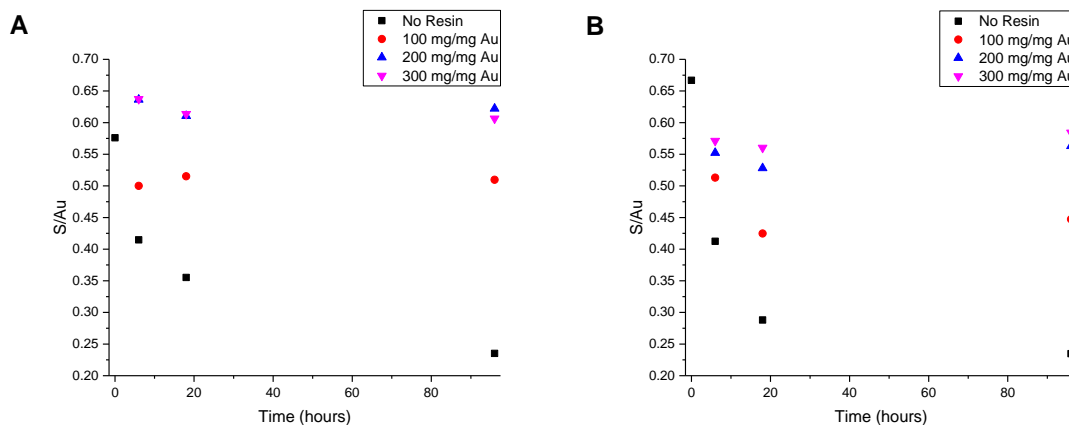


*Figure 35: Sulfur to gold molar ratio measured by (A) XPS and (B) ICP-AES of GNP-7 (PEGCOOH).*

# IV. Conclusions and Further Work

The different experiments performed demonstrated the importance of the passivation phase during aqueous Brust-Schiffrin synthesis. Four different batches were used changing one parameter at the time: pegamine particles were synthesized at either 18 °C or 25 °C and pH ~ 12 while carboxylic acid PEG particles were synthesized at 18 °C and pH ~ 12 (pH adjustment achieved with NaOH) or > 12.5 (large excess of NaOH). Two major trends were observed: the particle growth, at both core and whole particle level, and the ligand density decrease with increasing time of passivation.

UV-Vis (surface plasmon band increase) and SEC (peak displacement) demonstrated that the growth was gradual and started as soon as the nucleation finished. Other size measurement techniques such as TEM, DLS and DCS were shown to be less sensitive, only displaying differences at higher time points (greater than 9 hours of passivation). Moreover, after 24 hours of passivation, the pegamine particle distribution lost its gaussian shape and even displayed a second population at 25 °C on DCS and SEC distributions. This appears to indicate that, rather than a regular core growth, the mechanism in place is probably an aggregation process.

$^1$H NMR and LC-CAD-MS showed that the ligand ratios on the bifunctional GNP remained stable over the time of passivation. The targeted ratio of 50:50 between the oligo-PEG and $\alpha$-Galactose-C$_2$ was obtained. On the other hand, the ligand density exhibited a gradual decrease after the nucleation. This decrease was observed for both ligands using LC-CAD-MS, XPS and ICP-AES. The drop in organic material density on the core can be attributed to the sodium borohydride etching properties[20]. The NaBH$_4$ effect overcomes the potential backfilling (increase of ligand density due to the excess of ligands that fills the empty sites on the particle core)[46]. It is interesting to see that the oligo-PEG and $\alpha$-Galactose-C$_2$ are etched with similar kinetics, which correlates with their close capacity to cap the core during the nucleation (addition of ~ equimolar amounts).

Apart from time, other parameters affected the passivation: ligands, pH and temperature. Positive particles with pegamine (PEG(5)NH$_2$) exhibited higher growth increase than those with negative carboxylic acid (PEG(8)COOH). That is consistent with reports of ligands bearing amine and thiol groups promoting aggregation[47]. The pegamine particles synthesized showed higher growth increase at 25 °C than at 18 °C. A large excess of NaOH (pH > 12.5) promoted a higher growth increase than an adjustment to pH ~ 12 with the carboxylic acid PEG GNP.

The high pH resulting from the excess of sodium hydroxide could be responsible for the GNP aggregation, as it also produced a degradation of the organic material on the shell with the oxidation of α-galactose to galacturonic acid.

As previously mentioned, ultrafiltration is the most common method used to purify GNP solutions. Although equipment and method development can and should be adapted to the scale, the overall length of the process may increase when the synthesis is performed at a larger scale. In order to achieve the removal of sodium borohydride and investigate the consequences on the passivation process, two exchange resins were used as an approach to scavenge sodium borohydride. IRA-400 and IRA-743 were compared with both positive and negative GNP models to assess the boron removal and, consequently, the inhibition of the particle growth (observed by UV-Vis). IRA-400 demonstrated a stronger capacity than IRA-743 to remove the boron from the crude GNP solution, preventing plasmon from arising even after 18 hours.

The amount of IRA-400 per gold was then optimized for effective boron scavenging. Incubation of GNP for 30 minutes with 200 mg of IRA-400 per mg of gold in a simple open system, was able to remove almost 90 % of the $NaBH_4$, and to quench the related passivation effects even after four days. A comprehensive analysis showed the absence of significant size increase at both the core and overall particle level. Moreover, LC-CAD-MS, XPS and ICP-AES showed that the ligand density remained stable after $NaBH_4$ removal by the resin, while the absence of the resin resulted in a significant density reduction.

These experiments provided insights into the passivation phase, and into how to manage it in order to attain the desired product. To improve the control of the process, standardization, automation and data acquisition are critical, as is an exhaustive control of the parameters of synthesis and purification (e.g. solvent, equivalents, concentrations, volumes, temperature, pH, time, mixing). In fact, deviations of material specifications could lead to problems of inter-batch reproducibly, and, consequently, negatively affect the GNP performance during downstream chemical steps (e.g. ligand exchange or post-functionalization) or biochemical/biological assays.

Apart from passivation, pre-nucleation and nucleation also impact the nanoparticles and should be studied. An extensive investigation of the critical parameters of synthesis should be performed for every GNP candidate, in order to obtain the most robust control of the product key attributes, which would allow a smoother transition to clinical trials or commercial development.

IRA-400 (and IRA-473) were chosen because they emerged from the sparse literature and the experimental setup was rudimentary. Therefore, there is room for improvement with further investigation with other resins and optimization of the system (pressure, temperature, time, washing). One potential application of the ion exchange resins would be the possibility to perform subsequent reactions of functionalization without purification by ultrafiltration. This would have a tremendous impact on the efficiency of processes at industrial level.

To achieve the control of process aforementioned, reliable analyses are critical. This study demonstrated the importance of a comprehensive array with optimized techniques. Regarding the particle size, UV-Vis and SEC were the most sensitive techniques, but they lack the capacity to obtain an absolute value of core or overall size, unlike TEM or DLS/DCS. For the ligand density, LC-CAD-MS provided the most sensitive analysis, and was able to discriminate between the ligands, while ICP-AES and XPS only provided an estimation of the overall ligand density through a molar S/Au ratio. In order to increase the analytical control, individual quantification of the ligands should be implemented. For LC methods, this means using a calibration curve with standard materials and improving the peak resolution, while quantitative NMR (qNMR) could be performed using an internal standard[48,49].

# V. Materials and Methods

## 1. Synthesis of the GNP

GNP were synthesized with a modified Brust-Schiffrin method using a Syrris Atlas Potassium reactor with a 500 mL jacketed torispherical vessel and a 500-50 mm blade propeller stirrer without baffles. The temperature was equilibrated before addition of the reagents and maintained during the syntheses using Julabo CF40 Cryo-Compact Circulator. The reactions were carried out at 18 or 25 °C with fast stirring (750 rpm). Time, pH and temperature were monitored. $H_2O$ (Ultrapure, Milli-Q® Advantage A10 Water Purification System) was the solvent used for both synthesis and purification. The addition of the different reagents was performed from the top of the vessel within minutes (~ 15 min) using a 150-80-8 mm funnel.

The purifications were performed using 10 kDa Amicon 15-Ultra filters (Merck Millipore) in a centrifuge (Thermo Scientific Heraeus Labofuge 400 R) using the following protocol. First, a 10 min cycle 4500 rcf/4 °C to concentrate all the material, followed by 3 washes of 10 min 4500 rcf/4 °C with $H_2O$. The final products were filtered with a 0.22 μm membrane, resuspended in $H_2O$ and stored in an amber glass vial at 4 °C.

### a. $(PEG(5)NH_2)(\alpha\text{-Galactose-}C_2)@Au_{102}$

$HAuCl_4 \cdot 3H_2O$ (1 equivalent, 500 mg, 1.270 mmol, 50 mL, Sigma-Aldrich) was added to an excess of disulfide ligands $PEG(5)NH_2$ (0.75 equivalent, 564 mg, 0.953 mmol, 170 mL, Galchimia) and $\alpha$-Galactose-$C_2$ (0.75 equivalent, 456 mg, 0.953 mmol, 170 mL, Galchimia) 50:50 molar ratio. Aqueous NaOH solution (~ 10 mL 1 M NaOH) was used to modulate the pH to ~ 12. Freshly prepared $NaBH_4$ (1 M in $H_2O$, 20 equivalents, 961 mg, 25.4 mmol, 25 mL, Sigma-Aldrich/Appli Chem) was quickly added to form the particles. During the nucleation, the gold concentration was 3 mM and the final volume of the reaction around 425 mL (85 % of the reactor capacity).
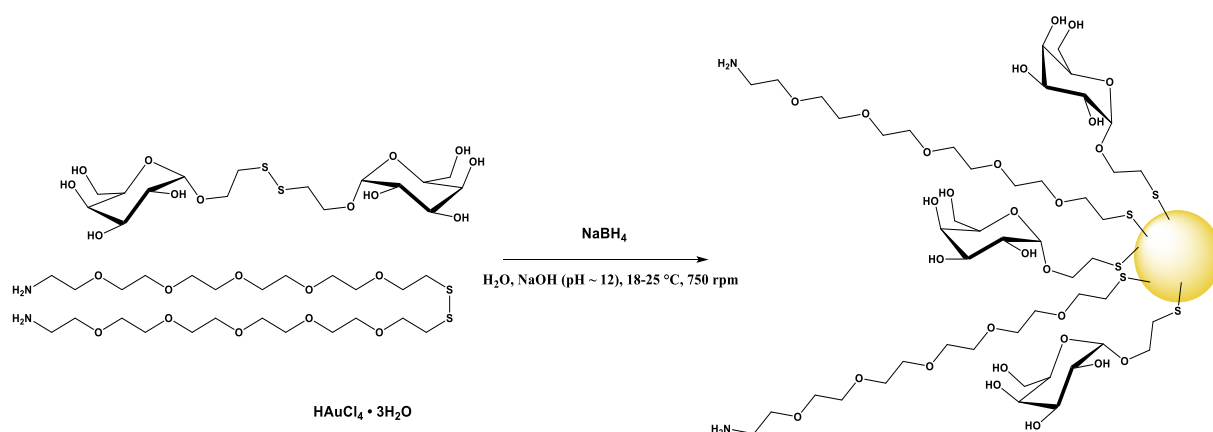
*Figure 36: (PEG(5)NH₂)(α-Galactose-C₂)@Au₁₀₂ synthesis.*

- **GNP-1 (PEG(5)NH₂)(α-Galactose-C₂)@Au₁₀₂**

The reaction was performed at 18 °C. 2 minutes after addition of NaBH₄, the stirring speed was dropped to 400 rpm. At different time points (0, 0.5, 1, 2, 5, 9 and 24 hours) aliquots of 34 mL were taken out using a pipette gun. The aliquots were purified by centrifugal ultrafiltration and resuspended in 4 mL H₂O.

- **GNP-2 (PEG(5)NH₂)(α-Galactose-C₂)@Au₁₀₂**

The batch was produced in the exact same conditions as GNP-1, except for the temperature: 25 °C (instead of 18 °C).

- **GNP-5 (PEG(5)NH₂)(α-Galactose-C₂)@Au₁₀₂**

The batch was produced in the same conditions as GNP-1.

3 minutes after addition of NaBH₄, the solution was recovered in a 500 mL Duran bottle and the reactor was washed with 25 mL H₂O, for a final volume of crude GNP solution of 450 mL.

An aliquot was taken immediately (t = 0) from the reactor and purified by centrifugal ultrafiltration. The rest of the solution was transferred to four 250 mL Erlenmeyer flasks in equal volume (80 mL, approximately 45 mg Au). Two resins were used: Amberlite IRA-400 chloride form (20 g, Sigma-Aldrich) and Amberlite IRA743 free base (20 g, Sigma-Aldrich). The Erlenmeyer flasks contained: (1) 450 mg of IRA-400 per mg of gold, (2) 450 mg of IRA-400 per mg of gold, (3) 450 mg of IRA-743 per mg of gold and (4) no resin.

After 30 min at room temperature with mild agitation (700 rpm using a magnetic stir bar), (1), (2) and (3) were filtered using a Büchner funnel with a fritted glass disc to remove the resin and transferred to another capped Erlenmeyer flask with no resin for (1) and (3) or with 450 mg of IRA-743 per mg of gold for (2). After 30 min at room temperature with mild agitation, (2) was filtered using a Büchner funnel and transferred to another capped Erlenmeyer flask with no resin.

From the Erlenmeyer flasks, 25 mL aliquots were taken out after 6 and 18 hours using a pipette gun. The aliquots were purified by centrifugal ultrafiltration and resuspended in 2.5 mL $H_2O$. Unfiltered aliquots (5 mL) were also collected.

### b. (PEG(8)COOH)($\alpha$-Galactose-C$_2$)@Au$_{102}$

The reactions were performed at 18 °C. HAuCl$_4$•3H$_2$O (1 equivalent, 500 mg, 1.270 mmol, 50 mL, Sigma-Aldrich) was added to an excess of disulfide ligands PEG(8)COOH (0.90 equivalent, 1046 mg, 1.143 mmol, 170 mL, Acadechem) and $\alpha$-Galactose-C$_2$ (0.60 equivalent, 365 mg, 0.762 mmol, 170 mL, Galchimia) 60:40 molar ratio. Aqueous NaOH solution (~ 10 mL 1 M NaOH) was used to modulate the pH to ~ 12. Freshly prepared NaBH$_4$ (1 M in $H_2O$, 20 equivalents, 961 mg, 25.4 mmol, 25 mL Sigma-Aldrich/Appli Chem) was quickly added to form the particles. During the nucleation, the gold concentration was 3 mM and the final volume of the reaction around 425 mL (85 % of the reactor capacity).



*Figure 37: (PEG(8)COOH)($\alpha$-Galactose-C$_2$)@Au$_{102}$ synthesis.*

- **GNP-3 (PEG(8)COOH)($\alpha$-Galactose-C$_2$)@Au$_{102}$**

2 minutes after addition of NaBH$_4$, the stirring speed was dropped to 400 rpm. At different time points (0, 0.5, 1, 2, 5, 9 and 24 hours ) aliquots of 34 mL were retrieved using a pipette gun. The aliquots were purified by centrifugal ultrafiltration and resuspended in 4 mL H$_2$O.

- **GNP-4 (PEG(8)COOH)($\alpha$-Galactose-C$_2$)@Au$_{102}$**

The batch was produced in the same conditions as GNP-3, except for the pH, which was raised before nucleation to >12.5 (~ 100 mL 1M NaOH) instead of ~ 12.0 (~ 10 mL 1M NaOH). Also, the ligands were dissolved in 125 mL H$_2$O each.

- **GNP-6 (PEG(8)COOH)($\alpha$-Galactose-C$_2$)@Au$_{102}$**

The batch was produced in the exact same conditions as GNP-4. The resin treatment protocol was the same as for GNP-5.

c. (PEG(8)COOH)($\beta$-Glucose-C$_2$)@Au$_{102}$

- **GNP-7 (PEG(8)COOH)($\beta$-Glucose-C$_2$)@Au$_{102}$**

The reaction was performed at 18 °C. HAuCl$_4$•3H$_2$O (1 equivalent, 500 mg, 1.270 mmol, 50 mL, Sigma-Aldrich) was added to an excess of disulfide ligands PEG(8)COOH (0.85 equivalent, 988 mg, 1.079 mmol, 155 mL, Acadechem) and $\beta$-Glucose-C$_2$ (0.65 equivalent, 395 mg, 0.825 mmol, 155 mL Galchimia) ~ 55:45 molar ratio. Aqueous NaOH solution (~ 40 mL 1 M NaOH) was used to modulate the pH to ~ 12.5. Freshly prepared NaBH$_4$ (1 M in 0.01M NaOH, 20 equivalents, 961 mg, 25.4 mmol, 25 mL, Sigma-Aldrich) was quickly added to form the particles. During the nucleation, the gold concentration was 3 mM and the final volume of the reaction around 425 mL (85 % of the reactor capacity).
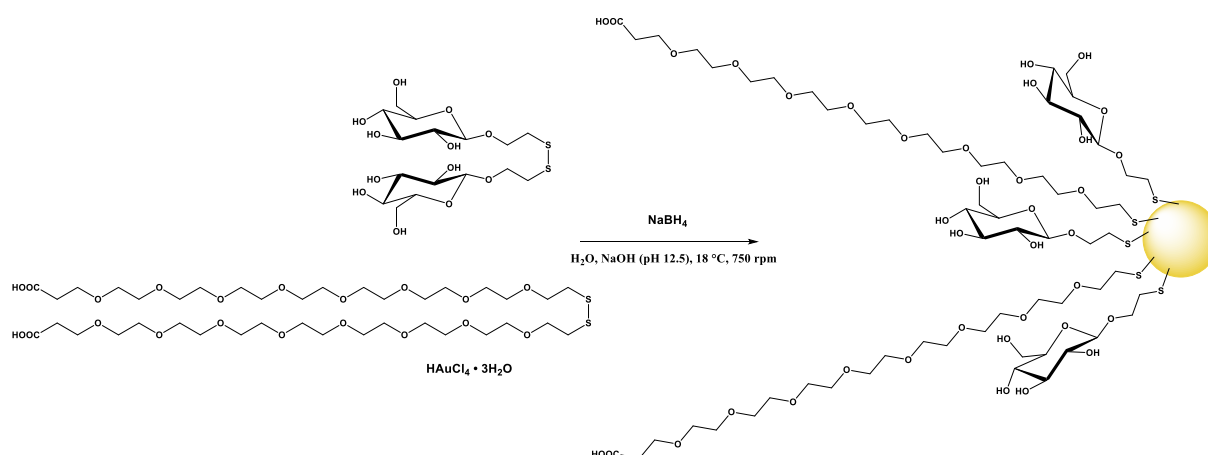


*Figure 38: (PEG(8)COOH)($\beta$-Glucose-C$_2$)@Au$_{102}$ synthesis.*

3 minutes after addition of $NaBH_4$, the solution was recovered in a 500 mL Duran bottle and the reactor was washed with 25 mL $H_2O$ for a final volume of crude GNP solution of 450 mL.

An aliquot was taken immediately (t = 0) from the reactor and purified by centrifugal ultrafiltration. The rest of the solution was transferred to three 250 mL Erlenmeyer flasks in equal volume (90 mL, approximately 50 mg Au). Amberlite IRA-400 chloride form was used (5, 10 and 15 g). The Erlenmeyer flasks contained: (1) 300 mg of IRA-400 per mg of gold, (2) 200 mg of IRA-400 per mg of gold, (3) 100 mg of IRA-400 per mg of gold and (4) no resin. After 30 min at room temperature with mild agitation (700 rpm using a magnetic stir bar), (1), (2) and (3) were filtered using a Büchner funnel with a fritted glass disc to remove the resin and transferred to another capped Erlenmeyer flask with no resin.

From the Erlenmeyer flasks, 25 mL aliquots were taken out after 6, 18 and 96 hours using a pipette gun. The aliquots were purified by centrifugal ultrafiltration and resuspended in 2.5 mL $H_2O$. Unfiltered aliquots (5 mL) were also collected.

## 2. Characterization of the GNP

### a. Microwave Plasma - Atomic Emission Spectrometry (MP-AES)

GNP solutions (20-50 μL) were digested with 200 μL of *aqua regia*, then diluted up to 10 mL using 3 % (v/v) HCl. The elemental analysis of Au ($\lambda = 257.595$ nm), B ($\lambda = 249.772$ nm) and Na ($\lambda = 588.995$ nm) was performed using Agilent 4200 MP-AES with MP Expert software version 1.5.16821.

### b. pH

Crison Instruments Basic 20 pH meter and Hach Sension+ 5208 pH probe were used.

### c. UV-Vis Spectrophotometry

GNP UV-Vis spectra ($\lambda$ 200-700 nm) were obtained using Perkin-Elmer Lambda 35 UV-Vis Spectrophotometer with 2 mL of 20 μg/mL Au GNP aqueous solution in a quartz cuvette.

### d. Transmission Electron Microscopy (TEM)

Samples were prepared under ambient conditions by desiccating a 0.35 μL droplet of a 30 μg/mL Au GNP aqueous solution (150 μg/mL Au for 4 nm GNP) on a hydrophilized carbon film surface. Ultrathin film supports type #01824 were used (Ted Pella Inc.). The hydrophilization was performed for 2 minutes with 25 mA strong glow discharge treatment in a K100X plasma chamber (Quorum Technologies Ltd). Image data was acquired in a transmission electron microscope of type JEM-2100F [Model EM-20014, UHR, 200 kV] (JEOL) equipped with a digital camera of type F-216 (TVIPS). Usually, wider field of view images at X150k magnification were assembled with the spotscan utility of the TVIPS EMMENU4 software from a beam shift based 4x4 images matrix. Analyses were performed at CIC BiomaGUNE (San Sebastian, Spain). Data processing was performed using ImageJ.

### e. Dynamic Light Scattering (DLS)

Size (hydrodynamic diameter) measurements were performed with 1 mL of 200 μg/mL Au GNP solutions in 10 mM PBS with Malvern Zetasizer Nano-ZS. Size was expressed by volume (%) as an average of 3 measurements taken at 25 °C at a 173-degree scattering angle in a plastic cuvette.

## f. Differential Centrifugation Sedimentation (DCS)

Sizing analysis was performed using a CPS DC24000UHR disc centrifuge (CPS Instruments, Inc.). An 8-24 % sucrose gradient was created in 11 mL water. A series of solutions of varying sucrose concentration were injected sequentially (from high to low concentration) to generate the gradient. This was followed by a dodecane injection (500 µL), to reduce gradient evaporation. The gradient was allowed to stabilize and to reach thermal equilibrium for approximately 30 min prior to data acquisition. Polyvinylchloride (PVC) calibration standards (0.237 µm, 50 µL injection volume) were analyzed prior to each GNP sample (100 µL, 100 µg/mL Au) to ensure that the instrument was operating optimally and with a high level of accuracy. Analyses were performed at 24 000 rpm with the light detector adjusted to a position suitable for the analysis of ultrasmall GNP. Particle size was calculated based on an assumed GNP density of 5.0 g/cm$^3$.

## g. Size Exclusion Chromatography (SEC)

GNP solutions at 200 µg/mL Au were incubated in 10 mM PBS or Borax/NaOH for 30 min at room temperature. AKTA Pure FPLC system (GE Healthcare) was equipped with a SEC column Superdex 200 Increase 10/300 GL (GE Healthcare). The injection volume was 20 µL, the flow rate was isocratic at 0.5 mL/min in 10 mM PBS or Borax/NaOH, and the detection wavelengths were 220 and 400 nm using U9-M UV-Vis detector. The analyses were performed at room temperature. The device was controlled using UNICORN software 7.0.

## h. HPLC-DAD (reverse phase)

Solvents used for the mobile phase were acetonitrile and $H_2O$ (Scharlab, LC-MS grade). Trifluoroacetic acid (Merck, Analytical quality) was used to acidify the mobile phase.

An aliquot containing 2.5 µg Au from a 125 µg/mL Au GNP solution was injected directly into an Agilent 1260 Infinity HPLC-DAD system. Data processing were performed with OpenLab CDS software. Separations were performed on an XSelect CSH C18 column, 130 Å, (150 × 4.6 mm i.d., 3.5 µm particle size) and a XSelect CSH C18 VanGuard precolumn, 130 Å, (5 × 3.9 mm i.d., 3.5 µm particle size) (Waters). Solvents used as mobile phase were as follows: A: 0.1 % trifluoroacetic acid in $H_2O$; B: 0.1 % trifluoroacetic acid in acetonitrile. Elution conditions applied were as follows: 0-1.5 min, 5 % B isocratic; 1.5-9 min, linear gradient 5-98 % B; 9-11.5 min, 98 % B isocratic; washing and reconditioning of the column. Flow rate was 1 mL/min and injection volume 20 µL. The system operated at 35 ºC.

### i. X-ray Photoelectron Spectrometry (XPS)

Samples were deposited on glass slides and dried in a Desiccator Cabinet (Scienceware) for at least 48 hours. XPS experiments were performed in a SPECS Sage HR 100 spectrometer with a non-monochromatic X-ray source (Magnesium Kα line of 1253.6 eV energy and 251 W), placed perpendicularly to the analyzer axis and calibrated using the 3d5/2 line of Ag with full width at half maximum (FWHM) of 1.1 eV. The selected resolution for the spectra was 15 eV of Pass Energy and 0.15 eV/step. All measurements were made in an ultra-high vacuum (UHV) chamber at a pressure around $2 \cdot 10^{-8}$ mbar. An electron flood gun was used for charge neutralization. In the fittings, asymmetric and Gaussian-Lorentzian functions were used (after a Shirley background correction) where the FWHM of all the peaks were constrained, while the peak positions and areas were set free. Adventitious carbon 1s line was fixed for calibration at 284.8 eV. Analyses were performed at CIC BiomaGUNE (San Sebastian, Spain).

### j. Inductively Coupled Plasma - Atomic Emission Spectroscopy (ICP-AES)

100 μL of a 5 mg/mL Au GNP solution were digested with 200 μL *aqua regia*, then diluted to 1 mL using 3 % (v/v) HCl. The elemental analysis (Au and S) was performed using Agilent 5100 Synchronous Vertical Dual View (SVDV) ICP-OES at Servicio Central de Análisis de Bizkaia (UPV/EHU, Leioa).

# VI.   Annex
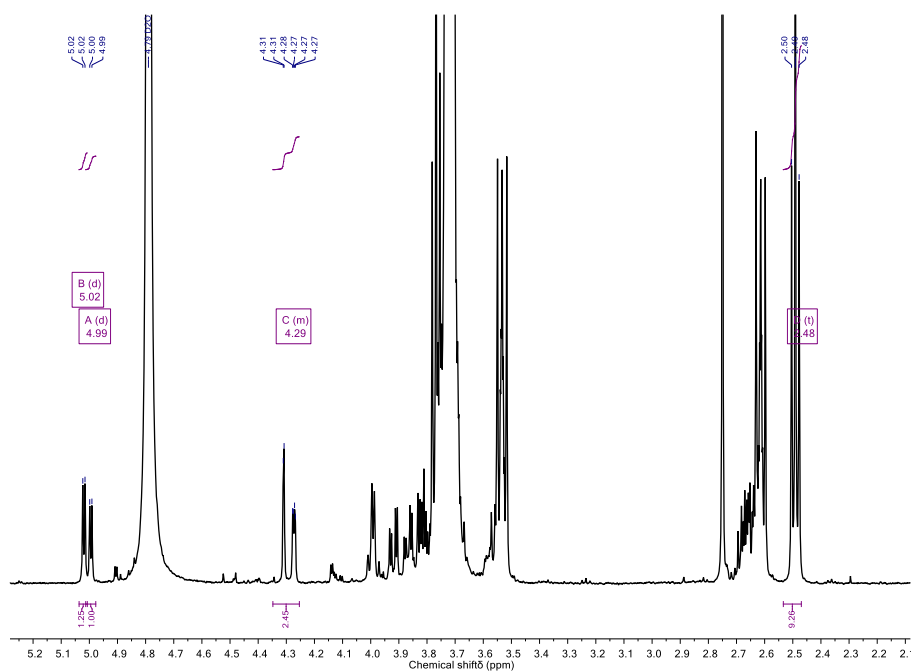


*Figure 39: $^1H$ NMR (500 MHz, $D_2O$, KCN/KOH treatment) of GNP-4 (PEGCOOH, 18 °C, pH > 12.5) after 24 hours of passivation. (A) α-Galactose-$C_2$ δ 4.99 (H-1, d, 1H), (B) α-Galactose-$C_2$ degradation derivative δ 5.02 (H-1, d, 1H); 4.29 (m, 2H), (C) PEG(8)COOH δ 2.48 (-$CH_2$-COOH, t, 2H).*
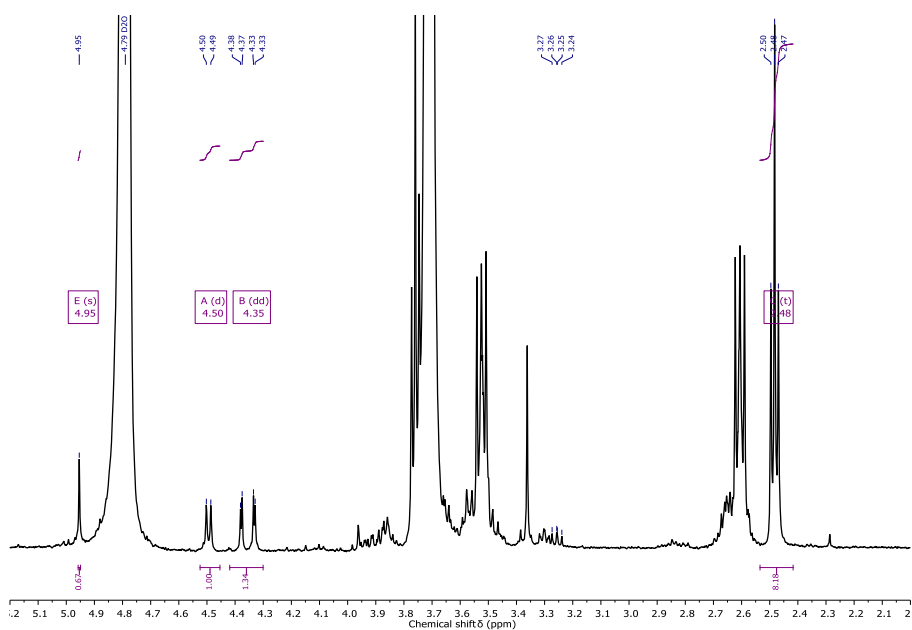


*Figure 40: $^1H$ NMR (500 MHz, $D_2O$, KCN/KOH treatment) of GNP-7 (PEGCOOH) after 96 hours of passivation. (A) β-Glucose-$C_2$ δ 4.50 (d, 1H, H-1), (B) β-Glucose-$C_2$ degradation derivative δ 4.95 (H-1, s, 1H); 4.35 (dd, 2H), (C) PEG(8)COOH δ 2.48 (-$CH_2$-COOH, t, 2H).*

# VII. References

1.      Brust, M., Walker, M., Bethell, D., Schiffrin, D. J. & Whyman, R. Synthesis of thiol-derivatised gold nanoparticles in a two-phase Liquid–Liquid system. *J. Chem. Soc. Chem. Commun.* 801–802 (1994).

2.      Zhao, P., Li, N. & Astruc, D. State of the art in gold nanoparticle synthesis. *Coord. Chem. Rev.* **257**, 638–665 (2013).

3.      Arvizo, R., Bhattacharya, R. & Mukherjee, P. Gold nanoparticles: opportunities and challenges in nanomedicine. *Expert Opin. Drug Deliv.* **7**, 753–763 (2010).

4.      Desai, N. Challenges in Development of Nanoparticle-Based Therapeutics. *AAPS J.* **14**, 282–295 (2012).

5.      Hostetler, M. J. *et al.* Alkanethiolate Gold Cluster Molecules with Core Diameters from 1.5 to 5.2 nm: Core and Monolayer Properties as a Function of Core Size. *Langmuir* **14**, 17–30 (1998).

6.      Porter, Lon A. *et al.* Gold and Silver Nanoparticles Functionalized by the Adsorption of Dialkyl Disulfides. *Langmuir* **14**, 7378–7386 (1998).

7.      Shon, Y.-S., Mazzitelli, C. & Murray, R. W. Unsymmetrical Disulfides and Thiol Mixtures Produce Different Mixed Monolayer-Protected Gold Clusters. *Langmuir* **17**, 7735–7741 (2001).

8.      Negishi, Y. *et al.* Kinetic Stabilization of Growing Gold Clusters by Passivation with Thiolates. *J. Phys. Chem. B* **110**, 12218–12221 (2006).

9.      Yonezawa, T., Yasui, K. & Kimizuka, N. Controlled Formation of Smaller Gold Nanoparticles by the Use of Four-Chained Disulfide Stabilizer. *Langmuir* **17**, 271–273 (2001).

10.     Shimmin, R. G., Schoch, A. B. & Braun, P. V. Polymer Size and Concentration Effects on the Size of Gold Nanoparticles Capped by Polymeric Thiols. *Langmuir* **20**, 5613–5620 (2004).

11.     Jørgensen, J. M., Erlacher, K., Pedersen, J. S. & Gothelf, K. V. Preparation Temperature Dependence of Size and Polydispersity of Alkylthiol Monolayer Protected Gold Clusters. *Langmuir* **21**, 10320–10323 (2005).

12. Briñas, R. P., Hu, M., Qian, L., Lymar, E. S. & Hainfeld, J. F. Gold Nanoparticle Size Controlled by Polymeric Au(I) Thiolate Precursor Size. *J. Am. Chem. Soc.* **130**, 975–982 (2008).

13. Azubel, M. & Kornberg, R. D. Synthesis of Water-Soluble, Thiolate-Protected Gold Nanoparticles Uniform in Size. *Nano Lett.* **16**, 3348–3351 (2016).

14. Meng, X., Liu, Z., Zhu, M. & Jin, R. Controlled reduction for size selective synthesis of thiolate-protected gold nanoclusters Aun (n = 20, 24, 39, 40). *Nanoscale Res. Lett.* **7**, 277 (2012).

15. Wei, A., Mehtala, J. G. & Patri, A. K. Challenges and Opportunities in the Advancement of Nanomedicines. *J. Control. Release Off. J. Control. Release Soc.* **164**, 236–246 (2012).

16. Van Reis, R. & Zydney, A. Membrane separations in biotechnology. *Curr. Opin. Biotechnol.* **12**, 208–211 (2001).

17. Sweeney, S. F., Woehrle, G. H. & Hutchison, J. E. Rapid Purification and Size Separation of Gold Nanoparticles via Diafiltration. *J. Am. Chem. Soc.* **128**, 3190–3197 (2006).

18. Rosenberg, E., Hepbildikler, S., Kuhne, W. & Winter, G. Ultrafiltration concentration of monoclonal antibody solutions: Development of an optimized method minimizing aggregation. *J. Membr. Sci.* **342**, 50–59 (2009).

19. Zydney, A. L. & Kuriyel, R. 4 High-Performance Tangential Flow Filtration for Protein Separations. in *Downstream Processing of Proteins: Methods and Protocols* 35–46 (Humana Press, 2000).

20. Ansar, S. M. *et al.* Removal of Molecular Adsorbates on Gold Nanoparticles Using Sodium Borohydride in Water. *Nano Lett.* **13**, 1226–1229 (2013).

21. Schaaff, T. G. & Whetten, R. L. Controlled Etching of Au:SR Cluster Compounds. *J. Phys. Chem. B* **103**, 9394–9396 (1999).

22. Jin, R. *et al.* Size Focusing: A Methodology for Synthesizing Atomically Precise Gold Nanoclusters. *J. Phys. Chem. Lett.* **1**, 2903–2910 (2010).

23. Chen, S., Templeton, A. C. & Murray, R. W. Monolayer-Protected Cluster Growth Dynamics. *Langmuir* **16**, 3543–3548 (2000).

24. E, X., Zhang, Y., Zou, J.-J., Zhang, X. & Wang, L. Shape evolution in Brust–Schiffrin synthesis of Au nanoparticles. *Mater. Lett.* **118**, 196–199 (2014).

25. Tsai, D.-H. *et al.* Orthogonal analysis of functional gold nanoparticles for biomedical applications. *Anal. Bioanal. Chem.* **407**, 8411–8422 (2015).

26. Mourdikoudis, S., Pallares, R. M. & Thanh, N. T. K. Characterization techniques for nanoparticles: comparison and complementarity upon studying nanoparticle properties. *Nanoscale* **10**, 12871–12934 (2018).

27. Kumar, A. & Dixit, C. K. 3 - Methods for characterization of nanoparticles. in *Advances in Nanomedicine for the Delivery of Therapeutic Nucleic Acids* 43–58 (Woodhead Publishing, 2017).

28. Colangelo, E. *et al.* Characterizing Self-Assembled Monolayers on Gold Nanoparticles. *Bioconjug. Chem.* **28**, 11–22 (2017).

29. Pichugina, D. A., Kuz'menko, N. E. & Shestakov, A. F. Ligand-protected gold clusters: the structure, synthesis and applications. *Russ. Chem. Rev.* **84**, 1114 (2015).

30. Jadzinsky, P. D., Calero, G., Ackerson, C. J., Bushnell, D. A. & Kornberg, R. D. Structure of a Thiol Monolayer-Protected Gold Nanoparticle at 1.1 Å Resolution. *Science* **318**, 430–433 (2007).

31. Zhang, J., Li, Z., Zheng, K. & Li, G. Synthesis and characterization of size-controlled atomically precise gold clusters. *Phys. Sci. Rev.* **3**, (2018).

32. Liu, H. *et al.* Control of Surface Ligand Density on PEGylated Gold Nanoparticles for Optimized Cancer Cell Uptake. *Part. Part. Syst. Charact.* **32**, 197–204 (2015).

33. Uz, M., Bulmus, V. & Alsoy Altinkaya, S. Effect of PEG Grafting Density and Hydrodynamic Volume on Gold Nanoparticle–Cell Interactions: An Investigation on Cell Cycle, Apoptosis, and DNA Damage. *Langmuir* **32**, 5997–6009 (2016).

34. Lund, T. *et al.* The influence of ligand organization on the rate of uptake of gold nanoparticles by colorectal cancer cells. *Biomaterials* **32**, 9776–9784 (2011).

35. Albanese, A. & Chan, W. C. W. Effect of Gold Nanoparticle Aggregation on Cell Uptake and Toxicity. *ACS Nano* **5**, 5478–5489 (2011).

36.    Verma, A. & Stellacci, F. Effect of Surface Properties on Nanoparticle–Cell Interactions. *Small* **6**, 12–21 (2018).

37.    Goodman, C. M., McCusker, C. D., Yilmaz, T. & Rotello, V. M. Toxicity of Gold Nanoparticles Functionalized with Cationic and Anionic Side Chains. *Bioconjug. Chem.* **15**, 897–900 (2004).

38.    Yu, L. & Matthews, M. A. Hydrolysis of sodium borohydride in concentrated aqueous solution. *Int. J. Hydrog. Energy* **36**, 7416–7422 (2011).

39.    Rohm and Haas Company. Sodium Borohydride Digest - DOW. https://nshosting.dow.com/doc-archive/industry/pharma_medical/chemical_reagents/reducing _agents/sodium_borohydride_digest.pdf (2003).

40.    Parsaei, M., Goodarzi, M. S. & Nasef, M. M. Adsorption study for removal of boron using ion exchange resin in batch system. in *International Conference on Environmental Sciences and Technology IPCBEE* vol. 6 398–402 (2011).

41.    Chesney, A. Selected highlights in the application of ion-exchangers as supports for reagents in organic synthesis. *Green Chem.* **1**, 209–219 (1999).

42.    Alvarez, M. M. *et al.* Optical Absorption Spectra of Nanocrystal Gold Molecules. *J. Phys. Chem. B* **101**, 3706–3712 (1997).

43.    Zakaria, H. M. *et al.* Small Molecule- and Amino Acid-Induced Aggregation of Gold Nanoparticles. *Langmuir* **29**, 7661–7673 (2013).

44.    Lang, N. J., Liu, B. & Liu, J. Characterization of glucose oxidation by gold nanoparticles using nanoceria. *J. Colloid Interface Sci.* **428**, 78–83 (2014).

45.    Polowczyk, I. *et al.* Amberlite IRA-400 and IRA-743 chelating resins for the sorption and recovery of molybdenum(VI) and vanadium(V): Equilibrium and kinetic studies. *Hydrometallurgy* **169**, 496–507 (2017).

46.    Dai, Q., Walkey, C. & Chan, W. C. W. Polyethylene Glycol Backfilling Mitigates the Negative Impact of the Protein Corona on Nanoparticle Cell Targeting. *Angew. Chem. Int. Ed.* **53**, 5093–5096 (2014).

47.    Chegel, V. *et al.* Gold Nanoparticles Aggregation: Drastic Effect of Cooperative Functionalities in a Single Molecular Conjugate. *J. Phys. Chem. C* **116**, 2683–2690 (2012).

48.     Smith, A. M. *et al.* Quantitative Analysis of Thiolated Ligand Exchange on Gold Nanoparticles Monitored by 1H NMR Spectroscopy. *Anal. Chem.* **87**, 2771–2778 (2015).

49.     Wu, M. *et al.* Solution NMR Analysis of Ligand Environment in Quaternary Ammonium-Terminated Self-Assembled Monolayers on Gold Nanoparticles: The Effect of Surface Curvature and Ligand Structure. *J. Am. Chem. Soc.* **141**, 4316–4327 (2019).

# Chapter II

# LC-CAD-MS as a tool for the characterization of GNP non-UV absorbent ligands, development of a pre-treatment method (TCEP) and comparison with $^{1}$H NMR characterization

# I.  Introduction

## 1.  Summary of the analytical techniques to characterize GNP

Due to their inherent complexity, gold nanoparticles require state of the art analytical techniques to be fully characterized.

In the pharmaceutical industry, analytical development and validation are generally performed following the International Conference on Harmonization (ICH) guidelines, more precisely, Q2(R1): "Validation of Analytical Procedures" and Q14 "Analytical Procedure Development and Revision of Q2(R1) Analytical Validation". Typical validation parameters are specificity, accuracy, precision (which includes repeatability, intermediate precision and reproducibility), sensitivity, detection limit, quantitation limit, working range, linearity and robustness[1].

On top of matching the parameters mentioned above, analytical techniques must be used in a complementary fashion. This is particularly challenging because it requires multidisciplinary skills and access to a number of different instrumentation/facilities[2].

Nowadays, a wide range of techniques have been developed and published but, although GNP share common features, the analysis should be adapted to each construct[3]. Not only should the critical parameters be established and monitored, but the amount of material needed and the cost of the analysis should also be considered. Appropriate characterization is essential from the R&D phase through to commercial production and should be strengthened as the product progresses toward human/commercial use. It ensures the quality of the material (matching specification, intra and inter batch reproducibility) and allows a follow-up of its properties over time (ageing: adsorption, shrinking, agglomeration, sedimentation, surface ligands degradation) or after reconstitution (e.g. freeze drying and resuspension)[4].

Traditionally, the size of nanoparticles is determined by scattering techniques: Dynamic Light Scattering (DLS), analytical centrifugation: Differential Centrifugation Sedimentation (DCS) and microscopy: Transmission Electron Microscopy (TEM), while the surface chemistry is characterized by spectroscopy: Ultraviolet–Visible spectrophotometry (UV-Vis), Infrared spectroscopy (IR), Nuclear Magnetic Resonance (NMR), Mass Spectrometry (MS), X-ray Photoelectron Spectrometry (XPS), sometimes using chromatography (liquid or gas), and thermal analysis: Thermogravimetric Analysis (TGA)[5,6] (*Figure 1*).

Key features of the GNP and the analytical techniques performed to measure them are listed in *Table 1*.

**Shell Composition: ligand(s) identification, ratio, density, charge, quantification**

**Identification, Ratio, Quantification: NMR (¹H-NMR), reverse phase LC (DAD, CAD) and MS**

**Charge: ZP**

**pH**

**Density: TGA, Elemental Analyses: XPS, ICP-AES**

**Au Concentration: MP-AES, ICP-MS**

**TEM, UV-Vis**

**Core Size and Shape**

**Particle Size**

**DLS, DCS, LC (SEC)**

*Figure 1: Critical parameters of the GNP: core size and shape, particle size and shell composition with the corresponding analytical techniques.*

*Table 1: Key features of the GNP and their corresponding analytical techniques[2,7,8].*

| Parameter Monitored | Analytical Technique |
|---|---|
| Size, shape, distribution, agglomeration | TEM, DLS, DCS, UV-Vis, LC (SEC) |
| Detection (image of gold core) | TEM |
| Elemental/chemical composition, concentration | MP-AES, ICP-AES, ICP-MS, XPS |
| Shell composition, ligands density, arrangement | TGA, XPS, ICP-AES, NMR (¹H NMR), pH, LC (Reverse Phase), MS |
| Surface charge | ZP |

76

**Nuclear Magnetic Resonance** (NMR) spectroscopy is a powerful tool to study the GNP structure and performance/properties. It is a versatile and usually non-destructive method that can be used to analyze the final product as well as GNP formation and growth. The core and the ligand-shell can both be characterized[9].

NMR techniques have been used to understand several aspects of the GNP ligand shell architecture. For nanoparticles with good solubility, it is possible to study the molecules bound to the surface using solution-phase NMR techniques. By combining one- and two-dimensional NMR, several research groups have been able to determine the ligand shell morphology and the organization on the surface (e.g. random, patchy, stripped or Janus)[10,11], understand the binding mode of ligands on GNP[12,13], identify (nature and integrity) and semi-quantify (ratio and quantity) the ligands[14,15,16,17].

The limitations of NMR are the relatively large amount of sample needed to perform an analysis due to the method low sensitivity, the instrument cost and the need for a skilled operator.

**Proton Nuclear Magnetic Resonance** ($^1$H NMR) spectroscopy allows the identification and quantification of the shell ligands and their impurities. It has the advantage of being able to detect every organic specie (with hydrogen atoms) without derivatization. The relative integration of well resolved ligand peaks allows the determination of ratios and an internal standard (e.g. acetonitrile) can be used to estimate their quantities[18].

Nevertheless, it can be difficult to obtain reliable information because the $^1$H NMR peaks display a significant broadening as a result of attachment to the particle surface[9]. *Figure 2* shows the $^1$H NMR spectrum in Deuterium Oxide ($D_2O$) of a 2 nm core GNP: $(PEG(8)COOH)_{22}(\alpha\text{-Galactose-}C_2)_{22}@Au_{102}$. Only broad resonance peaks are visible ($\delta$ 5.02 ppm: anomeric proton of $\alpha$-Galactose-$C_2$; 4.2-3.5 ppm: $\alpha$-Galactose-$C_2$ and methylene-PEG protons; 2.48 ppm: PEG protons -$CH_2$-COOH). The attachment of all the ligands to the gold core can be proven by the absence of sharp signals in the spectrum.
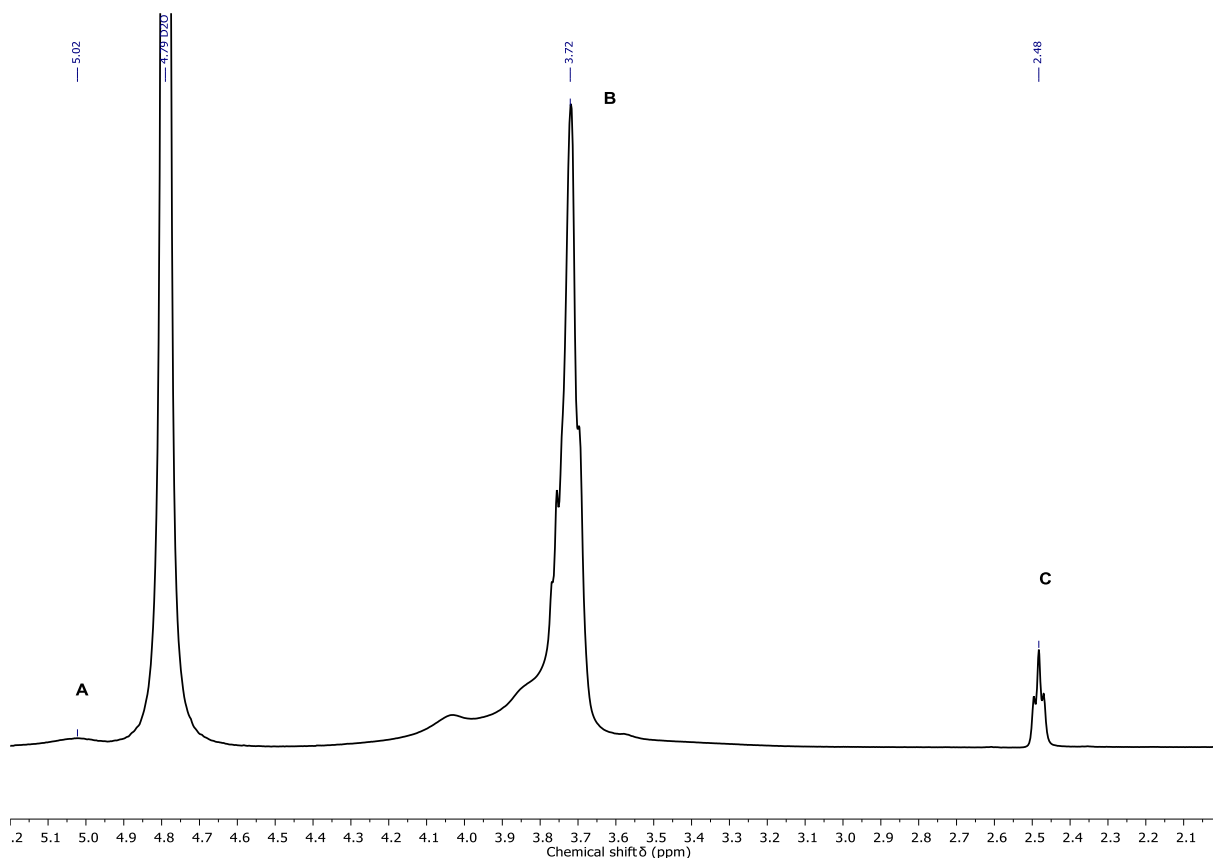
*Figure 2: $^1H$ NMR (500 MHz, $D_2O$) of $(PEG(8)COOH)_{22}(\alpha$-Galactose-$C_2)_{22}@Au_{102}$. (A) $\alpha$-Galactose-$C_2$ H-1 $\delta$ 5.02, (B) $\alpha$-Galactose-$C_2$ and PEG(8)COOH $\delta$ 4.2-3.5 and (C) PEG(8)COOH $\delta$ 2.48 (t, 2H) signals do not allow proper identification and ratio determination due to their broadening*

An alternative strategy to achieve better sensitivity, specificity and reproducibility is to cleave the ligands from the GNP and eventually etch the core using a specific reagent. We called this step *pre-treatment.* Once released, the ligand peaks are sharp and, as the peak intensities are proportional to their concentrations, a comparison of their area enables an estimation of their relative percentages on the GNP surface. To allow reliable measurements, the ligands should be completely cleaved upon reaction with an etching reagent but not be degraded through side reactions. Side reactions can take the form of chemical degradation (e.g. oxidation) or recombination of thiols groups to form disulfides (homo or heterodimers). Importantly, the etching reagent should have a low level of interference (absence or low spectroscopic signal). Pre-treatment is discussed later in the *section 3* of this chapter introduction.

**Liquid Chromatography** (LC) is a powerful analytical (and purification) tool to characterize both the whole GNP and the ligands of the shell. It matches most of the key criteria mentioned before, is high-throughput and cost effective, but requires optimization for each construct. As with $^1$H NMR, GNP digestion is often necessary to release the ligands from the core (*see section 3*).

There are several types of LC such as HPLC (High-Performance Liquid Chromatography), UHPLC (Ultra-High-Performance Liquid Chromatography), or FPLC (Fast Protein Liquid Chromatography). Polarity-based separation is usually performed using Reverse Phase (RP) (e.g. C18 column) while size-based separation is done by Size Exclusion Chromatography (SEC). UV-Vis is most common type of detector. It can either record discrete wavelengths or a spectrum using for instance a Diode Array Detector (DAD). To detect non-UV absorbing compounds, a Mass Spectrometer (MS) or other types of detectors such as Charged Aerosol Detector (CAD), Evaporative Light Scattering Detector (ELSD) or Nitrogen Chemiluminescence Detector (NCD) can be used. Using these detectors alone or in combination with other techniques, several research groups have been able to quantify the GNP ligands. Smith et al.[19] were able to quantify the total amount of PEG and to distinguish the bound and unbound PEG on 30 nm GNP after etching. Similar results were obtained by Zhou et al.[20] with the quantification of individual ligands on GNP by Fourier Transform Infrared Spectroscopy (FTIR) and HPLC-MS-UV-NCD.

**Size Exclusion Chromatography** (SEC) has been used to determine the particle size and distribution of GNP and quantum dots[21]. In this case, the GNP are not etched prior to their analysis. Unlike Reverse Phase chromatography, molecules are separated according to their size: the larger molecules elute before their smaller counterparts. Compared to other particle size analytical techniques (e.g. DLS, DCS), SEC has the advantage of being very reliable, with high resolution, and is fast and scalable[22]. It can resolve different populations of GNP in the case of a polydisperse sample. The main drawback is accessing standards that should ideally be of the same size and chemical composition (surface ligands). In addition, the stationary and mobile phase should be carefully chosen to avoid GNP adsorption on the column and to obtain a complete recovery of the sample injected[23].

**Mass spectrometry** (MS) can be performed as a standalone technique[24] or in combination with Liquid Chromatography (LC-MS)[25] or Gas Chromatography[26] (GC-MS). In LC-MS, Electrospray Ionization (ESI) is the most common ionization technique and the most used detectors are the Quadrupole Mass Analyzer (QMS, QqQ), Time-Of-Flight (TOF), Fourier Transform Ion Cyclotron Resonance (FTICR), Ion Trap or Orbitrap. Tandem Mass Spectrometry (MS/MS) is often used to obtain more detailed information with a Triple Quadrupole mass spectrometer (TQMS), Quadrupole Time-Of-Flight mass spectrometer (QTOF) or Quadrupole Ion Trap[27]. Standalone MS is usually performed with Laser Desorption Ionization (LDI), Matrix Assisted Laser Desorption Ionization (MALDI), or by direct infusion in the MS detector. The main drawback of MS is the instrument and maintenance cost and the challenge in analyzing the mass spectrometric data.

MS has been used to characterize GNP core size and surface ligands and proved itself reliable with ultrasmall nanoparticles. One of the major contributions of MS in the GNP field was the discovery of magic-numbers, approximations of the number of gold atoms per GNP[24,28]. The surface ligands have also been characterized through MS, although, due to the fragmentation and lack of ionization efficiency, the characterization without digestion (pre-treatment) remains challenging. Using a LDI-MS technique, Yan et al.[29] were able to determine the ligand composition of monolayer-protected GNP. Similar experiments were performed by applying FTICR-MS and a combination of LDI and MALDI. For instance, Nicolardi et al.[30] presented a characterization of the surface chemistry of GNP incorporating peptides and a mixture of complex carbohydrates (Lewis[X] and tetramannoside).

**X-ray Photoelectron Spectrometry** (XPS) informs about the elemental and electronical compositions of the GNP. It is particularly useful to determine the ligand density with the relative amount of sulfur and gold (S/Au) and to study the oxidation state of the gold core[31]. Although not as reliable, elements such a nitrogen and carbon can be used to estimate the ligand density or ratio[32,33]. Techane et al.[34] used XPS for the study of ligand exchange of amino-gold nanoparticles and Gobbo et al.[35] measured the degree of functionalization of GNP by click-chemistry. Ligand binding to the core can also be verified through detection of bound and unbound ligands[34].

**Elemental analyses** MP-AES (Microwave Plasma - Atomic Emission Spectrometry), ICP-AES (Inductively Coupled Plasma - Atomic Emission Spectroscopy) and ICP-MS (Inductively Coupled Plasma - Mass Spectrometry) are used to measure the atomic

composition and the concentration of the samples. An acidic pre-treatment step with *aqua regia* (HCl/HNO$_3$) is usually performed to digest the GNP and the matrix. Depending on the technique, elements such as Au, B, Na, P, S may be quantified. Using the sulfur to gold ratio, the packing ligand density can be determined[36,37].

**UV-Vis spectrophotometry** is used to obtain information about the GNP size, shape, distribution and agglomeration, by studying surface plasmon band intensity and its maximum (spherical GNP: 520 nm)[38]. Ligands possessing a chromophore can also be identified. It is a simple, fast and cheap method.

**Dynamic Light Scattering** (DLS) is widely used to obtain the particle hydrodynamic size and distribution (Polydispersity Index PDI)[39]. It is a rapid, cheap and non-destructive method. The size resolution is nevertheless limited, and it does not perform well with polydispersed samples. It is very sensitive to contamination such as dust and fibers, that can lead to artifacts and data misinterpretation.

**Differential Centrifugation Sedimentation** (DCS) and the related technique, Analytical Ultracentrifugation (AUC), determine the entire particle size and distribution. These methods are sensitive to changes of the core size and the organic shell thickness. Unlike DLS, DCS can resolve polydisperse samples[40].

**Transmission Electron Microscopy** (TEM) determines the size, shape, distribution and agglomeration of the particles. It is not a spectroscopic method and therefore can assert the presence of GNP by direct detection[41]. The main drawbacks of TEM are challenges in sampling and the instrument cost.

**Thermogravimetric analysis** (TGA) is a destructive method which measures the mass of the sample over time as the temperature changes. It can provide the relative organic/inorganic composition of the GNP[42].

**Zeta Potential** (ZP) measures the surface charge of particles and is a predictive value of the stability of the solution (high stability with inter-particles repulsion if $\pm$ 30 mV). The method, if not performed in optimum conditions, can generate unreliable data that lacks precision and repeatability[43].

**pH** is dependent on the ligand species and varies with the concentration.

## 2. Liquid Chromatography - Charged Aerosol Detection - Mass Spectrometry

Liquid Chromatography - Charged Aerosol Detection - Mass Spectrometry (LC-CAD-MS) combines in an HPLC or UHPLC system three types of detectors: a UV-Vis (DAD), a Charged Aerosol Detector (CAD) and a Mass Spectrometer (MS).

Charged Aerosol Detection can detect weak or non-UV absorbing compounds. For GNP ligands, it is an alternative to derivatization of thiol group ligands with chromophoric compounds such as Ellman's reagent and Aldrithiol[44].

The CAD detector is mass dependent, and the response does not depend on the spectral or physicochemical properties of the analytes. This feature means that it, theoretically, generates an identical response for identical amounts of different analytes, which is very useful in the absence of standard materials. That is, for instance, the case of ligands obtained through GNP post-functionalization (*see Chapter III*), where a chemical reaction is performed between a ligand on the GNP surface and a molecule bearing a compatible functional group.

In brief, the mechanism of the CAD involves the nebulization of the eluent into droplets that are dried in an evaporation tube to form aerosol particles. The particles are then charged into a mixing chamber and quantified using an electrometer (*Figure 3*)[45].

Compared to Evaporative Light Scattering Detection (ELSD) or Nitrogen Chemiluminescence Detection (NCD), CAD shows superior sensitivity and consistency. Other advantages of the CAD method include compatibility with most solvents, high dynamic range, relatively low cost and ease of use. The CAD response is affected by the mobile phase composition, but the issue is overcome by using LC systems with inverse gradient compensation. When combined with a MS detector, this approach gives information (molecular weight) that the CAD method alone lacks[46].
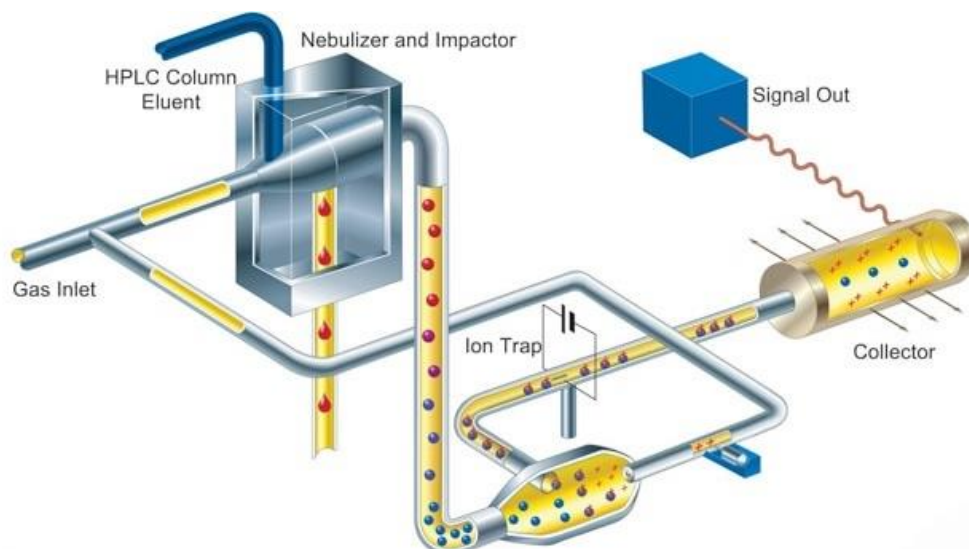
*Figure 3: Principle of a Charged Aerosol Detector[47].*

CAD detection, although now being used routinely, can be of little help with some compounds. ^{1}H NMR is then of great use to complement the information given by LC-CAD-MS. ^{1}H NMR has been compared to LC/MS[26,29] and CAD data in previous publications[48].

CAD suits ultrasmall GNP with non-UV-absorbing ligands: PEG and carbohydrates. Both classes have been studied by CAD: carbohydrates ranging from monosaccharides to oligo- and polysaccharides[49] and PEG of different lengths[50].

To date, only one publication reports on the use of CAD on GNP. Smith et al.[19] used CAD to identify and quantify PEG of different lengths (2-20 kDa) on 30 nm GNP. The GNP were treated with two different methods: potassium cyanide (KCN) to dissolve the particle core and release the ligands and dithiothreitol (DTT) to displace the ligands from the core. KCN treatment gave a clear solution whilst DTT treatment required separation of the ligands from GNP aggregates by centrifugation. HPLC-CAD was performed with the material obtained to identify and quantify the PEG using a calibration curve. The two pre-treatments were compared, and other techniques were used as controls (TEM and ICP-MS). Robust and reproducible results were obtained.

## 3. Pre-treatment: gold etching agents and disulfide bond reducing reagents

Pre-treatment is often needed to characterize the ligand shell of the GNP. *Figure 4* shows the analytical techniques used for characterization of GNP, classified as direct methods and methods requiring GNP etching or digestion of the sample.
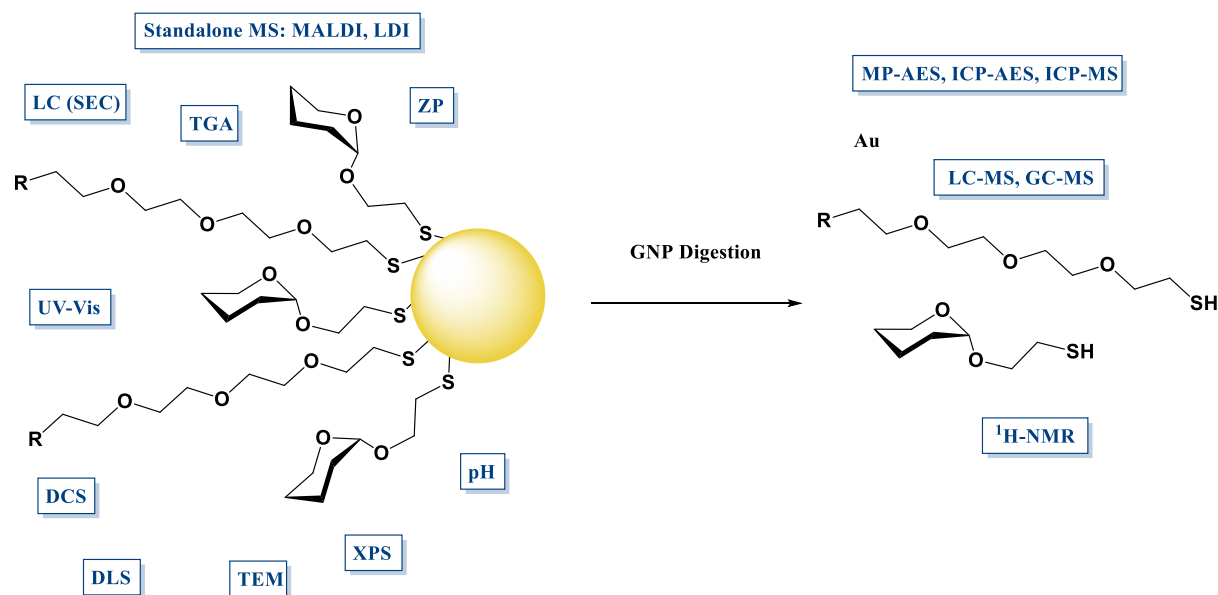


*Figure 4: Classification of the analytical techniques by the need or not of a pre-treatment.*

Traditional gold etching techniques with oxidizing agents can be used for GNP[51,52]. Aqueous solutions of potassium cyanide (KCN) dissolve gold via the formation of the soluble cyano-complex $[Au(CN)_2]^-$. Iodine ($I_2$) also oxidizes gold, forming gold iodide (AuI). The solubility of AuI is improved by adding potassium iodide (KI) to the solution. Mixtures of concentrated hydrochloric acid and nitric acid ($HCl/HNO_3$ 1:3, *aqua regia*) can digest gold at room temperature.

Many research groups have applied these etching methods to characterize the ligands on GNP. Milestone et al.[18] digested GNP with *aqua regia* and quantified ligand exchange. Chengzhi Huang et al.[53] studied the mechanism of etching gold nanoparticles with iodine/iodide. Murray et al.[54] treated alkanethiol GNP with iodine and cyanide to explore the reactivity and the steric environment of the monolayer ligand shells. Similar experiments were developed by Reed et al.[55] to demonstrate the stability of lipid-coated gold nanoparticles after treatment with cyanide. As previously mentioned, Smith et al.[19] used KCN to etch 30 nm GNP before LC-CAD characterization.

Although they are efficient, these chemicals suffer from major drawbacks. *Aqua regia* whilst routinely used for elemental analysis[36] is unsuitable for the characterization of most ligands due to its capacity to rapidly degrade organic materials. As demonstrated by Fisher et al.[26] iodine etching leads to disulfide formation. Likewise, KCN favors spontaneous disulfide reduction because of the alkaline pH of the solution required to avoid to formation of the highly toxic hydrogen cyanide gas (HCN)[56].

Midatech Pharma previously developed an analytical method for ligand identification and ratio calculation by $^1$H NMR (500 MHz, D$_2$O) using a pre-treatment with KCN (0.3 M in 0.1 M KOH) that results in a clear solution within minutes. *Figure 5* shows $^1$H NMR spectra after KCN/KOH treatment of three 2 nm core GNP: (PEG(5)NH$_2$)$_{22}$($\alpha$-Galactose-C$_2$)$_{22}$@Au$_{102}$, (PEG(5)NH$_2$)$_{26}$($\beta$-Glucose-C$_2$)$_{18}$@Au$_{102}$ and (PEG(8)COOH)$_{22}$($\alpha$-Galactose-C$_2$)$_{22}$@Au$_{102}$.
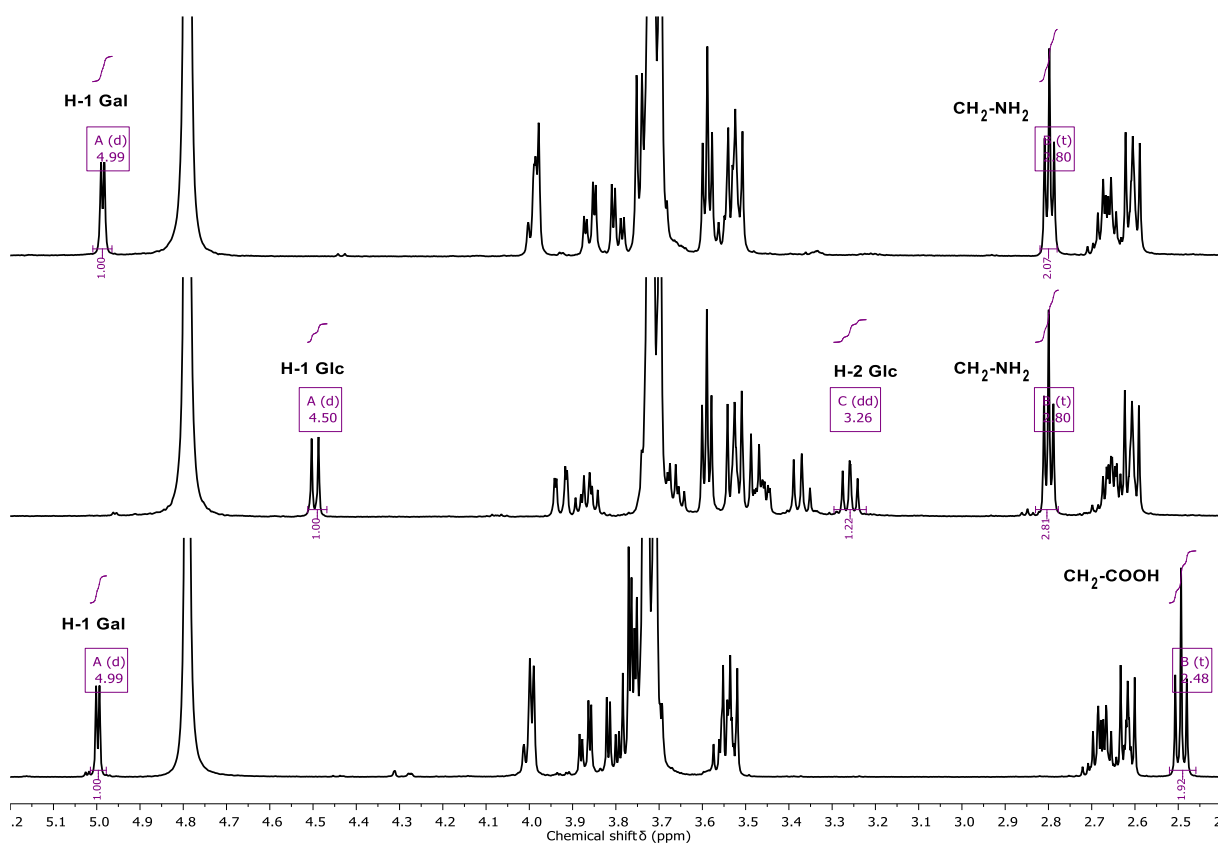


*Figure 5: $^1$H NMR (500 MHz, D$_2$O) of (I) (PEG(5)NH$_2$)$_{22}$($\alpha$-Galactose-C$_2$)$_{22}$@Au$_{102}$, (II) (PEG(5)NH$_2$)$_{26}$($\beta$-Glucose-C$_2$)$_{18}$@Au$_{102}$ and (III) (PEG(8)COOH)$_{22}$($\alpha$-Galactose-C$_2$)$_{22}$@Au$_{102}$ gold nanoparticles after KCN/KOH treatment. The integration of the $\alpha$-Galactose-C$_2$ protons is performed using mainly the anomeric proton H-1 Gal $\delta$ 4.99 (d, 1H). PEG(5)NH$_2$ can be integrated using the -CH$_2$-NH$_2$ protons $\delta$ 2.80 (t, 2H). $\beta$-Glucose-C$_2$ integration is performed using mainly the anomic proton H-1 Glc $\delta$ 4.50 (d, 1H). H-2 Glc $\delta$ 3.26 (dd, 1H) can also be used. PEG(8)COOH can be integrated using the -CH$_2$-COOH protons $\delta$ 2.48 (t, 2H).*

The integration of characteristic peaks corresponding to each ligand gives their ratio on the GNP. The peaks were selected after careful study of the starting material's spectra. Ligands were analyzed in $D_2O$ and $KCN/KOH/D_2O$ since the cyanide and the pH affect the signals (*Figure 23 to Figure 29 in the annex*).

Although KCN/KOH performs well for many constructs, it has a few drawbacks, the rapid formation of homo- or hetero-disulfides, making the preparation unsuitable for chromatographic methods, the alteration of ligand signals in $^1H$ NMR spectra and the degradation of sensitive ligands.

Sodium borohydride is a possible alternative to the gold oxidizing methods described above. Although mostly known as an essential ingredient for the GNP Brust-Schiffrin synthesis[57], $NaBH_4$ can also detach the ligands bound to gold nanoparticles[58]. A detailed experiment regarding the influence of $NaBH_4$ on GNP during their synthesis is described in *Chapter I.*
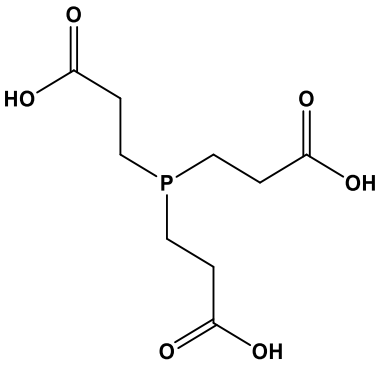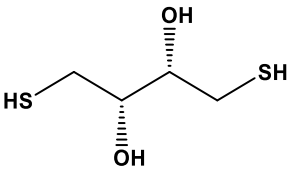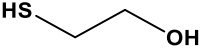
Another alternative is to use disulfide bond reducing agents. Effective reagents have been developed for biochemical applications (e.g. disulfide bond reduction in proteins)[52]. Among these molecules, two thiol-containing reducing agents: β-mercaptoethanol[59] and dithiothreitol (DTT)[19] have been extensively used for ligand release on GNP.

Schulz et al.[60] used DTT (and KCN) to study the effect of anchoring groups on GNP stability which was assessed by the absence of DTT related aggregation. Maus et al.[61] also employed DTT to strip off the ligands from the core and recover them after pellet centrifugation in an experiment designed to look at the desorption of ligands over time. Tsai et al.[62] studied the displacement efficiency of DTT depending on the S-Au bond strength, the ligand molecular weight and its conformation. The experiments mentioned above were performed on particles with a gold core size greater than 10 nm.

Nonetheless, despite being routinely used for other purposes, Tris(2-carboxyethyl)phosphine (TCEP) has not been applied to GNP to the best of our knowledge. Unlike β-mercaptoethanol and DTT, it is a phosphine reducing agent that does not contain thiol groups.

*Table 2* summarizes the characteristics of β-mercaptoethanol, DTT and TCEP.

*Table 2: Advantages and drawbacks of the different disulfide bond reducing agents.*

| Molecule | TCEP | DTT | β-mercaptoethanol |
|---|---|---|---|
| Synonyms | Tris(2-carboxyethyl)phosphine | Dithiothreitol or Cleland's reagent | 2-Mercaptoethanol, BME, 2BME, 2-ME or β-met |
| Scheme | Chemical Formula: $C_9H_{15}O_6P$<br>Molecular Weight: 250.19 | Chemical Formula: $C_4H_{10}O_2S_2$<br>Molecular Weight: 154.24 | Chemical Formula: $C_2H_6OS$<br>Molecular Weight: 78.13 |
| Advantages | Potent, odorless, versatile[63], soluble and stable in aqueous solution[64], thiol free (no cross linking), resistant to air oxidation, non-reversible reaction, wide pH efficiency range. | Potent[65], non-reversible reaction, soluble in aqueous solution. | Liquid (ready to use), soluble in aqueous solution, volatile (can be removed from the sample). |
| Drawbacks | Non-volatile. | Possible formation of side products (cross linking), unstable: impossible to prepare a stock solution, non-volatile, pH sensitive (mostly efficient at pH > 7). | Toxic, stench, equilibrium reaction (re-oxidation), possible formation of side products (cross linking), less powerful than DTT. |

## II.   Objectives

This chapter describes attempts to improve the ligand-corona characterization of ultrasmall gold nanoparticles. Using a library of gold nanoparticles, different etching reagents have been screened to find an alternative to KCN/KOH. Then, using the best performing reagent: TCEP, a chromatographic method: LC-CAD-MS, was developed using ^{1}H NMR with KCN/KOH etching as a control.

GNP are multivalent, in that they can bear multiple ligands on their surface. There are three major routes to obtain the desired ligands on the corona: one-pot synthesis (e.g. BSS)[57], ligand place exchange[66] and post-functionalization[67].

For multifunctional GNP, corona characterization remains challenging with a battery of parameters to elucidate, namely identification of the ligands and their impurities, determination of the ratio between the ligands and quantification. Moreover, post-functionalization, while very straightforward as a synthetic method, is particularly problematic in terms of characterization because there is often no reference material available, as the final molecule is formed on the GNP (*see Chapter III*).

Firstly, the focus was put on the pre-treatment of the GNP. In fact, etching the gold core and releasing the ligands is essential for both LC and ^{1}H NMR analysis. Different etching and reduction methods have been investigated, namely $I_2$/KI, $NaBH_4$, β-mercaptoethanol, DTT and TCEP. The primary purpose of these experiments was to compare them with the KCN/KOH treatment, as judged by their capacity to give a transparent solution without pellet or stains.

The best alternative pre-treatment agent, TCEP, was then used to compare the ligand ratio by ^{1}H NMR with 2 nm core bifunctional GNP. The GNP library was essentially composed of one-pot synthetized particles bearing Midatech Pharma's four most used ligands: PEG(8)COOH, PEG(5)$NH_2$, α-Galactose-$C_2$ and β-Glucose-$C_2$.

Secondly, as KCN/KOH is unsuited for most chromatographic applications, TCEP was used as a pre-treatment agent for LC-CAD-MS. The liquid chromatography was performed using Thermo-Fisher UltiMate 3000 UHPLC system with Corona Veo RS CAD and LCQ Fleet Ion trap MS detectors (*Figure 6*). The results were compared to ^{1}H NMR data after KCN/KOH pre-treatment. On top of the CAD data (retention time and peak area of the compounds), in line MS was used to get the m/z values for the molecules, allowing their identification.

A broad library of 2 nm core GNP was chosen with special focus on non-UV absorbent molecules of biological interest: PEG and carbohydrates. As with the first part, bifunctional one-pot synthetized GNP were analyzed. Moreover, PEG ligands of the GNP were used to perform post-functionalization reactions with molecules carrying complementary moieties such as carbohydrates or protecting/functional groups, and the percentages of the new products in the corona were defined using the CAD intrinsic feature (mass dependent) which generates an identical response for identical amounts of different analytes.

As TCEP is an important part of the work mentioned above, the signals related to it and its derivatives by ^{1}H NMR and LC-CAD-MS were also reported.



*Figure 6: Thermo-Fisher (1) UltiMate 3000 UHPLC system, (2) Corona Veo RS CAD detector and (3) LCQ Fleet Ion trap Mass Spectrometer used for the GNP characterization.*

# III.  Results and Discussion

## 1. Synthesis of ultrasmall gold nanoparticles

A library of ultrasmall multifunctional GNP was prepared using the one-pot Brust-Schiffrin synthesis strategy and post-functionalization.

Brust-Schiffrin syntheses were performed using a benchtop reactor. Within minutes, $HAuCl_4$ and homo-disulfide ligands were dissolved in water and added to the reactor. Sodium hydroxide was used to obtain an alkaline pH and a fresh aqueous solution of $NaBH_4$ was added quickly to form the particles. After completion of the reaction, the mixture was purified by centrifugal ultrafiltration or tangential flow filtration. The ratio between the ligands on the GNP was controlled by the amount added to the solution.

Five ligands were used for the BSS: 2'-Thioethyl β-D-glucopyranoside (β-Glucose-$C_2$) (**1**), 2'-Thioethyl α-D-galactopyranoside (α-Galactose-$C_2$) (**2**), 2'-[2-(2-Thiooethoxy)ethyl]-2-acetamido-2-deoxy-β-D-glucopyranoside (β-*N*-Acetyl-Glucosamine-$EG_2$) (**3**), α-Thio-ω-aminoethyl penta(ethylene glycol) (PEG(5)$NH_2$) (**4**) and α-Thio-ω-(propionic acid) octa(ethylene glycol) (PEG(8)COOH) (**5**) (*Figure 7*).

Post-functionalization was performed using the terminal functionality of the oligo-PEG on the GNP (either -$NH_2$ or -COOH). The degree of functionalization was controlled by the number of equivalents of complementary molecules added to the GNP solution. The mixtures were purified by centrifugal ultrafiltration.

Bifunctional GNP with PEG(5)$NH_2$ (**4**) were used to perform one-step amidations to present new functional groups such as azide (**6**), carboxylic acid (**7**) and acetamide (**8**). Derivatives of α-mannose (**9**) and β-galactose (**10**) were also linked to the pegamine (*Figure 8*).

In a more complex pathway, bifunctional PEG(5)$NH_2$ (**4**) GNP were used to perform a three-step post functionalization. Amidation with a tert-butyloxycarbonyl (Boc) protected amino-oxy compound was performed (**11**), followed by the removal of the Boc group, and the coupling of the resulting amino-oxy (-$CH_2$-OH-$NH_2$) to the non-modified oligosaccharides α-mannose1,2-α-mannose, 1,3-α-1,6-α-D-mannotriose and maltotriose through an oxime bond to form the structures (**12**), (**13**) and (**14**) (*Figure 9*).

PEG(8)COOH (**5**) GNP were also used present new functional groups such as hydroxyl (**16**) or to bind carbohydrate derivatives of α-mannose (**17**), α-mannose1,2-α-mannose (**18**) and β-galactose (**19**). A methyl-ester (**15**) was also formed with the carboxylic acid of the PEG (*Figure 10*).

The different ligands mentioned above with the respective molecular weight of their thiol form are summarized in *Table 3*.

*Table 3: Summary of the different ligands with their molecular weight (thiol compounds).*

| Compound | Simplified Name | Molecular Weight (g/mol) |
|:---:|:---:|:---:|
| 1 | β-Glucose-$C_2$ | 240.27 |
| 2 | α-Galactose-$C_2$ | 240.27 |
| 3 | β-*N*-Acetyl-Glucosamine-$EG_2$ | 325.38 |
| 4 | PEG(5)$NH_2$ | 297.41 |
| 5 | PEG(8)COOH | 458.56 |
| 6 | PEG(5)NH-CO-$C_5H_{10}$-$N_3$ | 436.57 |
| 7 | PEG(5)NH-CO-$C_2H_4$-COOH | 397.48 |
| 8 | PEG(5)NH-Ac | 339.45 |
| 9 | PEG(5)NH-CO-$C_2H_4$-α-Mannose | 531.61 |
| 10 | PEG(5)NH-CO-$C_4H_8$-β-Galactose | 559.67 |
| 11 | PEG(5)NH-CO-$CH_2$-O-NH-Boc | 470.58 |
| 12 | PEG(5)NH-CO-$CH_2$-O-N-(α-Mannose1,2-α-Mannose) | 694.74 |
| 13 | PEG(5)NH-CO-$CH_2$-O-N-(1,3-α-1,6-α-D-Mannotriose) | 856.88 |
| 14 | PEG(5)NH-CO-$CH_2$-O-N-(Maltotriose) | 856.88 |
| 15 | PEG(8)COOMe | 472.59 |
| 16 | PEG(8)CO-NH-$C_2H_4$-OH | 501.63 |
| 17 | PEG(8)CO-NH-$C_2H_4$-α-Mannose | 663.77 |
| 18 | PEG(8)CO-NH-$C_2H_4$-(α-Mannose1,2-α-Mannose) | 825.91 |
| 19 | PEG(8)CO-NH-$C_2H_4$-β-Galactose | 663.77 |
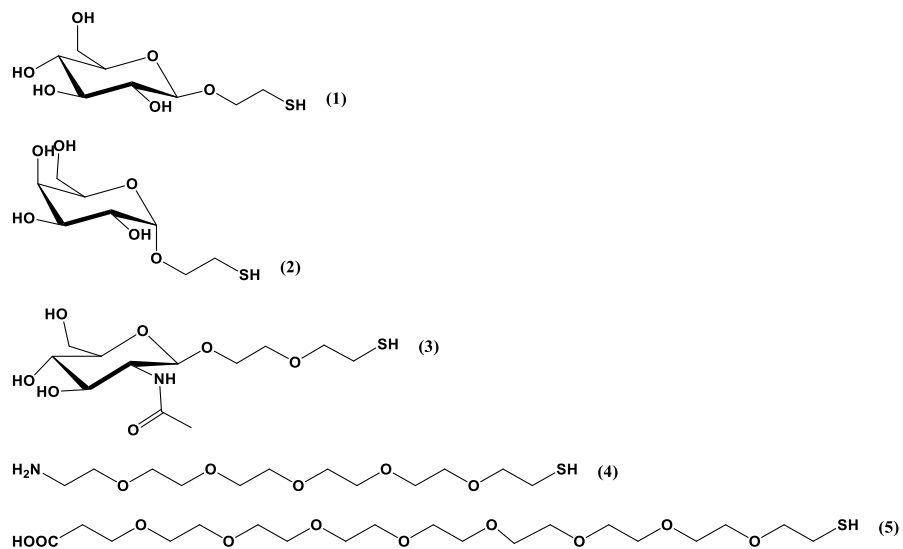
*Figure 7: Ligands used for one-pot synthesis (shown as thiols). (4) and (5) possess a terminal functional group -NH2 or -COOH, which is used for post-functionalization chemistry.*
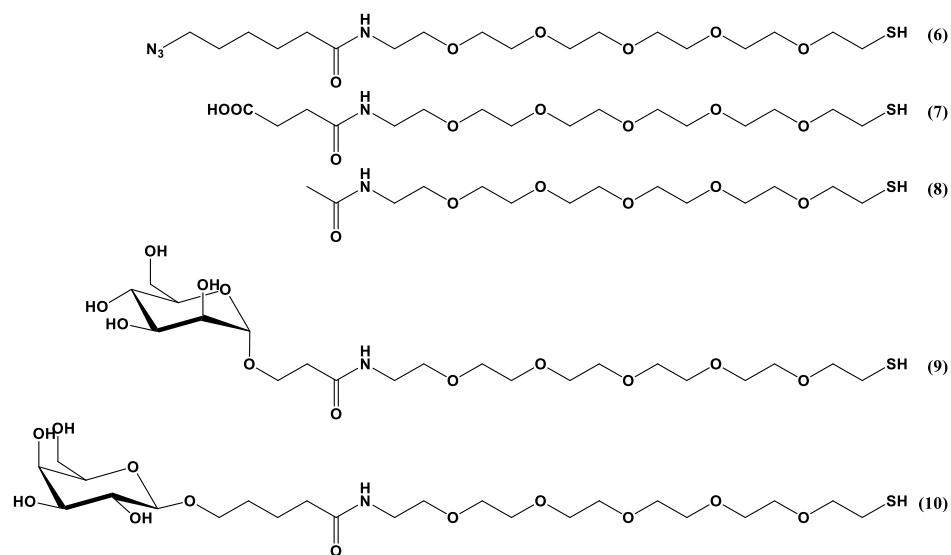


*Figure 8: Ligands obtained by one-step post-functionalization of PEG(5)NH2.*

*Figure 9: Ligands obtained through the post-functionalization of PEG(5)NH₂ with a multi-step synthesis: amide formation, Boc deprotection and oxime ligation. Structure (12), (13) and (14) are represented in an open ring form.*



*Figure 10: Ligands obtained by post-functionalization of PEG(8)COOH.*

## 2. Screening of the pre-treatment reagents

TCEP, DTT, β-mercaptoethanol, KI/I$_2$ and NaBH$_4$ were used under different conditions (amount, temperature, stirring and time of incubation) and up to amounts that were considered as realistic to perform an $^1$H NMR experiment. Only TCEP managed to match the completely clear solution with no pellet that was obtained with KCN/KOH treatment. DTT and β-mercaptoethanol solutions were transparent, but with a muddy brown or a dark goldish pellet, respectively. KI/I$_2$ solution gave yellowish to transparent solutions but with a dark to goldish pellet. Gas (dihydrogen) was released when NaBH$_4$ was added and a muddy black pellet was formed.

TCEP, on the other hand, under optimized conditions gave a completely clear solution with no pellet formation. Interestingly, although TCEP is known to reduce disulfides, it also etched the gold core. The mechanism involves a complex formed by two TCEP molecules and an atom of gold (*Figure 11*)[68].
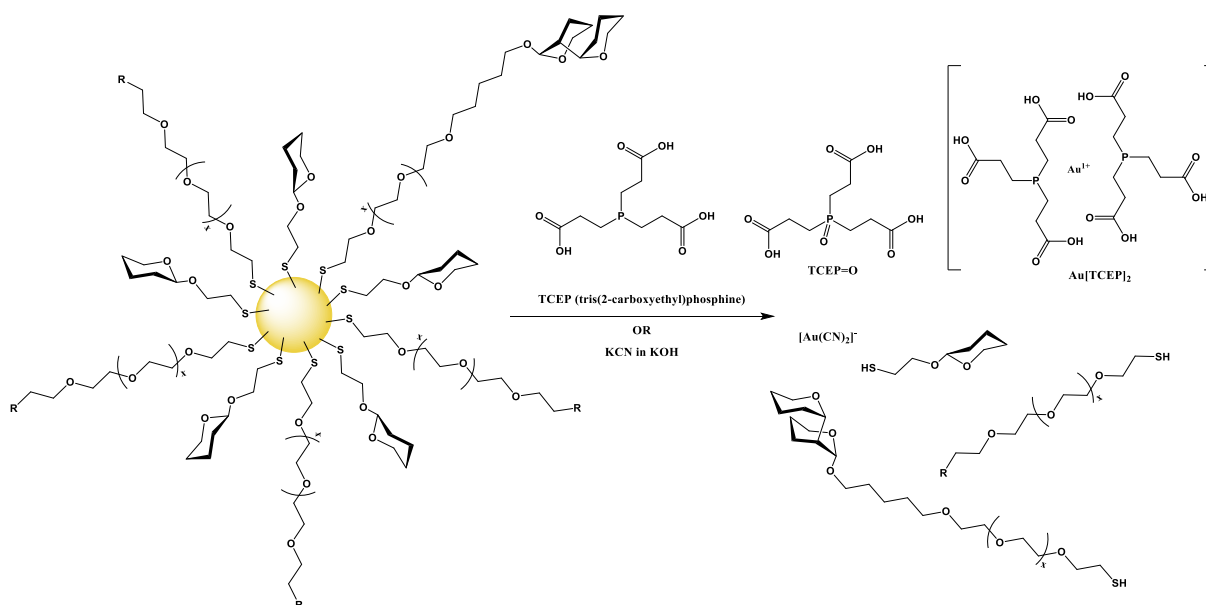


*Figure 11: Ligand release and core etching using TCEP or KCN/KOH. After etching with TCEP (MW: 250.19), the oxidized form TCEP=O (MW: 266.19) and a complex of Au[TCEP]$_2$ (MW: 697.34) are formed. KCN/KOH forms the dicyanoaurate(I) complex anion. KCN/KOH treatment produces both thiol and disulfide (homo or hetero) ligands while TCEP generates only thiol compounds.*

## 3. General methodology to identify and determine ligand ratios in GNP by $^1$H NMR after TCEP treatment

The treatment with TCEP was optimized in order to find a compromise between the minimum quantity required to get complete etching whilst avoiding interference with NMR signals of the sample.

### a. Characterization of the ligands

$^1$H NMR spectra of disulfide ligands used for the one-pot syntheses were measured in D$_2$O, and in deuterated aqueous solutions of KCN/KOH or TCEP. Also, the PEG ligands in their thiol form were analyzed with TCEP to compare them with their disulfide counterparts. All the spectra are shown *in the annex* (*Figure 23 to Figure 29*). *Table 4* summarizes the signals selected for the ligand ratio determinations.

*Table 4: Protons chosen to identify the ligand ratio on GNP from treated ligands.*

| Ligand | ID Proton KCN | $\delta$ (ppm) KCN/KOH | ID Proton TCEP | $\delta$ (ppm) TCEP |
|---|---|---|---|---|
| (1) β-Glucose-C$_2$ | H-1 | 4.52 (d, 1H) | H-1 | 4.49 (d, 1H) |
| (2) α-Galactose-C$_2$ | H-1 | 5.03 (d, 1H) | H-4 and H-5 | 3.99 (m, 2H) |
| (3) β-*N*-Acetyl-Glucosamine-EG$_2$ | H-1 | 4.59 (d, 1H) | N/A | N/A |
| (4) PEG(5)NH$_2$ | -CH$_2$-NH$_2$ | 2.85 (t, 2H) | -CH$_2$-NH$_2$ | 3.21 (t, 2H) |
| (5) PEG(8)COOH | -CH$_2$-COOH | 2.54 (t, 2H) | -CH$_2$-CH$_2$-COOH | 3.79 (t, 2H) |

**KCN/KOH** mostly affected peaks close to the terminal sulfur atom of the ligands, -CH$_2$-SS or -CH$_2$-CH$_2$-SS, displacing the signal and modifying the peak shape for all the ligands. For the PEG molecules (PEG(5)NH$_2$ and PEG(8)COOH), the terminal -CH$_2$-NH$_2$, -CH$_2$-CH$_2$-NH$_2$ and -CH$_2$-COOH signals remained relatively unaffected and were well resolved. -CH$_2$-CH$_2$-COOH, on the other hand, was poorly resolved. The monosaccharides H-1 (anomeric proton) of α-Galactose-C$_2$, β-Glucose-C$_2$ and β-*N*-Acetyl-Glucosamine-EG$_2$ were also relatively unaffected as was the H-2 proton of the β-Glucose-C$_2$.

**TCEP** treatment of PEG showed a good resolution of signals for -CH$_2$-NH$_2$, -CH$_2$-CH$_2$-NH$_2$ and -CH$_2$-CH$_2$-COOH but not for -CH$_2$-COOH. In presence of the disulfide ligands, the oxidized form of TCEP (TCEP=O) appeared due the consumption of TCEP when reducing the disulfide bonds.

Disulfide and thiol spectra, except for the presence of TCEP=O, matched perfectly suggesting the complete reduction of disulfides in presence of TCEP to form -$CH_2$-SH. -$CH_2$-SH was well resolved for all the ligands except for the PEG(8)COOH in the disulfide form (where the signal overlaps with TCEP=O).

The $\alpha$-Galactose-$C_2$ H-1 proton was affected by the solvent ($D_2O$) peak making a proper integration impossible but H-4 and H-5 were well resolved. $\beta$-Glucose-$C_2$ H-1 proton was well resolved.

### b. GNP characterization

Bifunctional GNP were then analyzed by ^{1}H NMR after KCN/KOH or TCEP pre-treatment. The addition ratios during the syntheses were 50:50 with slight variations of $\pm$ 10 % for PEG(5)$NH_2$ and the monosaccharides ($\alpha$-Galactose-$C_2$ or $\beta$-Glucose-$C_2$) to assess the sensitivity. The conditions used for the synthesis of PEG(5)$NH_2$/$\alpha$-Galactose-$C_2$ 50:50 were repeated three times to see the reproducibility of the results. PEG(8)COOH and $\alpha$-Galactose-$C_2$ were added in a 55:45 ratio.

For the treated GNP, the chemical shifts selected from the raw ligands were slightly displaced with KCN but were identical with TCEP. Besides, TCEP maintained all the ligands in the reduced, thiol form.

The TCEP oxidized form was visible: $\delta$ 2.67 (dt, 6H, -$CH_2$-P) and $\delta$ 2.21 (dt, 6H, -$CH_2$-COOH) confirming the reduction of the Au-S bonds. Also, important signals corresponding to the Au[TCEP]$_2$ complex[68] were visible in the spectra: $\delta$ 2.75 (m, 6H, -$CH_2$-P) and $\delta$ 2.38 (m, 6H, -$CH_2$-COOH) (*Figure 12*).

H-1 protons of $\alpha$-Galactose-$C_2$ or $\beta$-Glucose-$C_2$ and -$CH_2$-$NH_2$ protons of the PEG(5)$NH_2$ were well resolved in both TCEP and KCN/KOH conditions. -<u>$CH_2$</u>-$CH_2$-COOH partially overlapped the $\alpha$-Galactose-$C_2$ protons hindering accurate integration (*Figure 13*).

The ligand ratios obtained with KCN/KOH and TCEP were similar with differences of less than 5 % for all the batches (*Table 5*). For the five $\alpha$-Galactose-$C_2$/PEG(5)$NH_2$ GNP batches, the difference were never greater than 2 %. On the other hand, $\alpha$-Galactose-$C_2$/PEG(8)COOH GNP showed the limitation of ^{1}H NMR analysis using TCEP with the overlapping of characteristic signals. Nevertheless, a similar ratio with the two methods of etching was obtained (4 % difference).

The results by $^1$H NMR with either KCN/KOH or TCEP were compared to the ligand ratios used during the syntheses. The addition ratios and the proportions on the GNP were the same for $\alpha$-Galactose-C$_2$/PEG(5)NH$_2$ GNP (**GNP-1** to **GNP-5**), while $\beta$-Glucose-C$_2$/PEG(5)NH$_2$ (**GNP-6** to **GNP-8**) and $\alpha$-Galactose-C$_2$/PEG(8)COOH (**GNP-9**) particles displayed slight differences. The analysis of $\alpha$-Galactose-C$_2$/PEG(5)NH$_2$ and $\beta$-Glucose-C$_2$/PEG(5)NH$_2$ GNP showed a good inter-batch reproducibility and sensitivity with 10 % difference of addition ratios discerned with either KCN/KOH and TCEP.

*Table 5: Comparison of the ligand ratios on GNP by $^1$H NMR after KCN/KOH and TCEP treatments.*

| Batch | Ligand I | Ligand II | Recipe's Ratio Ligand I / II (%) | $^1$H NMR KCN/KOH Ratio Ligand I / II (%) | $^1$H NMR TCEP Ratio Ligand I / II (%) |
|---|---|---|---|---|---|
| GNP-1 | (2) $\alpha$-Galactose-C$_2$ | (4) PEG(5)NH$_2$ | 50 | 50 | 51 |
| GNP-2 | | | 50 | 51 | 50 |
| GNP-3 | | | 50 | 51 | 52 |
| GNP-4 | | | 60 | 61 | 63 |
| GNP-5 | | | 40 | 40 | 40 |
| GNP-6 | (1) $\beta$-Glucose-C$_2$ | | 50 | 39 | 42 |
| GNP-7 | | | 60 | 50 | 54 |
| GNP-8 | | | 40 | 31 | 34 |
| GNP-9 | (2) $\alpha$-Galactose-C$_2$ | (5) PEG(8)COOH | 45 | 48 | 52 |
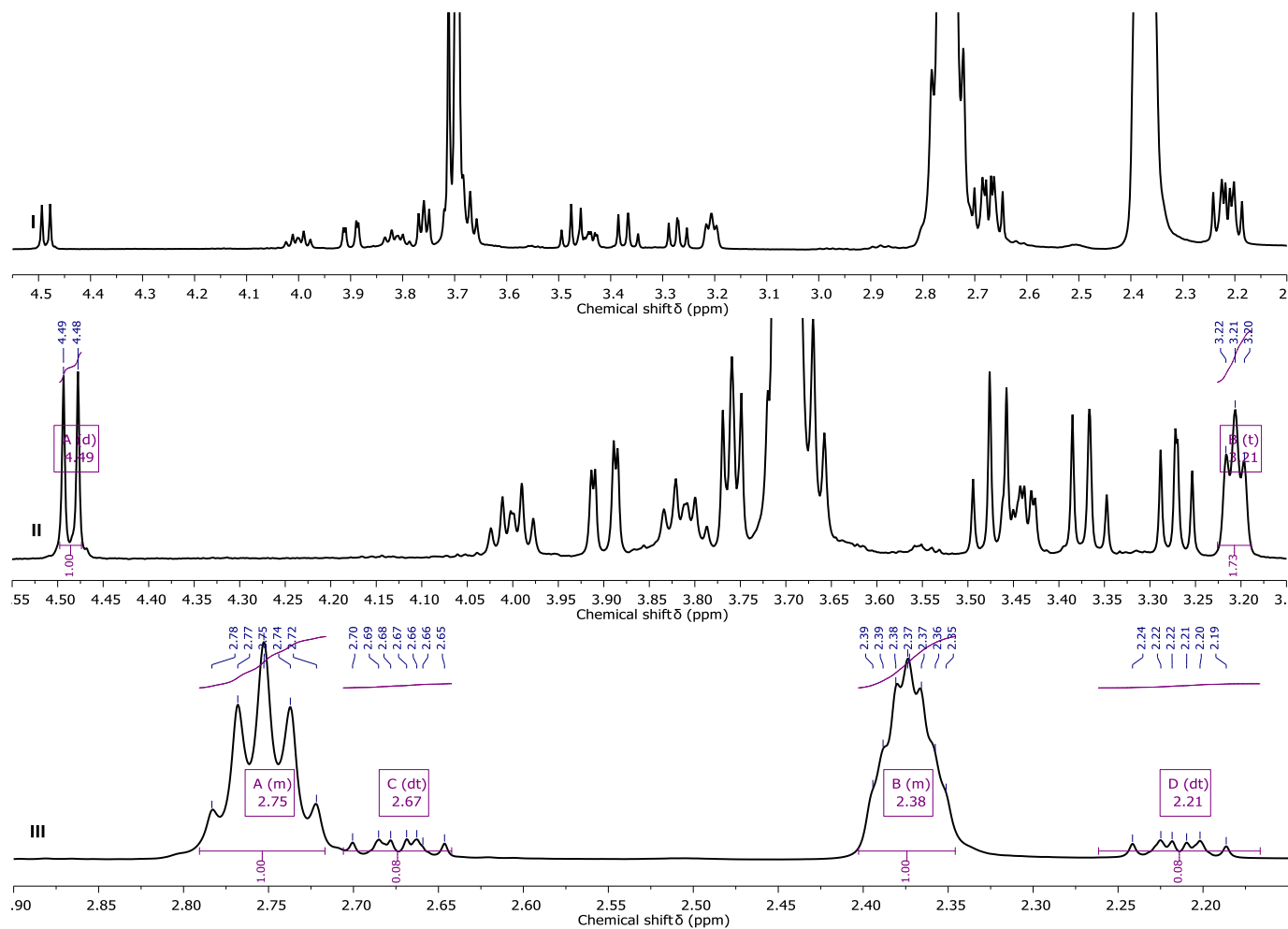
Figure 12: $^1H$ NMR (500 MHz, $D_2O$) of (I) (PEG(5)$NH_2$)($\beta$-Glucose-$C_2$)@$Au_{102}$ (GNP-7) in TCEP. (II) Zoom on the ligand peaks. Integration of $\beta$-Glucose-$C_2$ H-1 anomeric proton $\delta$ 4.49 (d, 1H, area: 1) and PEG(5)$NH_2$ -$CH_2$-$NH_2$ $\delta$ 3.21 (t, 2H, area: 1.73) gives a ratio of 54:46 between the two species. (III) Zoom on TCEP and derivatives peaks. New signals corresponding to Au[TCEP]$_2$ are present at $\delta$ 2.75 (m, 6H, -$CH_2$-P) and $\delta$ 2.38 (m, 6H, -$CH_2$-COOH). TCEP=O signals appear at $\delta$ 2.67 (dt, 6H, -$CH_2$-P) and $\delta$ 2.21 (dt, 6H, -$CH_2$-COOH). No TCEP signals are visible.
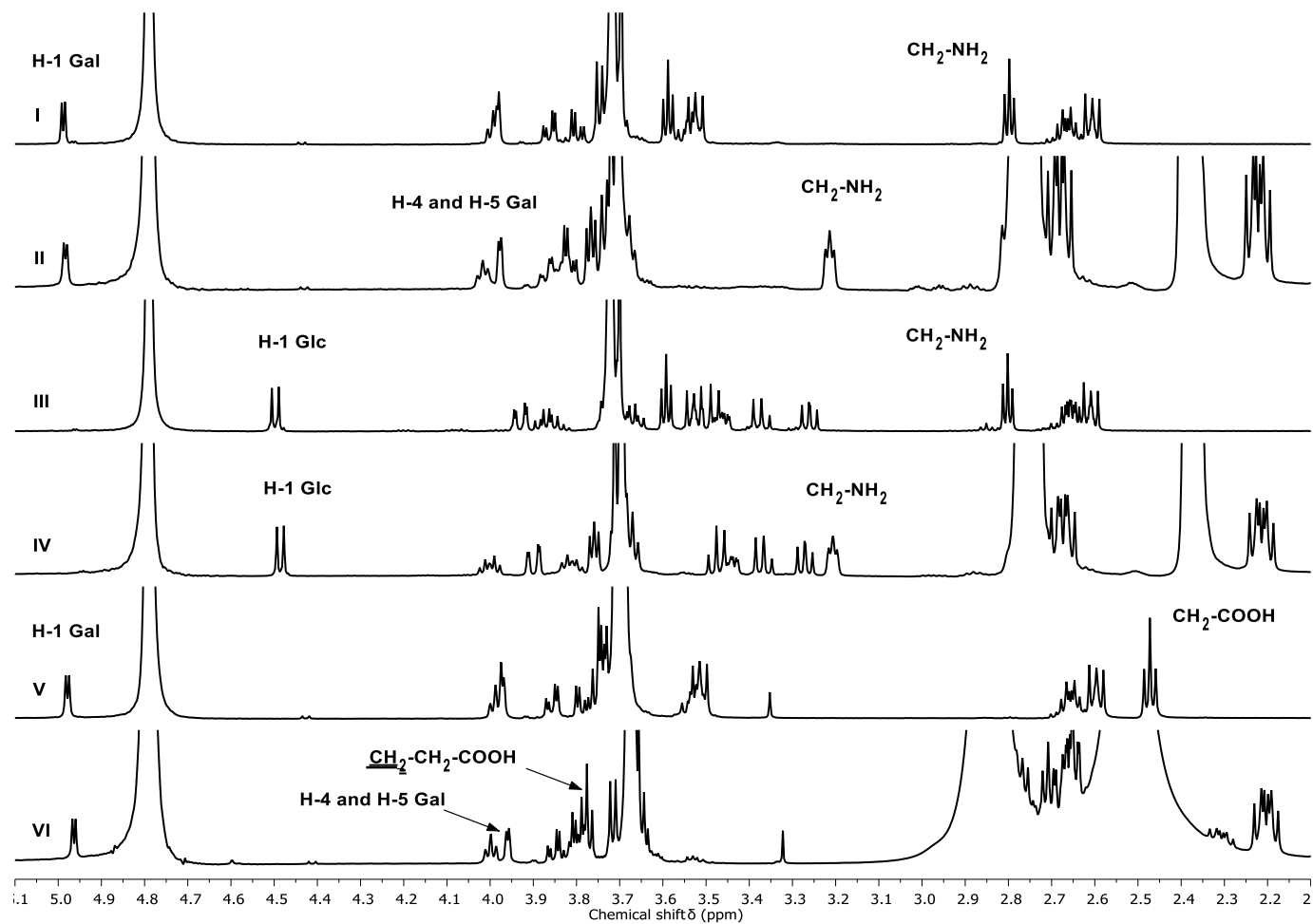
*Figure 13: $^1H$ NMR (500 MHz, $D_2O$) of (PEG(5)NH$_2$)($\alpha$-Galactose-C$_2$)@Au$_{102}$ in (I) KCN/KOH and (II) TCEP, (PEG(5)NH$_2$)($\beta$-Glucose-C$_2$)@Au$_{102}$ in (III) KCN/KOH and (IV) TCEP and (PEG(8)COOH)($\alpha$-Galactose-C$_2$)@Au$_{102}$ in (V) KCN/KOH and (VI) TCEP. Characteristic peaks for integration are annotated H-1 Gal KCN $\delta$ 4.99 (d, 1H), H-4 and H-5 Gal TCEP $\delta$ 3.99 (m, 2H), H-1 Glc KCN $\delta$ 4.50 (d, 1H) and TCEP $\delta$ 4.49 (d, 1H), -CH$_2$-NH$_2$ KCN $\delta$ 2.80 (t, 2H) and TCEP $\delta$ 3.21 (t, 2H), -CH$_2$-COOH KCN $\delta$ 2.48 (t, 2H) and -CH$_2$-CH$_2$-COOH TCEP $\delta$ 3.78 (t, 2H).*

## 4. General methodology to identify and determine ligand ratios in GNP by LC-CAD-MS after TCEP treatment

### a. Proof of concept

Following the successful demonstration that the treatment with TCEP gave comparable results to KCN/KOH by $^1$H NMR, the methodology was adapted to a liquid chromatography method with CAD and MS detectors.

To identify the peaks related to the ligands, the raw disulfide molecules used for the one-pot Brust–Schiffrin synthesis, ligands (**1**) to (**5**) were treated with TCEP to obtain the thiol form and identify them by means of their retention time (RT) and m/z value (*see Table 11 in the annex*). Then, particles treated with TCEP were injected in the LC-CAD-MS system. The ligand RT and m/z were identical to those obtained with the raw materials. TCEP related peaks were identified by comparing the profile of a blank injection, a disulfide ligand with TCEP and the treated GNP (*Figure 14*).
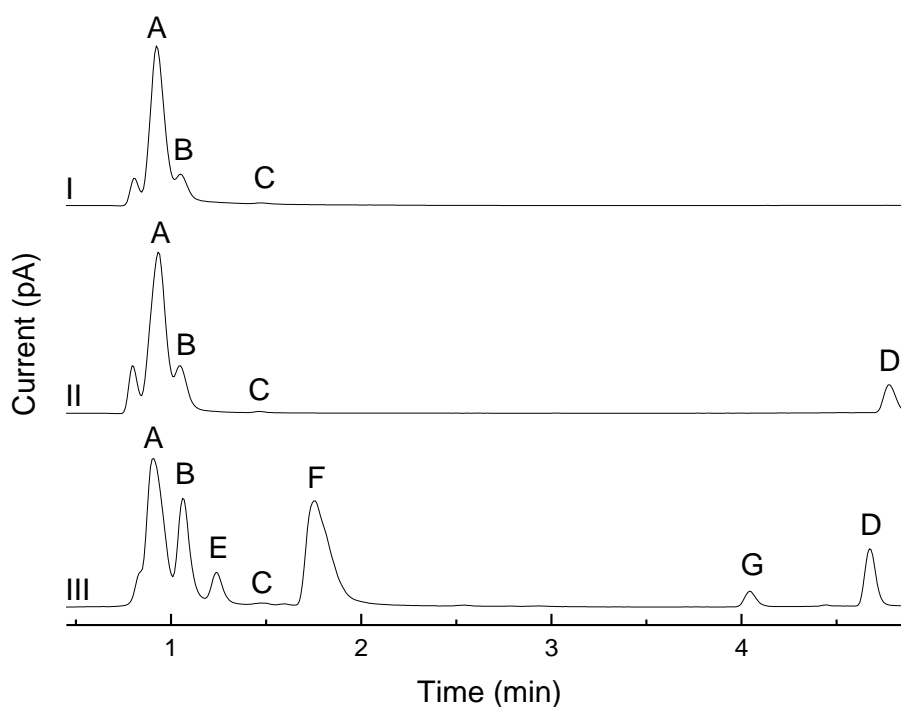


*Figure 14: LC-CAD chromatograms with MS assignation of (I) TCEP blank in H$_2$O. (A) TCEP (RT: 0.968 min; m/z: 251), (B) TCEP=O (RT: 1.094 min; m/z: 267), (C) TCEP Derivative I (RT: 1.473 min; m/z: 223, 445, 467, 473, 511). (II) PEG(5)NH$_2$-SS with TCEP in H$_2$O. (D) PEG(5)NH$_2$ (RT: 4.781 min; m/z: 298). (III) (PEG(5)NH$_2$)(α-Galactose-C$_2$)@Au$_{102}$ after TCEP treatment. (E) α-Galactose-C$_2$ (RT: 1.238 min; area: 0.661; m/z: 241, 380, 500), (F) Au[TCEP]$_2$ (RT: 1.759 min; m/z: 697), (G) TCEP Derivative II (RT: 4.041 min; m/z: 251, 283, 618, 697), (D) PEG(5)NH$_2$ (RT: 4.672 min; area: 1.050; m/z: 298). (E) and (D) give a ratio of 44:56 between the two ligands (based on molecular weights α-Galactose-C$_2$ 240 and PEG(5)NH$_2$ 297).*

The TCEP blank, apart from the injection peak (not annotated), showed three peaks with characteristic retention times and m/z. They correspond to TCEP (**A**), the oxidized TCEP (TCEP=O) (**B**) and a small quantity of TCEP Derivative I (**C**). TCEP=O spontaneously appears over time when TCEP is dissolved in water.

The example of the disulfide ligand PEG(5)NH$_2$ incubated with TCEP revealed the same TCEP related peaks. Only one more peak corresponding to the thiol form of the ligand PEG(5)NH$_2$ (**D**) is visible confirming the complete reduction of the disulfide (m/z of thiol).

The GNP (PEG(5)NH$_2$)($\alpha$-Galactose-C$_2$)@Au$_{102}$ treated with TCEP exhibited the same TCEP related peaks (**A**), (**B**) and (**C**) as well as the thiol ligands $\alpha$-Galactose-C$_2$ (**E**) and PEG(5)NH$_2$ (**D**). Peaks (**F**) and (**G**) were new and identified as the TCEP-Au complex Au[TCEP$_2$] (m/z 697) and TCEP Derivative II, respectively. The areas and the molecular weights of the ligand peaks were used to obtain a ligand ratio that was compared to that obtained by $^1$H NMR.

It should be noted that batch to batch retention times are slightly different, most likely due to the variability of the mobile phase and matrix effects. Nevertheless, the m/z and the standards allow reliable identification of the ligands. Also, for compounds present in low amounts, such as the TCEP Derivatives I and II, the m/z could not be determined accurately because of the background noise. Monosaccharides with a short alkyl side chain, $\alpha$-Galactose-C$_2$ and $\beta$-Glucose-C$_2$, also responded poorly to the MS detector because of their chemical nature (poor ionization)[69].

### b. GNP library screening

Bifunctional GNP synthetized by BSS and using ligands (**1**) to (**5**) were studied in various combinations. Peaks for each ligand were identified and the ratios were determined. *Table 6* shows the comparison of the ratios by LC-CAD-MS with TCEP (*Figure 15*) and $^1$H NMR with KCN/KOH (*Figure 16*). Data obtained with the MS detector for the peaks are also reported and compared with the molecular weight of the ligands.

*Table 6: Ligand ratios obtained by $^1$H NMR and LC-CAD-MS with bifunctional GNP. m/z for each compound is reported.*

| Batch Number | Ligand I (MW) | Ligand II (MW) | $^1$H NMR Ratio (%) | CAD Ratio (%) | MS m/z |
|---|---|---|---|---|---|
| GNP-10 | (2) α-Galactose-C$_2$ (240.27) | (5) PEG(8)COOH (458.56) | 51:49 | 56:44 | [**241**, 380, 500, 534] [**459**, 476] |
| GNP-11 | (1) β-Glucose-C$_2$ (240.27) | (5) PEG(8)COOH (458.56) | 44:56 | 47:53 | [**241**, 340, 544] [**459**, 476] |
| GNP-12 | (2) α-Galactose-C$_2$ (240.27) | (4) PEG(5)NH$_2$ (297.41) | 49:51 | 45:55 | [**241**, 380, 555] [**298**] |
| GNP-13 | (1) β-Glucose-C$_2$ (240.27) | (4) PEG(5)NH$_2$ (297.41) | 42:58 | 41:59 | [**241**, 380, 534] [**298**] |
| GNP-14 | (2) α-Galactose-C$_2$ (240.27) | (3) β-*N*-Acetyl-Glucosamine-EG$_2$ (325.38) | 50:50 | 52:48 | [**241**, 385, 562] [204, **326**, 348, 668] |

For the five batches analyzed, the ligands were well resolved. The difference between the techniques was not greater than 5 % (**GNP-10**: 5 %, **GNP-11**: 3 %, **GNP-12**: 4 %, **GNP-13**: 1 % and **GNP-14**: 2 %). The m/z matched the molecular weights and confirmed the structures. α-Galactose-C$_2$ and β-Glucose-C$_2$ MS spectra exhibited many m/z values but the "correct" m/z (241) was always present.
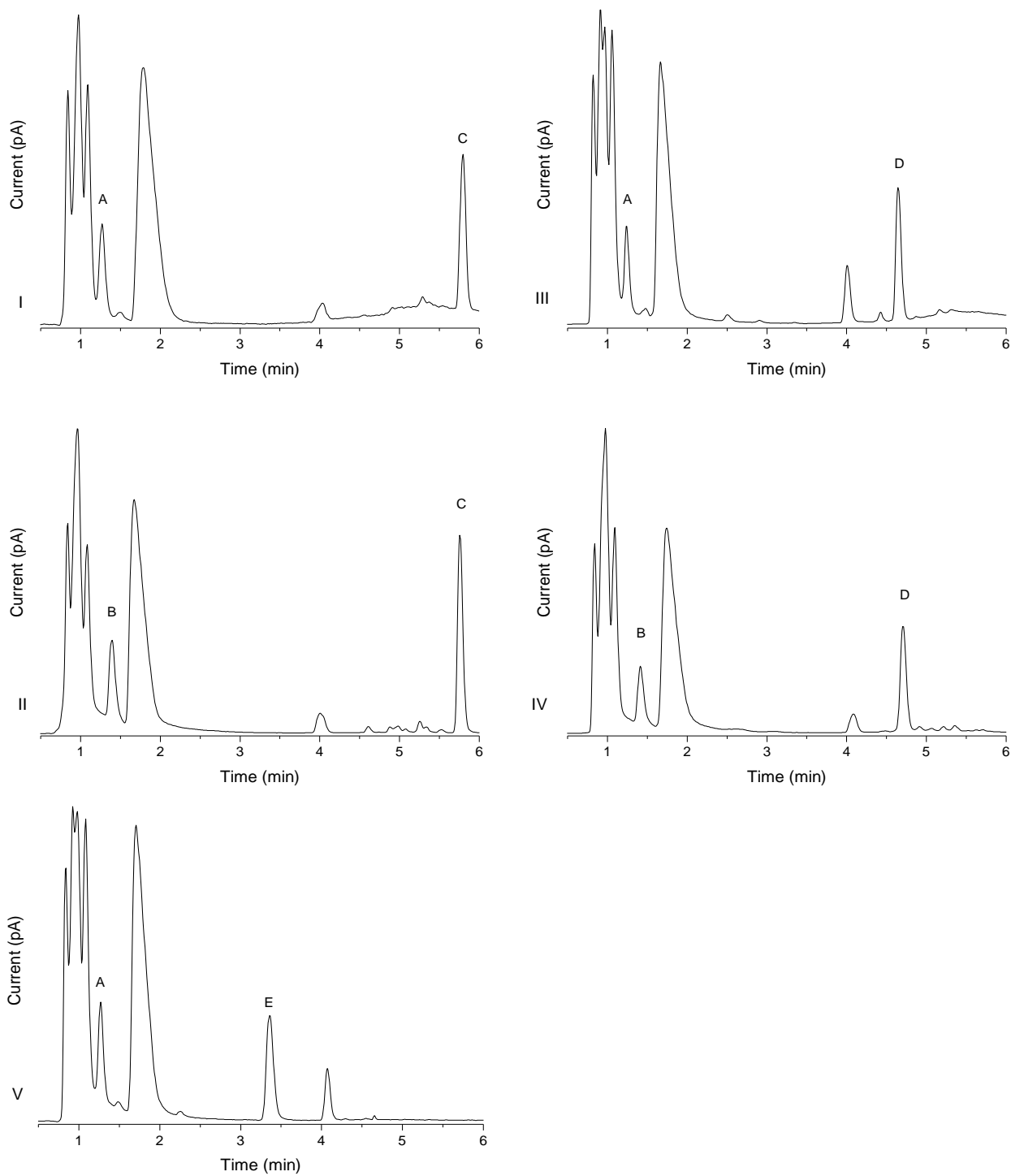
*Figure 15: LC-CAD chromatograms with MS assignation of (I) GNP-10, (II) GNP-11, (III) GNP-12, (IV) GNP-13 and (V) GNP-14 after TCEP treatment. (A) α-Galactose-C$_2$ (RT: 1.271 min; m/z: 241), (B) β-Glucose-C$_2$ (RT: 1.397 min; m/z: 241), (C) PEG(8)COOH (RT: 5.758 min; m/z: 459, 476) (D) PEG(5)NH$_2$ (RT: 4.655 min; m/z: 298) and (E) β-N-Acetyl-Glucosamine-EG$_2$ (RT: 3.359 min; m/z: 204, 326, 348, 668).*

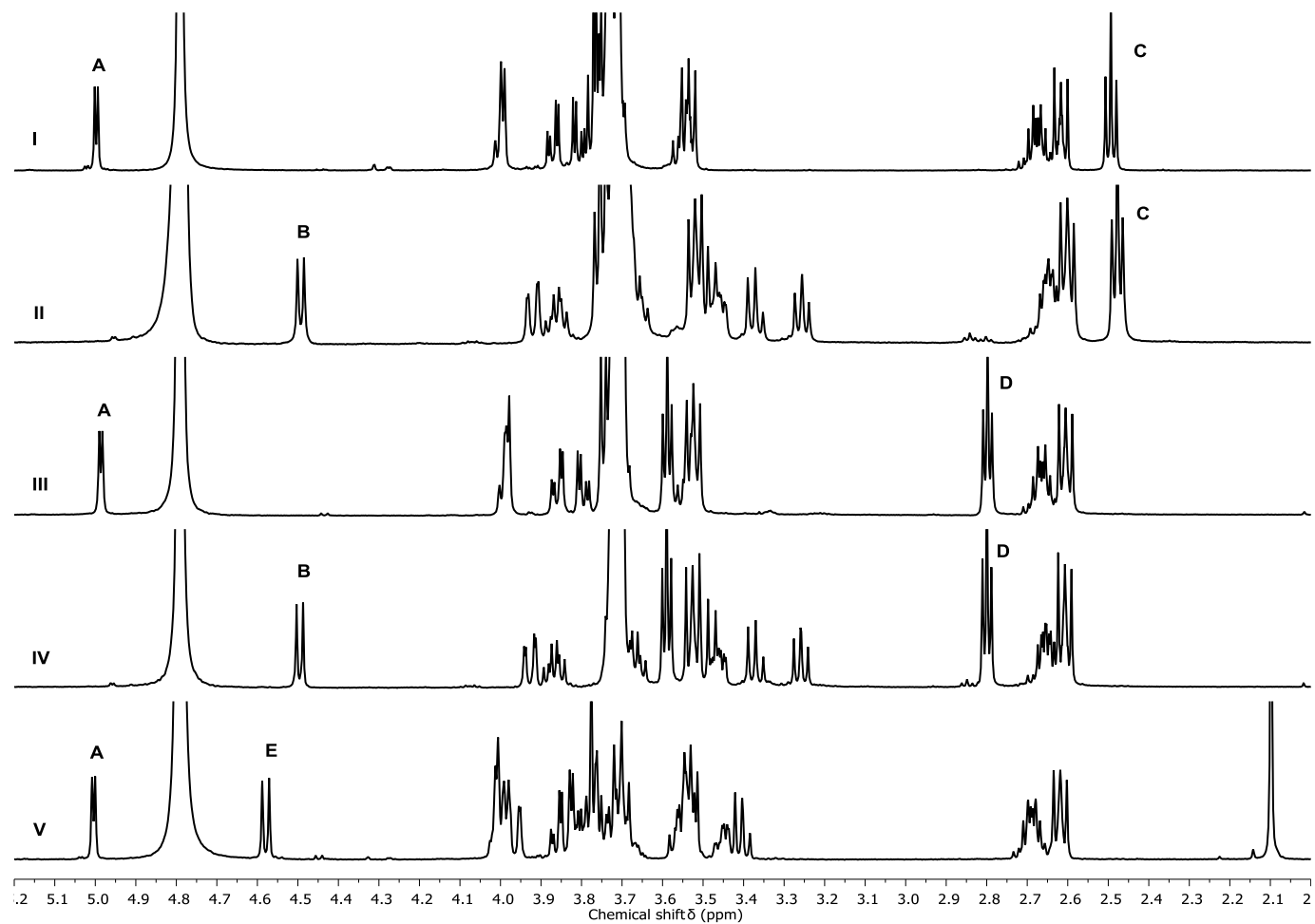*Figure 16:* $^1H$ *NMR (500 MHz, $D_2O$) of (I) GNP-10, (II) GNP-11, (III) GNP-12, (IV) GNP-13 and (V) GNP-14 after KCN/KOH treatment. (A) α-Galactose-$C_2$ δ 4.99 (H-1, d, 1H), (B) β-Glucose-$C_2$ δ 4.50 (H-1, d, 1H), (C) PEG(8)COOH δ 2.48 (-$CH_2$-COOH, t, 2H), (D) PEG(5)$NH_2$ δ 2.80 (-$CH_2$-$NH_2$, t, 2H) and (E) β-N-Acetyl-Glucosamine-$EG_2$ δ 4.58 (H-1, d, 1H).*

Using the bifunctional particle $(PEG(5)NH_2)_{26}(\beta\text{-Glucose-}C_2)_{18}@Au_{102}$ (**GNP-13**), several post-functionalization reactions were performed. The pegamine derivatization was confirmed by the appearance of new signals and/or the decrease of the $PEG(5)NH_2$ peaks by ^{1}H NMR and LC-CAD-MS. ^{1}H NMR signals of the newly formed compounds were selected for their good resolution, and the relative drop in intensity of the pegamine terminal methylene proton signal ($\text{-}CH_2\text{-}NH_2$) confirmed formation of the amide ($\text{-}CH_2\text{-}NH\text{-}CO\text{-}R$) (*Figure 18*). Using LC-CAD-MS, new peaks were integrated using the CAD area and their molecular weight was used to obtain the ratios. MS also confirmed the identity (*Figure 17*).

The amidation of 6-azido-hexanoic acid and succinic anhydride changed the terminal function of the GNP PEG to an azide: **GNP-15**, compound (**6**) and a carboxylic acid: **GNP-16**, compound (**7**), respectively. Using Sulfo-NHS-Acetate, an acetamide was obtained: **GNP-17**, compound (**8**). The monosaccharide derivatives, $\alpha$-Mannose-$C_2H_4$-$NH_2$ and $\beta$-Galactose-$C_4H_8$-$NH_2$, were linked to the PEG, allowing their presentation on the outer part of the GNP: **GNP-18**, compound (**9**) and **GNP-19**, compound (**10**). Residual pegamines after coupling with the carbohydrates were protected with Sulfo-NHS-Acetate to form compound (**8**). Ratios of the post-functionalized GNP are listed in *Table 7*.

*Table 7: Ratios obtained by ^{1}H NMR and LC-CAD-MS after functionalization of $(PEG(5)NH_2)_{26}(\beta\text{-Glucose-}C_2)_{18}@Au_{102}$. m/z for each compound is reported. Ligands I and II are (1) $\beta$-Glucose-$C_2$ (240.27) and (4) $PEG(5)NH_2$ (297.41).*

| Batch Number | Ligand III (MW) | Ligand IV (MW) | ^{1}H NMR Ratio (%) | CAD Ratio (%) | MS m/z |
|---|---|---|---|---|---|
| GNP-15 | (6) PEG(5)NH-CO-$C_5H_{10}$-$N_3$ (436.57) | - | 45:12:43 | 50:14:36 | [241, 467] [298] [**437**, 454] |
| GNP-16 | (7) PEG(5)NH-CO-$C_2H_4$-COOH (397.48) | - | 44:8:48 | 46:8:46 | [241, 467] [298] [**398**, 414] |
| GNP-17 | (8) PEG(5)NH-Ac (339.45) | - | 44:4:52 | 45:4:51 | [241, 260, 380, 544] [298] [**340**, 357] |
| GNP-18 | (9) PEG(5)NH-CO-$C_2H_4$-$\alpha$-Mannose (531.61) | (8) PEG(5)NH-Ac (339.45) | 46:5:39:10 | 47:2:38:13 | [241, 544] [298] [**532**, 549] [**340**, 357] |
| GNP-19 | (10) PEG(5)NH-CO-$C_4H_8$-$\beta$-Galactose (559.67) | (8) PEG(5)NH-Ac (339.45) | 44:3:49:4 | 50:1:41:8 | [241, 380, 368, 534] [298] [**560**, 577] [**340**, 357] |

For the five batches analyzed, the ligands peaks were well resolved. Focusing on the percentage of newly formed molecules, the differences measurement by the two techniques was not greater than 8 % (**GNP-15**: 7 %, **GNP-16**: 2 %, **GNP-17**: 1 %, **GNP-18**: 1 % and 3 % and **GNP-19**: 8 % and 4 %). The m/z matched the molecular weights confirming the structures.



*Figure 17: LC-CAD chromatograms with MS assignation  of (I) GNP-13, (II) GNP-15, (III) GNP-16, (IV) GNP-17, (V) GNP-18 and (VI) GNP-19 after TCEP treatment. (A) β-Glucose-C₂ (RT: 1.414 min; m/z: 241), (B) PEG(5)NH₂ (RT: 4.705 min; m/z: 298), (C) PEG(5)NH-CO-C₅H₁₀-N₃ (RT: 6.575 min; m/z: 437, 454), (D) PEG(5)NH-CO-C₂H₄-COOH (RT: 5.413 min; m/z: 398, 414), (E) PEG(5)NH-Ac (RT: 5.363 min; m/z: 340, 357) (F) PEG(5)NH-CO-C₂H₄-α-Mannose (RT: 5.059 min; m/z: 532, 549) and (G) PEG(5)NH-CO-C₄H₈-β-Galactose (RT: 5.135 min; m/z: 560, 577).*
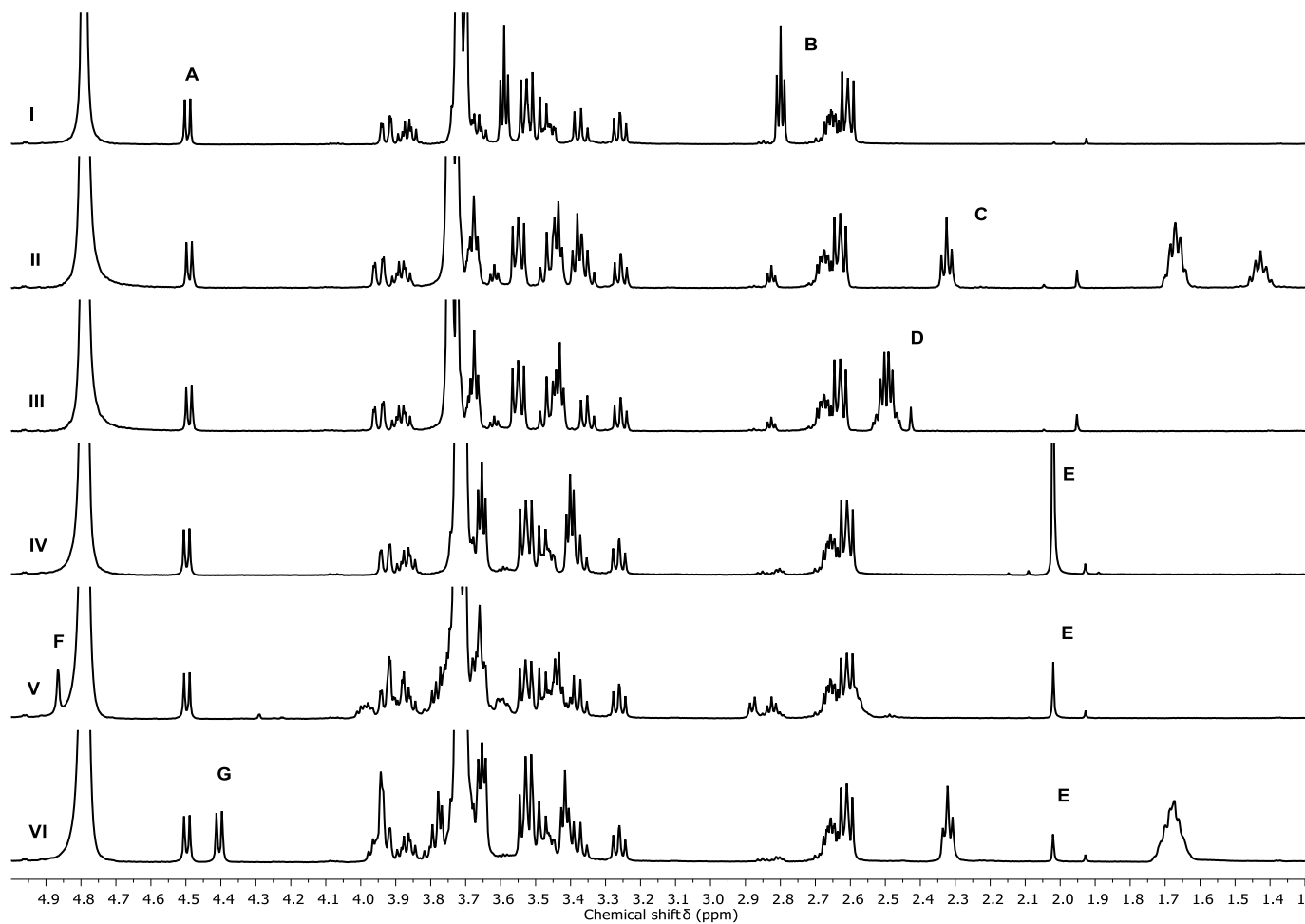
Figure 18: $^1H$ NMR (500 MHz, $D_2O$) of (I) GNP-13, (II) GNP-15, (III) GNP-16, (IV) GNP-17, (V) GNP-18 and (VI) GNP-19 after KCN/KOH treatment. (A) β-Glucose-$C_2$ δ 4.50 (H-1, d, 1H), (B) PEG(5)$NH_2$ δ 2.80 (-$CH_2$-$NH_2$, t, 2H), (C) PEG(5)NH-CO-$C_5H_{10}$-$N_3$ δ 2.32 (t, 2H), (D) PEG(5)NH-CO-$C_2H_4$-COOH δ 2.50 (m, 4H), (E) PEG(5)NH-Ac δ 2.02 (s, 3H), (F) PEG(5)NH-CO-$C_2H_4$-α-Mannose δ 4.86 (H-1, d, 1H) and (G) PEG(5)NH-CO-$C_4H_8$-β-Galactose (H-1, d, 1H).

Post-functionalization was then employed with another bifunctional particle $(PEG(5)NH_2)_{30}(\beta\text{-Glucose-C}_2)_{14}@Au_{102}$ (**GNP-8**), but with a more complex synthesis composed of three steps. An amide bond was formed between Boc-amino-oxy acetic acid and the pegamine. The Boc group was removed to expose the amino-oxy function on the outer part of the GNP, and finally, three different non-modified oligosaccharides were attached through formation of an oxime. The Boc-amino-oxy acetic acid binding was determined by ^{1}H NMR and LC-CAD-MS: **GNP-20**, compound (**11**). The oxime ligation yield, although confirmed by ^{1}H NMR (*Figure 20*), was impossible to quantify due the complexity of the spectra (absence of stereocontrol and numerous signals). By LC-CAD-MS, on the other hand, for the oxime linked compounds, only one well resolved peak was present and an estimation of the amount of α-Mannose1,2-α-mannose: **GNP-21**, compound (**12**), 1,3-α-1,6-α-D-Mannotriose: **GNP-22**, compound (**13**) and Maltotriose **GNP-23**, compound (**14**) was obtained. The identity of the structures was confirmed by MS (*Figure 19*). Ligand ratios of the post-functionalized GNP are listed in *Table 8*.

*Table 8: Ligand ratios obtained by ^{1}H NMR and LC-CAD-MS after functionalization of $(PEG(5)NH_2)_{30}(\beta\text{-Glucose-C}_2)_{14}@Au_{102}$. m/z for each compound is reported. Ligands I and II are (1) β-Glucose-C_2 (240.27) and (4) PEG(5)NH_2 (297.41).*

| Batch Number | Ligand III (MW) | ^{1}H NMR ratio | CAD ratio | MS m/z |
|---|---|---|---|---|
| GNP-20 | (11) PEG(5)NH-CO-CH_2-O-NH-Boc (470.58) | 42:16:42 | 58:6:36 | [241, 318, 385, 555] [298] [**471**, 488, 516] |
| GNP-21 | (12) PEG(5)NH-CO-CH_2-O-N-(α-Mannose1,2-α-Mannose) (694.74) | N/A | 52:11:37 | [241, 260, 531] [298] [**695**, 712, 717] |
| GNP-22 | (13) PEG(5)NH-CO-CH_2-O-N-(1,3-α-1,6-α-D-Mannotriose) (856.88) | N/A | 57:12:31 | [241, 380, 544] [298] [**857**, 874, 1120] |
| GNP-23 | (14) PEG(5)NH-CO-CH_2-O-N-(Maltotriose) (856.88) | N/A | 56:13:31 | [241, 260, 467] [298] [**857**, 874, 1121] |

The difference between the ^{1}H NMR and the LC-CAD-MS for the Boc amino-oxy functionalization was 6 % (**GNP-20**). The loading of the oligosaccharides was in line with the previous step (36 % of Boc amino-oxy by LC-CAD-MS) with 37 % (**GNP-21**) and 31 % (**GNP-22** and **GNP-23**) of the total formula. Importantly, the chromatograms only presented one peak corresponding to the compound sought (identity confirmed by MS) with few impurities.

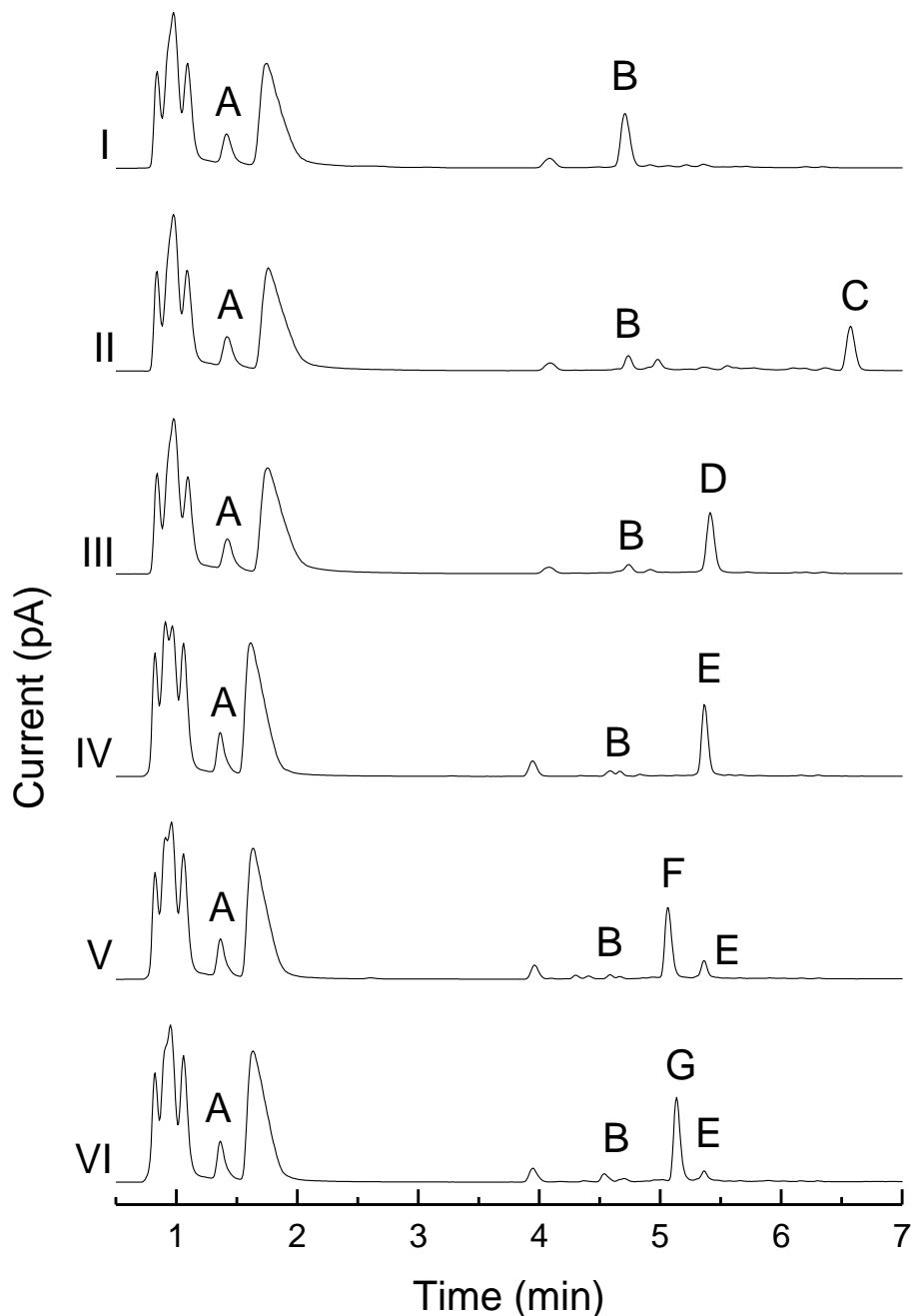*Figure 19: LC-CAD chromatograms with MS assignation of (I) GNP-8, (II) GNP-20, (III) GNP-21, (IV) GNP-22 and (V) GNP-23 after TCEP treatment. (A) β-Glucose-$C_2$ (RT: 1.439 min; m/z: 241), (B) PEG(5)$NH_2$ (RT: 4.781 min; m/z: 298), (C) PEG(5)NH-CO-$CH_2$-O-NH-Boc (RT: 6.474 min; m/z: 471, 488, 516), (D) PEG(5)NH-CO-$CH_2$-O-N-(α-Mannose1,2-α-Mannose) (RT: 5.001 min; m/z: 695, 712, 717), (E) PEG(5)NH-CO-$CH_2$-O-N-(1,3-α-1,6-α-D-Mannotriose) (RT: 4.950 min; m/z: 857, 874, 1120) and (F) PEG(5)NH-CO-$CH_2$-O-N-(Maltotriose) (RT:4.983 min; m/z: 857, 874, 1121).*
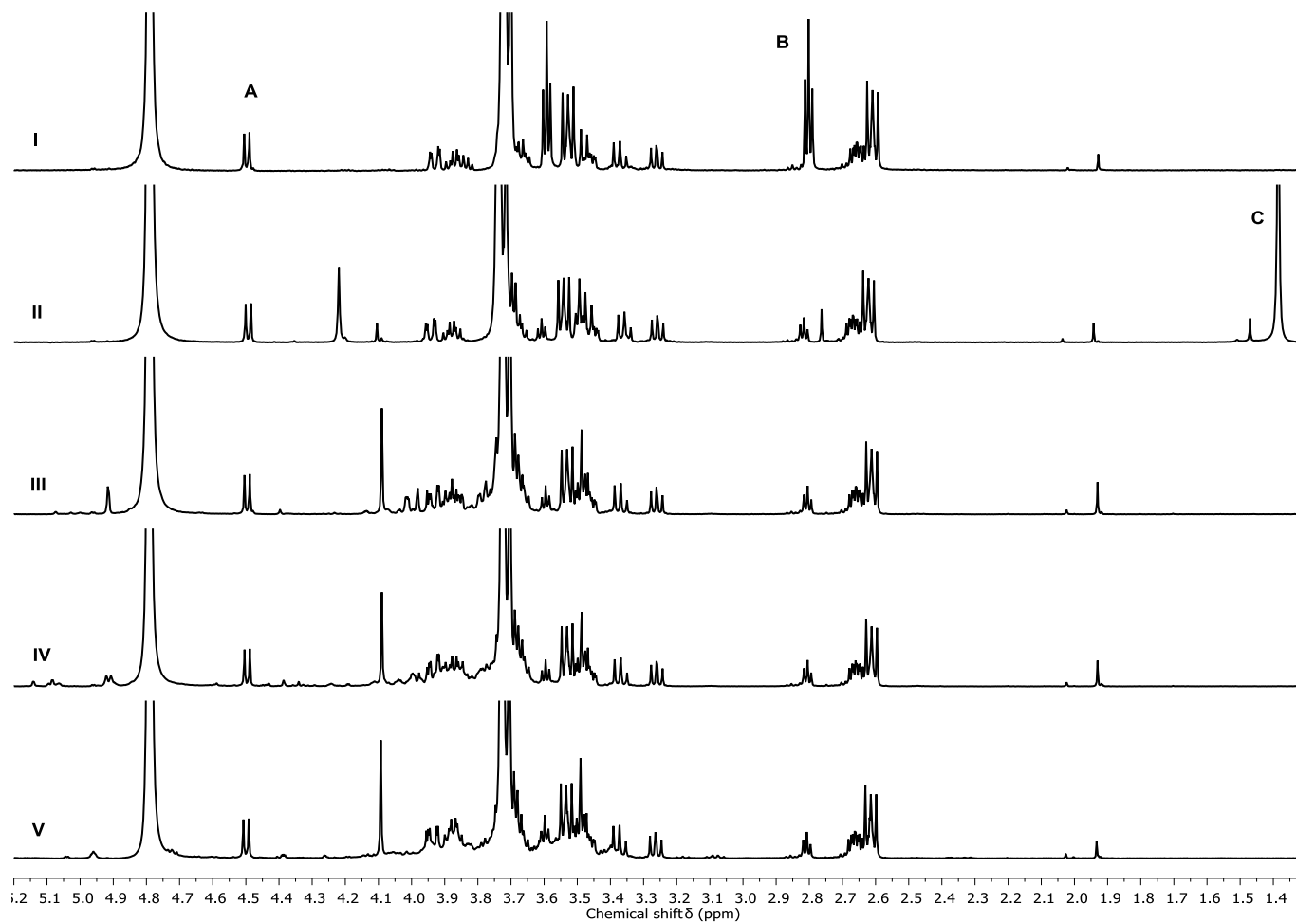
Figure 20: $^1H$ NMR (500 MHz, $D_2O$) of (I) GNP-8, (II) GNP-20, (III) GNP-21, (IV) GNP-22 and (V) GNP-23 after KCN/KOH treatment. (A) $\beta$-Glucose-$C_2$ $\delta$ 4.50 (H-1, d, 1H), (B) PEG(5)$NH_2$ $\delta$ 2.80 (-$CH_2$-$NH_2$, t, 2H), (C) PEG(5)NH-CO-$CH_2$-O-NH-Boc $\delta$ 1.39 (s, 9H). Percentages of oligosaccharides could not be determined.

To complete the library of compounds screened by LC-CAD-MS and confirm its versatility, a different bifunctional platform, $(PEG(8)COOH)_{26-22}(\alpha\text{-Galactose-C}_2)_{22-18}@Au_{102}$ (**GNP-10**) was used (*Figure 21 and Figure 22*). Using the terminal functional group of the PEG carboxylic acid, post-functionalization reactions were performed. Methanol/sulfuric acid was used to make the methyl-ester: **GNP-24**, compound (**15**) and coupling with ethanolamine gave a ligand that presented a hydroxyl on the outer part of the GNP: **GNP-25**, compound (**16**). Derivatives of α-Mannose: **GNP-26**, compound (**17**), α-Mannose1,2-α-Mannose: **GNP-27**, compound (**18**) and β-Galactose: **GNP-28**, compound (**19**) were linked to the GNP through an amide bond using the amine function of their ethyl side chain. Ligand ratios of the post-functionalized GNP are listed in *Table 9*.

*Table 9: Ligand ratios obtained by $^1$H NMR and LC-CAD-MS after functionalization of $(PEG(8)COOH)(\alpha\text{-Galactose-C}_2)@Au_{102}$. m/z for each compound is reported. Ligands I and II are (2) α-Galactose-C$_2$ (240.27) and (5) PEG(8)COOH (458.56).*

| Batch Number | Ligand III (MW) | $^1$H NMR ratio | CAD ratio | MS m/z |
|---|---|---|---|---|
| GNP-24 | (15) PEG(8)COOMe (472.59) | 50:0:50 | 55:3:42 | [241, 393, 500] [459, 476] [413, **473**, 490] |
| GNP-25 | (16) PEG(8)CO-NH-C$_2$H$_4$-OH (501.63) | 56:11:32 | 51:11:38 | [241, 380, 500] [459, 476] [**502**, 519] |
| GNP-26 | (17) PEG(8)CO-NH-C$_2$H$_4$-α-Mannose (663.77) | 42:36:22 | 45:33:22 | [241, 380, 534] [459, 476] [**664**, 681] |
| GNP-27 | (18) PEG(8)CO-NH-C$_2$H$_4$-(α-Mannose1,2-α-Mannose) (825.91) | 52:21:27 | 56:21:23 | [241, 380, 500] [459, 476] [433, **826**, 843, 910, 1258] |
| GNP-28 | (19) PEG(8)CO-NH-C$_2$H$_4$-β-Galactose (663.77) | 52:22:26 | 55:21:24 | [241, 380, 529, 565] [459, 476] [352, **664**, 681] |

For the five batches analyzed, the ligands were well resolved. Focusing on the percentage of newly formed molecules, the difference between the techniques was not greater than 8 % (**GNP-24**: 8 %, **GNP-25**: 6 %, **GNP-26**: 0 %, **GNP-27**: 4 % and **GNP-28**: 2 %). The m/z matched the molecular weights confirming the structures. The use of LC-CAD-MS overcame one issue of the KCN/KOH method: the harsh conditions that can degrade ligands. In fact, the methyl-ester was hydrolyzed by KCN/KOH to form methanol but left intact by the treatment with TCEP, as confirmed by the MS m/z.
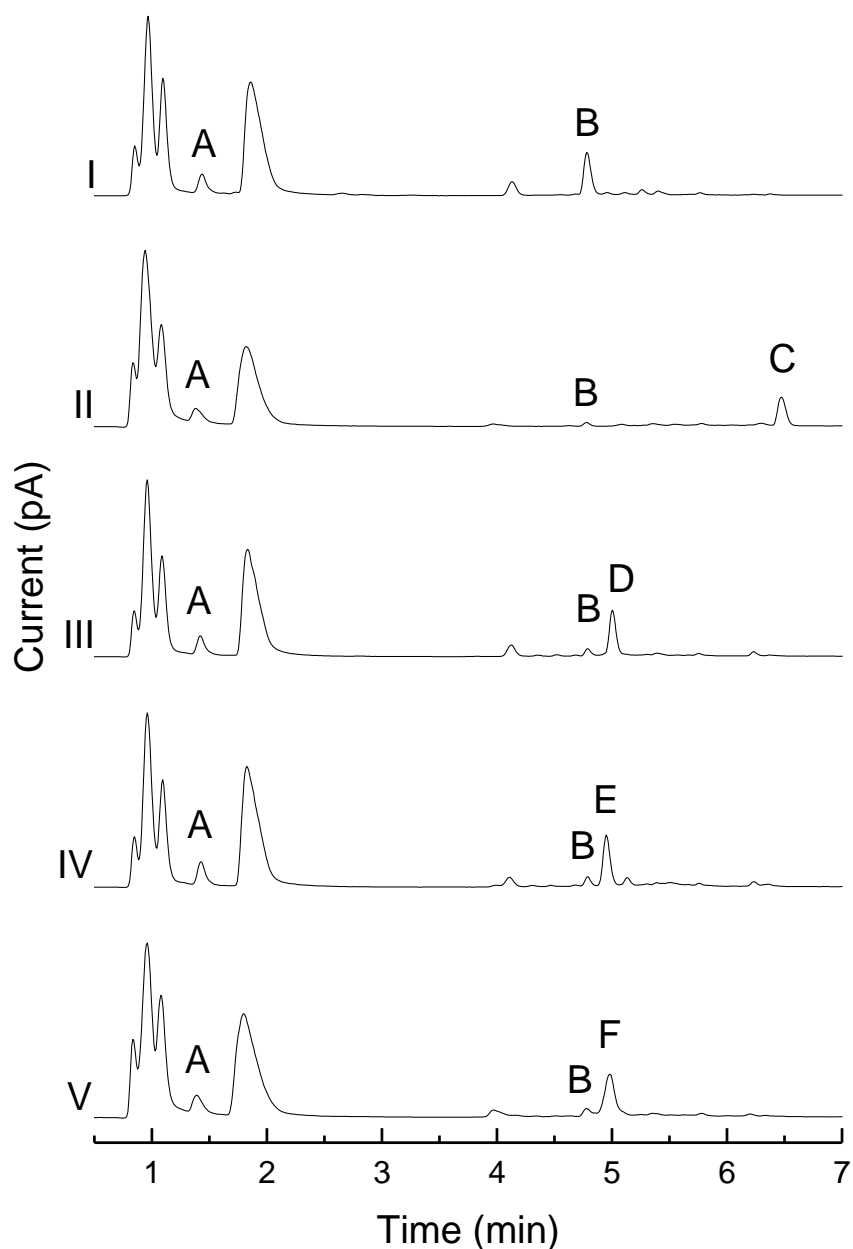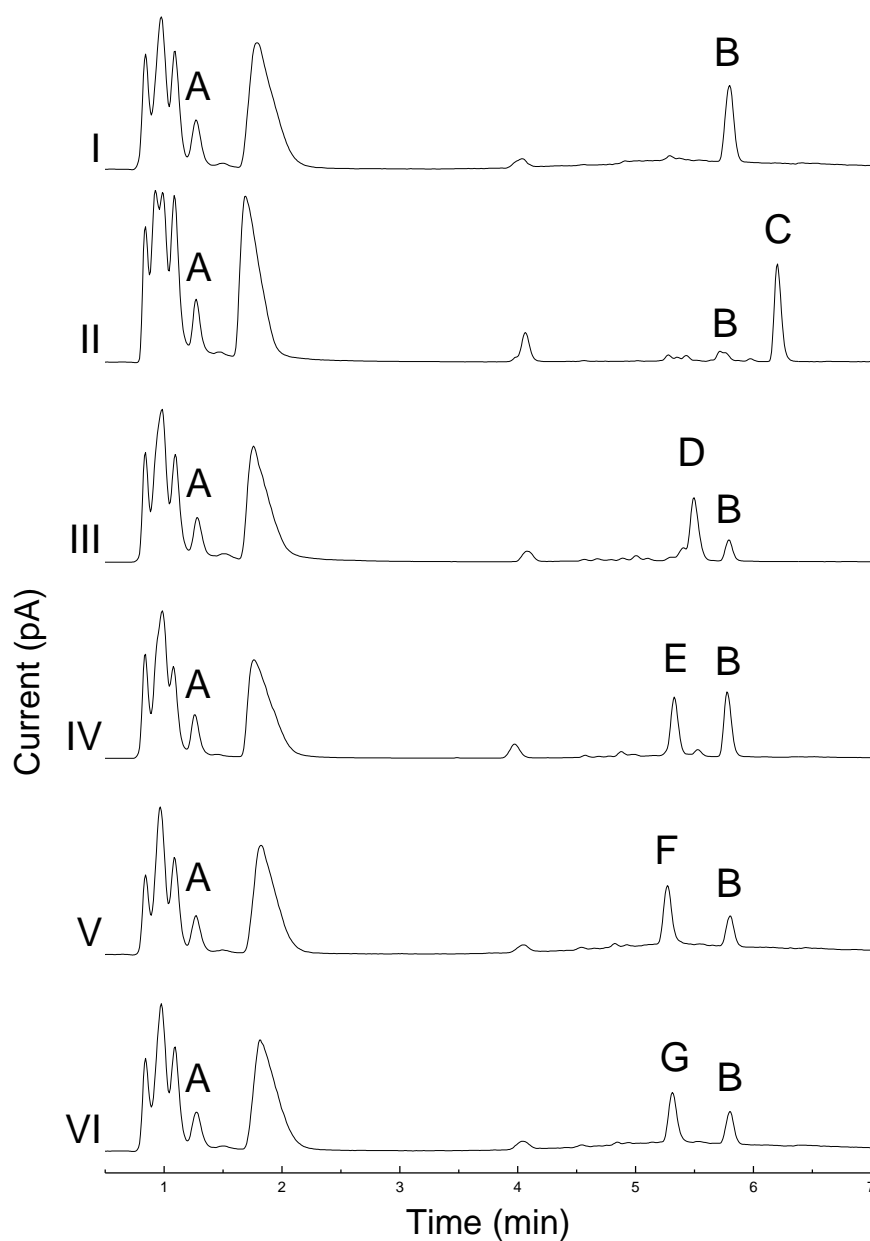
*Figure 21: LC-CAD chromatograms with MS assignation of (I) GNP-10, (II) GNP-24, (III) GNP-25, (IV) GNP-26, (V) GNP-27 and (VI) GNP-28 after TCEP treatment. (A) $\alpha$-Galactose-C$_2$ (RT: 1.271 min; m/z: 241), (B) PEG(8)COOH (RT: 5.800 min; m/z: 459, 476), (C) PEG(8)COOMe (RT: 6.204 min; m/z: 413, 473, 490), (D) PEG(8)CO-NH-C$_2$H$_4$-OH (RT: 5.497 min; m/z: 502, 519), (E) PEG(8)CO-NH-C$_2$H$_4$-$\alpha$-Mannose (RT: 5.328 min; m/z: 664, 681), (F) PEG(8)CO-NH-C$_2$H$_4$-($\alpha$-Mannose1,2-$\alpha$-Mannose) (RT: 5.269 min; m/z: 433, 826, 843, 910, 1258) and (G) PEG(8)CO-NH-C$_2$H$_4$-$\beta$-Galactose (RT: 5.312 min; m/z: 352, 664, 681).*
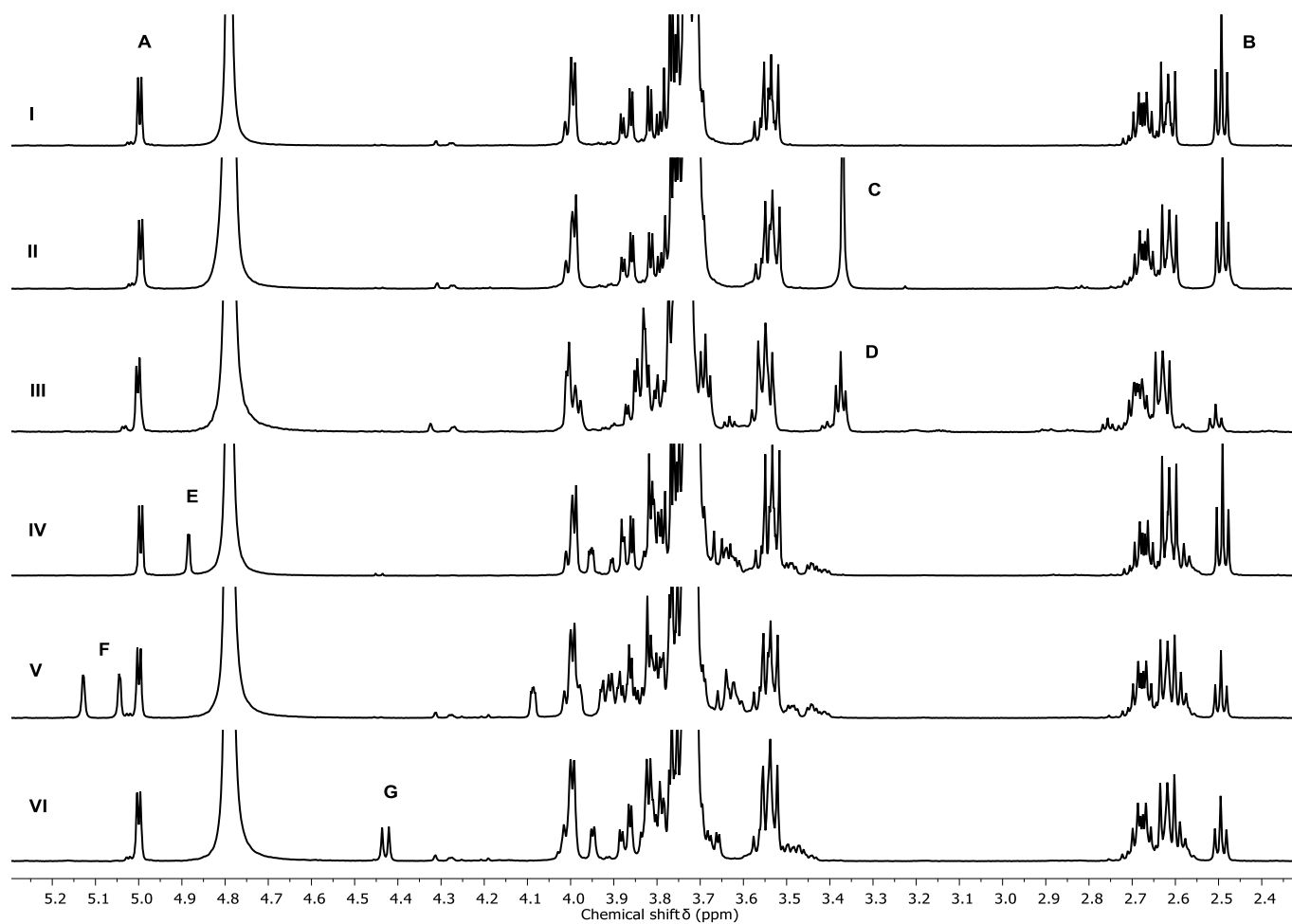
Figure 22: $^1H$ NMR (500 MHz, $D_2O$) (I) GNP-10, (II) GNP-24, (III) GNP-25, (IV) GNP-26, (V) GNP-27 and (VI) GNP-28 after TCEP treatment. (A) α-Galactose-$C_2$ δ 4.99 (H-1, d, 1H), (B) PEG(8)COOH δ 2.48 (-$CH_2$-COOH, t, 2H), (C) MeOH δ 3.37 (s, 3H), -COOMe is actually not present and MeOH can been seen as well as PEG(8)COOH since the ester is hydrolyzed in KCN/KOH, (D) PEG(8)CO-NH-$C_2H_4$-OH δ 3.37 (t, 2H), (E) PEG(8)CO-NH-$C_2H_4$-α-Mannose δ 4.88 (H-1, d, 1H), (F) PEG(8)CO-NH-$C_2H_4$-(α-Mannose1,2-α-Mannose) δ 5.13 (d, 1H) and (G) PEG(8)CO-NH-$C_2H_4$-β-Galactose δ 4.43 (H-1, d, 1H).

# IV.   Conclusions and Further Work

The complete and clean etching of the GNP (no pellet, no stains) was only achieved using TCEP and KCN/KOH with the conditions tested. The relatively large quantities and the concentration of sample used (minimum required for ^{1}H NMR) could explain the fact that DTT was not able etch completely the GNP, although thiol ligands in high excess have demonstrated GNP etching capabilities[70].

The equivalence of the TCEP and KCN/KOH methods for determining ligand ratios was confirmed with ^{1}H NMR. Good reproducibility between batches with the same ratio has been shown, as well as enough sensitivity to spot 10 % differences.

Nevertheless, the integration can be complicated when the signals of the ligands overlap each other or interfere with TCEP related signals: TCEP, TCEP=O and Au[TCEP]$_2$ complex with gold[68]. These signals have a chemical shift between $\delta$ 2-3 ppm. An alternative to TCEP could be other phosphines such as tris(3-hydroxypropyl)phosphine (THPP), which would exhibit different ^{1}H NMR signals and have a different polarity[71].

Moving forward, TCEP is an agent able to completely etch the particles and, unlike KCN/KOH, can maintain the ligands as monomeric thiols, which is of critical importance for chromatographic techniques. TCEP treatment was used with LC-CAD-MS and compared to ^{1}H NMR after KCN/KOH treatment. A library of bifunctional one-pot synthesized GNP was screened and showed a deviation of ligand ratio of less than 5 % between the two methods. As with ^{1}H NMR, peaks related to the TCEP were also identified and their structures were confirmed by mass spectrometry. Different post-functionalization reactions were performed using PEG with either a terminal amine or carboxylic acid group. Looking at the percentage of the newly formed ligand, the difference between the two techniques was not greater than 8 %. The ligand ratios calculated by CAD, done without calibration standards, demonstrated the suitability of the mass dependent response with the compounds studied (monosaccharides, oligo-PEG, alkyl or carbohydrate-functionalized oligo-PEG).

LC-CAD-MS showed its superiority, when multi-step reactions with more complex ligands were performed (amino-oxy pathway, oxime binding with oligosaccharides), and ^{1}H NMR spectra complexity hindered accurate ligand ratio determination. Also, the milder conditions that could be used with TCEP allowed identification of a methyl-ester compound that was degraded by the KCN/KOH treatment.

The combination of the mass-dependent property of the charged aerosol detector for the calculation of the ligand ratio and mass spectrometry for the identity, makes LC-CAD-MS a technique of choice for ligand identification on ultrasmall GNP. Its use is essential, since many ligands analyzed are not suitable for UV detection or lack a standard for their quantification.

Nevertheless, the CAD methodology is not completely universal and development work still needs to be done with other classes of molecules. The chromatographic part of the analysis is key to obtain good resolution of the compounds and must be optimized depending on the ligands. The poor MS response of monosaccharides with short side chains is an issue that needs to be overcome, possibly by improving the ionization method (ionization was performed in positive mode).

Comparing ratios with another chromatographic method using a different detector would also be interesting. For instance, using a Refractive Index (RI) detector, which can detect carbohydrates[72] and PEG[73].

LC-CAD-MS with ultrasmall GNP is not designed to replace ^{1}H NMR, but rather complement it. It has the undeniable advantage of consuming less material, making it a prefect tool for early development, when materials are typically available in small quantities. As demonstrated in this chapter, not only the technique but also its fine tuning (pre-treatment), enable the proper analysis of the GNP. *Table 10* summarizes the advantages and drawbacks of each technique.

*Table 10: Relative advantages and drawbacks of ^{1}H NMR and LC-CAD-MS.*

| Technique | Advantages | Drawbacks |
|---|---|---|
| ^{1}H NMR | Universal | Material consuming, difficult interpretation for complex molecules |
| LC-CAD-MS | No need for standards (CAD mass dependent response), easy identification with m/z (MS), sensitive | Not universal, need for chromatographic development |

# V.   Materials and Methods

## 1.  GNP Characterization

The batches were characterized using pH, TEM, UV-Vis, DLS, DCS, MP-AES, XPS, ICP-AES, $^1$H NMR and LC-CAD-MS. The absence of a surface plasmon band at 520 nm in the UV-Vis spectra and the TEM/DLS/DCS results matched with the ultrasmall particle size and distribution criteria. XPS and ICP-AES confirmed that the ligand density was correct.

$^1$H NMR and LC-CAD-MS methods as well as the pre-treatments are described below.

### a.   Pre-treatment screening

4-5 mg Au of 2 nm GNP were put in presence of 0.3 M KCN in 0.1 M KOH, TCEP, DTT, β-mercaptoethanol, KI/I$_2$ and NaBH$_4$ with variations of key parameters (amount, volume, solvent, temperature, time, pH). Volume varied from 500 μL to 2 mL, temperature from 25 °C to 60 °C, time from minutes to days. Apart from H$_2$O, methanol was used with KI/I$_2$. TCEP was employed in H$_2$O (pH 2-3) and buffered a pH 7. The etching was visually checked.

### b.   $^1$H NMR

β-Glucose-C$_2$ (**1**), α-Galactose-C$_2$ (**2**), β-*N*-Acetyl-Glucosamine-EG$_2$ (**3**), PEG(5)NH$_2$ (**4**) and PEG(8)COOH (**5**) in their disulfide form were dissolved in D$_2$O, 0.3 M KCN in 0.1 M KOH (solvent D$_2$O) and with an excess of TCEP (solvent D$_2$O). Thiol forms of PEG(5)NH$_2$ (**4**) and PEG(8)COOH (**5**) were dissolved in D$_2$O and with an excess of TCEP (solvent D$_2$O).

4-5 mg Au of 2 nm core GNP (10 mg Au for 4 nm core GNP) were incubated with 600 μL of 0.3 M KCN in 0.1 M KOH (solvent D$_2$O) after having removed H$_2$O, either by exchange with D$_2$O using centrifugal ultrafiltration (Amicon 10 kDa filters) or freeze drying. Particles were incubated at 40 °C for 2 hours (80 °C for 6 hours for 4 nm core particles) with strong agitation to prevent pelleting (950 rpm) using Thermo Scientific Digital Heating Shaking Drybath. The complete etching was visually checked: transparent solution with no pellet.

4-5 mg Au of 2 nm core GNP were incubated with 1 mL of fresh 50-100 μM TCEP (solvent D$_2$O) after having removed H$_2$O, either by exchange with D$_2$O using centrifugal ultrafiltration (Amicon 10 kDa filters) or freeze drying. Particles were incubated at 50 °C overnight with strong agitation to prevent pelleting (950 rpm) using Thermo Scientific Digital Heating Shaking Drybath. The complete etching was visually checked: transparent solution with no pellet.

Experiments were performed at 298 K on a Bruker AVANCE III 500 spectrometer at CIC BiomaGUNE (San Sebastian, Spain) (500 MHz, $D_2O$). Data processing was performed using MestReNova 10.0.2.

### c. UHPLC-CAD-MS

Solvents used for the mobile phase were acetonitrile and $H_2O$ (Scharlab, LC-MS grade). Formic acid (Scharlab, LC-MS grade) was used to acidify the mobile phase. A commercial 0.5 M Tris(2-carboxyethyl)phosphine hydrochloride solution (aqueous solution; pH 7.0 adjusted with ammonium hydroxide, Sigma-Aldrich) was used to etch the particles.

For 2 nm GNP, the GNP amount equivalent to 450 μg of Au was incubated with 20 μL of a 0.5 M TCEP solution and $H_2O$ up to 1 mL. Mixing was carried out by vortexing. Particles were incubated at 40 °C for 2 hours with strong agitation to prevent pelleting (950 rpm) using Thermo Scientific Digital Heating Shaking Drybath. It was considered to have complete etching when, visually, a transparent solution with no pellet was attained.

For 4 nm GNP, the GNP amount equivalent to 350 μg of Au was incubated with 15 μL of 0.3 M KCN and 0.01 M KOH and $H_2O$ up to 190 μL. Mixing was carried out by vortexing. Particles were incubated at 80 °C for 10 minutes with strong agitation to prevent pelleting (950 rpm) using Thermo Scientific Digital Heating Shaking Drybath. It was considered to have complete etching when, visually, a transparent solution with no pellet was attained. To the etched solution, 10 μL of 0.05 M TCEP made from a commercial neutral 0.5 M solution was added.

Thermo UltiMate 3000 Rapid Separation Liquid Chromatography system comprising a dual gradient standard pump, Corona Veo RS CAD detector (Chromeleon 7.0 software) in line with LCQ Fleet Ion trap Mass Spectrometer detector (Xcalibur 2.2 SP1 software) and Thermo Viper tubing (0.13 mm ID) was used for all experiments.

Separations were performed on an Acquity UPLC BEH C18 column, 130 Å, (100 × 2.1 mm i.d., 1.7 μm particle size) and an Acquity UPLC BEH C18 VanGuard precolumn, 130 Å, (5 × 2.1 mm i.d., 1.7 μm particle size) (Waters).

Solvents used as mobile phase were as follows: A: 0.1 % formic acid in $H_2O$; B: 0.1 % formic acid in acetonitrile. Elution conditions applied were as follows: 0-0.5 min, 5 % B isocratic; 0.5-6 min, linear gradient 5-98 % B; 6-7 min, 98 % B isocratic; washing and reconditioning of the column.

Flow rate was 0.350 mL/min and injection volume 5 µL. The system operated at 35 ºC. The Corona Veo RS Evaporation temperature was set at 35 ºC; Power function: 1.0; Data collection Rate: 2 Hz; Signal Filter: 3.6 seconds. ESI-MS analysis was performed in the positive ion mode. Nitrogen was used as desolvation gas. The ESI parameters of the source were: capillary temperature 150 ºC, the source heater temperature was held at 45 ºC, a potential of 3.8 kV was used on the capillary for positive ion mode. MS spectra, within the m/z range 150–2000 amu, were obtained at 35 V cone voltage.

## 2. GNP Synthesis

### a. One-Pot ultrasmall GNP

Various bifunctional ultrasmall gold nanoparticles with a 2 nm core (**GNP-1** to **GNP-14**) were synthesized via a modified Brust–Schiffrin method, using a Syrris Atlas Potassium reactor with 100 mL/500 mL/1 L jacketed torispherical vessels. The reactions were carried out at 16-18 °C with fast stirring (750 rpm). Time, pH, and time and temperature were continuously monitored. $H_2O$ (Ultrapure, MilliQ) was the solvent used for both synthesis and purification. The different reagents were added from the top of the vessel within minutes (~ 15 min) using a 150-80-8 mm funnel.

$HAuCl_4 \cdot 3H_2O$ (1 equivalent, 0.1-5 g, Sigma-Aldrich) was added to an excess of disulfide ligands (β-Glucose-$C_2$, α-Galactose-$C_2$, PEG(5)$NH_2$, PEG(8)COOH or β-$N$-Acetyl-Glucosamine-$EG_2$, 0.75-1.5 equivalents, Galchimia, Acadechem and Wuxi AppTec). NaOH was used to adjust the pH (alkaline ~ 12). Freshly prepared $NaBH_4$ in excess (5-20 equivalents, aqueous or dissolved in 0.01-0.1 M NaOH, Sigma-Aldrich/Appli Chem) was quickly added to form the particles. During the nucleation, the gold concentration was 3-15 mM and the final volume of the reaction corresponded to 85 % of the reactor capacity.

After 0-2 hours, the purification was performed using 10 kDa Amicon 15-Ultra filters or a Repligen KR2i TFF system with D06-E005-05-N or D06-E010-05-N hollow fibers (5-10 kDa pore size). The final products were filtered with a 0.22 µm membrane, resuspended in $H_2O$ and stored in an amber glass vial at 4 °C.

**GNP-1**: $^1$H NMR (500 MHz, KCN/KOH, D$_2$O) α-Galactose-C$_2$ δ 4.99 (d, 1H, H-1, area: 1) and PEG(5)NH$_2$ δ 2.80 (t, 2H, -CH$_2$-NH$_2$, area: 2.01). Ratio: α-Galactose-C$_2$/PEG(5)NH$_2$ 50:50. $^1$H NMR (500 MHz, TCEP, D$_2$O) α-Galactose-C$_2$ δ=4.99 (m, 2H, H-5, H-4, area: 1) and PEG(5)NH$_2$ δ 3.21 (t, 2H, -CH$_2$-NH$_2$, area: 0.97). Ratio: α-Galactose-C$_2$/PEG(5)NH$_2$ 51:49.

**GNP-2**: $^1$H NMR (500 MHz, KCN/KOH, D$_2$O) α-Galactose-C$_2$ δ 4.99 (d, 1H, H-1, area: 1) and PEG(5)NH$_2$ δ 2.80 (t, 2H, -CH$_2$-NH$_2$, area: 1.95). Ratio: α-Galactose-C$_2$/PEG(5)NH$_2$ 51:49. $^1$H NMR (500 MHz, TCEP, D$_2$O) α-Galactose-C$_2$ δ 3.98 (m, 2H, H-5, H-4, area: 1) and PEG(5)NH$_2$ δ 3.20 (t, 2H, -CH$_2$-NH$_2$, area: 1.01). Ratio: α-Galactose-C$_2$/PEG(5)NH$_2$ 50:50.

**GNP-3**: $^1$H NMR (500 MHz, KCN/KOH, D$_2$O) α-Galactose-C$_2$ δ 4.99 (d, 1H, H-1, area: 1) and PEG(5)NH$_2$ δ 2.80 (t, 2H, -CH$_2$-NH$_2$, area: 1.96). Ratio: α-Galactose-C$_2$/PEG(5)NH$_2$ 51:49. $^1$H NMR (500 MHz, TCEP, D$_2$O) α-Galactose-C$_2$ δ 3.99 (m, 2H, H-5, H-4, area: 1) and PEG(5)NH$_2$ δ 3.21 (t, 2H, -CH$_2$-NH$_2$, area: 0.93). Ratio: α-Galactose-C$_2$/PEG(5)NH$_2$ 52:48.

**GNP-4**: $^1$H NMR (500 MHz, KCN/KOH, D$_2$O) α-Galactose-C$_2$ δ 4.99 (d, 1H, H-1, area: 1) and PEG(5)NH$_2$ δ 2.80 (t, 2H, -CH$_2$-NH$_2$, area: 1.29). Ratio: α-Galactose-C$_2$/PEG(5)NH$_2$ 61:39. $^1$H NMR (500 MHz, TCEP, D$_2$O) α-Galactose-C$_2$ δ 3.99 (m, 2H, H-5, H-4, area: 1) and PEG(5)NH$_2$ δ 3.21 (t, 2H, -CH$_2$-NH$_2$, area: 0.60). Ratio: α-Galactose-C$_2$/PEG(5)NH$_2$ 63:37.

**GNP-5**: $^1$H NMR (500 MHz, KCN/KOH, D$_2$O) α-Galactose-C$_2$ δ 4.99 (d, 1H, H-1, area: 1) and PEG(5)NH$_2$ δ 2.80 (t, 2H, -CH$_2$-NH$_2$, area: 3.00). Ratio: α-Galactose-C$_2$/PEG(5)NH$_2$ 40:60. $^1$H NMR (500 MHz, TCEP, D$_2$O) α-Galactose-C$_2$ δ 3.99 (m, 2H, H-5, H-4, area: 1) and PEG(5)NH$_2$ δ 3.21 (t, 2H, -CH$_2$-NH$_2$, area: 1.47). Ratio: α-Galactose-C$_2$/PEG(5)NH$_2$ 40:60.

**GNP-6**: $^1$H NMR (500 MHz, KCN/KOH, D$_2$O) β-Glucose-C$_2$ δ 4.50 (d, 1H, H-1, area: 0.93) and PEG(5)NH$_2$ δ 2.80 (t, 2H, -CH$_2$-NH$_2$, area: 2.89). Ratio: β-Glucose-C$_2$/PEG(5)NH$_2$ 39:61. $^1$H NMR (500 MHz, TCEP, D$_2$O) β-Glucose-C$_2$ δ 4.49 (d, 1H, H-1, area: 1) and PEG(5)NH$_2$ δ 3.21 (t, 2H, -CH$_2$-NH$_2$, area: 2.81). Ratio: β-Glucose-C$_2$/PEG(5)NH$_2$ 42:58.

**GNP-7**: $^1$H NMR (500 MHz, KCN/KOH, D$_2$O) β-Glucose-C$_2$ δ 4.50 (d, 1H, H-1, area: 1) and PEG(5)NH$_2$ δ 2.80 (t, 2H, -CH$_2$-NH$_2$, area. 1.97). Ratio: β-Glucose-C$_2$/PEG(5)NH$_2$ 50:50. $^1$H NMR (500 MHz, TCEP, D$_2$O) β-Glucose-C$_2$ δ 4.49 (d, 1H, H-1, area: 1) and PEG(5)NH$_2$ δ 3.21 (t, 2H, -CH$_2$-NH$_2$, area: 1.70). Ratio: β-Glucose-C$_2$/PEG(5)NH$_2$ 54:46.

**GNP-8**: $^1$H NMR (500 MHz, KCN/KOH, D$_2$O) β-Glucose-C$_2$ δ 4.50 (d, 1H, H-1, area: 1) and PEG(5)NH$_2$ δ 2.80 (t, 2H, -CH$_2$-NH$_2$, area: 4.35). Ratio: β-Glucose-C$_2$/PEG(5)NH$_2$ 31:69. $^1$H NMR (500 MHz, TCEP, D$_2$O) β-Glucose-C$_2$ δ 4.49 (d, 1H, H-1, area: 1) and PEG(5)NH$_2$ δ 3.21 (t, 2H, -CH$_2$-NH$_2$, area: 3.83). Ratio: β-Glucose-C$_2$/PEG(5)NH$_2$ 34:66. LC-CAD-MS: β-Glucose-C$_2$ (RT: 1.439 min; area: 0.739; m/z: 241, 467, 531) and PEG(5)NH$_2$ (RT: 4.781 min; area: 1.529; m/z: 298). Ratio: β-Glucose-C$_2$/PEG(5)NH$_2$ 37:63.

**GNP-9**: $^1$H NMR (500 MHz, KCN/KOH, D$_2$O) α-Galactose-C$_2$ δ 4.98 (d, 1H, H-1, area: 1) and PEG(8)COOH δ 2.47 (t, 2H, -CH$_2$-COOH, area: 2.21). Ratio: α-Galactose-C$_2$/ PEG(8)COOH 48:52. $^1$H NMR (500 MHz, TCEP, D$_2$O) α-Galactose-C$_2$ δ 3.98 (m, 2H, H-5, H-4, area: 1) and PEG(8)COOH δ 3.78 (t, 2H, -<u>CH$_2$</u>-CH$_2$-COOH, area: 0.94). Ratio: α-Galactose-C$_2$/PEG(8)COOH 52:48.

**GNP-10-a**: $^1$H NMR (500 MHz, KCN/KOH, D$_2$O) α-Galactose-C$_2$ δ 5.00 (d, 1H, H-1, area: 1) and PEG(8)COOH δ 2.49 (t, 2H, -CH$_2$-COOH, area: 1.92). Ratio: α-Galactose-C$_2$/ PEG(8)COOH 51:49. LC-CAD-MS: α-Galactose-C$_2$ (RT: 1.271 min; area: 2.202; m/z: 241, 380, 500, 534) and PEG(8)COOH (RT: 5.800 min; area: 3.295; m/z: 459, 476). Ratio: α-Galactose-C$_2$ /PEG(8)COOH 56:44.

**GNP-10-b**: $^1$H NMR (500 MHz, KCN/KOH, D$_2$O) α-Galactose-C$_2$ δ 4.99 (d, 1H, H-1, area: 1) and PEG(8)COOH δ 2.48 (t, 2H, -CH$_2$-COOH, area: 2.77). Ratio: α-Galactose-C$_2$/ PEG(8)COOH 42:58. LC-CAD-MS: α-Galactose-C$_2$ (RT: 1.246 min; area: 2.050; m/z: 241, 380, 500, 534) and PEG(8)COOH (RT: 5.775 min; area: 4.196; m/z: 459, 476). Ratio: α-Galactose-C$_2$ /PEG(8)COOH 48:52.

**GNP-11**: $^1$H NMR (500 MHz, KCN/KOH, D$_2$O) β-Glucose-C$_2$ δ 4.49 (d, 1H, H-1, area: 1) and PEG(8)COOH δ 2.48 (t, 2H, -CH$_2$-COOH, area: 2.57). Ratio: β-Glucose-C$_2$/PEG(8)COOH 44:56. LC-CAD-MS: β-Glucose-C$_2$ (RT: 1.397 min; area: 2.429; m/z: 241, 340, 544) and PEG(8)COOH (RT: 5.758 min; area: 5.334; m/z: 459, 476). Ratio: β-Glucose-C$_2$/PEG(8)COOH 47:53.

**GNP-12**: $^1$H NMR (500 MHz, KCN/KOH, D$_2$O) $\alpha$-Galactose-C$_2$ $\delta$ 4.99 (d, 1H, H-1, area: 1) and PEG(5)NH$_2$ $\delta$ 2.80 (t, 2H, -CH$_2$-NH$_2$, area: 2.07). Ratio: $\alpha$-Galactose-C$_2$/PEG(5)NH$_2$ 49:51. LC-CAD-MS: $\alpha$-Galactose-C$_2$ (RT: 1.246 min; area: 1.735; m/z: 241, 380, 555) and PEG(5)NH$_2$ (RT: 4.647 min; area: 2.652; m/z: 298) Ratio: $\alpha$-Galactose-C$_2$/PEG(5)NH$_2$ 45:55.

**GNP-13**: $^1$H NMR (500 MHz, KCN/KOH, D$_2$O) $\beta$-Glucose-C$_2$ $\delta$ 4.50 (d, 1H, H-1, area: 1) and PEG(5)NH$_2$ $\delta$ 2.80 (t, 2H, -CH$_2$-NH$_2$, 2.81). Ratio: $\beta$-Glucose-C$_2$/PEG(5)NH$_2$ 42:58. LC-CAD-MS: $\beta$-Glucose-C$_2$ (RT: 1.364 min; area: 0.806; m/z: 241, 380, 534) and PEG(5)NH$_2$ (RT: 4.655 min; area: 1.445; m/z: 298). Ratio: $\beta$-Glucose-C$_2$/PEG(5)NH$_2$ 41:59.

**GNP-14**: $^1$H NMR (500 MHz, KCN/KOH, D$_2$O) $\alpha$-Galactose-C$_2$ $\delta$ 5.00 (d, 1H, H-1, area: 1) and $\beta$-*N*-Acetyl-Glucosamine-EG$_2$ $\delta$ 4.58 (d, 1H, H-1, area: 1). Ratio: $\alpha$-Galactose-C$_2$/$\beta$-N-Acetyl-Glucosamine-EG$_2$ 50:50. LC-CAD-MS: $\alpha$-Galactose-C$_2$ (RT: 1.271 min; area: 2.304; m/z: 241, 385, 562) and $\beta$-*N*-Acetyl-Glucosamine-EG$_2$ (RT: 3.359 min; area: 2.911; m/z: 204, 326, 348, 668). Ratio: $\alpha$-Galactose-C$_2$/$\beta$-*N*-Acetyl-Glucosamine-EG$_2$ 52:48.

### b. Post-Functionalization

The amounts of reactants to perform the post-functionalization reactions were obtained using the following equations:

$$[Functional\ PEG]\ (mol/L) = \frac{[Au]\ (mol/L) * 44\ or\ 290\ ligands\ per\ core}{102\ or\ 2000\ Au\ atoms\ per\ core} * PEG\ Ratio\ in\ the\ formula$$

The concentration of functional PEG (mol/L) is estimated using the theoretical number of 44 ligands/102 Au atoms per GNP for a core size of 2 nm and 290 ligands/2000 Au atoms per GNP for a core size of 4 nm[74,75]. PEG ratio (0 to 1) is determined by ligand characterization ($^1$H NMR or LC-CAD-MS).

The amounts of the complementary building blocks are expressed based on the PEG amount and are calculated using the following equation:

$$Building\ Block\ (mg) = [Functional\ PEG]\ (mol/L) * Volume\ (ml) * Building\ Block\ MW\ (g/mol) * x\ Equivalents$$

Reactions were performed with gold concentrations varying from 2-7 mg/mL and amounts varying from 5 to 50 mg Au. After completion of the reaction, the purifications were performed using 10 kDa Amicon 15-Ultra filters. Samples were resuspended in H$_2$O and stored in amber glass vials at 4 °C.

- Azide route: **GNP-15**

EDC and Sulfo-NHS in excess (5 equivalents each, Sigma-Aldrich and Thermo-Fisher) were used to activate 6-azido-hexanoic acid (5 equivalents, Iris Biotech) in $H_2O$. The activated compound was added to GNP-13 ($\beta$-Glucose-$C_2$)$_{26}$(PEG(5)NH$_2$)$_{18}$@Au$_{102}$ in 10 mM PBS. The reaction was stirred overnight at room temperature and [Au] 3 mg/mL to obtain **GNP-15** with compound (**6**).

GNP-15: $^1$H NMR (500 MHz, KCN/KOH, $D_2O$) $\beta$-Glucose-$C_2$ $\delta$ 4.50 (d, 1H, H-1, area: 1), PEG(5)NH$_2$ $\delta$ 2.80 (t, 2H, -CH$_2$-NH$_2$: area: 0.55) and R-CO-$C_5H_{10}$-N$_3$ $\delta$ 2.32 (t, 2H, area: 1.91); 1.67 (m, 4H); 1.43 (tt, 2H). Ratio: $\beta$-Glucose-$C_2$/PEG(5)NH$_2$/R-CO-$C_5H_{10}$-N$_3$ 45:12:43.

LC-CAD-MS: $\beta$-Glucose-$C_2$ (RT: 1.423  min; area: 1.797; m/z: 241, 467), PEG(5)NH$_2$ (RT: 4.739 min; area: 0.629; m/z: 298) and R-CO-$C_5H_{10}$-N$_3$ (RT: 6.575 min; area: 2.408; m/z: 437, 454). Ratio: $\beta$-Glucose-$C_2$/PEG(5)NH$_2$/R-CO-$C_5H_{10}$-N$_3$ 50:14:36.

- Succinic anhydride route: **GNP-16**

An excess of succinic anhydride (20 equivalents, Sigma-Aldrich) in DMSO was added to GNP-13 in 0.1 M sodium bicarbonate (NaHCO$_3$). The reaction was stirred overnight at room temperature and [Au] 5 mg/mL to obtain **GNP-16** with compound (**7**).

**GNP-16**: $^1$H NMR (500 MHz, KCN/KOH, $D_2O$) $\beta$-Glucose-$C_2$ $\delta$ 4.49 (d, 1H, H-1, area: 1), PEG(5)NH$_2$ $\delta$ 2.83 (t, 2H, -CH$_2$-NH$_2$, area: 0.34) and R-CO-$C_2H_4$-COOH $\delta$ 2.50 (m, 4H, area: 4.31). Ratio: $\beta$-Glucose-$C_2$/PEG(5)NH$_2$/R-CO-$C_2H_4$-COOH 44:8:48.

LC-CAD-MS: $\beta$-Glucose-$C_2$ (RT: 1.422  min; area: 1.838; m/z: 241, 467), PEG(5)NH$_2$ (RT: 4.739 min; area: 0.382; m/z: 298) and R-CO-$C_2H_4$-COOH (RT: 5.413 min; area: 3.041; m/z: 398, 414). Ratio: $\beta$-Glucose-$C_2$/PEG(5)NH$_2$/R-CO-$C_2H_4$-COOH 46:8:46.

- Acetamide protection route: **GNP-17**

An excess of Sulfo-NHS-Acetate (5 equivalents, Thermo-Fisher) in 10 mM PBS was added to GNP-13 in $H_2O$. The reaction was stirred overnight at room temperature and [Au] 7 mg/mL to obtain **GNP-17** with compound (**8**).

**GNP-17**: [^1]H NMR (500 MHz, KCN/KOH, $D_2O$) β-Glucose-$C_2$ δ 4.50 (d, 1H, H-1, area: 1), PEG(5)$NH_2$ δ 2.80 (t, 2H, -$CH_2$-$NH_2$, area: 0.17) and PEG(5)-NH-Ac δ 2.02 (s, 3H, area: 3.51). Ratio: β-Glucose-$C_2$/PEG(5)$NH_2$/PEG(5)-NH-Ac 44:4:52.

LC-CAD-MS: β-Glucose-$C_2$ (RT: 1.364 min; area: 1.988; m/z: 241, 260, 380, 440, 544), PEG(5)$NH_2$ (RT: 4.664 min; area :0.191; m/z: 298) and PEG(5)-NH-Ac (RT: 5.363 min; area: 3.156; m/z: 340, 357). Ratio: β-Glucose-$C_2$/PEG(5)$NH_2$/PEG(5)-NH-Ac 45:4:51.

- Amine GNP and carboxylic acid monosaccharide route: **GNP-18** and **GNP-19**

EDC and Sulfo-NHS in excess (5 equivalents each, Sigma-Aldrich and Thermo-Fisher) were used to activate either 2-Carboxyethyl α-D-mannopyranoside (3 equivalents, M233-034-1) or 4-Carboxybutyl β-D-galactopyranoside (3 equivalents, Iris Biotech) in $H_2O$. The activated compounds were added to GNP-13 in 10 mM PBS. The reactions were stirred overnight at room temperature and [Au] 3 mg/mL, then stopped by centrifugal ultrafiltration. After resuspension of the GNP in $H_2O$, **GNP-18** with compound (**9,** α-Mannose) and **GNP-19** with compound (**10**, β-Galactose) were obtained. A second step of post-functionalization to protect the residual amine groups of the two GNP was performed using an excess of Sulfo-NHS-Acetate (5 equivalents, Thermo-Fisher) in 10 mM PBS. The reactions were stirred overnight at room temperature and [Au] 7 mg/mL to obtain compound (**8,** acetamide) on both **GNP-18** and **GNP-19**.

**GNP-18**: [^1]H NMR (500 MHz, KCN/KOH, $D_2O$) β-Glucose-$C_2$ δ 4.50 (d, 1H, H-1, area: 1), PEG(5)$NH_2$ δ 2.81 (t, 2H, -$CH_2$-$NH_2$, area: 0.21), α-Mannose-$C_2H_4$-CO-R δ 4.86 (d, 1H, H-1, area: 0.84) and PEG(5)-NH-Ac δ 2.02 (s, 3H, area: 0.63). Ratio: β-Glucose-$C_2$/PEG(5)$NH_2$/ α-Mannose-$C_2H_4$-CO-R/PEG(5)-NH-Ac 46:5:39:10.

LC-CAD-MS: β-Glucose-$C_2$ (RT: 1.363 min; area: 1.852; m/z: 241, 544), PEG(5)$NH_2$ (RT: 4.663 min; area: 0.080; m/z: 298), α-Mannose-$C_2H_4$-CO-R (RT: 5.059 min; area: 3.263; m/z: 532, 549) and PEG(5)-NH-Ac (RT: 5.362 min; area: 0.743; m/z: 340, 357). Ratio: β-Glucose-$C_2$/PEG(5)$NH_2$/α-Mannose-$C_2H_4$-CO-R/PEG(5)-NH-Ac 47:2:38:13.

**GNP-19**: ^{1}H NMR (500 MHz, KCN/KOH, D$_2$O) β-Glucose-C$_2$ δ 4.50 (d, 1H, H-1, area: 1), PEG(5)NH$_2$ δ 2.80 (t, 2H, -CH$_2$-NH$_2$, area: 0.14), β-Galactose-C$_4$H$_8$-CO-R δ 4.40 (d, 1H, H-1, area: 1.13) and PEG(5)-NH-Ac δ 2.02 (s, 3H, area: 0.29). Ratio: β-Glucose-C$_2$/PEG(5)NH$_2$/β-Galactose-C$_4$H$_8$-CO-R/PEG(5)-NH-Ac 44:3:49:4.

LC-CAD-MS: β-Glucose-C$_2$ (RT: 1.364 min; area: 1.874; m/z: 241, 280, 368, 534), PEG(5)NH$_2$ (RT: 4.680 min; area: 0.058; m/z: 298), β-Galactose-C$_4$H$_8$-CO-R (RT: 5.135 min; area: 3.597; m/z: 560, 577) and PEG(5)-NH-Ac (RT: 5.362 min; area: 0.423; m/z: 340, 357). Ratio: β-Glucose-C$_2$/PEG(5)NH$_2$/β-Galactose-C$_4$H$_8$-CO-R/PEG(5)-NH-Ac 50:1:41:8.

- ▪ Amino-oxy GNP and oligosaccharide route: **GNP-20**, **GNP-21**, **GNP-22** and **GNP-23**

An excess of (Boc-aminooxy)acetic acid (5 equivalents, Sigma-Aldrich) was added to a mixture of EDC/NHS (3 equivalents each, Sigma-Aldrich) in DMSO. The activated compound was added to GNP-8 (β-Glucose-C$_2$)$_{30}$(PEG(5)NH$_2$)$_{14}$@Au$_{102}$ in DMSO. The reaction was stirred overnight at room temperature and [Au] 5 mg/mL to obtain the intermediate tert-butyloxycarbonyl protected amino-oxy GNP: **GNP-20** with compound (**11**). A 1:3 DMSO/H$_2$O solution was used for purification and storage.

Tert-butyloxycarbonyl was cleaved in pure trifluoracetic acid (Merck) after removal of the solvent by centrifugal ultrafiltration. The reaction was stirred for 3 hours at room temperature and [Au] 5 mg/mL. The mixture was diluted in H$_2$O and then purified to obtain the second intermediate product, the amino-oxy GNP (this material was not characterized as it was too unstable).

Immediately after deprotection, and assuming a 100 % yield of functionalization during the previous steps for calculation for the equivalents, either 5 equivalents of α-mannose1,2-α-mannose (Carbosynth), 1,3-α-1,6-α-D-mannotriose (Carbosynth) or maltotriose (Merck) were added to the amino-oxy GNP with 3 % aqueous acetic acid and a catalytic amount of aniline (Sigma-Aldrich). The reactions were stirred overnight at room temperature and [Au] 5 mg/mL to obtain **GNP-21** with compound (**12**, α-Mannose1,2-α-mannose), **GNP-22** with compound (**13**, 1,3-α-1,6-α-D-Mannotriose) and **GNP-23** with compound (**14**, Maltotriose).

**GNP-20**: $^1$H NMR (500 MHz, D$_2$O) β-Glucose-C$_2$ δ 4.49 (d, 1H, H-1, area: 1); 3.94 (dd, 1H); 3.26 (dd, 1H), PEG(5)NH$_2$ δ 2.82 (t, 2H, -CH$_2$-NH$_2$: area: 0.76) and Boc-NH-O-CH$_2$-CO-R δ 1.39 (s, 9H, area: 9.03). Ratio: β-Glucose-C$_2$/PEG(5)NH$_2$/Boc-NH-O-CH$_2$-CO-R 42:16:42. LC-CAD-MS: β-Glucose-C$_2$ (RT: 1.381 min; area: 0.937; m/z: 241, 318, 385, 555), PEG(5)NH$_2$ (RT: 4.782 min; area: 0.111; m/z: 298) and Boc-NH-O-CH$_2$-CO-R peak (RT: 6.474 min; area: 1.126; m/z: 471, 488, 516). Ratio: β-Glucose-C$_2$/PEG(5)NH$_2$/Boc-NH-O-CH$_2$-CO-R 58:6:36.

**GNP-21**: LC-CAD-MS: β-Glucose-C$_2$ (RT: 1.423 min; area: 0.736; m/z 241, 260, 531), PEG(5)NH$_2$ (RT: 4.791 min; area: 0.196; m/z: 298) and α-Mannose1,2-α-mannose-R (RT: 5.001 min; area: 1.472; m/z: 695, 712, 717). Ratio: β-Glucose-C$_2$/PEG(5)NH$_2$/ α-Mannose1,2-α-mannose-R 52:11:37.

**GNP-22**: LC-CAD-MS: β-Glucose-C$_2$ (RT: 1.422 min; area: 0.903; m/z: 241, 380, 544), PEG(5)NH$_2$ (RT: 4.790 min; area: 0.242; m/z 298) and 1,3-α-1,6-α-D-Mannotriose-R (RT: 4.950 min; area: 1.714; m/z: 857, 874, 1120). Ratio: β-Glucose-C$_2$/PEG(5)NH$_2$/ 1,3-α-1,6-α-D-Mannotriose-R 57:12:31.

**GNP-23**: LC-CAD-MS: β-Glucose-C$_2$ (RT: 1.389 min; area: 1.088; m/z: 241, 260, 467), PEG(5)NH$_2$ (RT: 4.781 min; area: 0.316; m/z: 298) and Maltotriose-R (RT: 4.983 min; area: 2.174; m/z: 857, 874, 1121). Ratio: β-Glucose-C$_2$/PEG(5)NH$_2$/Maltotriose-R 56:13:31.

- Carboxylic acid GNP and methyl-ester protection route: **GNP-24**

GNP-10 (α-Galactose-C$_2$)$_{22-26}$(PEG(8)COOH)$_{22-18}$@Au$_{102}$ was incubated in methanol (Sigma-Aldrich) with 2 % sulfuric Acid (H$_2$SO$_4$, Scharlau). The flask was put in ice and the reaction was stirred overnight with [Au] 5 mg/mL. The reaction was quenched by 0.1 M NaHCO$_3$ to obtain **GNP-24** with compound (**15**).

**GNP-24**: $^1$H NMR (500 MHz, KCN/KOH, D$_2$O) α-Galactose-C$_2$ δ 5.00 (d, 1H, H-1, area: 1); 4.00 (m, 2H), PEG(8)COOH δ 2.49 (t, 2H, -CH$_2$-COOH, area: 1.80) and MeOH δ 3.37 (s, 3H, area: 2.96). Ratio: α-Galactose-C$_2$/PEG(8)COOH/-COOMe 50:0:50. LC-CAD-MS: α-Galactose-C$_2$ peak (RT: 1.271 min; area: 2.132; m/z: 241, 393, 500), PEG(8)COOH (RT: 5.758 min; area: 0.207; m/z: 459, 476) and -COOMe (RT: 6.204 min; area: 3.234; m/z: 413, 473, 490). Ratio: α-Galactose-C$_2$/PEG(8)COOH/-COOMe 55:3:42.

- Carboxylic acid GNP and ethanolamine (hydroxyl) protection route: **GNP-25**

EDC and Sulfo-NHS in excess (3 equivalents each, Sigma-Aldrich and Thermo-Fisher) in $H_2O$ were used to activate the PEG(8)COOH of GNP-10 for 2 hours. A purification was performed with 10 kDa Amicon Ultra filters to remove the excess of coupling reagents and the activated GNP was resuspended in 10 mM PBS. Ethanolamine (5 equivalents, Sigma-Aldrich) in 10 mM PBS and sufficient 1 % hydrochloric acid (HCl, Fisher) to obtain a neutral pH were quickly added to the activated particle. The reaction was stirred overnight at room temperature and [Au] 5 mg/mL to obtain **GNP-25** with compound (**16**).

**GNP-25**: $^1$H NMR (500 MHz, KCN/KOH, $D_2O$) α-Galactose-$C_2$ δ 5.00 (d, 1H, H-1, area: 1), PEG(8)COOH δ 2.51 (t, 2H, -$CH_2$-COOH, area: 0.39) and OH-$C_2H_4$-NH-R δ 3.37 (t, 2H, area: 1.15). Ratio: α-Galactose-$C_2$/PEG(8)COOH/OH-$C_2H_4$-NH-R 56:11:32.
LC-CAD-MS: α-Galactose-$C_2$ (RT: 1.280    min; area: 2.185; m/z: 241, 380, 500), PEG(8)COOH (RT: 5.791 min; area: 0.958; m/z: 459, 476) and OH-$C_2H_4$-NH-R (RT: 5.497 min; area: 3.409; m/z: 502, 519). Ratio: α-Galactose-$C_2$/PEG(8)COOH/OH-$C_2H_4$-NH-R 51:11:38.

- Carboxylic acid GNP and amine monosaccharide route: **GNP-26**, **GNP-27** and **GNP-28**

EDC and Sulfo-NHS in excess (3 equivalents each, Sigma-Aldrich and Thermo-Fisher) in $H_2O$ were used to activate the PEG(8)COOH of GNP-10 for 2 hours. A purification was performed with 10 kDa Amicon Ultra filters to remove the excess of coupling reagents and the activated GNP was resuspended in 10 mM PBS. Either 2-Aminoethyl α-D-mannopyranoside (3 equivalents, M216-040-1), 2-Aminoethyl α-D-mannopyranosyl-(1,2)-D-mannopyranoside (3 equivalents, ADM552, CSIC Sevilla) and 2-Aminoethyl β-D-galactopyranoside (3 equivalents, ADM557, CSIC Sevilla) in 10 mM PBS were quickly added to the activated particle. The reactions were stirred overnight at room temperature and [Au] 2-5 mg/mL. The products were purified by centrifugal ultrafiltration to obtain **GNP-26** with compound (**17**, α-Mannose), **GNP-27** with compound (**18**, α-Mannose1,2α-Mannose) and **GNP-28** with compound (**19**, β-Galactose), respectively.

**GNP-26**: $^1$H NMR (500 MHz, KCN/KOH, D$_2$O) $\alpha$-Galactose-C$_2$ $\delta$ 5.00 (d, 1H, H-1, area: 1); 3.99 (m, 2H), PEG(8)COOH $\delta$ 2.49 (t, 2H, -CH$_2$-COOH, area: 1.71) and $\alpha$-Mannose-C$_2$H$_4$-NH-R $\delta$ 4.88 (d, 1H, H-1, area: 0.53). Ratio: $\alpha$-Galactose-C$_2$/PEG(8)COOH/$\alpha$-Mannose-C$_2$H$_4$-NH-R 42:36:22. LC-CAD-MS: $\alpha$-Galactose-C$_2$ (RT: 1.263 min; area: 1.820; m/z: 241, 380, 534), PEG(8)COOH (RT: 5.775 min; area: 2.528; m/z: 459, 476) and $\alpha$-Mannose-C$_2$H$_4$-NH-R (RT: 5.328 min; area: 2.541; m/z: 664, 681). Ratio: $\alpha$-Galactose-C$_2$/PEG(8)COOH/ $\alpha$-Mannose-C$_2$H$_4$-NH-R 45:33:22.

**GNP-27**: $^1$H NMR (500 MHz, KCN/KOH, D$_2$O) $\alpha$-Galactose-C$_2$ $\delta$ 5.00 (d, 1H, H-1, area: 1), PEG(8)COOH $\delta$ 2.49 (t, 2H, -CH$_2$-COOH, area: 0.81) and $\alpha$-Mannose1,2$\alpha$-Mannose-C$_2$H$_4$-NH-R $\delta$ 5.13 (d, 1H, area: 0.51); $\delta$ 5.05 (d, 1H). Ratio: $\alpha$-Galactose-C$_2$/PEG(8)COOH/ $\alpha$-Mannose1,2$\alpha$-Mannose-C$_2$H$_4$-NH-R 52:21:27. LC-CAD-MS: $\alpha$-Galactose-C$_2$ (RT: 1.271 min; area: 1.678; m/z: 241, 380, 500), PEG(8)COOH (RT: 5.800 min; area: 1.201; m/z:459, 476) and $\alpha$-Mannose1,2-$\alpha$-Mannose-C$_2$H$_4$-NH-CO-R (RT: 5.269 min; area: 2.437; m/z: 433, 826, 843, 910, 1258). Ratio: $\alpha$-Galactose-C$_2$/PEG(8)COOH$\alpha$-Mannose1,2$\alpha$-Mannose-C$_2$H$_4$-NH-R 56:21:23.

**GNP-28**: $^1$H NMR (500 MHz, KCN/KOH, D$_2$O) $\alpha$-Galactose-C$_2$ $\delta$ 5.00 (d, 1H, H-1, area: 1); 4.00 (m, 2H), PEG(8)COOH $\delta$ 2.50 (t, 2H, -CH$_2$-COOH, area: 0.86) and $\beta$-Galactose-C$_2$H$_4$-NH-R $\delta$ 4.43 (d, 1H, H-1, area: 0.49). Ratio: $\alpha$-Galactose-C$_2$/PEG(8)COOH/$\beta$-Galactose-C$_2$H$_4$-NH-R 52:22:26. LC-CAD-MS: $\alpha$-Galactose-C$_2$ (RT:1.279 min; area: 2.000; m/z: 241, 380, 529, 565), PEG(8)COOH (RT: 5.800 min; area: 1.426; m/z: 459, 476) and $\beta$-Galactose-C$_2$H$_4$-NH-R (RT: 5.312 min; area: 2.381; m/z: 352, 664, 681). Ratio: $\alpha$-Galactose-C$_2$/PEG(8)COOH/$\beta$-Galactose-C$_2$H$_4$-NH-R 55:21:24.

# VI. Annex

*Table 11: Ligand retention times and m/z obtained by LC-CAD-MS. Disulfide peaks are obtained in H2O and the thiols by incubation of the formers with TCEP.*

| TCEP Peaks | RT (min) | MS m/z |
|---|---|---|
| TCEP reduced (TCEP) | 0.968 | **251** |
| TCEP oxidized (TCEP=O) | 1.094 | **267** |
| TCEP Derivative I (in H2O) | 1.473 | 223, 445, 467, 473, 511 |
| Au[TCEP]2 | 1.759 | **697** |
| TCEP Derivative II (with GNP) | 4.041 | 251, 283, 618, 697 |

| (**1**) β-Glucose-C2 | RT (min) | MS m/z |
|---|---|---|
| β-Glucose-C2-SS | 3.460 | 279, 320, **479**, 496, 641, 737, 957, 976 |
| β-Glucose-C2-SH | 1.372 | **241**, 335, 420, 544, 582 |

| (**2**) α-Galactose-C2 | RT (min) | MS m/z |
|---|---|---|
| α-Galactose-SS | 2.130 | 279, 317, **479**, 496, 641, 737, 957, 976 |
| α-Galactose-SH | 1.254 | **241**, 380, 408, 500, 529, 565 |
| α-Galactose-SH degradation product (*see Chapter I*) | 1.423 | 245, 688, 695 |

| (**3**) β-*N*-Acetyl-Glucosamine-EG2 | RT (min) | MS m/z |
|---|---|---|
| β-*N*-Acetyl-Glucosamine-EG2-SS | 4.731 | 204, 344, 446, **649**, 666, 992, 1013 |
| β-*N*-Acetyl-Glucosamine-EG2-SH | 3.367 | 204, **326**, 348, 668 |

| (**4**) PEG(5)NH2 | RT (min) | MS m/z |
|---|---|---|
| PEG(5)NH2-SS | 5.010 | 298, **593** |
| PEG(5)NH2-SH | 4.781 | **298** |

| (**5**) PEG(8)COOH | RT (min) | MS m/z |
|---|---|---|
| PEG(8)COOH-SS | 6.179 | 458, 467, 477, **915**, 932, 954 |
| PEG(8)COOH-SH | 6.061 | **459**, 476 |
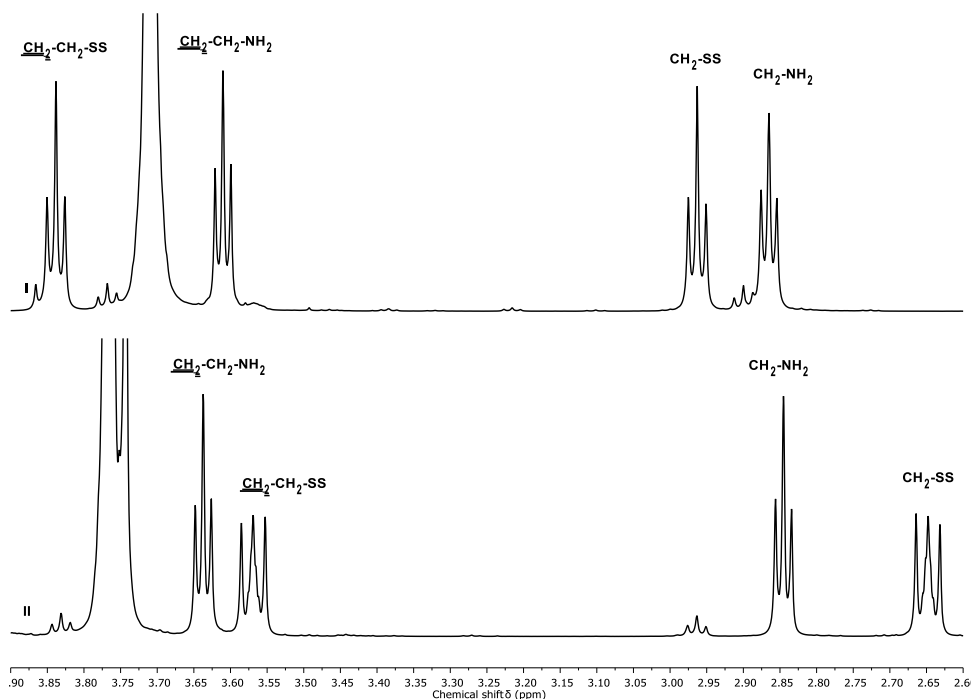
*Figure 23: $^1H$ NMR (500 MHz, $D_2O$) of PEG(5)NH₂-SS disulfide in (I) $D_2O$ and (II) KCN/KOH. -CH₂-NH₂ and -CH₂-CH₂-NH₂ protons remained relatively unaffected by KCN/KOH with a shift from $\delta 2.87$ (t, 2H) and $\delta 3.61$ (t, 2H) to $\delta 2.85$ (t, 2H) and $\delta 3.64$ (t, 2H), respectively. -CH₂-SS and -CH₂-CH₂-SS protons are displaced by KCN/KOH with a shift from $\delta 2.96$ (t, 2H) and $\delta 3.84$ (t, 2H) to $\delta 2.65$ (m, 2H) and $\delta 3.57$ (m, 2H), respectively.*



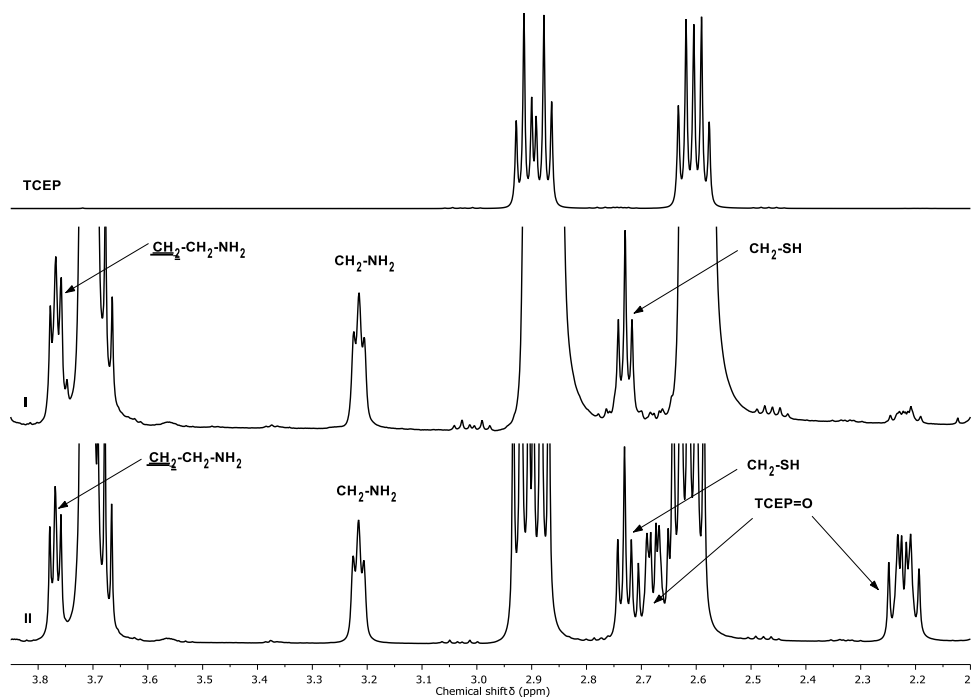*Figure 24: $^1H$ NMR (500 MHz, $D_2O$) of (I) TCEP in $D_2O$, (II) PEG(5)NH₂-SH thiol in TCEP and (III) PEG(5)NH₂-SS disulfide in TCEP. TCEP signals are present at $\delta 2.90$ (dt, 6H, -CH₂-P) and $\delta 2.60$ (dt, 6H, -CH₂-COOH). PEG(5)NH₂ -CH₂-NH₂ and -CH₂-CH₂-NH₂ protons have a shift of $\delta 3.21$ (t, 2H) and $\delta 3.77$ (t, 2H), respectively. -CH₂-SH protons are visible with a shift of $\delta 2.73$ (t, 2H) for both the thiol and the disulfide compounds with the same relative area. That confirms the capacity of TCEP to completely reduce disulfides into thiols. TCEP=O signals appear on the disulfide spectrum due the consumption of TCEP for the reduction of PEG(5)NH₂-SS at $\delta 2.68$ (dt, 6H, -CH₂-P) and $\delta 2.22$ (dt, 6H, -CH₂-COOH).*
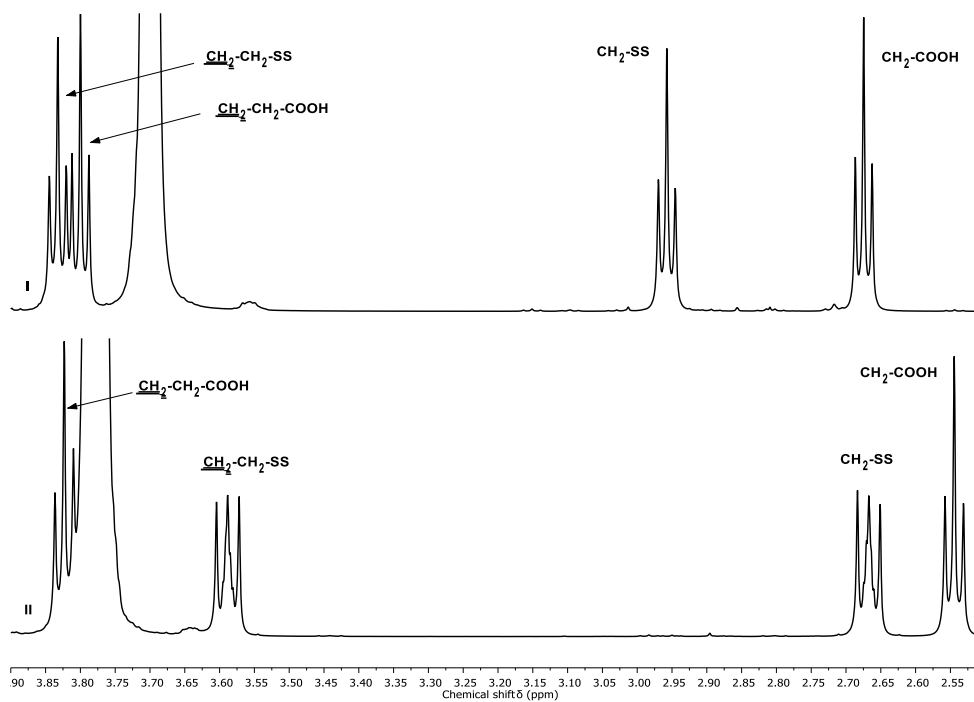
*Figure 25: ^{1}H NMR (500 MHz, D$_2$O) of (I) PEG(8)COOH-SS disulfide in (I) D$_2$O and (II) KCN/KOH. -CH$_2$-COOH and -CH$_2$-CH$_2$-COOH protons are slightly displaced by KCN/KOH with a shift from $\delta$ 2.67 (t, 2H) and $\delta$ 3.80 (t, 2H) to $\delta$ 2.54 (t, 2H) and $\delta$ 3.82 (t, 2H), respectively. -CH$_2$-SS and -CH$_2$-CH$_2$-SS protons are displaced by KCN/KOH with a shift from $\delta$ 2.96 (t, 2H) and $\delta$ 3.83 (t, 2H) to $\delta$ 2.67 (m, 2H) and $\delta$ 3.59 (m, 2H), respectively.*



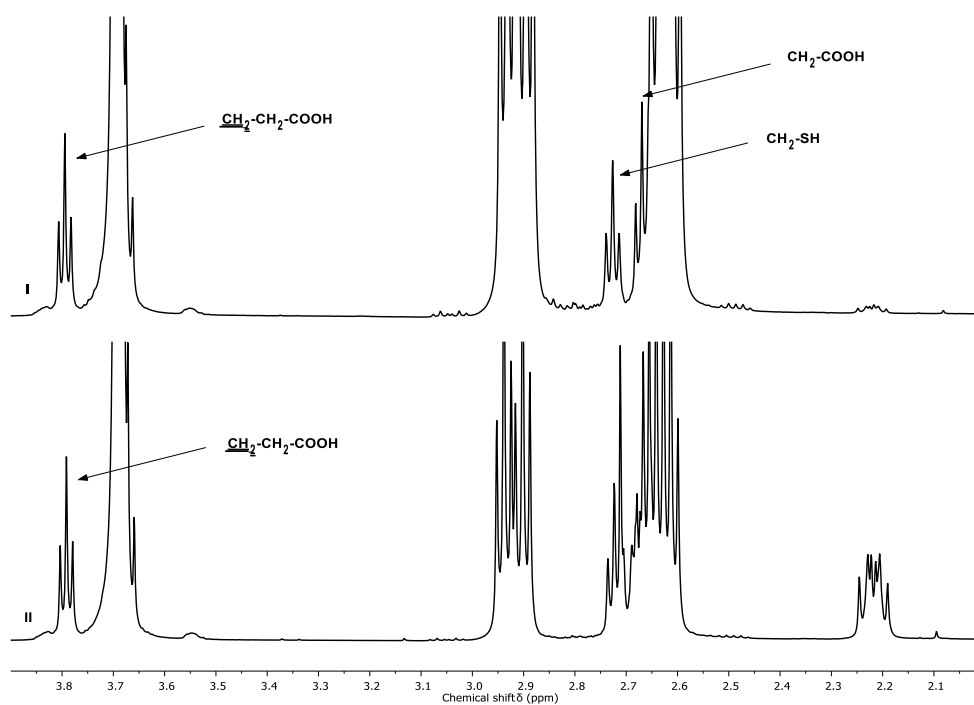*Figure 26: ^{1}H NMR (500 MHz, D$_2$O) of (I) PEG(8)COOH-SH thiol and (II) PEG(5)COOH-SS disulfide in TCEP. -CH$_2$-CH$_2$-COOH protons have a shift of $\delta$ 3.79 (t, 2H). -CH$_2$-SH protons are resolved with a shift of $\delta$ 2.73 (t, 2H) for the thiol but not for the disulfide (masked by TCEP=O). -CH$_2$-COOH $\delta$ 2.68 (t, 2H) is masked by TCEP and TCEP=O.*

*Figure 27: $^1$H NMR (500 MHz, $D_2O$) of $\alpha$-Galactose-$C_2$-SS disulfide in (I) $D_2O$, (II) KCN/KOH and (III) TCEP. The anomeric proton H-1 is relatively unaffected by KCN/KOH and TCEP with a shift from $\delta$ 4.99 (d, 1H) to $\delta$ 5.03 (d, 1H) and $\delta$ 4.98 (d, 1H), respectively. Although, with TCEP, the $D_2O$ peak prevents from proper integration of the H-1 peak. H-4 and H-5 $\delta$ 3.99 (m, 2H) are well resolved. -$CH_2$-SS is displaced by KCN/KOH with a shift from $\delta$ 3.02 (t, 2H) to $\delta$ 2.71 (m, 2H). -$CH_2$-SH is visible with TCEP $\delta$ 2.78 (q, 2H).*



*Figure 28: $^1$H NMR (500 MHz, $D_2O$) of $\beta$-Glucose-$C_2$-SS disulfide in (I) $D_2O$, (II) KCN/KOH and (III) TCEP. The anomeric proton H-1 is relatively unaffected by KCN/KOH and TCEP with a shift from $\delta$ 4.50 (d, 1H) to $\delta$ 4.52 (d, 1H) and $\delta$ 4.49 (d, 1H), respectively. H-2 is unaffected $\delta$ 3.28 (dd, 1H). -$CH_2$-SS is displaced by KCN/KOH with a shift from $\delta$ 3.01 (td, 2H) to $\delta$ 2.69 (m, 2H). -$CH_2$-SH is visible with TCEP $\delta$ 2.76 (t, 2H).*
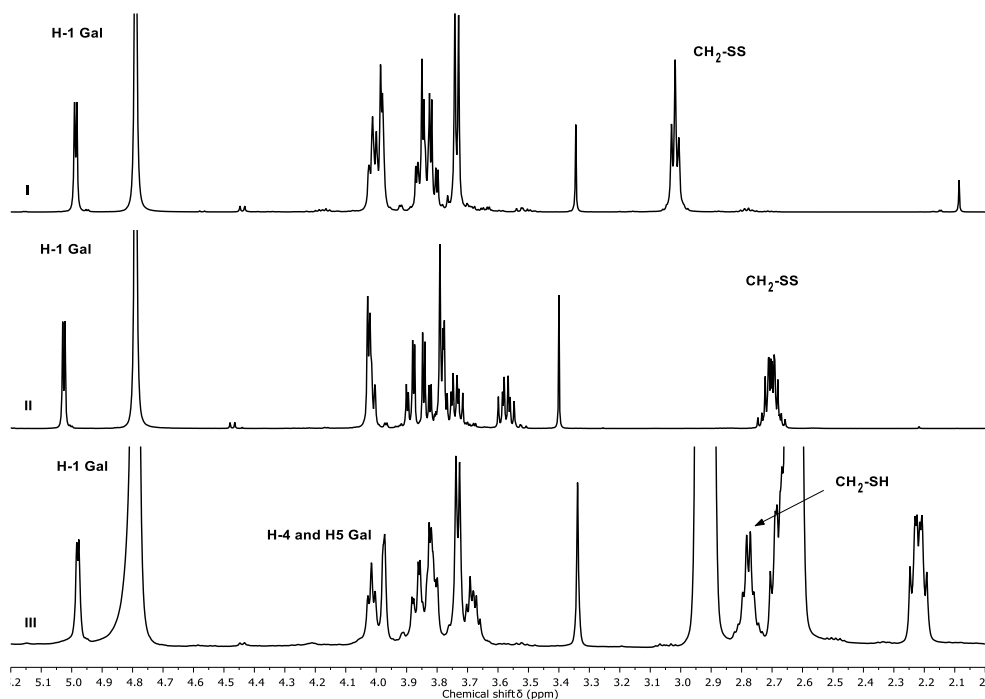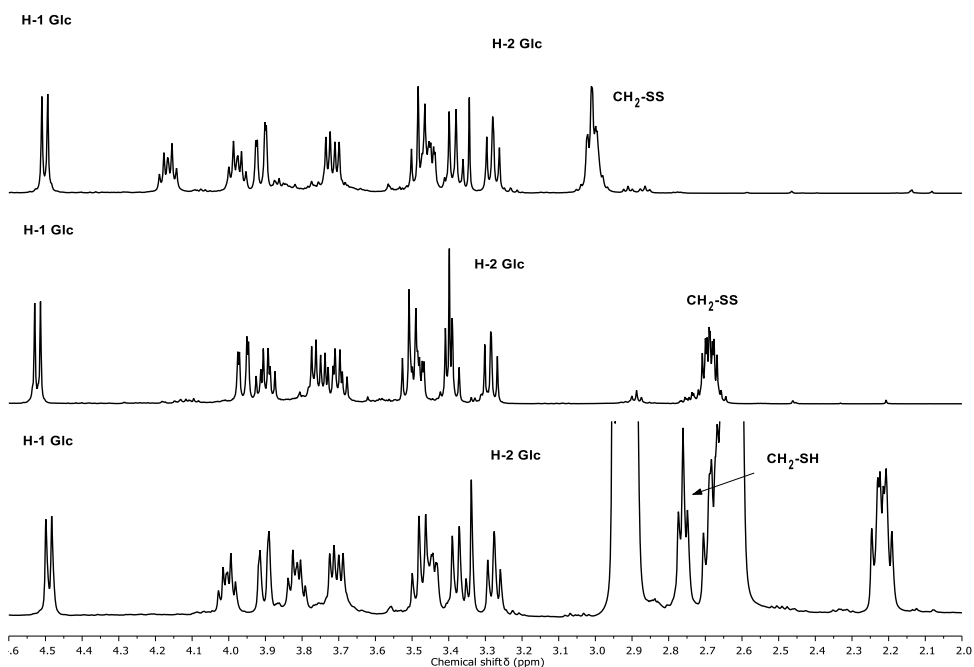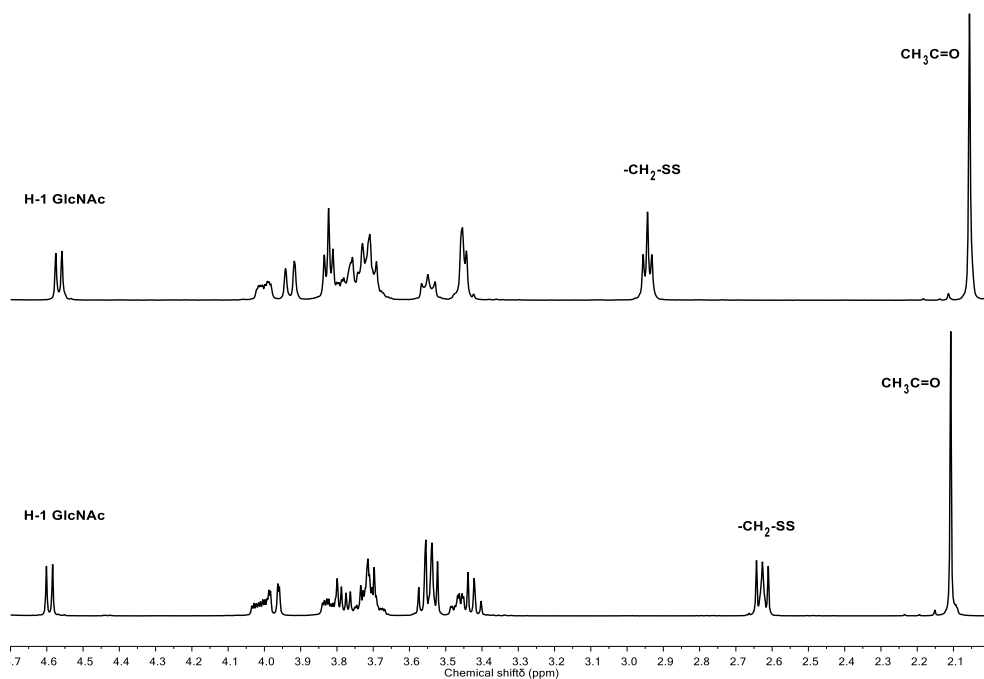
*Figure 29: ¹H NMR (500 MHz, D₂O) of β-N-Acetyl-Glucosamine-EG₂-SS disulfide in (I) D₂O and (II) KCN/KOH. The anomeric proton H-1 is relatively unaffected by KCN/KOH with a shift from δ 4.57 (d, 1H) to δ 4.59 (d, 1H). -CH₂-SS is displaced by KCN/KOH with a shift from δ 2.94 (td, 2H) to δ 2.63 (m, 2H). -CH₃=CO is visible with a shift by KCN/KOH from δ 2.06 (s, 3H) to δ 2.11 (s, 3H).*

# VII.  References

1.  ICH Official web site: ICH. https://www.ich.org/page/quality-guidelines.

2.  Mourdikoudis, S., Pallares, R. M. & Thanh, N. T. K. Characterization techniques for nanoparticles: comparison and complementarity upon studying nanoparticle properties. *Nanoscale* **10**, 12871–12934 (2018).

3.  Smith, A. M., Johnston, K. A., Crawford, S. E., Marbella, L. E. & Millstone, J. E. Ligand density quantification on colloidal inorganic nanoparticles. *Analyst* **142**, 11–29 (2016).

4.  Kumar, A. & Dixit, C. K. 3 - Methods for characterization of nanoparticles. in *Advances in Nanomedicine for the Delivery of Therapeutic Nucleic Acids* 43–58 (Woodhead Publishing, 2017).

5.  Colangelo, E. *et al.* Characterizing Self-Assembled Monolayers on Gold Nanoparticles. *Bioconjug. Chem.* **28**, 11–22 (2017).

6.  Zhang, J., Li, Z., Zheng, K. & Li, G. Synthesis and characterization of size-controlled atomically precise gold clusters. *Phys. Sci. Rev.* **3**, (2018).

7.  Lin, P.-C., Lin, S., Wang, P. C. & Sridhar, R. Techniques for physicochemical characterization of nanomaterials. *Biotechnol. Adv.* **32**, 711–726 (2014).

8.  Sapsford, K. E., Tyner, K. M., Dair, B. J., Deschamps, J. R. & Medintz, I. L. Analyzing nanomaterial bioconjugates: a review of current and emerging purification and characterization techniques. *Anal. Chem.* **83**, 4453–4488 (2011).

9.  Marbella, L. E. & Millstone, J. E. NMR Techniques for Noble Metal Nanoparticles. *Chem. Mater.* **27**, 2721–2739 (2015).

10. Liu, X., Yu, M., Kim, H., Mameli, M. & Stellacci, F. Determination of monolayer-protected gold nanoparticle ligand–shell morphology using NMR. *Nat. Commun.* **3**, 1182 (2012).

11. Wu, M. *et al.* Solution NMR Analysis of Ligand Environment in Quaternary Ammonium-Terminated Self-Assembled Monolayers on Gold Nanoparticles: The Effect of Surface Curvature and Ligand Structure. *J. Am. Chem. Soc.* **141**, 4316–4327 (2019).

12. Riccardi, L. *et al.* Nanoparticle-Based Receptors Mimic Protein-Ligand Recognition. *Chem* **3**, 92–109 (2017).

13.    Santos, J. I. *et al.* Assessing Carbohydrate–Carbohydrate Interactions by NMR Spectroscopy: The Trisaccharide Epitope from the Marine Sponge Microciona prolifera. *ChemBioChem* **10**, 511–519 (2009).

14.    Barrientos, Á. G., Fuente, J. M. de la, Rojas, T. C., Fernández, A. & Penadés, S. Gold Glyconanoparticles: Synthetic Polyvalent Ligands Mimicking Glycocalyx-Like Surfaces as Tools for Glycobiological Studies. *Chem. – Eur. J.* **9**, 1909–1921 (2003).

15.    Ojeda, R., de Paz, J. L., Barrientos, A. G., Martín-Lomas, M. & Penadés, S. Preparation of multifunctional glyconanoparticles as a platform for potential carbohydrate-based anticancer vaccines. *Carbohydr. Res.* **342**, 448–459 (2007).

16.    Wang, G., Guo, R., Kalyuzhny, G., Choi, J.-P. & Murray, R. W. NIR Luminescence Intensities Increase Linearly with Proportion of Polar Thiolate Ligands in Protecting Monolayers of Au38 and Au140 Quantum Dots. *J. Phys. Chem. B* **110**, 20282–20289 (2006).

17.    Gentilini, C. *et al.* Water-Soluble Gold Nanoparticles Protected by Fluorinated Amphiphilic Thiolates. *J. Am. Chem. Soc.* **130**, 15678–15682 (2008).

18.    Smith, A. M. *et al.* Quantitative Analysis of Thiolated Ligand Exchange on Gold Nanoparticles Monitored by 1H NMR Spectroscopy. *Anal. Chem.* **87**, 2771–2778 (2015).

19.    Smith, M. C., Crist, R. M., Clogston, J. D. & McNeil, S. E. Quantitative analysis of PEG-functionalized colloidal gold nanoparticles using charged aerosol detection. *Anal. Bioanal. Chem.* **407**, 3705–3716 (2015).

20.    Zhou, H., Li, X., Lemoff, A., Zhang, B. & Yan, B. Structural confirmation and quantification of individual ligands from the surface of multi-functionalized gold nanoparticles. *Analyst* **135**, 1210–1213 (2010).

21.    Pitkänen, L. & Striegel, A. M. Size-exclusion chromatography of metal nanoparticles and quantum dots. *Trends Anal. Chem. TRAC* **80**, 311–320 (2016).

22.    Liu, F.-K. Using Size-Exclusion Chromatography to Monitor Variations in the Sizes of Microwave-Irradiated Gold Nanoparticles. *ISRN Chromatogr.* **2012**, (2012).

23.    Süß, S., Metzger, C., Damm, C., Segets, D. & Peukert, W. Quantitative evaluation of nanoparticle classification by size-exclusion chromatography. *Powder Technol.* **339**, 264–272 (2018).

24. Harkness, K. M., Cliffel, D. E. & McLean, J. A. Characterization of thiolate-protected gold nanoparticles by mass spectrometry. *Analyst* **135**, 868–874 (2010).

25. Black, D. M., Robles, G., Bach, S. B. H. & Whetten, R. L. Gold Nanocluster Prospecting via Capillary Liquid Chromatography-Mass Spectrometry: Discovery of Three Quantized Gold Clusters in a Product Mixture of "2 nm Gold Nanoparticles". *Ind. Eng. Chem. Res.* **57**, 5378–5384 (2018).

26. Fisher, E. A., Duffy, S. J. & Meli, M.-V. The determination of ligand shell composition of bifunctional alkanethiol-capped gold nanoparticles using GC/MS/MS. *RSC Adv.* **5**, 33289–33293 (2015).

27. Giorgi, G. Mass Spectrometry and High Resolution Mass Spectrometry: An Overview. in *Molecular Technologies for Detection of Chemical and Biological Agents* 89–101 (Springer Netherlands, 2017).

28. Mori, T. & Hegmann, T. Determining the composition of gold nanoparticles: a compilation of shapes, sizes, and calculations using geometric considerations. *J. Nanoparticle Res.* **18**, 295 (2016).

29. Yan, B. *et al.* Laser desorption/ionization mass spectrometry analysis of monolayer-protected gold nanoparticles. *Anal. Bioanal. Chem.* **396**, 1025–1035 (2010).

30. Nicolardi, S. *et al.* Structural Characterization of Biofunctionalized Gold Nanoparticles by Ultrahigh-Resolution Mass Spectrometry. *ACS Nano* **11**, 8257–8264 (2017).

31. Bourg, M.-C., Badia, A. & Lennox, R. B. Gold−Sulfur Bonding in 2D and 3D Self-Assembled Monolayers: XPS Characterization. *J. Phys. Chem. B* **104**, 6562–6567 (2000).

32. Moulder, J. F., Stickle, W. F., Sobol, P. E. & Bomben, K. D. *Handbook of X Ray Photoelectron Spectroscopy: A Reference Book of Standard Spectra for Identification and Interpretation of Xps Data*. (Physical Electronics, 1995).

33. X-ray Photoelectron Spectroscopy (XPS) Reference Pages. http://www.xpsfitting.com/.

34. Techane, S. D., Gamble, L. J. & Castner, D. G. X-ray photoelectron spectroscopy characterization of gold nanoparticles functionalized with amine-terminated alkanethiols. *Biointerphases* **6**, 98–104 (2011).

35. Gobbo, P. *et al.* Versatile strained alkyne modified water-soluble AuNPs for interfacial strain promoted azide–alkyne cycloaddition (I-SPAAC). *J. Mater. Chem. B* **2**, 1764–1769 (2014).

36. Elzey, S. *et al.* Quantification of ligand packing density on gold nanoparticles using ICP-OES. *Anal. Bioanal. Chem.* **403**, 145–149 (2012).

37. Hinterwirth, H. *et al.* Quantifying Thiol Ligand Density of Self-Assembled Monolayers on Gold Nanoparticles by Inductively Coupled Plasma–Mass Spectrometry. *ACS Nano* **7**, 1129–1136 (2013).

38. Alvarez, M. M. *et al.* Optical Absorption Spectra of Nanocrystal Gold Molecules. *J. Phys. Chem. B* **101**, 3706–3712 (1997).

39. Zheng, T., Bott, S. & Huo, Q. Techniques for Accurate Sizing of Gold Nanoparticles Using Dynamic Light Scattering with Particular Application to Chemical and Biological Sensing Based on Aggregate Formation. *ACS Appl. Mater. Interfaces* **8**, 21585–21594 (2016).

40. Krpetić, Ž. *et al.* High-Resolution Sizing of Monolayer-Protected Gold Clusters by Differential Centrifugal Sedimentation. *ACS Nano* **7**, 8881–8890 (2013).

41. EUSMI / European Soft Matter Infrastructure. https://eusmi-h2020.eu/access/wp4/NSL-BIOMA.

42. Hostetler, M. J. *et al.* Alkanethiolate Gold Cluster Molecules with Core Diameters from 1.5 to 5.2 nm: Core and Monolayer Properties as a Function of Core Size. *Langmuir* **14**, 17–30 (1998).

43. Wang, W. *et al.* Zeta-potential data reliability of gold nanoparticle biomolecular conjugates and its application in sensitive quantification of surface absorbed protein. *Colloids Surf. B Biointerfaces* **148**, 541–548 (2016).

44. Moser, M. *et al.* Ellman's and Aldrithiol Assay as Versatile and Complementary Tools for the Quantification of Thiol Groups and Ligands on Nanomaterials. *Anal. Chem.* **88**, 8624–8631 (2016).

45. Gamache, P. H. & Kaufman, S. L. Principles of Charged Aerosol Detection. in *Charged Aerosol Detection for Liquid Chromatography and Related Separation Techniques* 1–65 (Wiley-Blackwell, 2017).

46.     Vehovec, T. & Obreza, A. Review of operating principle and applications of the charged aerosol detector. *J. Chromatogr. A* **1217**, 1549–1556 (2010).

47.     Charged Aerosol Detection for Liquid Chromatography - Thermo Fisher Scientific. https://www.thermofisher.com/uk/en/home/industrial/chromatography/chromatography-learning-center/liquid-chromatography-information/liquid-chromatography-innovations/charged-aerosol-detection-liquid-chromatography.html.

48.     Robinson, M. W. *et al.* Use of Calculated Physicochemical Properties to Enhance Quantitative Response When Using Charged Aerosol Detection. *Anal. Chem.* **89**, 1772–1777 (2017).

49.     Rohrer, J. S. & Kitamura, S. Determination of Carbohydrates Using Liquid Chromatography with Charged Aerosol Detection. in *Charged Aerosol Detection for Liquid Chromatography and Related Separation Techniques* 311–325 (Wiley-Blackwell, 2017).

50.     Kou, D., Manius, G., Tian, H. & Chokshi, H. P. Polymers and Surfactants. in *Charged Aerosol Detection for Liquid Chromatography and Related Separation Techniques* 327–339 (Wiley-Blackwell, 2017).

51.     Green, T. A. Gold etching for microfabrication. *Gold Bull.* **47**, 205–216 (2014).

52.     Hansen, R. E. & Winther, J. R. An introduction to methods for analyzing thiols and disulfides: Reactions, reagents, and practical considerations. *Anal. Biochem.* **394**, 147–158 (2009).

53.     Sun, S. *et al.* Visually monitoring the etching process of gold nanoparticles by KI/I2 at single-nanoparticle level using scattered-light dark-field microscopic imaging. *Nano Res.* **9**, 1125–1134 (2016).

54.     Templeton, A. C., Hostetler, M. J., Kraft, C. T. & Murray, R. W. Reactivity of Monolayer-Protected Gold Cluster Molecules: Steric Effects. *J. Am. Chem. Soc.* **120**, 1906–1911 (1998).

55.     Sitaula, S., Mackiewicz, M. R. & Reed, S. M. Gold nanoparticles become stable to cyanide etch when coated with hybrid lipid bilayers. *Chem. Commun.* 3013–3015 (2008).

56.     Mirzahosseini, A. & Noszál, B. The species- and site-specific acid–base properties of biological thiols and their homodisulfides. *J. Pharm. Biomed. Anal.* **95**, 184–192 (2014).

57.     Brust, M., Walker, M., Bethell, D., Schiffrin, D. J. & Whyman, R. Synthesis of thiol-derivatised gold nanoparticles in a two-phase Liquid–Liquid system. *J. Chem. Soc. Chem. Commun.* 801–802 (1994).

58.     Ansar, S. M. *et al.* Removal of Molecular Adsorbates on Gold Nanoparticles Using Sodium Borohydride in Water. *Nano Lett.* **13**, 1226–1229 (2013).

59.     Demers, L. M. *et al.* A Fluorescence-Based Method for Determining the Surface Coverage and Hybridization Efficiency of Thiol-Capped Oligonucleotides Bound to Gold Thin Films and Nanoparticles. *Anal. Chem.* **72**, 5535–5541 (2000).

60.     Schulz, F., Vossmeyer, T., Bastús, N. G. & Weller, H. Effect of the Spacer Structure on the Stability of Gold Nanoparticles Functionalized with Monodentate Thiolated Poly(ethylene glycol) Ligands. *Langmuir* **29**, 9897–9908 (2013).

61.     Maus, L., Spatz, J. P. & Fiammengo, R. Quantification and Reactivity of Functional Groups in the Ligand Shell of PEGylated Gold Nanoparticles via a Fluorescence-Based Assay. *Langmuir* **25**, 7910–7917 (2009).

62.     Tsai, D.-H. *et al.* Quantifying dithiothreitol displacement of functional ligands from gold nanoparticles. *Anal. Bioanal. Chem.* **404**, 3015–3023 (2012).

63.     Pierce TCEP-HCl - Thermo Fisher Scientific. https://www.thermofisher.com/order/catalog/product/20490.

64.     Bond-Breaker TCEP Solution, Neutral pH - Thermo Fisher Scientific. https://www.thermofisher.com/order/catalog/product/77720.

65.     DTT - Sigma Aldrich. https://www.sigmaaldrich.com/catalog/product/roche/dttro (2018).

66.     Hostetler, M. J., Templeton, A. C. & Murray, R. W. Dynamics of Place-Exchange Reactions on Monolayer-Protected Gold Cluster Molecules. *Langmuir* **15**, 3782–3789 (1999).

67.     Sperling, R. A. & Parak, W. J. Surface modification, functionalization and bioconjugation of colloidal inorganic nanoparticles. *Philos. Trans. R. Soc. Lond. Math. Phys. Eng. Sci.* **368**, 1333–1383 (2010).

68.     Gomes, S. Q. *et al.* Linear gold(I) complex with tris-(2-carboxyethyl)phosphine (TCEP): Selective antitumor activity and inertness toward sulfur proteins. *J. Inorg. Biochem.* **186**, 104–115 (2018).

69.     Brúder, P., Macášek, F. & Búriová, E. Electrospray ionization mass spectra of pentoses, hexoses, and 2-deoxy-2-fluoro-d-glucose. *Chem. Pap.* **62**, 547–552 (2008).

70.     Dreier, T. A. & Ackerson, C. J. Radicals are required for thiol etching of gold particles. *Angew. Chem. Int. Ed Engl.* **54**, 9249–9252 (2015).

71.     McNulty, J., Krishnamoorthy, V., Amoroso, D. & Moser, M. Tris(3-hydroxypropyl)phosphine (THPP): A mild, air-stable reagent for the rapid, reductive cleavage of small-molecule disulfides. *Bioorg. Med. Chem. Lett.* **25**, 4114–4117 (2015).

72.     Bruno, A. E. & Krattiger, B. Chapter 11 On-Column Refractive Index Detection of Carbohydrates Separated by HPLC and CE. in *Journal of Chromatography Library* (ed. El Rassi, Z.) vol. 58 431–446 (Elsevier, 1995).

73.     Li, N., Ziegemeier, D., Bass, L. & Wang, W. Quantitation of free polyethylene glycol in PEGylated protein conjugate by size exclusion HPLC with refractive index (RI) detection. *J. Pharm. Biomed. Anal.* **48**, 1332–1338 (2008).

74.     Jadzinsky, P. D., Calero, G., Ackerson, C. J., Bushnell, D. A. & Kornberg, R. D. Structure of a Thiol Monolayer-Protected Gold Nanoparticle at 1.1 Å Resolution. *Science* **318**, 430–433 (2007).

75.     Vergara, S. *et al.* Synthesis, Mass Spectrometry, and Atomic Structural Analysis of Au~2000(SR)~290 Nanoparticles. *J. Phys. Chem. C* **122**, 26733–26738 (2018).

# Chapter III


# Post-Functionalization of Ultrasmall Gold Nanoparticles

# I. Introduction

## 1. Methods of synthesis of ultrasmall GNP

"Covalent" functionalization of ultrasmall GNP can be performed through different methods[1] summarized in *Figure 1*.

- One-pot synthesis[2]: modified Brust-Schiffrin synthesis using sodium borohydride as a reducing agent in the presence of a gold salt and thiol or disulfide ligands.

- Post-functionalization[3]: use of the ligands bound to the GNP to perform conjugations through common organic synthetic routes with molecules bearing complementary functional groups.

- Ligand place exchange (LPE)[4]: incorporation of thiol or disulfide ligands in the GNP corona by either replacing those previously bound to the GNP or filling empty sites on the core[5].
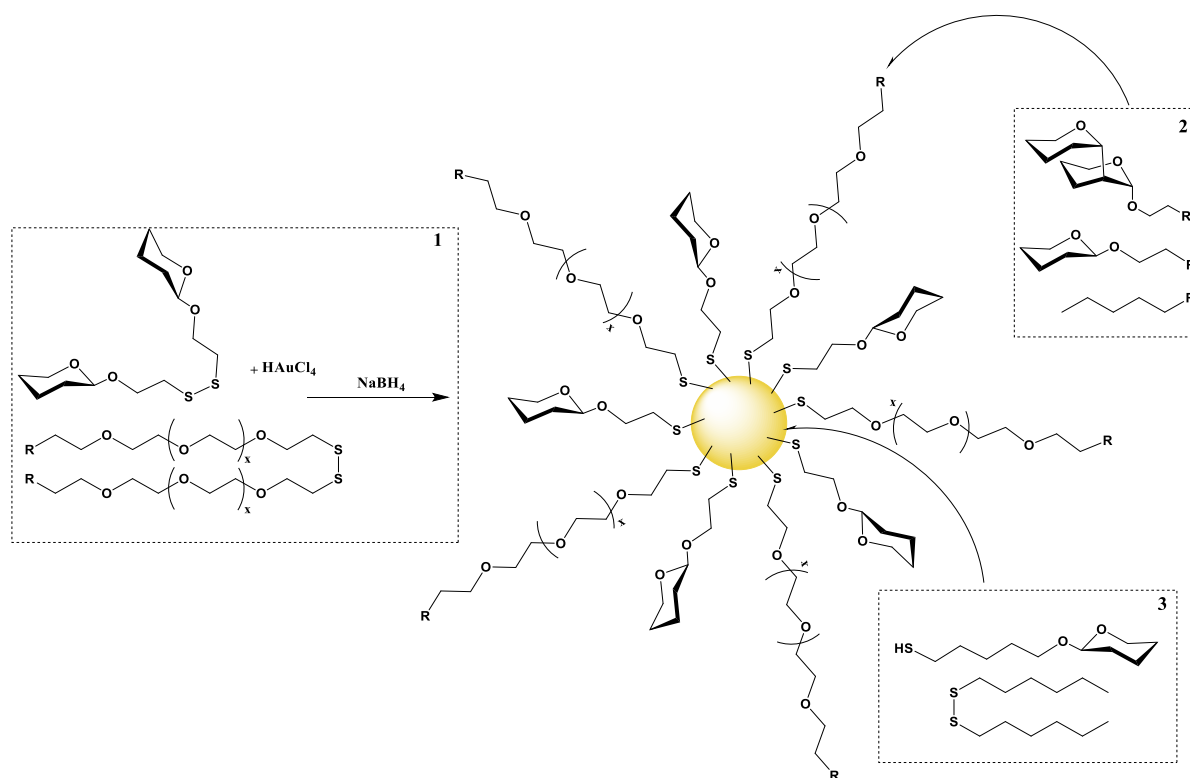


*Figure 1: Different "covalent" functionalization methods of ultrasmall GNP. (1) Modified Brust-Schiffrin synthesis. (2) Post-functionalization. (3) Ligand place exchange.*

## 2. Post-functionalization strategy

Post-functionalization consists in using simple specific organic reactions that can be defined as bioorthogonal chemistry. From a synthesis point of view, it has the advantage of allowing a direct control of the GNP/ligand ratio using simple stoichiometric variations. Moreover, the attachment points are usually at the terminal end of the GNP, which facilitates the presentation on the outer part of the platform (good orientation and separation from the core). Different molecules can be linked by this technique using parallel (concurrent addition to the GNP) or step by step (successive addition to the GNP with intermediate purification) chemistry to provide a mixed surface[3].

The other main advantage of post-functionalization reactions is the purification. Once the reaction is considered complete, the purification is commonly performed by ultrafiltration or dialysis. In this process, the excess of ligands or byproducts, along with smaller compounds, are removed by making them pass through a membrane with a define MWCO, while the GNP are retained.
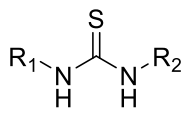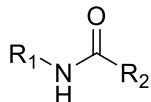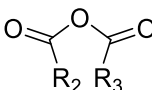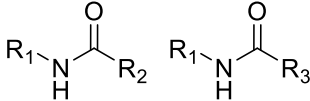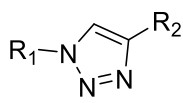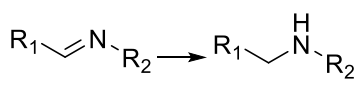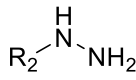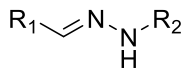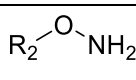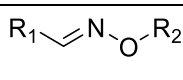
It can be argued that Brust-Schiffrin synthesis has the advantage of avoiding a multi-step reaction sequence. However, it also has some major drawbacks, such as being harder to control, the requirement for recipe tuning for each construct and the need of an excess of ligands to protect the core and halt the particle growth, maintaining the ultrasmall size. That is particularly wasteful when complex custom thiol or disulfides derivatives, such as oligosaccharides[6,7] are required. Another downside is the aggressive conditions, due to the extreme pH and the presence of sodium borohydride used in the synthesis, which can degrade the ligands.

Easy, fast, selective and reproducible reactions with high yields are needed to post-functionalize gold nanoparticles. Bioconjugation reactions using organic chemistry principles have been extensively optimized and documented, leading to the creation of a library of suitable bonds formed by compatible functional groups, alongside their activation agents and catalysts[8]. These principles have then been widely applied to nanoparticles and adapted to GNP by tuning the reaction parameters (e.g. solvent, pH, temperature, concentrations)[9].

# 3. Pathways of post-functionalization

Reactions considered here have been classified in four groups: isothiourea condensation, amide condensation (amine with either a carboxylic acid or an anhydride), azide-alkyne Huisgen cycloaddition (click chemistry) and Schiff base-like reactions (reductive amination, hydrazone ligation and oxime ligation) (*Table 1*).

*Table 1: Different pathways of post-functionalization considered.*

| Chemistry | Reactant 1 | Reactant 2 | Activation Agent - Catalyst | Product |
|---|---|---|---|---|
| Isothiourea Condensation | $R_1NH_2$ Amine | $R_2NCS$ Isothiocyanate | - | Isothiourea |
| Amide Condensation | | $R_2COOH$ Carboxylic acid | EDC and (Sulfo-)NHS | Amide |
| Anhydride and Amine Condensation | | Anhydride | - | Amides |
| Azide-alkyne Huisgen cycloaddition (CuAAC) | $R_1N_3$ Azide | $R_2\equiv$ Alkyne | Cu(I) | Triazole ring |
| Reductive Amination | $R_1CHO$ Aldehyde | $R_2NH_2$ Amine | Reducing agent ($NaCNBH_3$, $NaBH_4$) | Secondary amine |
| Hydrazone Ligation | | Hydrazine | Aniline | Hydrazone |
| Oxime Ligation | | Aminooxy | Aniline | Oxime |

### a. Isothiourea condensation

The isothiourea condensation consists in the addition of an isothiocyanate to an amine. It has the advantage of feasible without requiring any activation agent or catalyst, takes place under mild conditions (room temperature) and, is usually complete after a few hours of incubation in an aqueous medium with slight alkaline pH (9).

This protocol was applied with success to couple α-mannose to GNP bearing a terminal amine[10]. For example, Morin et al. used this methodology to incorporate p-isothiocyanatophenyl α-D-mannopyranoside on the terminal amino group of polyamidoamine dendrimers coated GNP. The main drawback is the isothiocyanate instability in water[11].

### b. Amide condensation

The amide condensation consists in the coupling of a carboxylic acid to an amine. The reactions can be performed at room temperature and are usually complete after a few hours of incubation in an aqueous medium or an organic solvent such as DMSO. The amide bond has the advantage of being very stable.

Amide bond formation has been extensively used to functionalize multivalent platforms with drugs[12,13], antibodies[14], carbohydrates[15,16] or peptides[17]. Midatech Pharma used this strategy with success on 2 nm ultrasmall GNP to couple the SIKVAV peptide[18] (for tumor targeting) and methotrexate[19] (for psoriasis treatment).

This approach requires activating reagents. Among the commercially available reagents[20], 1-ethyl-3-(3-dimethylaminopropyl)carbodiimide (EDC) and N-hydroxysuccinimide (NHS) or N-hydroxysulfosuccinimide (sulfo-NHS) are the most used. They react with the carboxylic acid: first the EDC forms an O-acylisourea intermediate and then coupling with NHS or sulfo-NHS gives an amine-reactive (active) ester. The amide can be formed directly from the O-acylisourea, but the (sulfo-)NHS esters are more stable toward hydrolysis. When performed in aqueous medium, the activation of the carboxylic acid is more effective at slightly acidic pH (5-6), while the coupling with the amine is more efficient at neutral pH (7-8)[21]. If an organic solvent is used, an organic base such as 4-Dimethylaminopyridine (DMAP) can be added. The reaction is sensitive to high pH leading to a drop of the esters half-life from hours to minutes. Sulfo-NHS has the advantage of being more water-soluble and resistant to hydrolysis than NHS but comes with the downside of a higher steric hindrance.

For GNP functionalized with carboxylic acid, a centrifugation can be performed before the coupling to remove the excess of activation reagents[17] (*Figure 2*). In the case of amine functionalized GNP, the biomolecule which bears the carboxylic acid moiety should be incubated with the activation reagents before addition to the GNP[22]. The co-presence of activation reagents and amines packed on a surface could lead to side reactions, promoting crosslinking of amino-GNP[23]. For that reason, timings and equivalents should be carefully chosen.
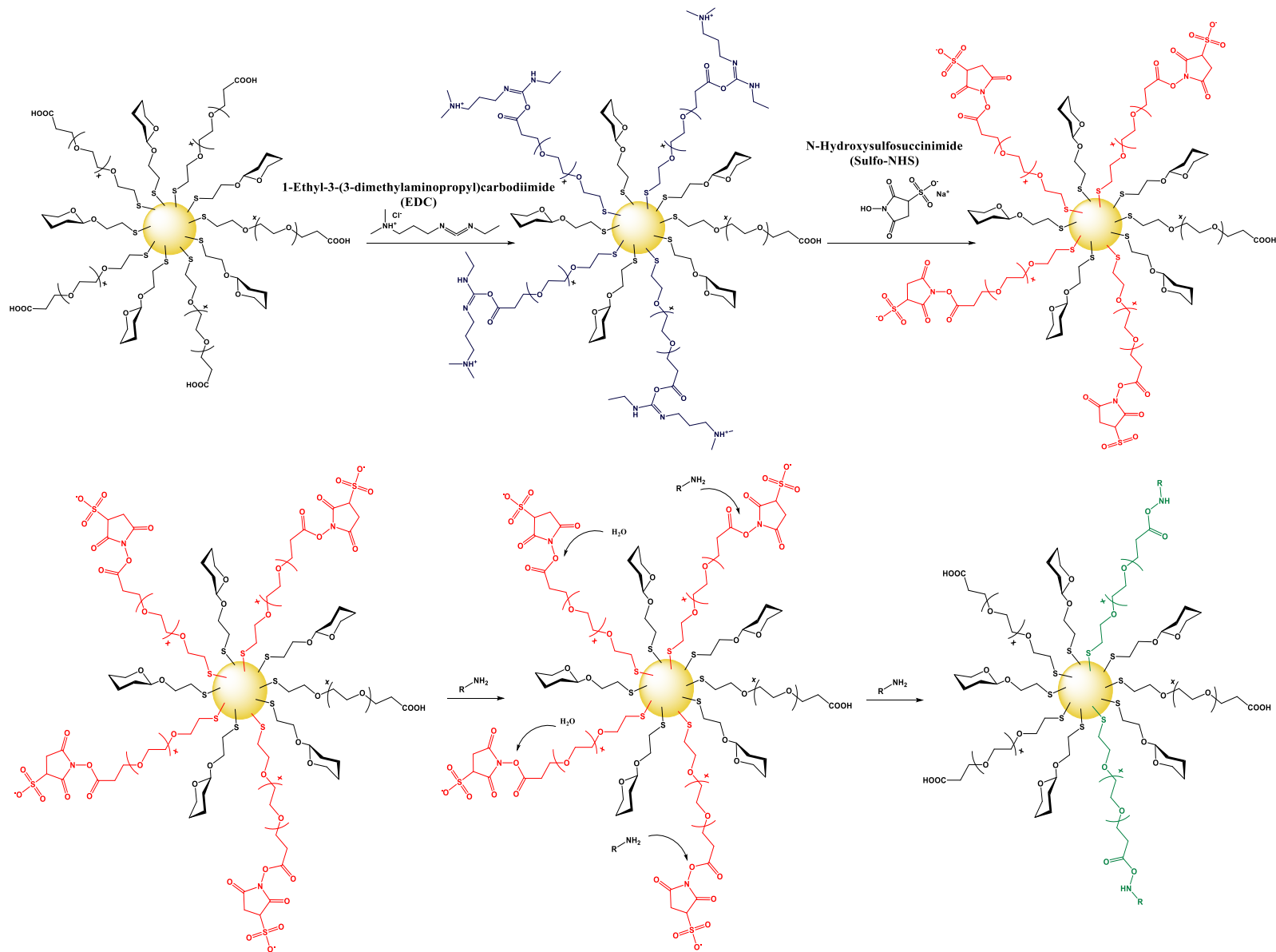
*Figure 2: Top: EDC and Sulfo-NHS activation of PEGCOOH-GNP. Bottom: Amide coupling of Sulfo-NHS ester activated-GNP with an amine molecule and ester hydrolysis.*

### c. Anhydride and amine condensation

Reaction of anhydrides with amines lead to amide condensations. The reaction can be performed at room temperature and is usually complete after a few hours of incubation in an aqueous medium or DMSO. The main difference with the carboxylic acid/amine condensation is the absence of activation agents. The anhydride, used in excess, readily binds to the amine. In the case of cyclic anhydrides, such as succinic anhydride, the nucleophilic attack by the amine on one of the anhydride carbonyls leads to the formation of an amide and the release of a carboxylic acid.

This reaction was performed with success to change amine terminal particles to carboxylic acid terminal[15]. For example, Harms et al. used succinic anhydride to turn amino-silica nanoparticles into constructs exhibiting a terminal carboxylic acid. That strategy was also used with success by Midatech Pharma to convert 2 nm positive bifunctional $\alpha$-Galactose-C$_2$/PEG(5)NH$_2$ GNP into negative $\alpha$-Galactose-C$_2$/PEG-succinic particles[24].

### d. Azide-alkyne Huisgen cycloaddition (click chemistry)

One of the most popular azide-alkyne Huisgen cycloaddition, also known as click chemistry, is the Cu(I)-promoted Azide-Alkyne [3 +2] Cycloaddition (CuAAC), which consists in the formation of a triazole ring, by the cycloaddition of an azide and an alkyne, using copper as a catalyt[25]. The reactions can be performed at room temperature and are usually complete after few hours of incubation in an aqueous medium. CuAAC has the advantage of being highly specific (as it uses functional groups that are typically not present in biomolecules) and is solvent and pH insensitive (pH 4-12). On the other hand, the main drawback is the toxicity that may arise if the copper is not properly removed from the final product.

Azide-alkyne cycloaddition (including CuAAC and Strain-promoted Azide-Alkyne Cycloaddition SPAAC) has been widely used to couple GNP (bearing either an alkyne or an azide) to biomolecules including carbohydrates[1].

### e. Schiff base-like: reductive amination, hydrazone and oxime ligation

Carbonyl groups such as aldehydes (or ketones) can be used to perform bioorthogonal Schiff base-like reactions. Reductive amination, for instance, is a two-step reaction between an amine and an aldehyde. The unstable Schiff Base obtained during the first step is then reduced to form a secondary amine. Several one-step reactions have also been described, for instance, hydrazine or amino-oxy functions are commonly used to obtain hydrazones and oximes, respectively[8].

These reactions have the advantage of being feasible with non-modified carbohydrates, using their reducing end (aldehyde) as the attachment point. In the context of carbohydrate chemistry, this is extremely attractive since there is no need to derivatize the sugars.

Oxime coupling can be considered as a "carbonyl click-reaction" due to its high efficiency and specificity, and can be performed in aqueous conditions, with water as the only side product[26,27]. Compared to hydrazone, oxime bonds have shown a superior stability toward hydrolysis at neutral pH, making the molecules more biocompatible[28]. Moreover, the oxime ligation has the advantage of being performed under mild conditions, compared to reductive amination, which needs a strong reducing agent such as sodium cyanoborohydride ($NaCNBH_3$) or sodium borohydride ($NaBH_4$), which could damage the GNP[29,30].

Oxime ligation has proved its effectiveness with a wide range of mono and oligosaccharides for microarray analyses[31]. Several glyconanoparticles obtained by carbonyl click reaction have been reported. Citrate stabilized gold nanoparticles have been coupled to non-modified carbohydrates via hydrazone[32] or oxime bonds[33,34] and tested with lectins such as Concanavalin A (ConA) and *Erythrina cristagalli* lectin (ECA). Moreover, ultrasmall bifunctional gold nanoparticles bearing an amino-oxy function have been coupled to glycosphingolipids using the oxime post-functionalization strategy[35].

The main drawback of oxime ligation with carbohydrates is that it leaves the reducing end monomer in an equilibrium between ring-opened (E and Z forms) and ring-closed (α and β-pyranose)[31,33]. This can affect the recognition domain for monosaccharides. However, the effect of ring-opened terminal sugar is less evident for most large oligosaccharides, since the binding motif is less likely to be affected by the reducing end unit.
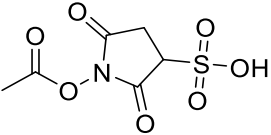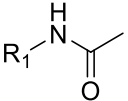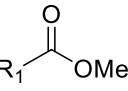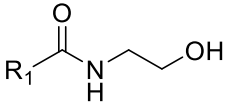
Oxime reactions can be performed at mildly acidic pH (pH 4-5, sodium acetate buffer) to improve the reaction rate and yield. The most often used catalyst is aniline[36], although it should be noted that a wide range of alternatives to aniline with improved performance have been developed[37,38,39].

One approach to obtain an amino-oxy function on GNP is to use a tert-butyloxycarbonyl (Boc) protected compound (e.g. Boc-aminooxyacetic acid[40]) and to couple it with an amine linker of the GNP through an amide bond. Then, the Boc protecting group can be cleaved using a strong acid (e.g. trifluoroacetic acid)[41] to form amino-oxy or alkoxyamines GNP.

### f. Protective Groups

Post-functionalization protections can also be performed in order to change the physicochemical properties of the GNP (e.g. to obtain negative controls) (*Table 2*). An amine can be protected as an acetamide[42] using the commercially available reagent Sulfo-NHS-Acetate[43]. A carboxylic acid can be protected as a methyl-ester[44] using a catalytic amount of sulfuric acid in methanol. To obtain a neutral charge, a hydroxyl terminal group can be introduced using the previously described amide condensation method. Protective groups have been chosen because of their stability (no degradation at physiological pH) and capacity of being cleaved under selective conditions[45].

*Table 2: Protective groups.*

| Protective Group | Reactant 1 | Reactant 2 | Activation Agent - Catalyst | Product |
|---|---|---|---|---|
| Acetamide | $R_1NH_2$ Amine | Sulfo-NHS-Acetate | - | Acetamide |
| Methyl-ester | $R_1COOH$ Carboxylic acid | MeOH Methanol | $H_2SO_4$ | Methyl-ester |
| Hydroxyl | | Ethanolamine | EDC and (Sulfo-)NHS | Amide |

## 4. α-D-Mannose: a monosaccharide of interest for post-functionalization screening

α-D-Mannose is an essential monosaccharide for most living organisms, including humans[46]. Combined with proteins, peptides (glycoproteins and proteoglycans) or lipids (glycolipids), its importance in cell-cell communication, homeostasis and deregulation processes (e.g. cancer, auto-immune diseases, allergies) makes it a key target for pharmaceutical research. Moreover, diseases such as HIV infection rely on mannose dependent mechanisms[47]. C-type lectin receptors present on the surface of immune cells such as DC-SIGN and Langerin are mannose specific[48].

GNP coating with α-mannose derivatives through post-functionalization reactions allow the presentation on a globular-shaped scaffold of multiple copies of the carbohydrate[49].

## II.  Objectives

The main objective of this chapter is to study and compare different pathways of post-functionalization with ultrasmall GNP. One-pot Brust-Schiffrin synthesized bifunctional GNP (with an average core size of 2 nm) were used as a base to perform bioorthogonal reactions. Bifunctional GNP had two different ligands: an oligo-PEG: PEG(8)COOH or PEG(5)NH$_2$ and the C$_2$ alkyl side chained monosaccharide: β-Glucose-C$_2$ or α-Galactose-C$_2$.

Apart from the physicochemical and biological relevance, using the ligands mentioned above possesses several advantages. Firstly, they are readily available thanks to the H2020 European research program Nanofacturing[50] (Grant agreement ID: 642870). Secondly, the syntheses of the bifunctional 2 nm oligo-PEG/monosaccharide GNP are well-controlled and reproducible, giving reliable material, in relatively high quantity, for the subsequent post-functionalization steps.

To develop and compare the pathways, α-mannose was chosen as the complementary biomolecule. A range of α-mannose derivatives with different alkyl side chain, either long[51,52] (C$_6$) or short[53,54] (C$_2$) and various terminal groups (alkyne, azide, carboxylic acid, amine, isothiocyanate) was designed. The α-mannose derivatives were used for one- or multi-step reactions with the aforementioned bifunctional GNP. Also, straightforward chemical routes to protect the oligo-PEG of the GNP were designed. Finally, a method to simplify carbohydrate binding to GNP, using chemistry at the reducing end of oligosaccharides, was developed (oxime pathway).

Pegamine (5 EG units) and β-Glucose-C$_2$ GNP were functionalized using one-step amide and isothiourea binding protocols with α-mannose carboxylic acid and isothiocyanate derivatives, respectively. Two-step CuAAC click-chemistry reactions were performed with GNP bearing a terminal azide or alkyne group and the complementary α-mannose derivatives. Succinic anhydride was also used to change the PEG terminal function to a carboxylic acid and bind α-mannose amine derivatives. Non-modified oligosaccharides were bound to the GNP in a three-step reaction. The amine was also protected with an acetamide using a commercial building block (*Figure 3*). Following the same principles, a GNP made of an oligo-PEGCOOH (8 EG units) and α-Galactose-C$_2$ was functionalized with an amine α-mannose derivative in a one-step amide coupling reaction. Ester and hydroxyl protection were also studied using methanol and ethanolamine, respectively (*Figure 4*).

Figure 3: Different reactions of post-functionalization performed on PEG(5)NH₂-GNP. (1) Direct α-mannose derivatives binding by amide or isothiourea couplings. (2) GNP terminal function conversion with succinic anhydride and α-mannose derivative binding. (3) Two-step CuAAC click chemistry. (4) Three-step oxime binding with non-modified oligosaccharides. (5) Acetate protection using Sulfo-NHS-Acetate.

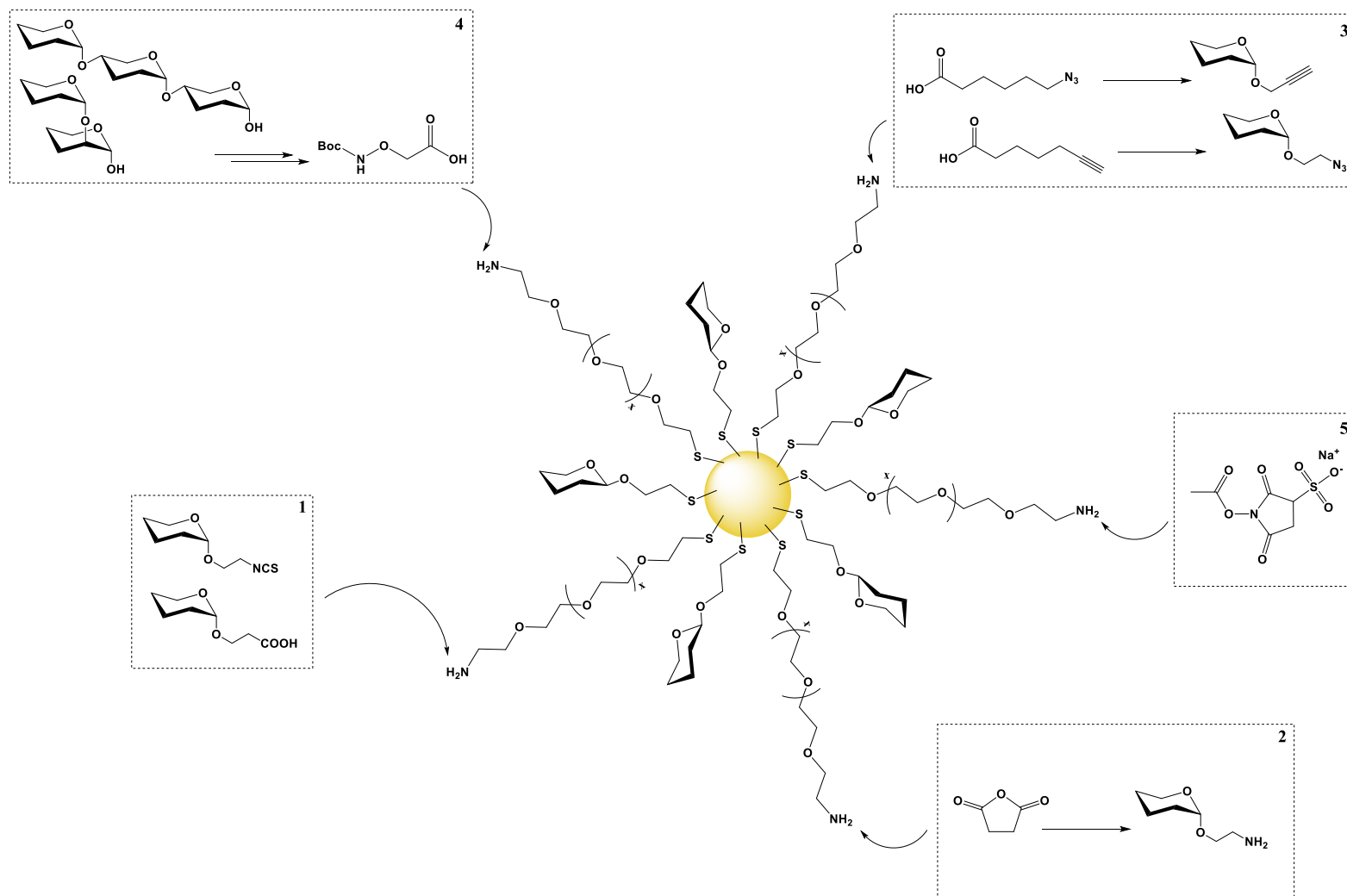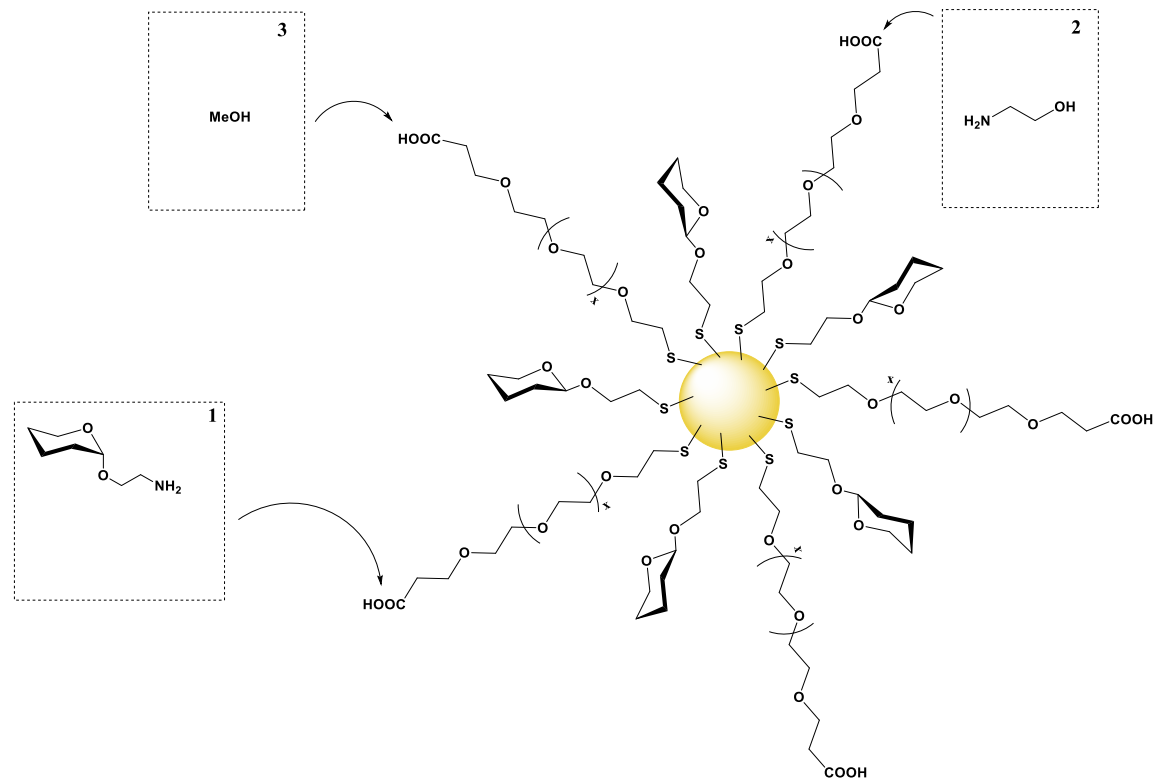*Figure 4: Different reactions of post-functionalization performed on PEG(8)COOH-GNP. (1) Direct α-mannose derivative binding by amide coupling. (2) Hydroxyl protection using ethanolamine. (3) Ester protection using methanol.*

# III.   Results and Discussion

## 1. α-Mannose derivative library

Several bifunctional alkyl building blocks were purchased to prepare α-D-mannose derivatives (*Figure 5*). The alkyl chains possessed a terminal hydroxyl group to perform O-glycosylations with α-D-mannopyranose pentaacetate (disarmed donor) and obtain α-D-mannose tetraacetate conjugated structures[55,56]. The other end of the chain presented either an intermediate or the final functional group to carry out bioorthogonal reactions with the complementary moieties displayed on the GNP[57]. The intermediate carbohydrates are shown in *Table 3* and the final products in *Table 4*.

Glycosylation[53,54,58] of linkers **1**, **2**, **9**, **10**, **15** and **16** with pentaacetylated α-mannose and boron trifluoride diethyl etherate (BF$_3$.OEt$_2$) as promotor gave the mannoglycosides **3**, **4**, **11**, **12**, **17** and **18** with moderate yields (12-55 %). The α-anomeric configuration of the acetylated mannoconjugates and the purity was confirmed by ^{1}H NMR. Mannoside **3** could not be isolated from the starting material α-D-mannopyranose pentaacetate while **4** and **18** presented traces of the linkers **2** and **16,** respectively. The mixtures were used without complete purification in further steps.

The bromide atom of manno-derivatives **17** and **18** was substituted by an azide (N$_3$) group in a nucleophilic substitution (S$_N$2 reaction)[54,59] using phase transfer catalysts[60,61] to obtain the azide-compounds **19** and **20**.

From the azide group, a tandem Staudinger-aza-Wittig reaction[62] was performed to obtain isothiocyanate derivatives **23** and **24**.

Removal of the acetates was carried out by Zemplén deacetylation[63] to obtain the deacetylated mannoglycosides **5**, **6**, **13**, **14**, **21**, **22**, **25** and **26** with quantitative yields.

Ester hydrolysis of the carboxylmethyl compounds **5** and **6** was done using sodium hydroxide in water[64] to obtain the terminal carboxylic acid manno-derivatives **7** and **8**.

From the deprotected azide compounds **21** and **22**, a Staudinger reduction[54,58] was carried out to obtain the amine derivatives **27** and **28**.

Final products were characterized by ^{1}H NMR and ^{13}C NMR to confirm the identity and the purity of the mannose derivatives[65].
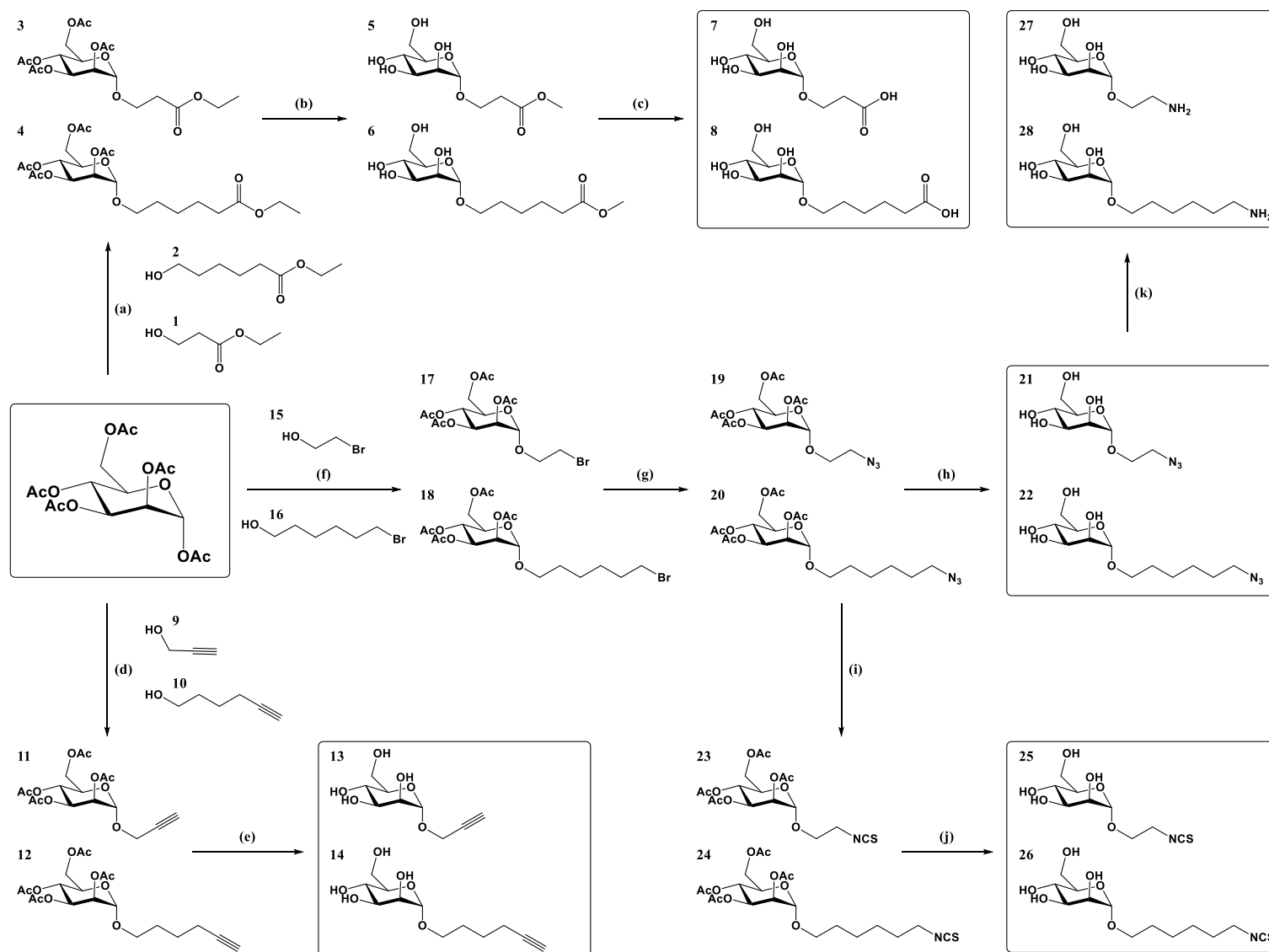
Figure 5: Synthetic pathways to obtain α-mannose derivatives. (**a**), (**d**) and (**f**) BF₃.OEt₂, CH₂Cl₂, RT, 18 h. (**g**) NaN₃, TBAI, DB₁₈C₆, N,N-dimethylformamide, RT, 72 h. (**i**) CS₂, PPh₃, Toluene, 50 °C, 18 h. (**b**), (**e**), (**h**) and (**j**) MeONa, MeOH, RT, 2-18 h. (**c**) NaOH, H₂O, RT, 18 h. (**k**) PPh₃, tetrahydrofuran/H₂O, RT, 18 h.

*Table 3: Intermediaries of synthesis.*

| Molecule | Compound reference number |
|---|---|
| 2-Ethoxycarbonylethyl 2,3,4,6-tetra-*O*-acetyl-α-D-mannopyranoside | 3 |
| 5-Ethoxycarbonylpentyl 2,3,4,6-tetra-*O*-acetyl-α-D-mannopyranoside | 4 |
| 2-Methoxycarbonylethyl α-D-mannopyranoside | 5 |
| 5-Methoxycarbonylpentyl α-D-mannopyranoside | 6 |
| 2-Propynyl 2,3,4,6-tetra-*O*-acetyl-α-D-mannopyranoside | 11 |
| 5-Hexynyl 2,3,4,6-tetra-*O*-acetyl-α-D-mannopyranoside | 12 |
| 2-Bromoethyl 2,3,4,6-tetra-*O*-acetyl-α-D-mannopyranoside | 17 |
| 6-Bromohexyl 2,3,4,6-tetra-*O*-acetyl-α-D-mannopyranoside | 18 |
| 2-Azidoethyl 2,3,4,6-tetra-*O*-acetyl-α-D-mannopyranoside | 19 |
| 6-Azidohexyl 2,3,4,6-tetra-*O*-acetyl-α-D-mannopyranoside | 20 |
| 2-Isothiocyanatoethyl 2,3,4,6-tetra-*O*-acetyl-α-D-mannopyranoside | 23 |
| 6-Isothiocyanatohexyl 2,3,4,6-tetra-*O*-acetyl-α-D-mannopyranoside | 24 |

*Table 4: Final α-Mannose conjugate structures and binding mode to the GNP.*

| Molecule | Compound reference number | Coupling mode to GNP |
|---|---|---|
| 2-Carboxyethyl α-D-mannopyranoside | 7 | Amide |
| 5-Carboxypentyl α-D-mannopyranoside | 8 | Amide |
| 2-Propynyl α-D-mannopyranoside | 13 | Click Chemistry CuAAC |
| 5-Hexynyl α-D-mannopyranoside | 14 | Click Chemistry CuAAC |
| 2-Azidoethyl α-D-mannopyranoside | 21 | Click Chemistry CuAAC |
| 6-Azidohexyl α-D-mannopyranoside | 22 | Click Chemistry CuAAC |
| 2-Isothiocyanatoethyl α-D-mannopyranoside | 25 | Isothiourea |
| 6-Isothiocyanatohexyl α-D-mannopyranoside | 26 | Isothiourea |
| 2-Aminoethyl α-D-mannopyranoside | 27 | Amide |
| 6-Aminohexyl α-D-mannopyranoside | 28 | Amide |

## 2. Post-functionalization pathways

The post-functionalization was carried out on 2 nm core GNP. Three different base ultrasmall bifunctional constructs were obtained in quantities that allowed post-functionalization screening and analysis (*Table 5*).

*Table 5: Base bifunctional GNP obtained by modified Brust–Schiffrin synthesis (formulas are averaged).*

| Batch | Gold Nanoparticle Averaged Formula |
|-------|-----------------------------------|
| GNP-1 | $(PEG(5)NH_2)_{26}(\beta\text{-Glucose-}C_2)_{18}@Au_{102}$ |
| GNP-2 | $(PEG(5)NH_2)_{30}(\beta\text{-Glucose-}C_2)_{14}@Au_{102}$ |
| GNP-3 | $(PEG(8)COOH)_{22}(\alpha\text{-Galactose-}C_2)_{22}@Au_{102}$ |

Using the described base particles, a wide range of post-functionalization reactions were performed. $PEG(5)NH_2$ and $PEG(8)COOH$ linkers were used in single or multi-step protocols to obtain intermediate functional groups, protective groups or carbohydrate functionalization ($\alpha$-mannose or oligosaccharides) (*Figure 6 to Figure 8*).
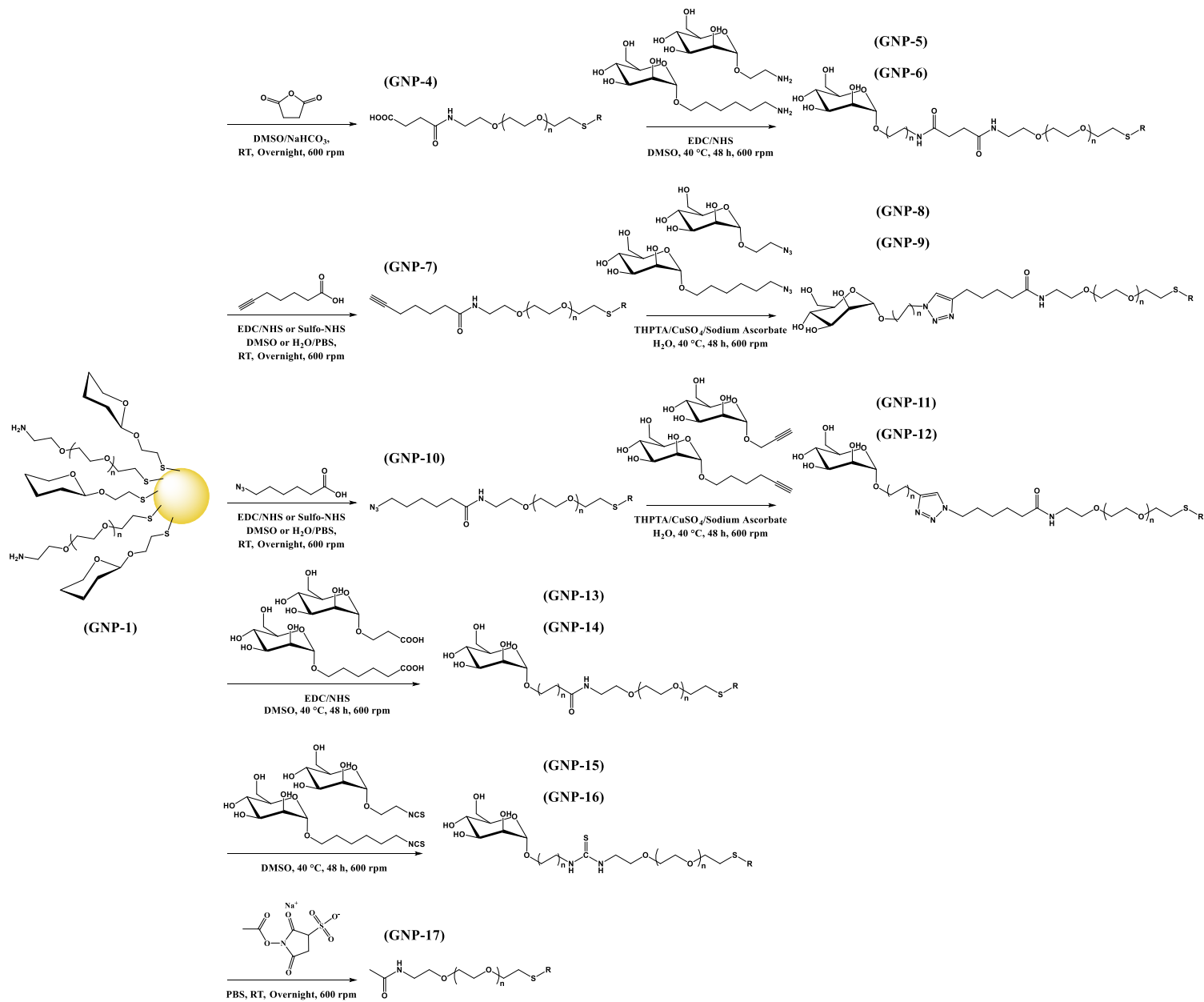
*Figure 6: Summary of the different pathways of post-functionalization with PEG(5)NH₂-GNP and resulting particles.*
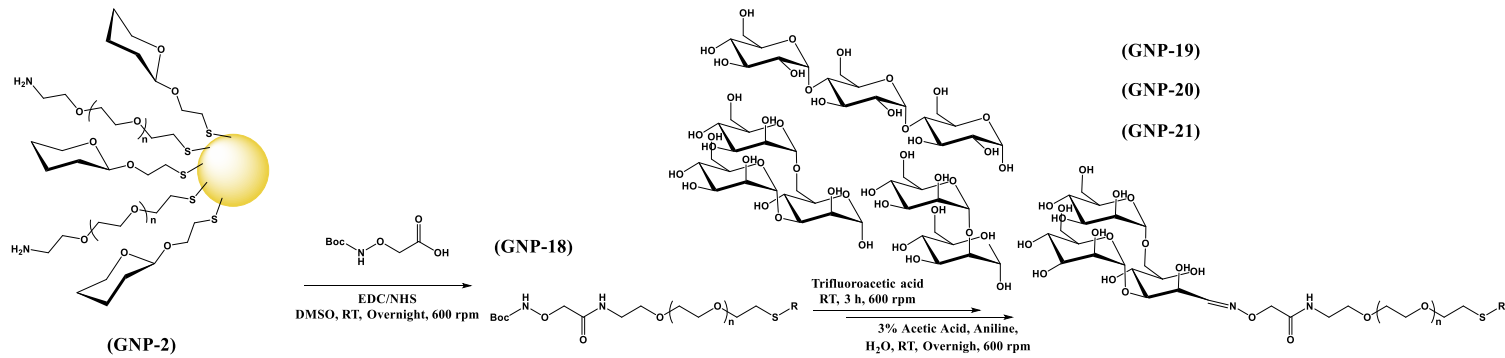
*Figure 7: Oxime pathway of post-functionalization of PEG(5)NH$_2$-GNP and resulting particles.*
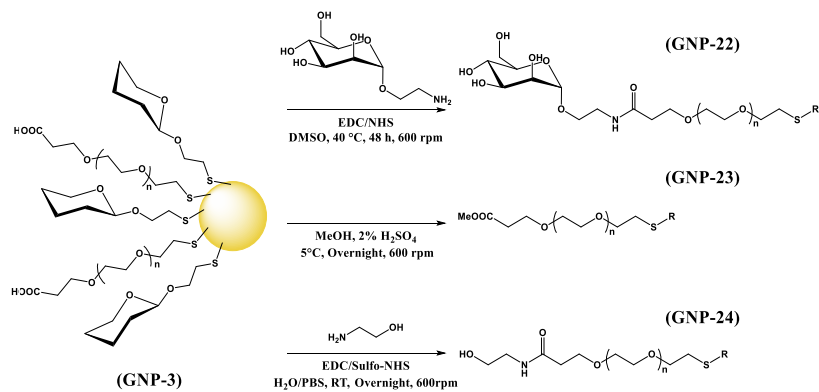
*Figure 8: Summary of the different pathways of post-functionalization with PEG(8)COOH-GNP and resulting particles.*

### a. Intermediate and protected GNP

The different intermediate or protecting groups were bound to the base GNP with quantitative yields, leading to an almost complete change of terminal functional group, according to $^1$H NMR (*Table 6*). The degree of functionalization (DF) was determined by integrating the relative areas of the methylene protons of the linkers (e.g. -CH$_2$-NH$_2$, -CH$_2$-COOH) (*Figure 9*).

*Table 6: Degrees of functionalization of the GNP with the intermediate and protective groups determined by $^1$H NMR.*

| Batch | Base Gold Nanoparticle | Ligand Bound - Terminal Group | PEG DF (%) |
|-------|------------------------|-------------------------------|------------|
| GNP-4 | GNP-1 (PEG(5)NH$_2$)$_{26}$($\beta$-Glucose-C$_2$)$_{18}$@Au$_{102}$ | Succinic anhydride - Carboxylic acid | 86 |
| GNP-7 | | 6-Heptynoic acid - Alkyne | 89 |
| GNP-10 | | 6-Azido-hexanoic acid - Azide | 91 |
| GNP-17 | | Sulfo-NHS-Acetate - Acetamide | 93 |
| GNP-18 | GNP-2 (PEG(5)NH$_2$)$_{30}$($\beta$-Glucose-C$_2$)$_{14}$@Au$_{102}$ | (Boc-aminooxy)acetic acid - Amino-Oxy | 72 (86 % LC-CAD-MS) |
| GNP-23 | GNP-3 (PEG(8)COOH)$_{22}$($\alpha$-Galactose-C$_2$)$_{22}$@Au$_{102}$ | Methanol - Methyl-ester | 100 |
| GNP-24 | | Ethanolamine - Hydroxyl | 74 |

PEG(5)NH$_2$ was derivatized into the following functional groups with the corresponding yields: a terminal carboxylic acid by succinic anhydride (**GNP-4**): 86 % yield; a terminal alkyne by 6-Heptynoic acid (**GNP-7**): 89 %; a terminal azide by 6-Azido-hexanoic acid (**GNP-10**): 91%; and a terminal Boc-amino-oxy by (Boc-aminooxy)acetic acid (**GNP-18**): 72 %. The DF was also determined for GNP-18 by LC-CAD-MS (86 %). PEG(5)NH$_2$ was protected as an acetamide with Sulfo-NHS-Acetate in a 93 % yield (**GNP-17**). PEG(8)COOH was protected as a methyl ester with methanol (**GNP-23**) and an hydroxyl using ethanolamine (**GNP-24**) with yields of 100 % and 74 %, respectively. These results show that short alkyl chains and small protecting groups can efficiently perform bioorthogonal chemistry with the oligo-PEG GNP.

The high yields of conversion of the pegamine terminal function allow subsequent reactions to be performed with $\alpha$-mannose derivatives (using GNP-4, GNP-7, GNP-10) and oligosaccharides (using GNP-17, after Boc deprotection).
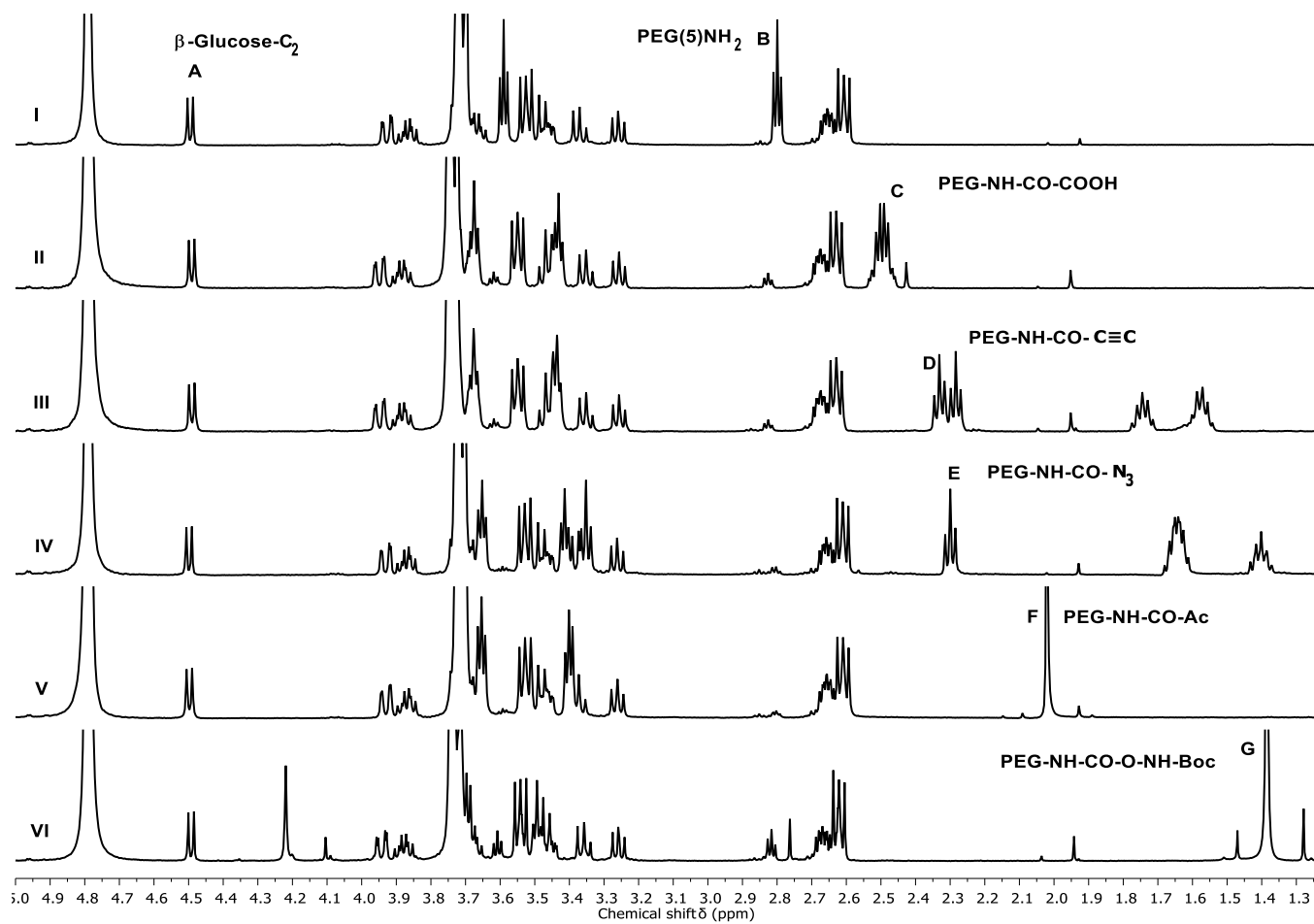
Figure 9: *$^1$H NMR (500 MHz, D$_2$O) of (I) GNP-1, (II) GNP-4, (III) GNP-7, (IV) GNP-10, (V) GNP-17 and (VI) GNP-18 after KCN/KOH treatment. (A) β-Glucose-C$_2$ δ 4.50 (H-1, d, 1H), (B) PEG(5)NH$_2$ δ 2.80 (-CH$_2$-NH$_2$, t, 2H), (C) PEG(5)NH-CO-C$_2$H$_4$-COOH δ 2.50 (m, 4H), (D) PEG(5)NH-CO-C$_4$H$_8$-C≡C δ 2.33 (t, 2H), (E) PEG(5)NH-CO-C$_5$H$_{10}$-N$_3$ δ 2.32 (t, 2H), (F) PEG(5)NH-Ac δ 2.02 (s, 3H) and (G) PEG(5)NH-CO-CH$_2$-O-NH-Boc δ 1.39 (s, 9H).*

### b. Carbohydrate functionalized GNP

The GNP were loaded with either 10 equivalents of α-mannose derivatives or 5 equivalents of oligosaccharides. As with the intermediate and protecting groups, the percentage of carbohydrate in the total formula was determined by integrating the relative areas of the methylene protons of the linkers as well as the protons α-mannose (e.g. anomeric H-1).

The percentages of carbohydrate varied from low (**GNP-5**: 11 %) to high (**GNP-16**: 49 %) (*Table 7*). Although the ^{1}H NMR interpretation is challenging and operator dependent, a few trends can be seen.

Direct coupling (one-step: amide and isothiourea) between the base GNP and the α-mannose derivatives resulted in the best functionalization yields (**GNP-13**: 35 %, **GNP-14**: 38 %, **GNP-15**: 33 %, **GNP-16**: 49 % and **GNP-22**: 44 %).

Carbohydrates with longer alkyl side chains repeatedly displayed higher yields than their short chain counterparts:
- **GNP-5**: 11 % vs **GNP-6**: 15 %
- **GNP-11**: 21 % vs **GNP-12**: 33 %
- **GNP-13**: 35 % vs **GNP-14**: 38 % (*Figure 10*)
- **GNP-15**: 33 % vs **GNP-16**: 49 %.

Comparing PEG(5)NH$_2$ and PEG(8)COOH in similar conditions (with a ethyl side chained α-mannose and coupling by amidation), no conclusion about the influence of the PEG chain length or charge on the yield can be drawn (**GNP-13**: 35 % and **GNP-22**: 44 %).

The product of the amino-oxy route could not be interpreted by ^{1}H NMR due to the complexity of the signals, but the LC-CAD-MS analysis showed surprisingly good yields (**GNP-19**: 37 % of α-Mannose1,2-α-Mannose, **GNP-20**: 31 % of 1,3-α-1,6-α-D-Mannotriose and **GNP-21**: 31 % of Maltotriose) considering the number of steps (3) and the steric hindrance of the oligosaccharides (2-3 units).

| Batch | α-Mannose Derivative | Gold Nanoparticle – Functional Group | Carbohydrate (%) |
|---|---|---|---|
| GNP-5 | 2-Aminoethyl α-D-mannopyranoside (**27**) | GNP-4 - Carboxylic Acid (Succinic) | 11 |
| GNP-6 | 6-Aminohexyl α-D-mannopyranoside (**28**) | | 15 |
| GNP-8 | 2-Azidoethyl α-D-mannopyranoside (**21**) | GNP-7 - Alkyne | 18 |
| GNP-9 | 6-Azidohexyl α-D-mannopyranoside (**22**) | | 18 |
| GNP-11 | 2-Propynyl α-D-mannopyranoside (**13**) | GNP-10 - Azide | 21 |
| GNP-12 | 5-Hexynyl α-D-mannopyranoside (**14**) | | 33 |
| GNP-13 | 2-Carboxyethyl α-D-mannopyranoside (**7**) | GNP-1 - Amine $(PEG(5)NH_2)_{26}(\beta\text{-Glucose-}C_2)_{18}@Au_{102}$ | 35 |
| GNP-14 | 5-Carboxypentyl α-D-mannopyranoside (**8**) | | 38 |
| GNP-15 | 2-Isothiocyanatoethyl α-D-mannopyranoside (**25**) | | 33 |
| GNP-16 | 6-Isothiocyanatohexyl α-D-mannopyranoside (**26**) | | 49 |
| GNP-22 | 2-Aminoethyl α-D-mannopyranoside (**27**) | GNP-2 - Carboxylic Acid $(PEG(8)COOH)_{22}(\alpha\text{-Galactose-}C_2)_{22}@Au_{102}$ | 44 |
| GNP-19 | α-Mannose1,2-α-Mannose | GNP-18 (deprotected Boc) - Amino-oxy | 37* |
| GNP-20 | 1,3-α-1,6-α-D-Mannotriose | | 31* |
| GNP-21 | Maltotriose | | 31* |

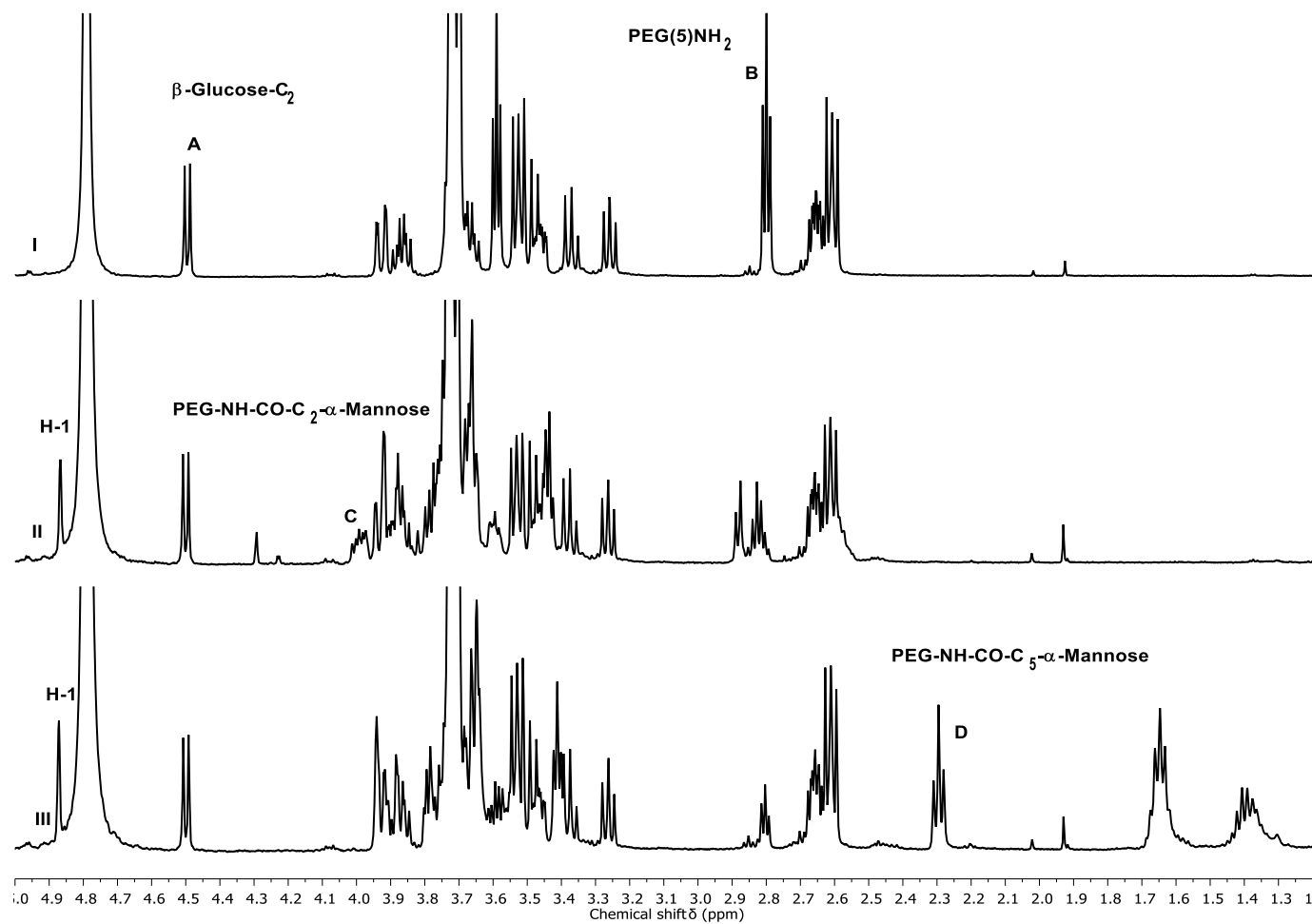Figure 10: $^1H$ NMR (500 MHz, $D_2O$) of (I) GNP-1, (II) GNP-13 and (III) GNP-14 after KCN/KOH treatment. (A) β-Glucose-$C_2$ δ 4.50 (H-1, d, 1H), (B) PEG(5)$NH_2$ δ 2.80 (-$CH_2$-$NH_2$, t, 2H), (C) PEG(5)NH-CO-$C_2H_4$-α-Mannose δ 3.99 (m, 1H) and (D) PEG(5)NH-CO-$C_5H_{10}$-α-Mannose 2.30 (t, 2H). α-Mannose H-1 (anomeric proton) δ 4.87 (d, 1H).

# IV.    Conclusions and Further Work

A variety of α-D-mannopyranoside derivatives with alkyl side chains were produced to investigate post-functionalization methods with ultrasmall gold nanoparticles. All the compounds were obtained in sufficient quantity and purity to be used with GNP. Nevertheless, the complexity of each pathway, its cost and the final yield should be considered to determine the best α-D-mannose building block. For instance, long alkyl side chains ($C_6$) could not be purified *in vacuo* (low molecular weight linkers ($C_2$) evaporate *in vacuo* with the solvent).

The adaptation of bioorthogonal chemistry to ultrasmall nanoparticle platforms using an oligo-PEG terminal group as a binding moiety was performed with success. Modification of the PEG functional group was achieved in quantitative yields, resulting in the presentation of new terminal groups (e.g. azide, alkyne, amino-oxy, acetamide, hydroxyl and ester). This validates post-functionalization as a direct and easy method to modify the terminal group of oligo-PEG on GNP using low molecular weight, commercially available molecules. The newly formed particles possess characteristics that allow them to either work as a building block for further reactions or to present different physicochemical properties.

Post-functionalization with α-mannose derivatives resulted in different yields depending on the route chosen. The main conclusion is that the simplest pathways provide the best yields. Longer alkyne chains also had positive effects on the yields, probably taking advantage of a lower steric hindrance provided by the spacing of the reactive group from the carbohydrate.

The long alkyl side chain ($C_6$) α-mannose isothiourea coupling to the pegamine resulted in the highest yield and has the advantage of not using coupling reagents. However, the instability of isothiocyanate-compounds in aqueous medium or when exposed to moisture is a major drawback in this approach[66,67].

Amide coupling has the advantage of being well characterized and widely employed with nanoparticles[68]. On the other hand, this approach requires the use of coupling reagents, such as EDC/NHS, which have significant downsides, for instance, the formation of side products or the instability of the NHS-ester in water. Yet, with both PEG(5)NH$_2$ and PEG(8)COOH GNP, amide coupling reactions provided relatively high yields, making this pathway the most suitable for further experiments.

CuAAC click chemistry gave lower yields when compared with isothiourea or amide couplings. Moreover, unlike with peptides/proteins, its selectivity is not an advantage when it comes to carbohydrates since they don't present moieties susceptible to undergo cross-reactions.

The amino-oxy pathway to form oxime bonds provided good results, despite the high number of steps and the complexity of the carbohydrates used ($\alpha$-mannose1,2-$\alpha$-mannose, 1,3-$\alpha$-1,6-$\alpha$-D-mannotriose and maltotriose). Once the challenges of synthesis optimization and characterization were overcome, the oxime pathway was shown to be a straightforward route for the functionalization of GNP. The absence of the need for derivatization of the carbohydrates makes it a versatile method to attach oligosaccharides at low cost and with minimal effort.

To obtain the degree of functionalization and assess the ligand identity, the characterization of the particle corona is of key importance. Although $^1$H NMR was predominantly used, it was replaced by LC-CAD-MS for samples whose $^1$H NMR spectra were not interpretable. One of the objectives of this study was to optimize $^1$H NMR and incorporate new techniques, such as LC-CAD-MS, in the characterization portfolio of ultrasmall GNP. This work is described in more detail in *Chapter II*.

The conclusions obtained are based on the model of 2 nm core GNP with 44 ligands and 102 Au atoms per core[69]. This formula is theoretical and averaged. In *Chapters I and II*, analytical techniques that provide insight regarding the density of ligands were developed, and the actual amounts of the ligands rather than theoretical assumptions, were determined. To obtain more reliable data, the base particles should therefore be characterized more extensively prior to the post-functionalization processes.

Finally, to carry on with the work described in this chapter, post-functionalization research should be done using a rational design approach. For instance, the role that steric hindrance plays in this process could be thoroughly assessed by studying the impact that different GNP core sizes (non-plasmonic and plasmonic) or PEG chain lengths (e.g. 0.5-5 KDa) have on post-functionalization. Using amide bonds as a standard, amino $\alpha$-D-mannopyranosides with different side chains lengths or flexibility (alkyl versus oligo-ethylene glycol[70]) could be tested to assess the point of saturation, i.e. when the reaction yield reaches a plateau. Moreover, the conditions of coupling should be screened modifying one parameter at the time (e.g. solvents, temperature, time, coupling reagents), in order to find the most efficient protocol.

# V. Materials and Methods

## 1. Synthesis and analysis of α-mannose derivatives

Thin-layer chromatography (TLC) was used to monitor reactions (Silica Gel 60 F$_{254}$, Merck) using p-Anisaldehyde/Sulfuric acid/Acetic acid in methanol or ethanol as visualization reagents. Chromatographic purification was performed using a pre-column (Silica Gel 60 F$_{254}$, Merck) and a commercial 40 μm silica cartridge adapted on a flash chromatography system (Reveleris, Grace Davison Discovery Science). The evaporative light scattering detector (ELSD, monitors non-UV-absorbent molecules) of the device was used to spot, fraction and recover the reaction products. Characterization of the final product and, when possible intermediates, was performed by $^{1}$H NMR spectroscopy (500 MHz, CDCl$_3$ or D$_2$O). Final products were also analyzed by $^{13}$C NMR (126 MHz, D$_2$O). Experiments were performed at 298 K on a Bruker AVANCE III 500 spectrometer at CIC BiomaGUNE (San Sebastian, Spain).
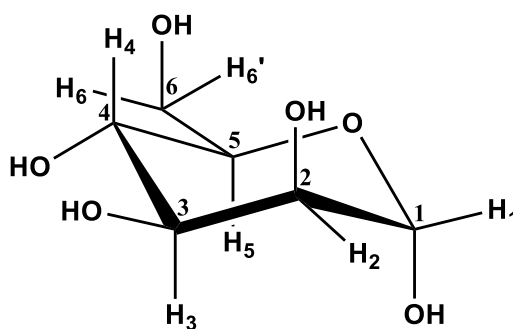


*Figure 11: α-Mannose with proton and carbon assignations.*

- General procedures for glycosylations: synthesis of **3**, **4**, **11**, **12**, **17** and **18**.

α-D-Mannopyranose pentaacetate (1 eq, Iris Biotech) was dissolved in anhydrous dichloromethane (CH$_2$Cl$_2$, 20-25 mL, Acros Organics) under an argon atmosphere. Linkers **1**, **2**, **9**, **10**, **15** or **16** (1.5-4 eq) and boron trifluoride diethyl etherate (BF$_3$.OEt$_2$) (1.5-4 eq, ρ 1.13 g/cm$^3$, Sigma-Aldrich) were added. The solution was stirred overnight at room temperature. After completion of the reaction determined by TLC, the reaction was quenched with triethylamine (Sigma-Aldrich) to neutral pH and the solvent evaporated *in vacuo*. The crude product was purified by flash chromatography on silica gel.

2-Ethoxycarbonylethyl 2,3,4,6-tetra-*O*-acetyl-α-D-mannopyranoside (**3**)

Prepared by the reaction of α-D-mannopyranose pentaacetate (2,2 g, 5.64 mmol) and ethyl 3-hydroxypropanoate (**1**) (948 μL, 8.45 mmol, ρ 1.054 g/cm$^3$, Combi-Blocks) with

BF₃.OEt₂ (1062 μL, 8.45 mmol). Flash chromatography (ethyl acetate/heptane, 1:4, SiO₂) resulted in a mixture of title compound (**3**) and α-D-mannopyranose pentaacetate.

**5-Ethoxycarbonylpentyl 2,3,4,6-tetra-*O*-acetyl-α-D-mannopyranoside (4)**

Prepared by the reaction of α-D-mannopyranose pentaacetate (3.0 g, 7.69 mmol) and ethyl 6-hydroxyhexanoate (**2**) (5.00 mL, 30.74 mmol, ρ 0.985 g/cm³, Sigma-Aldrich) with BF₃.OEt₂ (3.86 mL, 30.74 mmol). Flash chromatography (ethyl acetate/heptane, 1:10, SiO₂) resulted in a mixture of title compound (**4**) and linker (**2**).

**2-Propynyl 2,3,4,6-tetra-*O*-acetyl-α-D-mannopyranoside (11)**

Prepared by the reaction of α-D-mannopyranose pentaacetate (3.0 g, 7.69 mmol) and propargyl alcohol (2-propyn-1-ol) (**9**) (1.79 mL, 30.74 mmol, ρ 0.963 g/cm³, Sigma-Aldrich) with BF₃.OEt₂ (3.86 mL, 30.74 mmol). Flash chromatography (ethyl acetate/heptane, 1:3, SiO₂) gave the title compound (**11**) as a yellowish paste (700 mg, 1.81 mmol, 24 % yield). $^1$H NMR (500 MHz, CDCl₃) δ 5.35 – 5.25 (m, 3H, H-3, H-4, H-2), 5.02 (d, *J* = 1.8 Hz, 1H, H-1), 4.33 – 4.22 (m, 3H, H-6, -CH₂-O), 4.10 (dd, *J* = 12.2, 2.5 Hz, 1H, H-6'), 4.01 (ddd, *J* = 9.6, 5.1, 2.4 Hz, 1H, H-5), 2.47 (t, *J* = 2.4 Hz, 1H, -C≡CH), 2.16 (s, 3H, CH₃-C=O), 2.10 (s, 3H, CH₃-C=O), 2.03 (s, 3H, CH₃-C=O), 1.98 (s, 3H, CH₃-C=O).

**5-Hexynyl 2,3,4,6-tetra-*O*-acetyl-α-D-mannopyranoside (12)**

Prepared by the reaction of α-D-mannopyranose pentaacetate (2.0 g, 5.12 mmol) and 5-hexyn-1-ol (**10**) (2.26 mL, 20.49 mmol, ρ 0.89 g/cm³, Sigma-Aldrich) with BF₃.OEt₂ (2.57 mL, 20.49 mmol). Flash chromatography (ethyl acetate/heptane, 1:5, SiO₂) gave the title compound (**12**) as a yellowish paste (270 mg, 0.63 mmol, 12 %). $^1$H NMR (500 MHz, CDCl₃) δ 5.33 (dd, *J* = 10.0, 3.4 Hz, 1H, H-3), 5.26 (t, *J* = 10.0 Hz, 1H, H-4), 5.22 (dd, *J* = 3.4, 1.8 Hz, 1H, H-2), 4.80 (d, *J* = 1.7 Hz, 1H, H-1), 4.27 (dd, *J* = 12.2, 5.4 Hz, 1H, H-6), 4.10 (dd, *J* = 12.2, 2.4 Hz, 1H, H-6'), 3.97 (ddd, *J* = 9.9, 5.4, 2.4 Hz, 1H, H-5), 3.71 (dt, *J* = 9.7, 6.4 Hz, 1H, -CH₂-O), 3.48 (dt, *J* = 9.7, 6.3 Hz, 1H, -CH₂-O), 2.23 (dt, *J* = 6.9, 2.7 Hz, 2H, -C<u>H₂</u>-C≡CH), 2.14 (s, 3H, CH₃-C=O), 2.09 (s, 3H, CH₃-C=O), 2.03 (s, 3H, CH₃-C=O), 1.98 (s, 3H, CH₃-C=O), 1.96 (t, *J* = 2.6 Hz, 1H, -C≡CH), 1.73 (dq, *J* = 9.6, 8.2, 2.8 Hz, 2H, -CH₂-), 1.65 – 1.56 (m, 2H, -CH₂-).

2-Bromoethyl 2,3,4,6-tetra-*O*-acetyl-α-D-mannopyranoside (**17**)

Prepared by the reaction of α-D-mannopyranose pentaacetate (7.0 g, 17.93 mmol) and 2-bromo-1-ethanol (**15**) (5.09 mL, 71.73 mmol, ρ 1.76 g/cm$^3$, Sigma-Aldrich) with BF$_3$.OEt$_2$ (9.01 mL, 71.73 mmol). Flash chromatography (ethyl acetate/heptane, 1:3, SiO$_2$) gave the title compound (**17**) as a white solid (4.53 g, 9.95 mmol, 55 % yield). $^1$H NMR (500 MHz, CDCl$_3$) δ 5.34 (dd, *J* = 10.0, 3.4 Hz, 1H, H-3), 5.30 – 5.24 (m, 2H, H-4, H-2), 4.86 (d, *J* = 1.8 Hz, 1H, H-1), 4.26 (dd, *J* = 12.7, 5.9 Hz, 1H, H-6), 4.17 – 4.05 (m, 2H, H-5, H-6'), 3.97 (dt, J = 11.0, 6.3 Hz, 1H, -CH$_2$-O), 3.88 (dt, J = 11.3, 5.7 Hz, 1H, -CH$_2$-O), 3.51 (t, *J* = 6.0 Hz, 2H, -CH$_2$-Br), 2.15 (s, 3H, CH$_3$-C=O), 2.10 (s, 3H, CH$_3$-C=O), 2.04 (s, 3H, CH$_3$-C=O), 1.99 (s, 3H, CH$_3$-C=O).

6-Bromohexyl 2,3,4,6-tetra-*O*-acetyl-α-D-mannopyranoside (**18**)

Prepared by the reaction of α-D-mannopyranose pentaacetate (10.0 g, 25.62 mmol) and 6-bromo-1-hexanol (**16**) (10.06 mL, 76.86 mmol, ρ 1.384 g/cm$^3$, Sigma-Aldrich) with BF$_3$.OEt$_2$ (9.65 mL, 78.86 mmol). Flash chromatography (ethyl acetate/heptane, 1:5, SiO$_2$) resulted in a mixture of title compound (**18**) and linker (**16**) (450 mg total). $^1$H NMR (500 MHz, CDCl$_3$) δ 5.34 (dd, J = 10.0, 3.4 Hz, 1H, H-3), 5.27 (t, J = 10.0 Hz, 1H, H-4), 5.23 (dd, J = 3.4, 1.8 Hz, 1H, H-2), 4.80 (d, J = 1.8 Hz, 1H, H-1), 4.28 (dd, J = 12.2, 5.3 Hz, 1H, H-6), 4.11 (dd, J = 12.2, 2.5 Hz, 1H, H-6'), 3.97 (ddd, J = 9.9, 5.3, 2.4 Hz, 1H, H-5), 3.70 (dd, J = 9.6, 6.6 Hz, 1H, -CH$_2$-O), 3.46 (m, 1H, -CH$_2$-O), 3.42 (t, J = 6.7 Hz, 2H, -CH$_2$-Br), 2.15 (s, 3H, CH$_3$-C=O), 2.10 (s, 3H, CH$_3$-C=O), 2.04 (s, 3H, CH$_3$-C=O), 1.88 (m, 2H, -CH$_2$-), 1.68 – 1.35 (m, 6H, -CH$_2$-).

- General procedures for azide mannopyranosides: synthesis of **19** and **20**

Bromoalkyl-acetylated-mannopyranosides (1 eq) **17** or **18** were dissolved in N,N-dimethylformamide (30 mL, Acros Organics) under an argon atmosphere. Sodium azide (NaN$_3$, 1.5 eq, Sigma-Aldrich) and catalytic amounts of tetra-n-butylammonium iodide (TBAI, Sigma-Aldrich) and dibenzo-18-crown-6 (DB$_{18}$C$_6$, Sigma-Aldrich) were added. The solution was stirred at room temperature for 72 hours. After completion of the reaction determined by TLC, the crude mixture was diluted with ethyl acetate and washed successively with 0.1 M ammonium chloride (NH$_4$Cl), H$_2$O and brine. The organic layer was recovered, dried over anhydrous sodium sulfate (NaSO$_4$), filtered and the solvent removed by evaporation *in vacuo*. The crude product was purified by flash chromatography on silica gel.

2-Azidoethyl 2,3,4,6-tetra-*O*-acetyl-α-D-mannopyranoside (**19**)

Prepared by the reaction of 2-bromoethyl 2,3,4,6-tetra-*O*-acetyl-α-D-mannopyranoside (**17**) (4.53 g, 9.95 mmol) in N, N-dimethylformamide (30 mL) with $NaN_3$ (970 mg, 14.93 mmol). Flash chromatography (ethyl acetate/heptane, 1:4, $SiO_2$) gave the title compound (**19**) as a white powder (3.87 g, 9.27 mmol, 93 % yield). $^1$H NMR (500 MHz, $CDCl_3$) δ 5.35 (dd, $J$ = 10.0, 3.5 Hz, 1H, H-3), 5.32 – 5.24 (m, 2H, H-4, H-2), 4.86 (d, $J$ = 1.8 Hz, 1H, H-1), 4.28 (dd, $J$ = 12.3, 5.4 Hz, 1H, H-6), 4.12 (dd, $J$ = 12.3, 2.4 Hz, 1H, H-6'), 4.04 (ddd, $J$ = 9.9, 5.3, 2.4 Hz, 1H, H-5), 3.86 (ddd, $J$ = 10.6, 6.9, 3.7 Hz, 1H, -$CH_2$-O), 3.66 (ddd, $J$ = 10.6, 6.0, 3.6 Hz, 1H, -$CH_2$-O), 3.46 (qdd, J = 13.3, 6.4, 3.6 Hz, 2H, -$CH_2$-$N_3$), 2.15 (s, 3H, $CH_3$-C=O), 2.10 (s, 3H, $CH_3$-C=O), 2.04 (s, 3H, $CH_3$-C=O), 1.99 (s, 3H, $CH_3$-C=O).

6-Azidohexyl 2,3,4,6-tetra-*O*-acetyl-α-D-mannopyranoside (**20**)

Prepared by the reaction of the mixture containing 6-bromohexyl 2,3,4,6-tetra-*O*-acetyl-α-D-mannopyranoside (**18**) and 6-bromo-1-hexanol (**16**) (450 mg total, approximated 0.88 mmol) in N,N-dimethylformamide (30 mL) with $NaN_3$ (86 mg, 1.32 mmol). Flash chromatography (ethyl acetate/heptane, 1:5, $SiO_2$) gave the title compound (**20**) as a transparent paste (290 mg, 0.61 mmol, 2 % over 2 steps). $^1$H NMR (500 MHz, $CDCl_3$) δ 5.34 (dd, $J$ = 10.0, 3.5 Hz, 1H, H-3), 5.27 (t, $J$ = 10.0 Hz, 1H, H-4), 5.22 (dd, $J$ = 3.5, 1.8 Hz, 1H, H-2), 4.79 (d, $J$ = 1.7 Hz, 1H, H-1), 4.27 (dd, $J$ = 12.2, 5.3 Hz, 1H, H-6), 4.10 (dd, $J$ = 12.2, 2.5 Hz, 1H, H-6'), 3.97 (ddd, $J$ = 10.0, 5.3, 2.5 Hz, 1H, H-5), 3.67 (tt, $J$ = 15.0, 6.5 Hz, 1H, -$CH_2$-O), 3.44 (dt, $J$ = 9.6, 6.4 Hz, 1H, -$CH_2$-O), 3.27 (t, $J$ = 6.9 Hz, 2H, -$CH_2$-$N_3$), 2.15 (s, 3H, $CH_3$-C=O), 2.09 (s, 3H, $CH_3$-C=O), 2.04 (s, 3H, $CH_3$-C=O), 1.99 (s, 3H, $CH_3$-C=O), 1.67 – 1.55 (m, 6H, -$CH_2$-), 1.46 – 1.30 (m, 2H, -$CH_2$-).

- General procedures for isothiocyanate mannopyranosides: synthesis of **23** and **24**

Azidoalkyl-acetylated-mannopyranosides (1 eq) **19** and **20** were dissolved in toluene (30 mL, Scharlau). Carbon disulfide ($CS_2$, 10 eq, ρ 1.26 g/cm$^3$, Sigma-Aldrich) and triphenylphosphine (PPh$_3$, 3 eq, Sigma-Aldrich) were added. The solution was stirred whilst heating to reflux overnight at 50 °C. After completion of the reaction determined by TLC, the crude mixture was evaporated *in vacuo*. The crude product was purified by flash chromatography on silica gel.

2-Isothiocyanatoethyl 2,3,4,6-tetra-*O*-acetyl-α-D-mannopyranoside (**23**)

Prepared by the reaction of 2-azidoethyl 2,3,4,6-tetra-*O*-acetyl-α-D-mannopyranoside (**19**) (1.2 g, 2.88 mmol) dissolved in toluene (30 mL) with $CS_2$ (1.74 mL, 28.75 mmol) and $PPh_3$ (2.26 g, 8.63 mmol). Flash chromatography (ethyl acetate/heptane, 1:4, $SiO_2$) gave the title compound (**23**) as a white solid (1.21 g, 2.79 mmol, 97 % yield). $^1$H NMR (500 MHz, $CDCl_3$) δ 5.36 (dd, *J* = 10.0, 3.4 Hz, 1H, H-3), 5.32 – 5.24 (m, 2H, H-4, H-2), 4.87 (d, *J* = 1.8 Hz, 1H, H-1), 4.30 (dd, *J* = 12.3, 5.1 Hz, 1H, H-6), 4.12 (dd, *J* = 12.2, 2.5 Hz, 1H, H-6'), 4.08 (ddd, *J* = 9.6, 5.1, 2.4 Hz, 1H, H-5), 3.89 (m, 1H, -CH$_2$-O), 3.78 – 3.68 (m, 3H, -CH$_2$-O, -CH$_2$-NCS), 2.16 (s, 3H, CH$_3$-C=O), 2.11 (s, 2H, CH$_3$-C=O), 2.05 (s, 3H, CH$_3$-C=O), 1.99 (s, 2H, CH$_3$-C=O).

6-Isothiocyanatohexyl 2,3,4,6-tetra-*O*-acetyl-α-D-mannopyranoside (**24**)

Prepared by the reaction of 6-azidohexyl 2,3,4,6-tetra-*O*-acetyl-α-D-mannopyranoside (**20**) (100 mg, 0.24 mmol) dissolved in toluene (30 mL) with $CS_2$ (145 μL, 2.40 mmol) and $PPh_3$ (189 mg, 0.72 mmol). Flash chromatography (ethyl acetate/heptane, 1:4, $SiO_2$) gave the title compound (**24**) as a white solid (60 mg, 0.12 mmol, 51 % yield). $^1$H NMR (500 MHz, $CDCl_3$) δ 5.34 (dd, *J* = 10.0, 3.4 Hz, 1H, H-3), 5.28 (d, *J* = 10.4 Hz, 1H, H-4), 5.23 (dd, *J* = 3.5, 1.7 Hz, 1H, H-2), 4.80 (d, *J* = 1.7 Hz, 1H, H-1), 4.28 (dd, *J* = 12.2, 5.3 Hz, 1H, H-6), 4.11 (dd, *J* = 12.2, 2.6 Hz, 1H, H-6'), 3.97 (ddd, J = 9.9, 5.3, 2.5 Hz, 1H, H-5), 3.70 (dt, *J* = 9.7, 6.5 Hz, 1H, -CH$_2$-O), 3.53 (t, *J* = 6.6 Hz, 2H, -CH$_2$-NCS), 3.45 (dt, *J* = 9.6, 6.4 Hz, 1H, -CH$_2$-O), 2.15 (s, 3H, CH$_3$-C=O), 2.10 (s, 3H, CH$_3$-C=O ), 2.04 (s, 3H, CH$_3$-C=O), 1.99 (s, 3H, CH$_3$-C=O), 1.80 – 1.55 (m, 6H, -CH$_2$-), 1.51 – 1.36 (m, 4H, -CH$_2$-).

- General procedures for acetates deprotection: synthesis of **5**, **6**, **13**, **14**, **21**, **22**, **25** and **26**

Acetylated-mannopyranosides **3**, **4**, **11**, **12**, **19**, **20**, **23** and **24** were dissolved in anhydrous methanol (10-25 mL, Fluka). An excess of sodium methoxide (MeONa, Fluka) was added, and the solution was stirred at room temperature until determining visually the complete disappearance of the starting material by TLC. Amberlite resin IR-120 (H+, strongly acidic, Fluka) was added to obtain a neutral pH. The solution was filtered, and the solvent removed by evaporation *in vacuo*.

2-Methoxycarbonylethyl α-D-mannopyranoside (**5**)

Prepared by the overnight reaction in methanol (20 mL) with MeONa of the mixture containing 2-ethoxycarbonylethyl 2,3,4,6-tetra-*O*-acetyl-α-D-mannopyranoside (**3**) and α-D-mannopyranose pentaacetate. Flash chromatography (methanol/dichloromethane, 1:10, SiO$_2$) gave the title compound (**5**) as a solid (350 mg, 1.31 mmol, 23 % yield over 2 steps).

5-Methoxycarbonylpentyl α-D-mannopyranoside (**6**)

Prepared by the overnight reaction in methanol (25 mL) with MeONa of the mixture containing 5-ethoxycarbonylpentyl 2,3,4,6-tetra-*O*-acetyl-α-D-mannopyranoside (**4**) and ethyl 6-hydroxyhexanoate (**2**). Flash chromatography (methanol/dichloromethane, 1:10, SiO$_2$) gave the title compound (**6**) as a solid (440 mg, 1.43 mmol, 19 % yield over 2 steps).

2-Propynyl α-D-mannopyranoside (**13**)

Prepared by the reaction in methanol (20 mL) with MeONa for 2 hours of 2-propynyl 2,3,4,6-tetra-*O*-acetyl-α-D-mannopyranoside (**11**) (700 mg, 1.81 mmol). After evaporation, the title compound (**13**) was obtained as a red solid (380 mg, 1.74 mmol, 96 % yield). ^{1}H NMR (500 MHz, D$_2$O) δ 5.03 (dd, *J* = 312.3, 1.7 Hz, 1H, H-1), 4.31 (qd, *J* = 16.0, 2.4 Hz, 2H, -C$\underline{H}_2$-C≡CH), 3.95 (dd, *J* = 3.4, 1.7 Hz, 1H, H-2), 3.88 (dd, *J* = 12.3, 1.7 Hz, 1H, H-6), 3.81 – 3.74 (m, 2H, H-3, H-5), 3.70 – 3.63 (m, 2H, H-4, H-6'), 2.91 (t, *J* = 2.4 Hz, 1H, -C≡CH). ^{13}C NMR (126 MHz, D$_2$O) δ 98.7 (C-1), 78.8 (-C≡$\underline{C}$H), 76.1 (-$\underline{C}$≡CH), 73.1, 70.4, 69.9, 66.6 (C-5, C-2, C-3, C-4), 60.8 (C-6), 54.5 (-$\underline{C}$H$_2$-C≡CH).

5-Hexynyl α-D-mannopyranoside (**14**)

Prepared by the reaction in methanol (20 mL) with MeONa for 2 hours of 5-hexynyl 2,3,4,6-tetra-*O*-acetyl-α-D-mannopyranoside (**12**) (270 mg, 0.63 mmol). After evaporation, the title compound (**14**) was obtained as a yellowish paste (140 mg, 0.54 mmol, 85 % yield). ^{1}H NMR (500 MHz, D$_2$O) δ 4.87 (d, *J* = 1.7 Hz, 1H, H-1), 3.94 (dd, *J* = 3.5, 1.7 Hz, 1H, H-2), 3.89 (dd, *J* = 12.2, 1.7 Hz, 1H, H-6), 3.82 – 3.72 (m, 3H, H-3, H-5, -CH$_2$-O), 3.68 - 3.60 (m, 2H, H-6, H-4), 3.58 (dt, *J* = 10.0, 6.0 Hz, 1H, -CH$_2$-O), 2.37 (t, J= 2.7 Hz, 1H, -C≡CH), 2.26 (t, *J* = 7.0 Hz, 2H, -C$\underline{H}_2$-C≡CH), 1.73 (dqd, *J* = 8.8, 6.4, 3.3 Hz, 2H, -CH$_2$-), 1.66 – 1.53 (m, 2H, -CH$_2$-). ^{13}C NMR (126 MHz, D$_2$O) δ 99.7 (C-1), 85.9, 85.4 (-C≡$\underline{C}$H, -$\underline{C}$≡CH), 72.7, 70.6, 70.1, 67.3, 66.7, 60.9 (C-5, C-2, C-3, C-4, C-6, -$\underline{C}$H$_2$-C≡CH), 27.70, 24.54, 17.33 (-CH$_2$-CH$_2$-CH$_2$-).

2-Azidoethyl α-D-mannopyranoside (**21**)

Prepared by the reaction in methanol (20 mL) with MeONa for 2 hours of 2-azidoethyl 2,3,4,6-tetra-*O*-acetyl-α-D-mannopyranoside (**19**) (2.0 g, 4.79 mmol). After evaporation, the title compound (**21**) was obtained as a yellowish paste (1.17 g, 4.69 mmol, 98 % yield). $^1$H NMR (500 MHz, D$_2$O) δ 4.91 (d, $J$ = 1.7 Hz, 1H, H-1), 3.98 (dd, $J$ = 3.4, 1.8 Hz, 1H, H-2), 3.95 – 3.87 (m, 2H, -CH$_2$-O, H-6), 3.83 (dd, $J$ = 9.0, 3.3 Hz, 1H, H-3), 3.79 – 3.62 (m, 4H, -CH$_2$-O, H-6', H-5, H-4), 3.51 (qdd, $J$ = 13.7, 6.6, 3.1 Hz, 2H, -CH$_2$-N$_3$). $^{13}$C NMR (126 MHz, D$_2$O) δ 99.8 (C-1), 72.9, 70.4, 69.9, 66.7, 66.3 (C-5, C-2, C-3, C-4, -CH$_2$-O), 60.9 (C-6), 50.2 (-CH$_2$-N$_3$).

6-Azidohexyl α-D-mannopyranoside (**22**)

Prepared by the reaction in methanol (10 mL) with MeONa for 2 hours of 6-azidohexyl 2,3,4,6-tetra-*O*-acetyl-α-D-mannopyranoside (**20**) (200 mg, 0.42 mmol). After evaporation, the title compound (**22**) was obtained as a yellowish paste (150 mg, 0.49 mmol, 100 % yield). $^1$H NMR (500 MHz, D$_2$O) δ 4.86 (d, $J$ = 1.7 Hz, 1H, H-1), 3.93 (dd, $J$ = 3.5, 1.7 Hz, 1H, H-2), 3.88 (dd, $J$ = 12.2, 1.7 Hz, 1H, H-6), 3.81 – 3.71 (m, 3H, H-3, H-5, -CH$_2$-O), 3.68 - 3.59 (m, 2H, H-4, H-6'), 3.55 (dt, $J$ = 9.9, 6.1 Hz, 1H, -CH$_2$-O), 3.33 (t, $J$ = 6.9 Hz, 2H,-CH$_2$-N$_3$), 1.62 (m, 4H, -CH$_2$-CH$_2$-), 1.40 (m, 4H, -CH$_2$-CH$_2$-). $^{13}$C NMR (126 MHz, D$_2$O) δ 99.6 (C-1), 72.7, 70.6, 70.1, 67.8, 66.7 (C-5, C-2, C-3, C-4, -CH$_2$-O), 60.9 (C-6), 51.1 (-CH$_2$-N$_3$), 28.3, 27.9, 25.7, 24.9 (-CH$_2$-CH$_2$-CH$_2$-CH$_2$-).

2-Isothiocyanatoethyl α-D-mannopyranoside (**25**)

Prepared by the reaction in methanol (20 mL) with MeONa for 2 hours of 2-isothiocyanatoethyl 2,3,4,6-tetra-*O*-acetyl-α-D-mannopyranoside (**23**) (200 mg, 0.46 mmol). After evaporation, the title compound (**25**) was obtained as a white powder (120 mg, 0.45 mmol, 98 % yield). $^1$H NMR (500 MHz, D$_2$O) δ 4.88 (dd, $J$ = 10.4, 1.7 Hz, 1H, H-1), 4.05 (s, 2H), 3.97 – 3.89 (m, 2H), 3.87 (ddd, J = 12.2, 6.5, 2.4 Hz, 1H), 3.84 - 3.75 (m, 2H), 3.76 – 3.69 (m, 1H), 3.65 (dd, J = 9.5, 4.2 Hz, 1H), 3.54 (ddd, J = 13.8, 6.6, 3.8 Hz, 1H). $^{13}$C NMR (126 MHz, D$_2$O) δ 99.6 (C-1), 72.8, 70.5, 70.0, 66.6, 65.1 (C-5, C-2, C-3, C-4, -CH$_2$-O), 60.8 (C-6), 57.4 (-C̲H$_2$-NCS), 44.5 (-CH$_2$-NC̲S).

6-Isothiocyanatohexyl α-D-mannopyranoside (**26**)

Prepared by the reaction in methanol (10 mL) with MeONa for 2 hours of 6-isothiocyanatohexyl 2,3,4,6-tetra-*O*-acetyl-α-D-mannopyranoside (**24**) (60 mg, 0.12 mmol). After evaporation, the title compound (**26**) as a yellowish paste (30 mg, 0.09 mmol, 76 % yield). ^{1}H NMR (500 MHz, D$_2$O) δ 4.86 (d, *J* = 2.1 Hz, 1H, H-1), 3.96 - 3.92 (m, 2H, H-2, -CH$_2$-O), 3.89 (dd, *J* = 12.2, 2.0 Hz, 1H, H-6), 3.76 (tdd, J = 13.5, 9.3, 5.0 Hz, 3H, H-3, H-5, -CH$_2$-O), 3.69 – 3.51 (m, 4H, H-4, H-6', -CH$_2$-NCS), 1.74 – 1.57 (m, 4H, -CH$_2$-CH$_2$-), 1.49 – 1.33 (m, 4H, -CH$_2$-CH$_2$-). ^{13}C NMR (126 MHz, D$_2$O) δ 99.7 (C-1) 72.7, 70.6, 70.1, 67.7, 66.7 1 (C-5, C-2, C-3, C-4, -CH$_2$-O), 60.9 (C-6), 44.7 (-<u>C</u>H$_2$-NCS), 28.8, 28.3, 25.0, 24.6 (-CH$_2$-CH$_2$-CH$_2$-CH$_2$-).

- ▪ General procedures for carboxylate mannopyranosides: synthesis of **7** and **8**

Methoxycarbonyl-mannopyranosides **5** and **6** were dissolved in H$_2$O. 1 M aqueous sodium hydroxide (Sigma-Aldrich) was added and the solution was stirred overnight at room temperature. After completion of the reaction determined by TLC, Amberlite resin IR-120 (H+, strongly acidic, Fluka) was added to obtain a neutral pH. The solution was filtered, and the solvent removed *in vacuo*.

2-Carboxyethyl α-D-mannopyranoside (**7**)

Prepared by the reaction of 2-methoxycarbonylethyl α-D-mannopyranoside (**5**) (350 mg, 1.31 mmol) in H$_2$O (10 mL) with NaOH (3 mL). After evaporation, the title compound (**7**) was obtained as a white solid (300 mg, 1.19 mmol, 90 % yield). ^{1}H NMR (500 MHz, D$_2$O) δ 4.87 (d, *J* = 1.7 Hz, 1H, H-1), 3.99 (dt, *J* = 10.2, 6.1 Hz, 1H, -CH$_2$-O), 3.92 (dd, *J* = 3.4, 1.8 Hz, 1H, H-2), 3.88 (dd, *J* = 12.2, 1.6 Hz, 1H, H-6), 3.79 – 3.72 (m, 3H, H-3, H-5, -CH$_2$-O), 3.67 - 3.61 (m, 2H, H-4, H-6), 2.69 (t, *J* = 5.9 Hz, 2H, -CH$_2$-COOH). ^{13}C NMR (126 MHz, D$_2$O) δ 176.3 (-C=O), 99.8 (C-1), 72.74, 70.5, 70.0, 66.6, 63.2 (C-5, C-2, C-3, C-4, -CH$_2$-O), 60.8 (C-6), 34.4 (-<u>C</u>H$_2$-COOH).

5-Carboxypentyl α-D-mannopyranoside (**8**)

Prepared by the reaction of 5-methoxycarbonylpentyl α-D-mannopyranoside (**6**) (440 mg, 1.43 mmol) in H$_2$O (10 mL) with NaOH (3 mL). After evaporation, the title compound (**8**) was obtained as a white solid (390 mg, 1.33 mmol, 93 % yield). ^{1}H NMR (500 MHz, D$_2$O) δ 4.86 (d, J = 1.7 Hz, 1H, H-1), 3.93 (dd, J = 3.5, 1.7 Hz, 1H, H-2), 3.88 (dd, J = 12.2, 1.7 Hz, 1H,

H-6), 3.81 – 3.58 (m, 5H, H-3, H-5, -CH$_2$-O, H-4, H-6'), 3.55 (dt, J = 9.9, 6.1 Hz, 1H, -CH$_2$-O), 2.40 (t, J = 7.4 Hz, 2H, -CH$_2$-COOH), 1.74 – 1.58 (m, 4H, -CH$_2$-CH$_2$-), 1.41 (q, J = 7.6 Hz, 2H, -CH$_2$-). $^{13}$C NMR (126 MHz, D$_2$O) δ 179.0 (-C=O) 99.6 (C-1), 72.7, 70.6, 70.5, 70.1, 67.6, 66.7(C-5, C-2, C-3, C-4, -CH$_2$-O), 60.9 (C-6), 33.7 (-$\underline{C}$H$_2$-COOH), 28.1, 24.9, 24.0 (-CH$_2$-CH$_2$-CH$_2$-).

- ▪ General procedures for amine mannopyranosides: synthesis of **27** and **28**

Azidoalkyl-mannopyranosides (1 eq) **21** and **22** were dissolved in tetrahydrofuran/water (3:1 v/v). Triphenylphosphine (PPh$_3$, 3 eq, Sigma-Aldrich) was added and the solution was stirred overnight at room temperature. After completion of the reaction determined by TLC, the crude mixture was extracted with ethyl acetate. The aqueous layer was recovered, filtered and the solvent removed *in vacuo*.

2-Aminoethyl α-D-mannopyranoside (**27**)

2-Azidoethyl α-D-mannopyranoside (**21**) (500 mg, 2.01 mmol) was dissolved in tetrahydrofuran (15 mL) and H$_2$O (5 mL) with PPh$_3$ (1.58 g, 6.02 mmol) to give the title compound (**27**) as a yellowish paste (340 mg, 1.52 mmol, 76 % yield). $^1$H NMR (500 MHz, D$_2$O) δ 4.88 (d, J = 1.8 Hz, 1H, H-1), 3.97 (dd, J = 3.5, 1.8 Hz, 1H, H-2), 3.89 (dd, J = 12.1, 1.5 Hz, 1H, H6), 3.82 (qt, J = 6.0, 4.3, 3.6 Hz, 2H, -CH$_2$-O, H-3), 3.75 (ddd, J = 12.2, 4.5, 1.7 Hz, 1H, H-5), 3.71 – 3.55 (m, 3H, H-4, H-6, -CH$_2$-O), 3.01 – 2.90 (m, 2H, -CH$_2$-NH$_2$). $^{13}$C NMR (126 MHz, D$_2$O) δ 99.9 (C-1), 72.8, 70.5, 69.9, 66.8, 66.7 (C-5, C-2, C-3, C-4, -CH$_2$-O), 60.9 (C-6), 39.6 (-CH$_2$-NH$_2$).

6-Aminohexyl α-D-mannopyranoside (**28**)

6-Azidoethyl α-D-mannopyranoside (**22**) (70 mg, 0.23 mmol) was dissolved in tetrahydrofuran (7 mL) and H$_2$O (3 mL) with PPh$_3$ (180 mg, 0.69 mmol) to give the title compound (**28**) as a yellowish paste (40 mg, 0.14 mmol, 62 % yield). $^1$H NMR (500 MHz, D$_2$O) δ 4.86 (d, 1H, J= 2.0 Hz, H-1), 3.92 (m, 1H, H-2), 3.88 (dd, 1H, J= 12.5 Hz, 2.0 Hz, H-6), 3.76 (m, 3H, H-3, H-5, -CH$_2$-O), 3.65 (m, 2H, H-4, H-6'), 3.55 (m, 1H, -CH$_2$-O), 2.98 (t, 1H, J= 7.5 Hz, -CH$_2$-NH$_2$), 1.64 (m, 4H, -CH$_2$-CH$_2$-), 1.40 (m, 4H, -CH$_2$-CH$_2$-). $^{13}$C NMR (126 MHz, D$_2$O) δ 99.7 (C-1), 72.7, 70.6, 70.1, 67.7, 66.7 (C-5, C-2, C-3, C-4, -CH$_2$-O), 60.9 (C-6), 44.7 (-CH$_2$-NH$_2$), 28.8, 28.3, 25.6, 24.6 (-CH$_2$-CH$_2$-CH$_2$-CH$_2$-).

## 2. Synthesis and characterization of gold nanoparticles

To obtain the ligand identity and ratio, ^{1}H NMR, and to a lesser extent LC-CAD-MS, were used. Detailed synthesis protocols and analytical techniques are available in *Chapter II*.

### a. One-Pot ultrasmall GNP

- **GNP-1** = *GNP-13 Chap II*: $(PEG(5)NH_2)_{26}(\beta\text{-Glucose-}C_2)_{18}@Au_{102}$
- **GNP-2** = *GNP-8 Chap II*: $(PEG(5)NH_2)_{30}(\beta\text{-Glucose-}C_2)_{14}@Au_{102}$
- **GNP-3** = *GNP-10 Chap II*: $(PEG(8)COOH)_{22}(\alpha\text{-Galactose-}C_2)_{22}@Au_{102}$.

### b. Post-Functionalization

GNP-1 to GNP-3 were used for post-functionalization reactions. Reactions were performed with gold concentrations of 0.5-10 mg/mL and amounts varying from 5 to 50 mg Au. After completion of the reactions, the purifications were performed using 10 kDa Amicon 15-Ultra filters. Samples were resuspended in $H_2O$ and stored in an amber glass vial at 4 °C.

The amounts of reactants to perform the post-functionalization reactions were obtained using the equations described in *Chapter II*.

- Succinic anhydride and amine α-mannose route: **GNP-4**, **GNP-5** and **GNP-6**

An excess of succinic anhydride (20 equivalents, Sigma-Aldrich) diluted in DMSO was added to GNP-1 in 0.1 M sodium bicarbonate ($NaHCO_3$). The reaction was stirred overnight at room temperature with [Au] 0.5-5 mg/mL to obtain **GNP-4.**

The calculations for the equivalents of the following reactions were performed assuming a 100 % yield of functionalization during the previous step. DMSO was used as a solvent for the synthesis. EDC and NHS in excess (3 equivalents each, Sigma-Aldrich) were used to activate the -COOH of GNP-4. 10 equivalents of 2-Aminoethyl α-D-mannopyranoside (**27**) or 10 equivalents of 6-Aminohexyl α-D-mannopyranoside (**28**) were added to the activated particle. The reactions were stirred for 48 hours at 40 °C and [Au] 1 mg/mL to obtain **GNP-5** and **GNP-6**.

**GNP-4**: ^{1}H NMR (500 MHz, $D_2O$) β-Glucose-$C_2$ δ 4.49 (d, 1H, H-1, area: 1), PEG(5)NH$_2$ δ 2.83 (t, 2H, -CH$_2$-NH$_2$, area: 0.34) and R-CO-C$_2$H$_4$-COOH δ 2.50 (m, 4H, area 4.31). Ratio: β-Glucose-$C_2$/PEG(5)NH$_2$/R-CO-C$_2$H$_4$-COOH 44:8:48. Functionalization yield 86 %.

**GNP-5**: ^{1}H NMR (500 MHz, D$_2$O) β-Glucose-C$_2$ δ 4.50 (d, 1H, H-1, area :1), PEG(5)NH$_2$ δ 2.80 (t, 2H, -CH$_2$-NH$_2$, area: 0.30), R-CO-C$_2$H$_4$-COOH δ 2.47 (m, 4H, area: 3.07) and α-Mannose-C$_2$H$_4$-NH-CO-C$_2$H$_4$-CO-R δ 4.87 (d, 1H, H-1); 1.22 (t, 2H, area: 0.47). Ratio: β-Glucose-C$_2$/PEG(5)NH$_2$/R-CO-C$_2$H$_4$-COOH/α-Mannose-C$_2$H$_4$-NH-CO-C$_2$H$_4$-CO-R 46:7:36:11. α-Mannose 11 %.

**GNP-6**: ^{1}H NMR (500 MHz, D$_2$O) β-Glucose-C$_2$ δ 4.50 (d, 1H, H-1, area: 1), PEG(5)NH$_2$ δ 2.80 (t, 2H, -CH$_2$-NH$_2$, area: 0.29), R-CO-C$_2$H$_4$-COOH δ 2.47 (m, 4H, area: 2.93) and α-Mannose-C$_6$H$_{12}$-NH-CO-C$_2$H$_4$-CO-R δ 4.87 (d, 1H, H-1); 3.19 (t, 2H, area: 0.67). Ratio: β-Glucose-C$_2$/PEG(5)NH$_2$/R-CO-C$_2$H$_4$-COOH/α-Mannose-C$_6$H$_{12}$-NH-CO-C$_2$H$_4$-CO-R 45:7:33:15. α-Mannose 15 %.

- ▪ Alkyne GNP and azide α-mannose route: **GNP-7**, **GNP-8** and **GNP-9**

An excess of EDC and, either NHS using DMSO has a solvent, or sulfo-NHS using H$_2$O has a solvent were used in excess (3 equivalents each, Sigma-Aldrich and Thermo-Fisher) to activate 6-Heptynoic acid (3-5 equivalents, Sigma-Aldrich). The activated compound was added to GNP-1 in either DMSO or 10 mM PBS. The reaction was stirred overnight at room temperature and [Au] 3-5 mg/mL to obtain **GNP-7**.

The calculations for the equivalents of the following reactions were performed assuming a 100 % yield of functionalization during the previous step. H$_2$O was used as a solvent for the synthesis. 10 equivalents of 2-Azidoethyl α-D-mannopyranoside (**21**) or 6-Azidohexyl α-D-mannopyranoside (**22**) were added to GNP-7 with an excess of Tris(3-hydroxypropyltriazolylmethyl)amine (THPTA)/Copper sulfate (CuSO$_4$)/ Sodium Ascorbate. Sodium ascorbate was used as a reducing agent and THPTA as an accelerating ligand[71]. The reactions were stirred for 48 hours at 40 °C and [Au] 0.5 mg/mL to obtain **GNP-8** and **GNP-9**.

**GNP-7**: ^{1}H NMR (500 MHz, D$_2$O) β-Glucose-C$_2$ δ 4.49 (d, 1H, H-1, area: 1), PEG(5)NH$_2$ δ 2.83 (t, 2H, -CH$_2$-NH$_2$: area: 0.26) and R-CO-C$_4$H$_8$-C≡C δ 2.33 (t, 2H, area: 2.13); 2.28 (t, 2H); 1.74 (p, 2H); 1.57 (p, 2H). Ratio: β-Glucose-C$_2$/PEG(5)NH$_2$/R-CO-C$_4$H$_8$-C≡C 45:6:49. Functionalization yield 89 %.

**GNP-8**: [^1]H NMR (500 MHz, $D_2O$) β-Glucose-$C_2$ δ 4.50 (d, 1H, H-1, area: 1), PEG(5)$NH_2$ δ 2.80 (t, 2H, -$CH_2$-$NH_2$: area: 0.24), R-CO-$C_4H_8$-C≡C δ 2.29 (dt, 2H, area: 1.86) and α-Mannose-$C_2H_4$-1,2,3-Triazole-R δ 4.10 (dd, 1H); 3.00 (m, 1H, area: 0.44). Ratio: β-Glucose-$C_2$/PEG(5)$NH_2$/R-CO-$C_4H_8$-C≡C/α-Mannose-$C_2H_4$-1,2,3-Triazole-R 40:5:37:18. α-Mannose 18 %.

**GNP-9**: [^1]H NMR (500 MHz, $D_2O$) β-Glucose-$C_2$ δ 4.50 (d, 1H, H-1, area: 1); 3.26 (dd, 1H), PEG(5)$NH_2$ δ 2.79 (t, 2H, -$CH_2$-$NH_2$: area: 0.21), R-CO-$C_4H_8$-C≡C δ 2.29 (q, 2H, area: 1.90) and α-Mannose-$C_6H_{12}$-1,2,3-Triazole-R δ 4.41 (t, 2H, area: 0.87). Ratio: β-Glucose-$C_2$/PEG(5)$NH_2$/R-CO-$C_4H_8$-C≡C/α-Mannose-$C_6H_{12}$-1,2,3-Triazole-R 40:4:38:18. α-Mannose 18 %.

- ▪ Azide GNP and alkyne α-mannose route: **GNP-10**, **GNP-11** and **GNP-12**

An excess of EDC and, either NHS using DMSO has a solvent, or sulfo-NHS using $H_2O$ has a solvent were used in excess (3 equivalents each, Sigma-Aldrich and Thermo-Fisher) to activate 6-Azido-hexanoic acid (3-5 equivalents, Iris Biotech). The activated compound was added to GNP-1 in either DMSO or 10 mM PBS. The reaction was stirred overnight at room temperature and [Au] 3-10 mg/mL to obtain **GNP-10**.

The calculations for the equivalents of the following reactions were performed assuming a 100 % yield of functionalization during the previous step. $H_2O$ was used as a solvent for the synthesis. 10 equivalents of 2-Propynyl α-D-mannopyranoside (**13**) or 5-Hexynyl α-D-mannopyranoside (**14**) were added to GNP-10 with an excess of THPTA/$CuSO_4$/Sodium Ascorbate. The reactions were stirred for 48 hours at 40 °C and [Au] 0.5 mg/mL to obtain **GNP-11** and **GNP-12**.

**GNP-10**: [^1]H NMR (500 MHz, $D_2O$) β-Glucose-$C_2$ δ 4.50 (d, 1H, H-1, area: 1), PEG(5)$NH_2$ δ 2.80 (t, 2H, -$CH_2$-$NH_2$: area: 0.22) and R-CO-$C_5H_{10}$-$N_3$ δ 2.30 (t, 2H, area: 2.16); 1.65 (m, 4H); 1.40 (tt, 2H). Ratio: β-Glucose-$C_2$/PEG(5)$NH_2$/R-CO-$C_5H_{10}$-$N_3$ 46:5:49. Functionalization yield 91 %.

**GNP-11**: $^1$H NMR (500 MHz, D$_2$O) β-Glucose-C$_2$ δ 4.99 (d, 1H, H-1, area: 1), PEG(5)NH$_2$ δ 2.79 (t, 2H, -CH$_2$-NH$_2$: area: 0.30), R-CO-C$_5$H$_{10}$-N$_3$ δ 1.27 (p, 2H, area: 2.49) and α-Mannose-CH$_2$-2,3,4-Triazole-R δ 4.35 (m, 1H, area: 0.66). Ratio: β-Glucose-C$_2$/PEG(5)NH$_2$/R-CO-C$_5$H$_{10}$-N$_3$/α-Mannose-CH$_2$-2,3,4-Triazole-R 33:5:41:21. α-Mannose 21 %.

**GNP-12**: $^1$H NMR (500 MHz, D$_2$O) β-Glucose-C$_2$ δ 4.50 (d, 1H, H-1, area: 1); 3.26 (m, 1H), PEG(5)NH$_2$ δ 2.80 (t, 2H, -CH$_2$-NH$_2$: area: 0.20), R-CO-C$_5$H$_{10}$-N$_3$ δ 1.25 (p, 2H, area: 2.27) and α-Mannose-C$_4$H$_8$-2,3,4-Triazole-R δ 4.41 (t, 2H, area: 2.17) Ratio: β-Glucose-C$_2$/PEG(5)NH$_2$/R-CO-C$_5$H$_{10}$-N$_3$/α-Mannose-C$_4$H$_8$-2,3,4-Triazole-R 30:3:34:33. α-Mannose 33 %.

- Amine GNP and carboxylate α-mannose route: **GNP-13** and **GNP-14**

DMSO was used as a solvent for the synthesis. EDC and NHS in excess (3 equivalents each, Sigma-Aldrich) were used to activate 10 equivalents of 2-Carboxyethyl α-D-mannopyranoside (**7**) or 10 equivalents 5-Carboxypentyl α-D-mannopyranoside (**8**). The activated compounds were added to the GNP-1. The reactions were stirred for 48 hours at 40 °C and [Au] 1 mg/mL to obtain **GNP-13** and **GNP-14**.

**GNP-13**: $^1$H NMR (500 MHz, D$_2$O) β-Glucose-C$_2$ δ 4.50 (d, 1H, H-1, area: 1), PEG(5)NH$_2$ δ 2.81 (t, 2H, -CH$_2$-NH$_2$, area: 0.47) and α-Mannose-C$_2$H$_4$-CO-R δ 4.87 (d, 1H, H-1); 3.99 (m, 1H, area: 0.67). Ratio: β-Glucose-C$_2$/PEG(5)NH$_2$/α-Mannose-C$_2$H$_4$-CO-R 53:12:35. α-Mannose 35 %.

**GNP-14**: $^1$H NMR (500 MHz, D$_2$O) β-Glucose-C$_2$ δ 4.50 (d, 1H, H-1, area: 1), PEG(5)NH$_2$ δ 2.80 (t, 2H, -CH$_2$-NH$_2$, area: 0.66) and α-Mannose-C$_5$H$_{10}$-CO-R δ 4.87 (d, 1H, H-1); 2.30 (t, 2H, area: 1.65). Ratio: β-Glucose-C$_2$/PEG(5)NH$_2$/α-Mannose-C$_5$H$_{10}$-CO-R 47:15:38. α-Mannose 38 %.

- Amine GNP and isothiocyanate α-mannose route: **GNP-15** and **GNP-16**

DMSO was used as a solvent for the synthesis. 10 equivalents of 2-Isothiocyanatoethyl α-D-mannopyranoside (**25**) or 10 equivalents 6-Isothiocyanatohexyl α-D-mannopyranoside (**26**) were added to GNP-1. The reactions were stirred for 48 hours at 40 °C and [Au] 1 mg/mL to obtain **GNP-15** and **GNP-16**.

**GNP-15**: $^1$H NMR (500 MHz, D$_2$O) β-Glucose-C$_2$ δ 4.50 (d, 1H, H-1, area: 1, PEG(5)NH$_2$ δ 2.80 (t, 2H, -CH$_2$-NH$_2$, area: 1.12) and α-Mannose-C$_2$H$_4$-NCS-R δ 4.89 (d, 1H, H-1). PEG(5)NH$_2$ area of the starting material GNP-1 was subtracted to PEG(5)NH$_2$ area of the functionalized particle (2.65 - 1.12 = 1.53) to obtain the area of the newly formed ligand. Ratio: β-Glucose-C$_2$/PEG(5)NH$_2$/α-Mannose-C$_2$H$_4$-NCS-R 43:24:33. α-Mannose 33 %.

**GNP-16**: $^1$H NMR (500 MHz, D$_2$O) β-Glucose-C$_2$ δ 4.50 (d, 1H, H-1, area: 1), PEG(5)NH$_2$ δ 2.80 (t, 2H, -CH$_2$-NH$_2$, area: 0.39) and α-Mannose-C$_6$H$_{12}$-NCS-R δ 4.87 (d, 1H, H-1) is performed. PEG(5)NH$_2$ area of the starting material GNP-1 was subtracted to PEG(5)NH$_2$ area of the functionalized particle (2.65 - 0.39 = 2.26) to obtain the area of the newly formed ligand. Ratio: β-Glucose-C$_2$/PEG(5)NH$_2$/α-Mannose-C$_6$H$_{12}$-NCS-R 43:8:49. α-Mannose 49 %.

- Amine GNP and acetamide protection route: **GNP-17**

**GNP-17** = *GNP-17 Chap II*. Functionalization yield 93 %.

- Amino-oxy GNP and oligosaccharides route: **GNP-18**, **GNP-19**, **GNP-20** and **GNP-21**

  **GNP-18** = *GNP-20 Chap II*. Functionalization yield 72/86 %
  **GNP-19** = *GNP-21 Chap II*, α-Mannose1,2-α-Mannose 37 %
  **GNP-20** = *GNP-22 Chap II*, 1,3-α-1,6-α-D-Mannotriose 31 %
  **GNP-21** = *GNP-23 Chap II*, Maltotriose 31 %.

- Carboxylic acid GNP and amine α-mannose route: **GNP-22**

DMSO was used as a solvent for the synthesis. EDC and NHS in excess (3 equivalents each, Sigma-Aldrich) were used to activate the PEG(8)COOH of GNP-3. 10 equivalents of 2-Aminoethyl α-D-mannopyranoside (**27**) were added to the activated particle. The reaction was stirred for 48 hours at 40 °C and [Au] 1 mg/mL to obtain **GNP-22**.

**GNP-22**: $^1$H NMR (500 MHz, D$_2$O) α-Galactose-C$_2$ δ 4.98 (d, 1H, H-1, area: 1), PEG(8)COOH δ 2.49 (t, 2H, -CH$_2$-COOH, area: 0.05) and α-Mannose-C$_2$H$_4$-NH-R δ 4.87 (d, 1H, H-1, area: 0.82). Ratio: α-Galactose-C$_2$/PEG(8)COOH/α-Mannose-C$_2$H$_4$-NH-R 54:2:44. α-Mannose 44 %.

- Carboxylic acid GNP and methyl-ester protection route: **GNP-23**

**GNP-23** = *GNP-24 Chap II*. Functionalization yield 100 %.

- Carboxylic acid GNP and ethanolamine (hydroxyl) protection route: **GNP-24**

**GNP-24** = *GNP-25 Chap II*. Functionalization yield 74 %.

# VI. References

1. Poonthiyil, V., Lindhorst, T. K., Golovko, V. B. & Fairbanks, A. J. Recent applications of click chemistry for the functionalization of gold nanoparticles and their conversion to glyco-gold nanoparticles. *Beilstein J. Org. Chem.* **14**, 11–24 (2018).

2. Brust, M., Walker, M., Bethell, D., Schiffrin, D. J. & Whyman, R. Synthesis of thiol-derivatised gold nanoparticles in a two-phase Liquid–Liquid system. *J. Chem. Soc. Chem. Commun.* 801–802 (1994).

3. Algar, W. R. *et al.* The Controlled Display of Biomolecules on Nanoparticles: A Challenge Suited to Bioorthogonal Chemistry. *Bioconjug. Chem.* **22**, 825–858 (2011).

4. Hostetler, M. J., Templeton, A. C. & Murray, R. W. Dynamics of Place-Exchange Reactions on Monolayer-Protected Gold Cluster Molecules. *Langmuir* **15**, 3782–3789 (1999).

5. Smith, A. M. *et al.* Quantitative Analysis of Thiolated Ligand Exchange on Gold Nanoparticles Monitored by 1H NMR Spectroscopy. *Anal. Chem.* **87**, 2771–2778 (2015).

6. Barrientos, Á. G., Fuente, J. M. de la, Rojas, T. C., Fernández, A. & Penadés, S. Gold Glyconanoparticles: Synthetic Polyvalent Ligands Mimicking Glycocalyx-Like Surfaces as Tools for Glycobiological Studies. *Chem. – Eur. J.* **9**, 1909–1921 (2003).

7. Barrientos, A. G. *et al.* Modulating glycosidase degradation and lectin recognition of gold glyconanoparticles. *Carbohydr. Res.* **344**, 1474–1478 (2009).

8. Hermanson, G. T. Chapter 3 - The Reactions of Bioconjugation. in *Bioconjugate Techniques (Third edition)* 229–258 (Academic Press, 2013).

9. Froimowicz, P., Munoz-Espi, R., Landfester, K., Musyanovych, A. & Crespy, D. Surface-Functionalized Particles: From their Design and Synthesis to Materials Science and Bio-Applications. *Curr. Org. Chem.* **17**, 900–912 (2013).

10. Bogdan, N., Roy, R. & Morin, M. Glycodendrimer coated gold nanoparticles for proteins detection based on surface energy transfer process. *RSC Adv.* **2**, 985–991 (2012).

11. Pecháček, R., Velíšek, J. & Hrabcová, H. Decomposition Products of Allyl Isothiocyanate in Aqueous Solutions. *J. Agric. Food Chem.* **45**, 4584–4588 (1997).

12. Ma, P. *et al.* Inorganic nanocarriers for platinum drug delivery. *Mater. Today* **18**, 554–564 (2015).

13. Santiago, T. *et al.* Surface-enhanced Raman scattering investigation of targeted delivery and controlled release of gemcitabine. *Int. J. Nanomedicine* **12**, 7763–7776 (2017).

14. Jazayeri, M. H., Amani, H., Pourfatollah, A. A., Pazoki-Toroudi, H. & Sedighimoghaddam, B. Various methods of gold nanoparticles (GNPs) conjugation to antibodies. *Sens. Bio-Sens. Res.* **9**, 17–22 (2016).

15. Farr, T. D. *et al.* Imaging Early Endothelial Inflammation Following Stroke by Core Shell Silica Superparamagnetic Glyconanoparticles That Target Selectin. *Nano Lett.* **14**, 2130–2134 (2014).

16. Kang, B., Opatz, T., Landfester, K. & R. Wurm, F. Carbohydrate nanocarriers in biomedical applications: functionalization and construction. *Chem. Soc. Rev.* **44**, 8301–8325 (2015).

17. Wu, R. H. *et al.* A Facile Route to Tailoring Peptide-Stabilized Gold Nanoparticles Using Glutathione as a Synthon. *Molecules* **19**, 6754–6775 (2014).

18. Roskamp, M. *et al.* SIKVAV peptide functionalized ultra-small gold nanoparticles for selective targeting of α6β1 integrin in hepatocellular carcinoma. *J. Phys. Conf. Ser.* **829**, 012017 (2017).

19. Özcan, A. *et al.* Nanoparticle-coupled topical methotrexate can normalize immune responses and induce tissue remodeling in psoriasis. *J. Invest. Dermatol.* (2019).

20. Coupling Reagents -Bachem. https://www.google.com/url?sa=t&rct=j&q=&esrc=s&source=web&cd=1&cad=rja&uact=8 &ved=2ahUKEwiLrqGxpTcAhWE7BQKHedNAc0QFjAAegQIABAC&url=http%3A%2F% 2Fdocuments.bachem.com%2Fcoupling_reagents.pdf&usg=AOvVaw2X9eeVIXp7UYA51vI WzEBI.

21. NHS and Sulfo NHS - Thermo Fisher Scientific. http://www.thermofisher.com/order/catalog/product/24525.

22. Masereel, B. *et al.* Antibody immobilization on gold nanoparticles coated layer-by-layer with polyelectrolytes. *J. Nanoparticle Res.* **13**, 1573–1580 (2011).

23. Graça, V. C. *et al.* Ethylenediamine-Derived Chromatographic Ligand to Separate BSA, Lysozyme, and RNase A. *Chromatographia* **77**, 1529–1537 (2014).

24.    Boselli, L., Polo, E., Castagnola, V. & Dawson, K. A. Regimes of Biomolecular Ultrasmall Nanoparticle Interactions. *Angew. Chem. Int. Ed Engl.* **56**, 4215–4218 (2017).

25.    Meldal, M. & Tornøe, C. W. Cu-Catalyzed Azide−Alkyne Cycloaddition. *Chem. Rev.* **108**, 2952–3015 (2008).

26.    Collins, J., Xiao, Z., Müllner, M. & Connal, L. A. The emergence of oxime click chemistry and its utility in polymer science. *Polym. Chem.* **7**, 3812–3826 (2016).

27.    Ulrich, S., Boturyn, D., Marra, A., Renaudet, O. & Dumy, P. Oxime Ligation: A Chemoselective Click-Type Reaction for Accessing Multifunctional Biomolecular Constructs. *Chem. – Eur. J.* **20**, 34–41 (2014).

28.    Kalia, J. & Raines, R. T. Hydrolytic Stability of Hydrazones and Oximes. *Angew. Chem. Int. Ed Engl.* **47**, 7523–7526 (2008).

29.    Halkes, K. M., Souza, A. C. de, Maljaars, C. E. P., Gerwig, G. J. & Kamerling, J. P. A Facile Method for the Preparation of Gold Glyconanoparticles from Free Oligosaccharides and Their Applicability in Carbohydrate-Protein Interaction Studies. *Eur. J. Org. Chem.* **2005**, 3650–3659 (2005).

30.    Ansar, S. M. *et al.* Removal of Molecular Adsorbates on Gold Nanoparticles Using Sodium Borohydride in Water. (2013).

31.    Liu, Y. *et al.* Neoglycolipid Probes Prepared via Oxime Ligation for Microarray Analysis of Oligosaccharide-Protein Interactions. *Chem. Biol.* **14**, 847–859 (2007).

32.    Chuang, Y.-J., Zhou, X., Pan, Z. & Turchi, C. A convenient method for synthesis of glyconanoparticles for colorimetric measuring carbohydrate–protein interactions. *Biochem. Biophys. Res. Commun.* **389**, 22–27 (2009).

33.    Thygesen, M. B., Sauer, J. & Jensen, K. J. Chemoselective Capture of Glycans for Analysis on Gold Nanoparticles: Carbohydrate Oxime Tautomers Provide Functional Recognition by Proteins. *Chem. – Eur. J.* **15**, 1649–1660 (2009).

34.    Thygesen, M. B., Sørensen, K. K., Cló, E. & Jensen, K. J. Direct chemoselective synthesis of glyconanoparticles from unprotected reducing glycans and glycopeptide aldehydes. *Chem. Commun.* 6367–6369 (2009).

35. Nagahori, N., Abe, M. & Nishimura, S.-I. Structural and Functional Glycosphingolipidomics by Glycoblotting with an Aminooxy-Functionalized Gold Nanoparticle. *Biochemistry* **48**, 583–594 (2009).

36. Dirksen, A., Hackeng, T. M. & Dawson, P. E. Nucleophilic Catalysis of Oxime Ligation. *Angew. Chem. Int. Ed.* **45**, 7581–7584 (2006).

37. Rashidian, M. *et al.* A Highly Efficient Catalyst for Oxime Ligation and Hydrazone–Oxime Exchange Suitable for Bioconjugation. *Bioconjug. Chem.* **24**, 333–342 (2013).

38. Wendeler, M., Grinberg, L., Wang, X., Dawson, P. E. & Baca, M. Enhanced Catalysis of Oxime-Based Bioconjugations by Substituted Anilines. *Bioconjug. Chem.* **25**, 93–101 (2014).

39. Crisalli, P. & Kool, E. T. Water-soluble Organocatalysts for Hydrazone and Oxime Formation. *J. Org. Chem.* **78**, 1184–1189 (2013).

40. (Boc-aminooxy)acetic acid - Sigma Aldrich. https://www.sigmaaldrich.com/catalog/product/aldrich/15035 (2017).

41. Christman, K. L. *et al.* Protein Nanopatterns by Oxime Bond Formation. *Langmuir* **27**, 1415–1418 (2011).

42. Protection for the Amino Group. in *Greene's Protective Groups in Organic Synthesis* 895–1193 (Wiley-Blackwell, 2014).

43. Pierce Sulfo-NHS-Acetate - Thermo Fisher Scientific. https://www.thermofisher.com/order/catalog/product/26777 (2017).

44. Protection for the Carboxyl Group. in *Greene's Protective Groups in Organic Synthesis* 686–836 (Wiley-Blackwell, 2014).

45. Reactivities, Reagents, and Reactivity Charts. in *Greene's Protective Groups in Organic Synthesis* 1263–1332 (Wiley-Blackwell, 2014).

46. Loke, I., Kolarich, D., Packer, N. H. & Thaysen-Andersen, M. Emerging roles of protein mannosylation in inflammation and infection. *Mol. Aspects Med.* **51**, 31–55 (2016).

47. Sattin, S., Fieschi, F. & Bernardi, A. DC-SIGN as a Target for Drug Development Based on Carbohydrates. in *Carbohydrate Chemistry: State of the Art and Challenges for Drug Development* 379–394 (Imperial College Press, 2015).

48.     Li, R. E., van Vliet, S. J. & van Kooyk, Y. Using the glycan toolbox for pathogenic interventions and glycan immunotherapy. *Curr. Opin. Biotechnol.* **51**, 24–31 (2018).

49.     Lepenies, B., Lee, J. & Sonkaria, S. Targeting C-type lectin receptors with multivalent carbohydrate ligands. *Adv. Drug Deliv. Rev.* **65**, 1271–1281 (2013).

50.     The Development of Medium- and Large-Scale Sustainable Manufacturing Process Platforms for Clinically Compliant Solid Core Nanopharmaceuticals | NANOFACTURING Project | H2020 | CORDIS | European Commission. https://cordis.europa.eu/project/id/646364.

51.     Jang, K.-S. *et al.* Selective removal of anti-α-Gal antibodies from human serum by using synthetic α-Gal epitope on a core-shell type resin. *Biotechnol. Bioprocess Eng.* **13**, 445–452 (2008).

52.     Collot, M., Savreux, J. & Mallet, J.-M. New thioglycoside derivatives for use in odourless synthesis of MUXF3N-glycan fragments related to food allergens. *Tetrahedron* **64**, 1523–1535 (2008).

53.     Goyard, D. *et al.* Expedient synthesis of functional single-component glycoliposomes using thiol–yne chemistry. *J. Mater. Chem. B* **4**, 4227–4233 (2016).

54.     Yarlagadda, V., Konai, M. M., Manjunath, G. B., Ghosh, C. & Haldar, J. Tackling vancomycin-resistant bacteria with 'lipophilic–vancomycin–carbohydrate conjugates'. *J. Antibiot. (Tokyo)* **68**, 302–312 (2015).

55.     Boons, G.-J. Recent developments in chemical oligosaccharide synthesis. *Contemp. Org. Synth.* **3**, 173–200 (1996).

56.     Robina, I., Carmona, A. & J. Moreno-Vargas, A. Glycosylation Methods in Oligosaccharide Synthesis. Part 1. *Curr. Org. Synth.* **5**, 33–60 (2008).

57.     Kiessling, L. L. & Splain, R. A. Chemical Approaches to Glycobiology. *Annu. Rev. Biochem.* **79**, 619–653 (2010).

58.     Diwan, D. *et al.* Synthetic Assembly of Mannose Moieties Using Polymer Chemistry and the Biological Evaluation of Its Interaction towards Concanavalin A. *Molecules* **22**, 157 (2017).

59.     Ladmiral, V. *et al.* Synthesis of Neoglycopolymers by a Combination of "Click Chemistry" and Living Radical Polymerization. *J. Am. Chem. Soc.* **128**, 4823–4830 (2006).

60.     Varma, R. S., Naicker, K. P. & Aschberger, J. A Facile Preparation of Alkyl Azides from Alkyl Bromides and Sodium Azide Using 18-Crown-6 Ether Doped Clay. *Synth. Commun.* **29**, 2823–2830 (1999).

61.     Nakajima, Y., Kinishi, R., Oda, J. & Inouye, Y. Synthesis of Amino Compounds under Phase Transfer Conditions. *Bull. Chem. Soc. Jpn.* **50**, 2025–2027 (1977).

62.     García-Moreno, M. I. *et al.* One-step synthesis of non-anomeric sugar isothiocyanates from sugar azides. *Carbohydr. Res.* **337**, 2329–2334 (2002).

63.     Zemplén Deacetylation. in *Comprehensive Organic Name Reactions and Reagents* 3123–3128 (American Cancer Society, 2010).

64.     Collot, M., Wilson, I. B. H., Bublin, M., Hoffmann-Sommergruber, K. & Mallet, J.-M. Synthesis of cross-reactive carbohydrate determinants fragments as tools for in vitro allergy diagnosis. *Bioorg. Med. Chem.* **19**, 1306–1320 (2011).

65.     Pomin, V. H. Unravelling Glycobiology by NMR Spectroscopy. *Glycosylation* (2012).

66.     Jiménez Blanco, J. L. *et al.* A practical amine-free synthesis of symmetric ureas and thioureas by self-condensation if iso(thio)cyanates. *Synthesis* **1999**, 1907–1914 (1999).

67.     Barghash, R. F., Massi, A. & Dondoni, A. Synthesis of thiourea-tethered C-glycosyl amino acids viaisothiocyanate–amine coupling. *Org. Biomol. Chem.* **7**, 3319–3330 (2009).

68.     Conde, J. *et al.* Revisiting 30 years of biofunctionalization and surface chemistry of inorganic nanoparticles for nanomedicine. *Front. Chem.* **2**, (2014).

69.     Jadzinsky, P. D., Calero, G., Ackerson, C. J., Bushnell, D. A. & Kornberg, R. D. Structure of a Thiol Monolayer-Protected Gold Nanoparticle at 1.1 Å Resolution. *Science* **318**, 430–433 (2007).

70.     Shang, K. *et al.* Fabrication of Carbohydrate Chips Based on Polydopamine for Real-Time Determination of Carbohydrate–Lectin Interactions by QCM Biosensor. *Polymers* **10**, 1275 (2018).

71.     Presolski, S. I., Hong, V. P. & Finn, M. G. Copper-Catalyzed Azide–Alkyne Click Chemistry for Bioconjugation. *Curr. Protoc. Chem. Biol.* **3**, 153–162 (2011).

# Chapter IV


# Glyco-Gold Nanoparticles for Lectin Targeting

# I. Introduction

## 1. Glycans and C-type Lectins

Glycans are ubiquitous in nature and cover multiple structural and functional roles, such as energy storage, molecular recognition for intracellular trafficking and host-pathogen interactions[1]. The human monosaccharide library (D-α/β-mannose (Man), D-α-glucose (Glc), L-α-fucose (Fuc), D-β-galactose (Gal), D-α/β-*N*-acetylglucosamine (GlcNAc), D-α-*N*-acetylgalactosamine (GalNAc) and sialic acids (e.g. D-α-*N*-acetylneuraminic acid (NeuAc)), although quite limited in terms of building blocks, lead to an extensive number of oligomeric structures, due to the anomericity and the number of linkage positions. This heterogeneity is increased by the fact that glycans are usually conjugated to proteins (glycoproteins, proteoglycans) or lipids (glycolipids)[2].

C-type lectins or C-type lectin receptors (CLR) are a broad protein family of non-immune origin, with no catalytic activity, able to reversely bind exogenous or endogenous carbohydrates[3]. They possess one or several carbohydrate recognition domains (CRD) which determine their ligand specificity. C-type lectins are either secreted or transmembrane and many oligomerize, increasing the number of CRD per construct. Their common feature is the need for the divalent cation $Ca^{2+}$ to bind their respective ligands[4]. The binding features non-covalent hydrogen-bonding, hydrophobic stacking and, sometimes, ionic interactions. Water also plays an important role in the binding[3].

C-type lectin classification has been updated several times and is currently divided into 17 families, distinguished by their protein-domain architecture[5]. An updated list of human CLR is kept by the Imperial College London[6], and a comprehensive database has been created within the project UniLectin[7].

## 2. Antigen Presenting Cells and C-type Lectins

Transmembrane C-type lectins are present on Antigen Presenting Cells (APC), such as Dendritic Cells (DC) and macrophages, which recognize self and foreign glycoepitopes.

The immune system can be divided into two components: cellular and humoral, and into two subsystems: innate and adaptive (*Figure 1*).

APC are innate immunity cells. They have the capacity to capture, internalize, process and present antigens to lymphocytes. Naive T lymphocytes CD8^{+} and CD4^{+}, also referred to as T cells, are part of the adaptive immunity and bind to APC through major histocompatibility complex (MHC) of class I and II[8], respectively, in a process that leads to their activation and differentiation.

DC are professional APC with the capacity to induce a strong adaptive immune response in presence of a low level of antigen[9]. They are widely distributed and have high mobility, making them the sentinels of the body. They have an important uptake and presentation capacity and are also able to encounter and prime immature lymphocytes very efficiently[10].
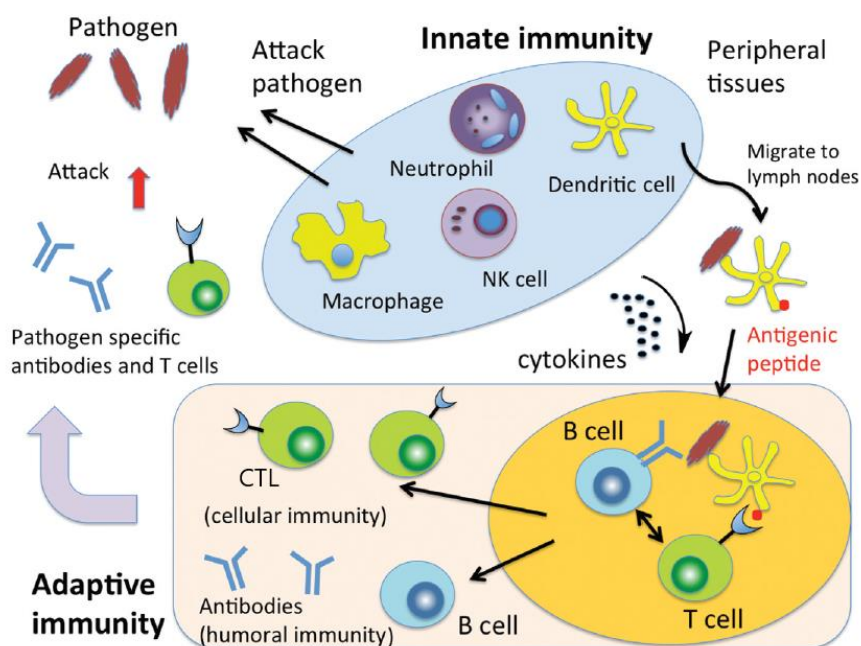


*Figure 1: Overview of the innate and adaptive immune system with its cellular and humoral components[11].*

C-type lectins on APC work as pattern recognition receptors (PRR) and recognize pathogen-associated molecular patterns (PAMP) and damaged-self-associated molecular patterns (DAMP)[11]. CLR mediated endocytosis triggers a cascade of intracellular signaling pathways that leads to phenotypical changes such as the presentation on the APC cell-surface of co-stimulatory molecules (CD80/CD86) and the secretion of cytokines and interferons[12]. Depending on the co-stimulating signals, CD4^{+} T lymphocytes differentiate to T helper Th1, Th2, Th17 or Treg cells, resulting in different immune responses. CD8^{+} T lymphocytes differentiate to Cytotoxic T Lymphocytes (CTL or Killer T Cells) (*Figure 2 and Figure 3*).

CLR implications exceed the infectious field, since they also play a role in sterile inflammations (non-pathogenic), such as auto-immune diseases, allergies or cancers. In the latter, CLR recognize tumor-associated carbohydrate antigens (TACA). Depending on the CLR engaged, tumor rejection or evasion can happen[13].
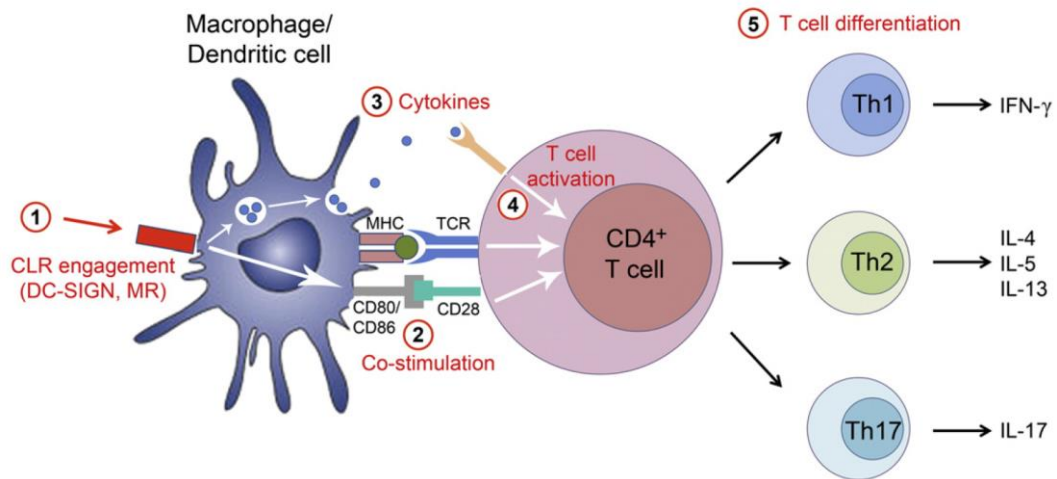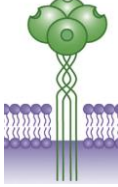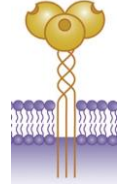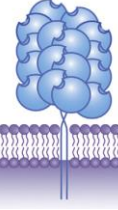


*Figure 2: Cascade of events following CLR binding to its ligand on APC[14].*

### a. Mannose-recognizing C-type Lectin Receptors (mrCLR)

APC possess numerous C-type lectin receptors with a variety of CRD[15]. Among them, mannose-recognizing C-type lectin receptors (mrCLR) include Dendritic Cell-Specific Intercellular adhesion molecule-3-Grabbing Non-integrin (DC-SIGN), the closely related DC-SIGNR, Langerin and Mannose Receptor (MMR or MR)[16] (*Table 1*).

The CRD of mrCLR generally contain an EPN (Glu-Pro-Asn) motif which gives them a specific affinity toward mannose and fucose essentially[17]. Depending on the type of ligand bound, different signaling cascades are activated[18]. mrCLR preferentially recognize the High Mannose ligand ($M_9$: $(Man)_9$-$(GlcNAc)_2$) and its truncated derivatives ($M_5$ and $M_3$), as well as the trimer 1,3-$\alpha$-1,6-$\alpha$-D-mannotriose or the dimer 2-*O*-($\alpha$-D-Mannopyranosyl)-D-mannopyranose ($\alpha$-mannose1,2$\alpha$-mannose)[19,20]. DC-SIGN and Langerin share common binding specificity toward $\alpha$-mannose and N-acetylglucosamine[21], but only the former can bind to Lewis[x] (Galactosyl-$\beta$-1,4-(fucosyl-$\alpha$-1,3)-*N*-acetylglucosamine) and Lewis[a] (Galactosyl-$\beta$-1,3-(fucosyl-$\alpha$-1,4)-*N*-acetylglucosamine) trisaccharides, while Langerin preferably recognizes sulfated sugars[22].

| Common denomination | Full denomination | Cluster of Differentiation (CD) | Cells expressing the CLR | CRD | Scheme |
|---|---|---|---|---|---|
| DC-SIGN [DC-SIGNR] | Dendritic Cell-Specific Intercellular adhesion molecule-3-Grabbing Non-integrin | CD209 [CD299] | Myeloid DC | 1 (tetramer) |  |
| Langerin | - | CD207 | Langerhans cells | 1 (trimer) |  |
| MMR (MR) | Mannose Receptor | CD206 | Myeloid DC and Macrophages | 8 (dimer) but only 2 CRD are binding carbohydrate ligands |  |

### b. DC-SIGN

DC-SIGN is a tetrameric C-type lectin with an inter CRD distance of 4 nm[23]. In addition to having four CRD, DC-SIGN also forms clusters/patches on the surface of dendritic cells, lowering the threshold to trigger the cluster glycoside effect[24]. DC-SIGN is implicated in the recognition and uptake of numerous pathogens, such as the viruses HSV (*Herpes simplex*), Human immunodeficiency virus (HIV), Dengue or Ebola, the bacteria *Mycobacterium tuberculosis* and *Helicobacter pylori* or the parasites *Schistosoma mansoni* and *Fasciola hepatica*[25,26]. Generally, DC-SIGN mediated uptake leads to an appropriate immune response and participates in the elimination of the pathogen. Nevertheless, in the case of HIV, the virus uses DC-SIGN and dendritic cells as a gateway to infect T cells[27].

DC-SIGN can also recognize tumor-associated carbohydrate antigens, such as the carcinoembryogenic antigen or Mac-2 binding protein present in some colorectal, pancreatic or lung cancers. Activation of anti-tumoral immunity using glycan complexes has been attempted with success, although tumors have also demonstrated a capacity to impair immune response through DC-SIGN and tumor associated macrophages (TAM)[13].

## 3. Targeting of C-type Lectins on Antigen Presenting Cells

The main goal of APC targeting using CLR is the design of vaccines in two major fields: anti-pathogenic and oncology[28,29]. CLR mediated enhancement of antigen uptake and tailored polarization of naive T lymphocytes could generate a customized immune response, triggering humoral immunity (B cells with antibodies) or cellular immunity (T cells with CTL).

To target C-type lectins, two approaches are possible: carbohydrates (or carbohydrate-derived ligands) and antibodies. Compared to the latter, carbohydrates have the drawbacks of interacting with various lectins and having weak interactions, with equilibrium dissociation constants ($K_D$) in the millimolar to micromolar range, but, on the other hand, they possess the advantage of triggering pre-existing signaling pathways. Glycan-based CLR targeting can, therefore, lead to the induction or redirection of a tailored and controlled adaptive immune response[12].

To improve the affinity and specificity of a glycan-based ligand to a CLR, two strategies can be used. Firstly, to modify the ligand using rational design to create glycomimetics with better activity, selectivity and physicochemical properties. Secondly, to take advantage of the cluster glycoside effect of a multivalent platform[30,31]. This phenomenon is achieved by the CLR oligomerization and/or clustering, and the multivalent presentation of the glycans[32]. The improved affinity involves chelate binding (simultaneous ligand-receptor bindings) or statistical rebinding (proximity effect)[3].

To obtain the highest interaction between a ligand and a lectin, its CRD topology should be fully understood to match the optimal distance, spatial orientation and valency. Multivalent platforms could be dendrimer, polymer, neoglycoprotein or nanoparticle based[14]. Apart from good affinity and specificity, monovalent compounds and multivalent platforms should also possess good pharmacological properties (e.g. solubility, toxicity, PKBD).

To understand and quantify the CLR-ligand interaction, several techniques are available. Determination of the equilibrium dissociation constant ($K_D$) or the or the half maximal inhibitory concentration ($IC_{50}$) can be performed, using surface plasmon resonance (SPR)[33], fluorescence[34], biolayer interferometry (BLI) or microarrays. Measurement of aggregation by dynamic light scattering (DLS) or minimum inhibitory concentration (MIC) by hemagglutination inhibition assays (HIA) are also common. Thermodynamic parameters can be measured using isothermal titration microcalorimetry (ITC). X-ray crystallography and NMR spectroscopy allow structural determination[3].
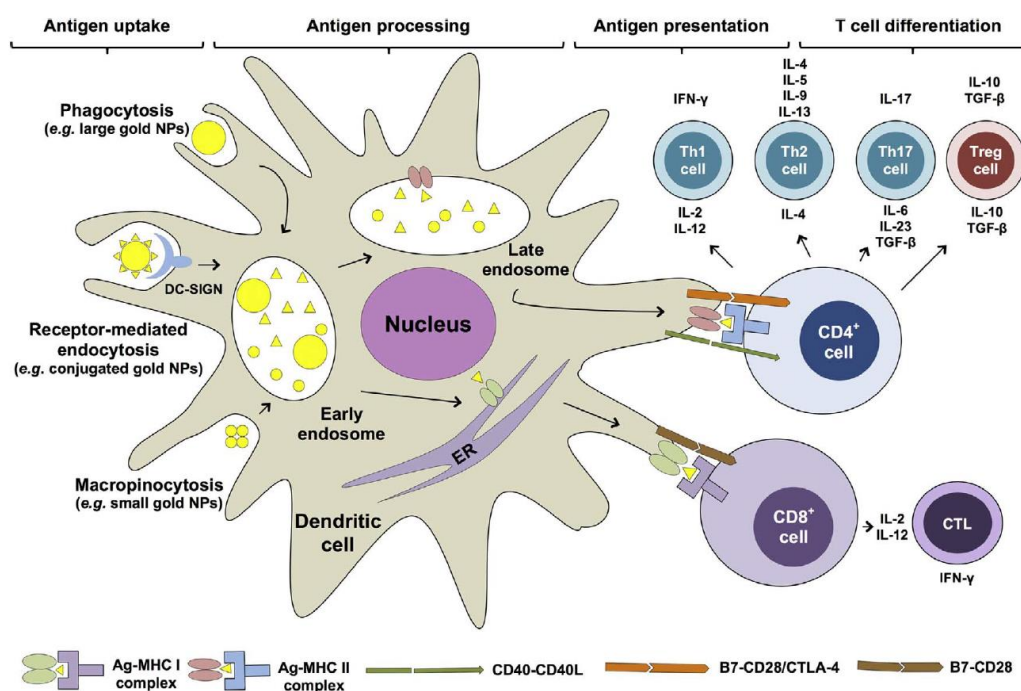
# 4. Gold Nanoparticles for C-type Lectin targeting



*Figure 3: Different phases following GNP-antigen uptake by APC[35].*

Gold nanoparticles possesses several advantages for the targeting of CLR:

- Highly customizable (size, shape, charge and surface functionalization) and can be finely adjusted to fit the CRD and obtain optimal affinity with the targeted lectin.
- High loading and co-presentation of ligands, for instance, a targeting agent and an active compound (e.g. a CLR binding ligand and an antigen)[14].
- Inert and stable[36].
- Passive targeting properties with tissue infiltration through enhanced permeability and retention (EPR) effect.
- Strong adjuvant properties[37].

To date and to the best of our knowledge, within the ultrasmall GNP field, only non-plasmonic Glyco-GNP (1.5-2 nm core) have been used to target DC-SIGN and elicit APC maturation. Structures bearing fucosylamide[38], galactofuranose[39], High Mannose and truncated epitopes have been published. SPR experiments showed that of these, the High Mannose derivative, α-mannose1,2α-mannose, was the best inhibitor[40]. The derivatives were tested *in vitro* using Raji and immature dendritic cells and showed a modest active cell uptake of GNP (measured by fluorescence)[41]. α-Mannose1,2α-mannose-GNP combined with peptides demonstrated an enhanced antigen presentation and T cell differentiation[42].

## II.  Objectives

In this chapter, the design of ultrasmall plasmonic and non-plasmonic GNP constructs for the targeting of C-type lectins, particularly DC-SIGN is reported.

The usual Brust-Schiffrin synthesis which produces an average core size of 2 nm has been modified to obtain particles with 4 nm cores. To target CLR, GNP incorporating α-mannose and derivatives were synthetized through post-functionalization reactions.

Two strategies were pursued:

- Using the monomer α-mannose and multiplying the number of molecules per particle using dendrons[43] (3 or 9 branched tridents)
- Using synthetic α-mannose1,2α-mannose[44] and the glycomimetics ISh045 and ISh046 developed to improve its affinity toward lectin receptors. The latter was designed to improve selectivity toward DC-SIGN, by not binding to Langerin[45].

To screen the constructs, two biochemical techniques were used: lectin microarray with fluorescent detection and biolayer interferometry. *In vitro* and *in vivo* assays were also performed.

The lectin microarray was performed with a broad variety of lectins. GNP were screened against lectins with different carbohydrate affinities (α-mannose, β-galactose or α-fucose). The lectins were tagged with a fluorophore and printed on a glass chip. GNP were incubated with the lectins and the chip was washed. The fluorescence of the chip was measured, and the GNP-incubated wells were compared to the buffer. A selective quenching of fluorescence depending on the CRD specificity of the lectins and the GNP functionalization was sought.

Biolayer interferometry analysis was accomplished with DC-SIGN. It is a fairly new technique, and while the affinity of lectins to glycoprotein[46] and glycoclusters[47] has been demonstrated using BLI, to the best of our knowledge, no work including GNP and human lectins has been published to date. The experiment consisted of coating DC-SIGN onto biosensor tips through biotin-streptavidin bonds and incubating the tips with different GNP to assess and eventually measure the binding.

An *in vitro* cell uptake assay was carried out on THP-1 cells, a cell line that expresses DC-SIGN. The expression was upregulated by treating the cells with interleukin 4 (IL-4) and phorbol 12-myristate 13-acetate (PMA)[48]. The GNP uptake was measured by the gold concentration in cells.

An *in vivo* PKBD assay in rats was conducted with GNP functionalized with α-mannose. Different organs, blood, urine and faeces were analyzed to determine the distribution of the GNP after parenteral injection.

# III.  Results and Discussion

## 1.  Gold Nanoparticle Library

Base GNP were obtained through a modified Brust–Schiffrin synthesis[49] using a software-controlled benchtop reactor. Two core sizes (2 and 4 nm) were produced by modulating the ratio between disulfide ligands and gold during the synthesis. 2 nm core GNP (non-plasmonic) were prepared using an excess of ligands, while 4 nm (plasmonic) were obtained with a minute amount (excess of ligands leads to a faster capping of the particles and blocks the core growth).

Two types of ligands were used to make the bifunctional GNP: a monosaccharide with a short $C_2$ side chain ($\beta$-Glucose-$C_2$ or $\alpha$-Galactose-$C_2$) and an oligo-polyethylene glycol (PEG(5)NH$_2$ or PEG(8)COOH).

The number of ligands and Au atoms per core were estimated using previously described models for 2 nm[50] and 4 nm[51] cores, according to the nano-scaling law[52]. The formulas were simplified for clarity (*Table 2*).

*Table 2: Bifunctional base GNP obtained by modified Brust–Schiffrin synthesis.*

| Batch | Core Size (nm) | Simplified Formula | Simplified Name |
|---|---|---|---|
| 1 | 2 | $(PEG(5)NH_2)_{22}(\alpha\text{-Galactose-}C_2)_{22}@Au_{102}$ | PEGNH$_2$ $\alpha$-Gal 2 nm |
| 2 | 2 | $(PEG(5)NH_2)_{26}(\beta\text{-Glucose-}C_2)_{18}@Au_{102}$ | PEGNH$_2$ $\beta$-Glc 2 nm |
| 3 | 2 | $(PEG(8)COOH)_{22\text{-}26}(\alpha\text{-Galactose-}C_2)_{22\text{-}18}@Au_{102}$ | PEGCOOH $\alpha$-Gal 2 nm |
| 4 | 4 | $(PEG(8)COOH)_{130}(\alpha\text{-Galactose-}C_2)_{160}@Au_{2000}$ | PEGCOOH $\alpha$-Gal 4 nm |

The terminal function of the PEG (amine or carboxylic acid) was used to perform post-functionalization reactions (*Figure 4*). The variety of molecules, but also the degree of functionalization provided a broad variety of constructs.
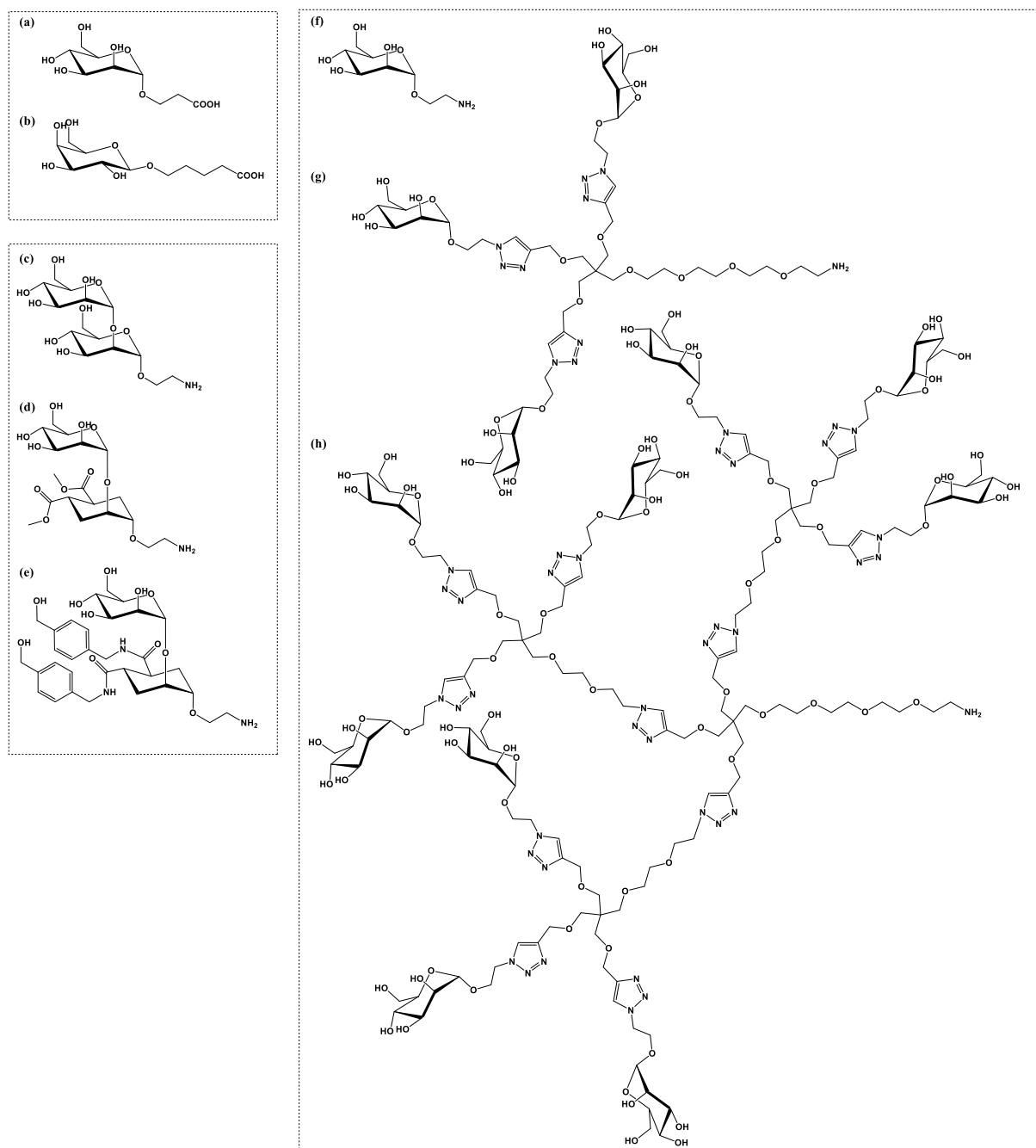
*Figure 4: Ligands bound to the GNP by post-functionalization. (a) α-Mannose and (b) β-Galactose with a terminal carboxylic acid on their side chain for conjugation with PEG(5)NH₂. (c) α-Mannose1,2α-mannose and its derivatives, the pseudo mannosides (d) ISh045 and (e) ISh046 have a side chain with a terminal amine for conjugation with PEG(8)COOH. (f) α-Mannose and the ramified (g) Dendron₃-α-Mannose and (h) Dendron₉-α-Mannose also have a terminal amine.*

α-Mannose (**a**) and β-Galactose (**b**) were coupled to the 2 nm pegamine GNP (**GNP-1** and **GNP-2**) with the goal of a complete loading of the amine groups. Approximately 20 carbohydrates (17-22) were bound to the GNP. The residual amines were capped with an acetate group (Ac), to avoid non-specific linking, using the commercially available Sulfo-NHS-Acetate. Control GNP without carbohydrate functionalization were protected by acetates (*Figure 5*).

α-Mannose and derivatives were bound to 2 nm PEG(8)COOH GNP (**GNP-3**). α-Mannose (**f**) loading was performed with two degrees of functionalization, complete (19 α-mannose) and partial (10 α-mannose). Other amine functionalized ligands were the disaccharide α-mannose1,2α-mannose (**c**), two pseudo-α-mannose1,2α-mannose: ISh045 (**d**) and ISh046 (**e**), Dendron$_3$-α-Mannose (**g**) and Dendron$_9$-α-Mannose (**h**). The loadings of PEG(8)COOH were partials with approximately 10 ligands per GNP (for d$_3$-αMan and d$_9$-αMan, the number of α-mannose molecules should be multiplied by the valence of the dendron: 21 and 63 α-mannose units, respectively) (*Figure 6*).

4 nm PEG(8)COOH GNP (**GNP-4**) were functionalized with the same ligands as GNP-3. 100-110 carbohydrate derivatives per GNP were loaded except for the dendrons (d$_3$-αMan 72 and d$_9$-αMan 52 molecules corresponding to 216 and 468 α-mannose units, respectively) (*Figure 7*).

2 nm core particles (**GNP-1** and **GNP-3**) were also functionalized with fluorophores to validate their ability to quench fluorescence using either fluorescein or (sulfo)rhodamine derivatives.

In total, twenty-seven constructs were obtained (*Table 2 and Table 3*; *fluorophore-loaded GNP not shown*).
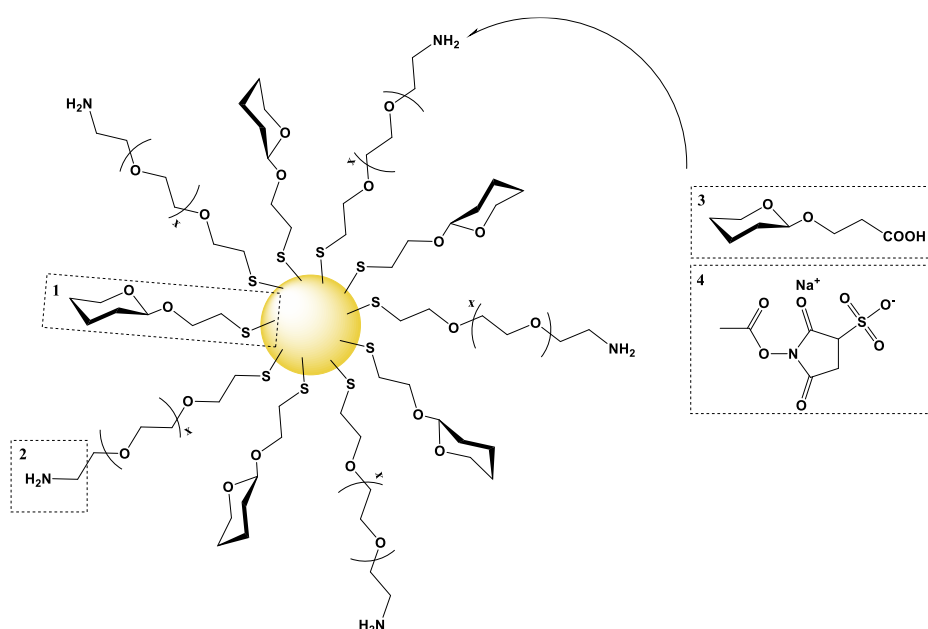


*Figure 5: Post-functionalization of (1) β-Glucose-C$_2$ or α-Galactose-C$_2$ and (2) PEG(5)NH$_2$ 2 nm GNP using (3) α-Mannose or β-Galactose with a side chain presenting a terminal carboxylic acid. (4) Sulfo-NHS-Acetate was used in a second step to protect the residual amines. Controls were obtained with Sulfo-NHS-Acetate without previous carbohydrate functionalization.*
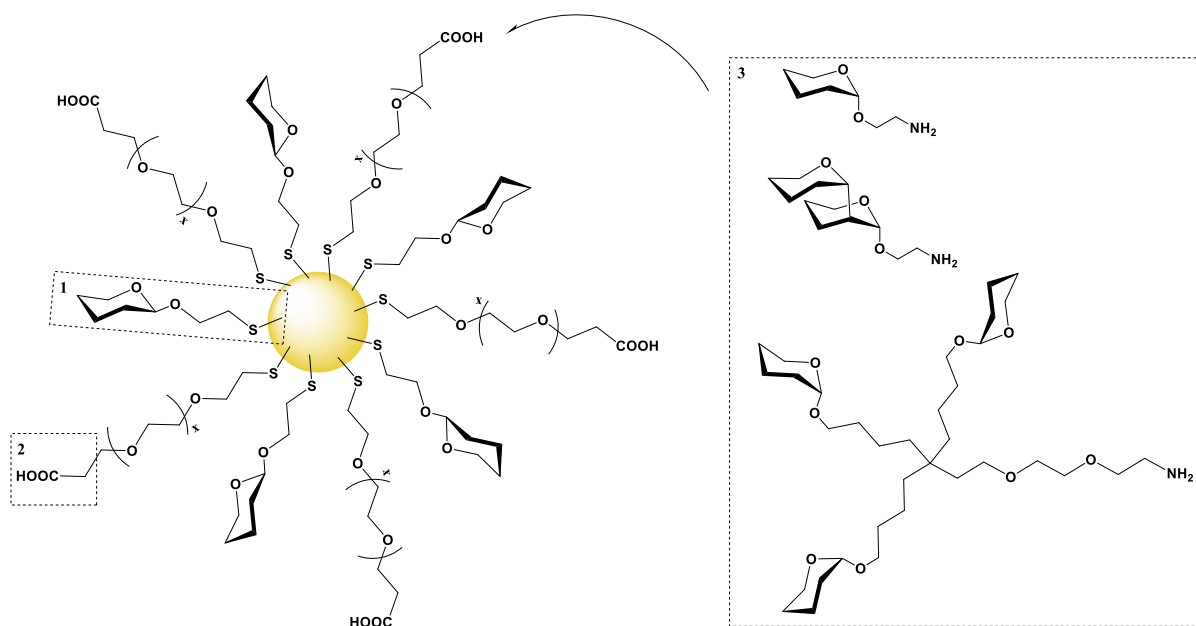
*Figure 6: Post-functionalization of (1) α-Galactose-C$_2$ and (2) PEG(8)COOH 2 nm GNP using (3)α-Mannose and derivatives with a side chain presenting a terminal amine.*
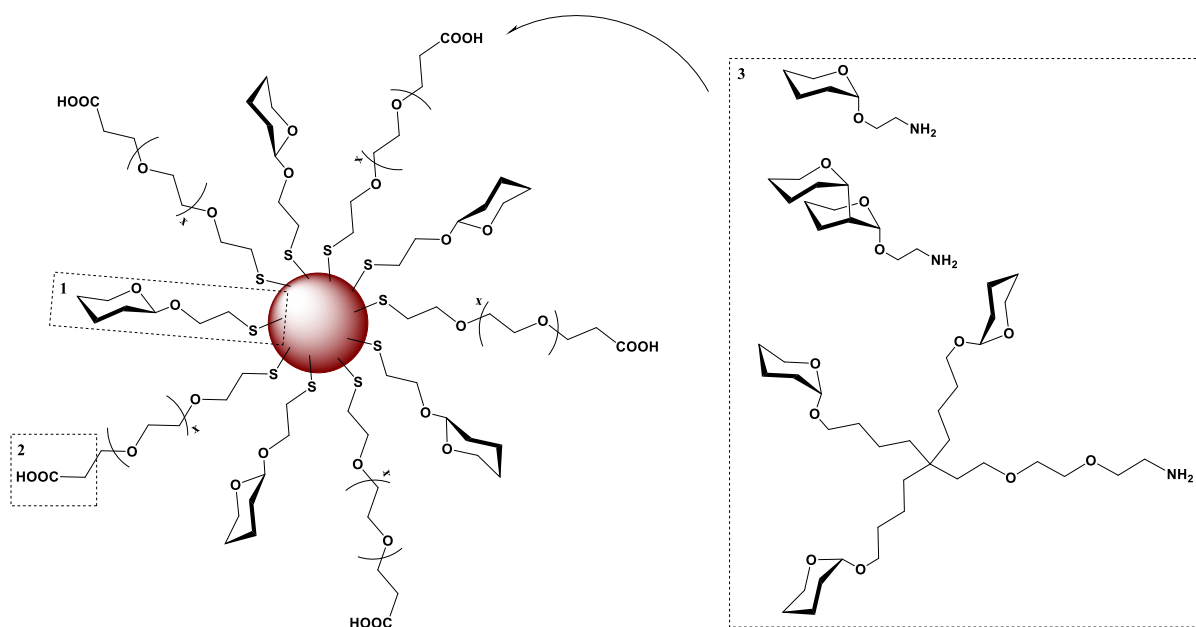


*Figure 7: Post-functionalization of (1) α-Galactose-C$_2$ and (2) PEG(8)COOH 4 nm GNP using (3)α-Mannose and derivatives with a side chain presenting a terminal amine.*

*Table 3: List of the different post-functionalized GNP.*

| Batch | Core Size (nm) | Simplified Formula | Simplified Name |
|---|---|---|---|
| 5 | 2 | ($\beta$-Galactose-C$_4$-CO-NH-PEG(5))$_{20}$(PEG(5)NHAc)$_2$(PEG(5)NH$_2$)$_1$($\alpha$-Galactose-C$_2$)$_{21}$@Au$_{102}$ | $\beta$-Gal PEGNH $\alpha$-Gal 2 nm |
| 6 | 2 | ($\alpha$-Mannose-C$_2$-CO-NH-PEG(5))$_{17}$(PEG(5)NHAc)$_3$(PEG(5)NH$_2$)$_2$($\alpha$-Galactose-C$_2$)$_{22}$@Au$_{102}$ | $\alpha$-Man PEGNH $\alpha$-Gal 2 nm |
| 7 | 2 | (PEG(5)NHAc)$_{21}$(PEG(5)NH$_2$)$_1$($\alpha$-Galactose-C$_2$)$_{22}$@Au$_{102}$ | PEGAc $\alpha$-Gal 2 nm |
| 8 | 2 | ($\beta$-Galactose-C$_4$-CO-NH-PEG(5))$_{22}$(PEG(5)NHAc)$_2$(PEG(5)NH$_2$)$_1$($\beta$-Glucose-C$_2$)$_{19}$@Au$_{102}$ | $\beta$-Gal PEGNH $\beta$-Glc 2 nm |
| 9 | 2 | ($\alpha$-Mannose-C$_2$-CO-NH-PEG(5))$_{17}$(PEG(5)NHAc)$_5$(PEG(5)NH$_2$)$_2$($\beta$-Glucose-C$_2$)$_{20}$@Au$_{102}$ | $\alpha$-Man PEGNH $\beta$-Glc 2 nm |
| 10 | 2 | (PEG(5)NHAc)$_{23}$(PEG(5)NH$_2$)$_2$($\beta$-Glucose-C$_2$)$_{19}$@Au$_{102}$ | PEGAc $\beta$-Glc 2 nm |
| 11 | 2 | ($\alpha$-Mannose-C$_2$-NH-CO-PEG(8))$_{19}$(PEG(8)COOH)$_1$($\alpha$-Galactose-C$_2$)$_{24}$@Au$_{102}$ | $\alpha$-Man 2 nm complete |
| 12 | 2 | ($\alpha$-Mannose-C$_2$-NH-CO-PEG(8))$_{10}$(PEG(8)COOH)$_{16}$($\alpha$-Galactose-C$_2$)$_{18}$@Au$_{102}$ | $\alpha$-Man PEGCOOH 2 nm partial |
| 13 | 2 | ($\alpha$-Mannose1,2$\alpha$-Mannose-NH-CO-PEG(8))$_{12}$(PEG(8)COOH)$_9$($\alpha$-Galactose-C$_2$)$_{23}$@Au$_{102}$ | $\alpha$-Man1,2-$\alpha$-Man PEGCOOH 2 nm |
| 14 | 2 | (ISh046-NH-CO-PEG(8))$_9$(PEG(8)COOH)$_{18}$($\alpha$-Galactose-C$_2$)$_{17}$@Au$_{102}$ | ISh046 PEGCOOH 2 nm |
| 15 | 2 | (ISh045-NH-CO-PEG(8))$_8$(PEG(8)COOH)$_{19}$($\alpha$-Galactose-C$_2$)$_{17}$@Au$_{102}$ | ISh045 PEGCOOH 2 nm |
| 16 | 2 | (Dendron$_3$-$\alpha$-Mannose-NH-CO-PEG(8))$_7$(PEG(8)COOH)$_{12}$($\alpha$-Galactose-C$_2$)$_{25}$@Au$_{102}$ | d$_3$-$\alpha$Man PEGCOOH 2 nm |
| 17 | 2 | (Dendron$_9$-$\alpha$-Mannose-NH-CO-PEG(8))$_7$(PEG(8)COOH)$_{13}$($\alpha$-Galactose-C$_2$)$_{24}$@Au$_{102}$ | d$_9$-$\alpha$Man PEGCOOH 2 nm |
| 18 | 4 | ($\alpha$-Mannose-C$_2$-NH-CO-PEG(8))$_{110}$(PEG(8)COOH)$_{20}$($\alpha$-Galactose-C$_2$)$_{160}$@Au$_{2000}$ | $\alpha$-Man PEGCOOH 4 nm |
| 19 | 4 | ($\alpha$-Mannose1,2$\alpha$-Mannose-NH-CO-PEG(8))$_{110}$(PEG(8)COOH)$_{20}$($\alpha$-Galactose-C$_2$)$_{160}$@Au$_{2000}$ | $\alpha$-Man1,2-$\alpha$-Man PEGCOOH 4 nm |
| 20 | 4 | (ISh046-NH-CO-PEG(8))$_{110}$(PEG(8)COOH)$_{20}$($\alpha$-Galactose-C$_2$)$_{160}$@Au$_{2000}$ | ISh046 PEGCOOH 4 nm |
| 21 | 4 | (ISh045-NH-CO-PEG(8))$_{104}$(PEG(8)COOH)$_{26}$($\alpha$-Galactose-C$_2$)$_{160}$@Au$_{2000}$ | ISh045 PEGCOOH 4 nm |
| 22 | 4 | (Dendron$_3$-$\alpha$-Mannose-NH-CO-PEG(8))$_{72}$( (PEG(8)COOH)$_{58}$($\alpha$-Galactose-C$_2$)$_{160}$@Au$_{2000}$ | d$_3$-$\alpha$Man PEGCOOH 4 nm |
| 23 | 4 | (Dendron$_9$-$\alpha$-Mannose-NH-CO-PEG(8))$_{52}$(PEG(8)COOH)$_{78}$($\alpha$-Galactose-C$_2$)$_{160}$@Au$_{2000}$ | d$_9$-$\alpha$Man PEGCOOH 4 nm |

## 2. Lectin Microarray: Fluorescence Quenching by Glyco-GNP

### a. Fluorescent GNP

To validate the fluorescence quenching ability of the studied GNP, 2 nm core constructs coated with fluorophores were designed (GNP-24 to GNP-27, *formula and characterization not shown*), using bioorthogonal covalent binding methods[53]. They exhibited a strong fluorescence quenching, which was reversed upon gold etching and ligand release by Tris(2-carboxyethyl)phosphine (TCEP) (*Figure 8, see in the annex*).
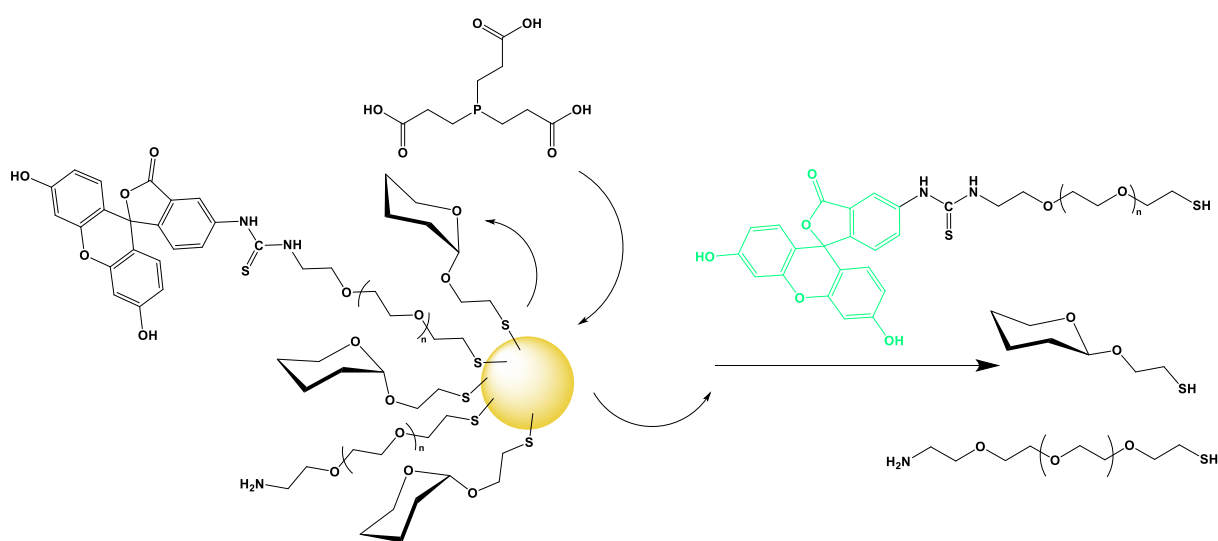


*Figure 8: Gold nanoparticle etching by TCEP and fluorescence release. Example of (PEG(5)NH-Fluorescein)$_{12}$(PEG(5)NH$_2$)$_{11}$($\alpha$-Galactose-C$_2$)$_{21}$@Au$_{102}$ .*

This result contradicts previous literature using fluorescent GNP (labeled with fluorescein isothiocyanate, FITC) to track their cellular internalization[41,54]. This could be attributed to the difference in linker lengths, which were longer compared to the PEG(8)COOH and PEG(5)NH$_2$ used in the assays reported here. In fact, not only is fluorescence quenching related to particle size, shape and distance between the fluorophore and the core, but also to the fluorophore itself (excitation and emission wavelengths). Smaller particles and a shorter distance between core and fluorophore usually result in a stronger quenching[55,56,57].

### b. Lectin Microarray

Lectin microarray allows rapid and sensitive profiling of glycans (*Figure 9*). It consists of a glass slide coated with reactive functional groups (e.g. NHS ester, epoxy), to which the lectins can be efficiently bound. The immobilization is usually performed by a robotic spotter. After spotting, the remaining reactive groups are blocked and the analyte to be screened is incubated on the slide. Finally, the slide is extensively washed and the binding measured[58].

To obtain reliable results, the orientation and the density of the lectin are critical parameters and the slide material (2D rigid versus 3D flexible) should be chosen carefully[59]. Lectin printing and drying should also be optimized to avoid, or at least, reduce, heterogeneous ring-shape (donut) spots[60].
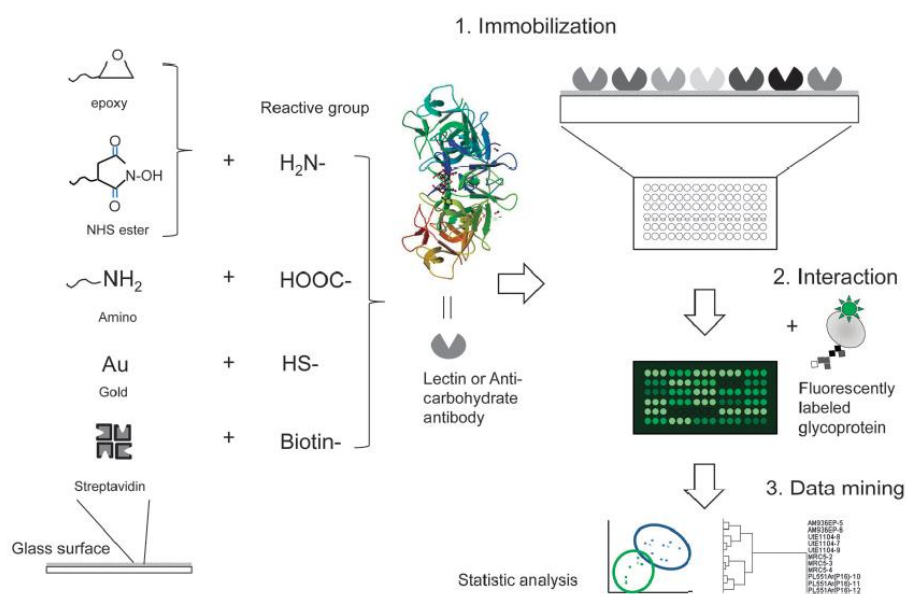


*Figure 9: Lectin (glycan) microarray principle using fluorescent detection[58].*

The usual microarray (lectin or glycan) uses confocal-type fluorescence to detect and quantify the interactions. Lectins on the slide are incubated with a fluorescent analyte (or subsequently tagged using a sandwich fluorescence technique) and the stronger the interaction the greater the fluorescence.

For the following experiment with GNP, the opposite principle was used: fluorescent lectins were printed on a chip and fluorescence quenching upon GNP binding was observed[61].

Taking advantage of the high-throughput characteristic of microarrays, GNP were screened against a range of plant (L-type), bacterial and fungal lectins before being tested with DC-SIGN (*Table 4*). Non-mammalian lectins are commonly used to validate and optimize assays due to their inexpensiveness and the wide variety available[58]. The L-type lectins, Concanavalin A (ConA), *Hippeastrum hybrid* Lectin (HHL) and *Narcissus pseudonarcissus* Lectin (NPA/NPL), are mannose specific. *Pseudomonas aeruginosa* agglutinin (PA-IL) and *Aleuria aurantia* Lectin (AAL) are galactose and fucose specific, respectively.

*Table 4: List of lectins used in the microarray and their carbohydrate specificities.*

| Name | Origin | Monosaccharide specificity | Preferred Sugar |
|---|---|---|---|
| ConA | *Canavalia ensiformis* | Mannose | High-Mannose |
| HHL | *Hippeastrum hybrid* | Mannose | High-Mannose |
| NPA = NPL | *Narcissus pseudonarcissus* | Mannose | High-Mannose |
| PA-IL | bacteria, *Pseudomonas aeruginosa* | Galactose | β-Galactose |
| AAL | fungus, *Aleuria aurantia* | Fucose | Core Fucose: Fucα1,6GlcNAc<br>Le$^X$: Galβ1,4(Fucα1,3)GlcNAc |
| DC-SIGN | human, from recombinant *Escherichia coli* | Mannose | High-Mannose |

The lectins were incubated with a fluorophore (Alexa Fluor 555 or Cy3), purified, and the degree of labeling was measured. Fluorescent tagging was performed to obtain approximately one fluorophore per lectin. Using a robotic spotter, the lectins were printed on an NHS-reactive slide. After incubation, empty sites were blocked, and the slide was washed. The lectin-coated fluorescent slide was incubated with the different GNP for 2 hours with a gold concentration of 0.1 mg/mL, and the slide was then washed (*Figure 10*). The fluorescence was measured, and the GNP-containing wells were compared to the buffer well to obtain the relative percentage of fluorescence. GNP presenting a strong binding to the lectins remained on the slide after washing and the fluorescence was quenched.
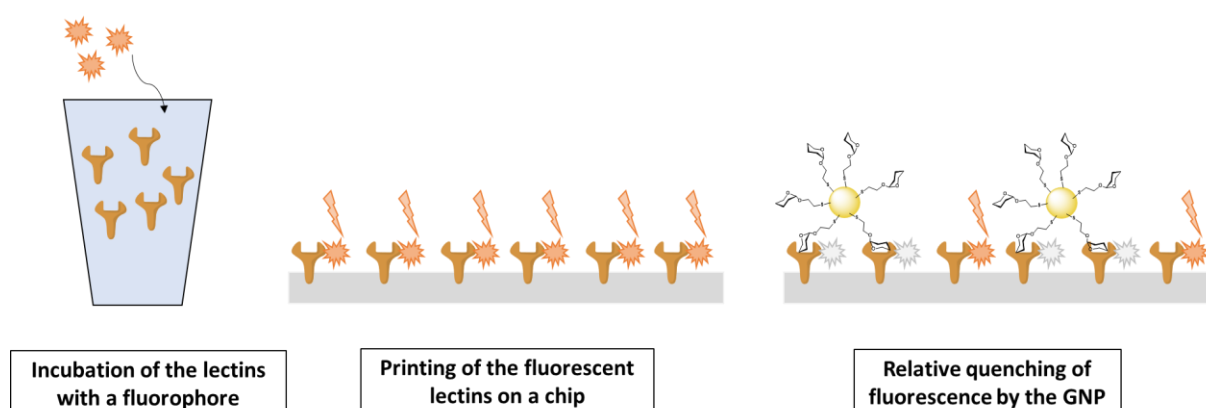


Incubation of the lectins with a fluorophore

Printing of the fluorescent lectins on a chip

Relative quenching of fluorescence by the GNP

*Figure 10: General principle of microarray with fluorescent lectins and GNP.*

*Figure 11: Relative fluorescence of (I) 2 nm PEG(5)NH$_2$, (II) 2 nm PEG(8)COOH and (III) 4 nm PEG(8)COOH GNP derivatives incubated on a chip printed with ConA.*
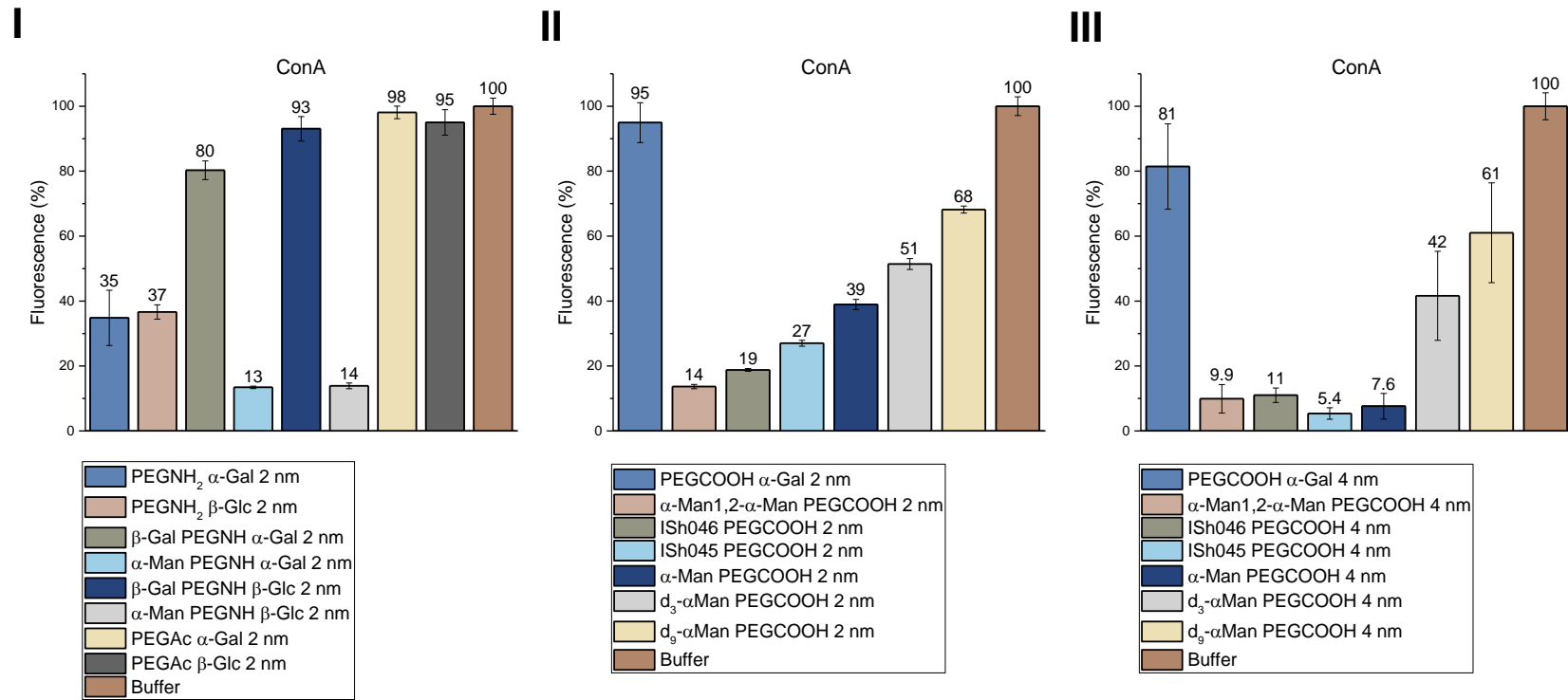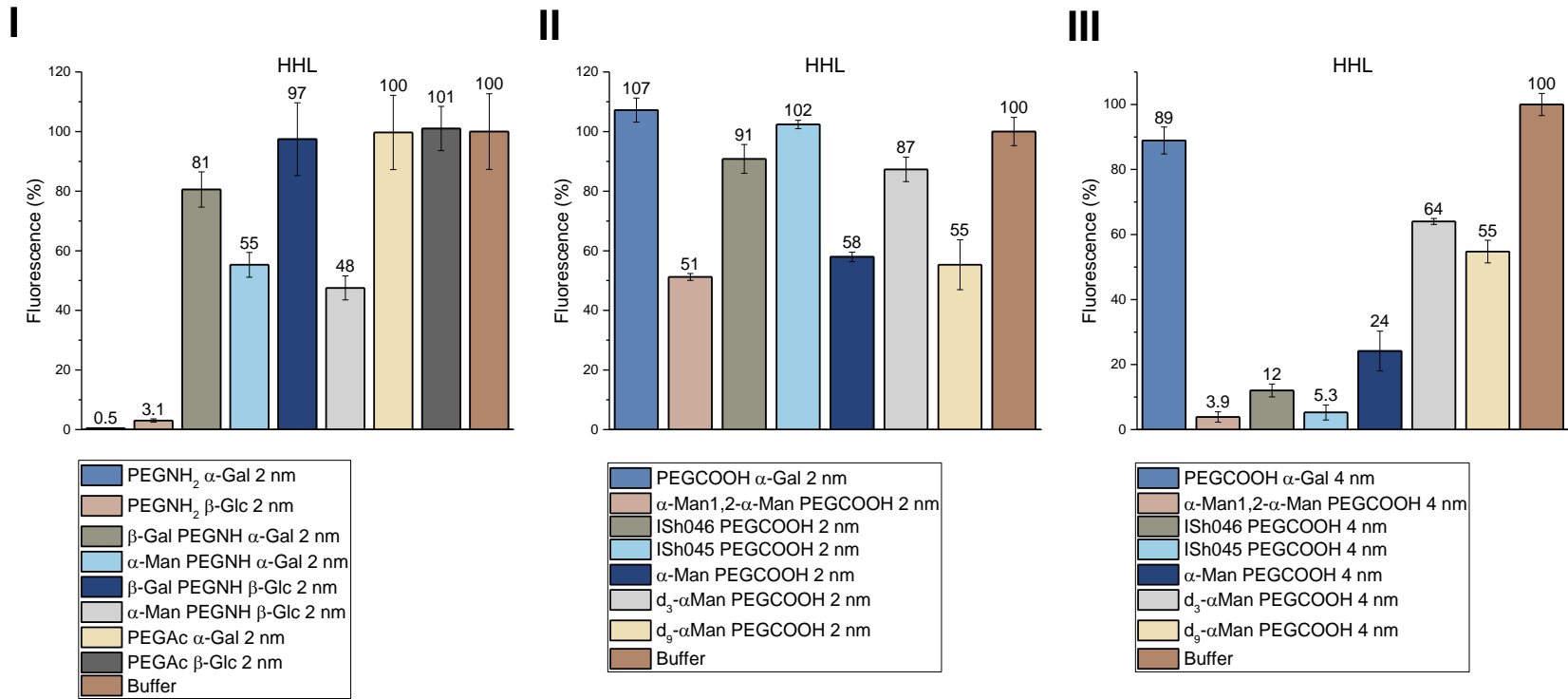
*Figure 12: Relative fluorescence of (I) 2 nm PEG(5)NH₂, (II) 2 nm PEG(8)COOH and (III) 4 nm PEG(8)COOH GNP derivatives incubated on a chip printed with HHL.*

*Figure 13: Relative fluorescence of (I) 2 nm PEG(5)NH₂, (II) 2 nm PEG(8)COOH and (III) 4 nm PEG(8)COOH GNP derivatives incubated on a chip printed with NPL.*

*Figure 14: Relative fluorescence of (I) 2 nm PEG(5)NH$_2$, (II) 2 nm PEG(8)COOH and (III) 4 nm PEG(8)COOH GNP derivatives incubated on a chip printed with PA-IL.*
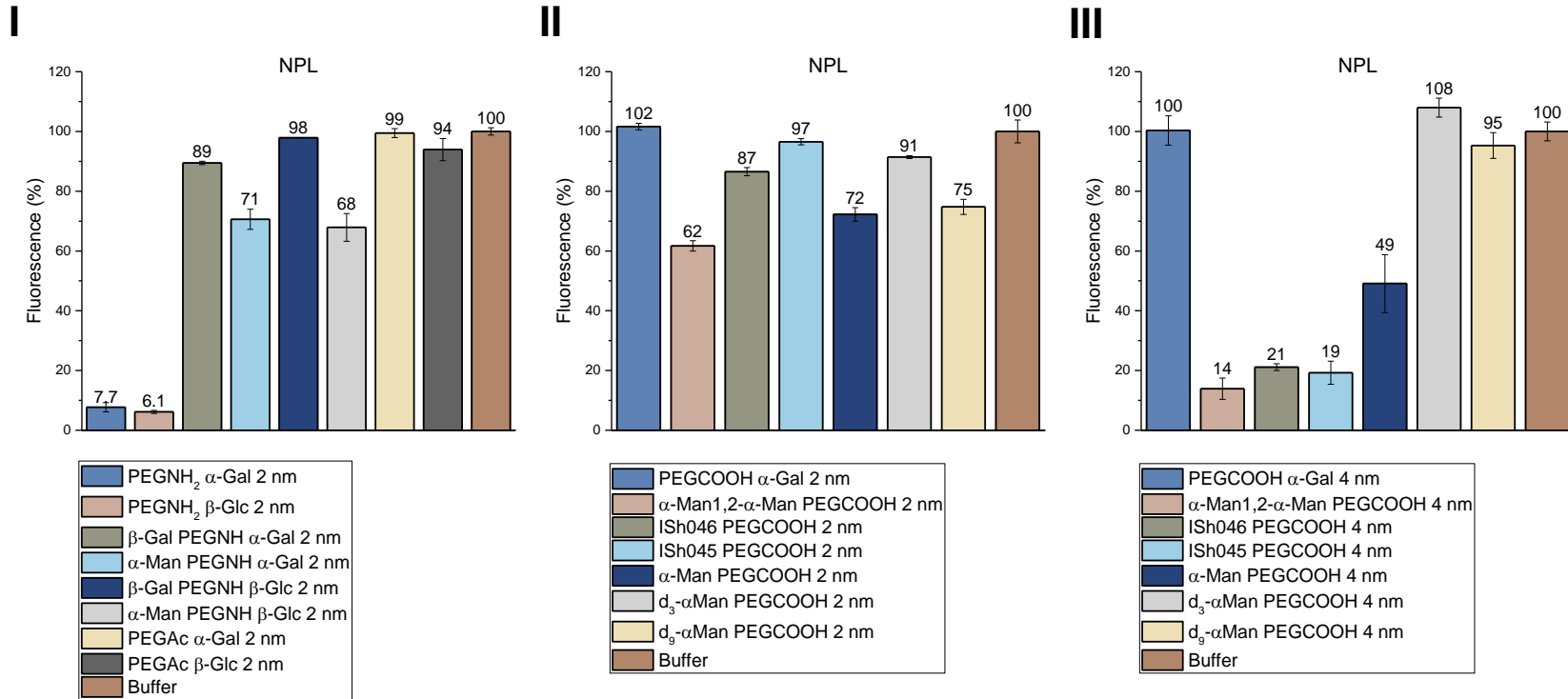
*Figure 15: Relative fluorescence of (I) 2 nm PEG(5)NH2, (II) 2 nm PEG(8)COOH and (III) 4 nm PEG(8)COOH GNP derivatives incubated on a chip printed with AAL.*
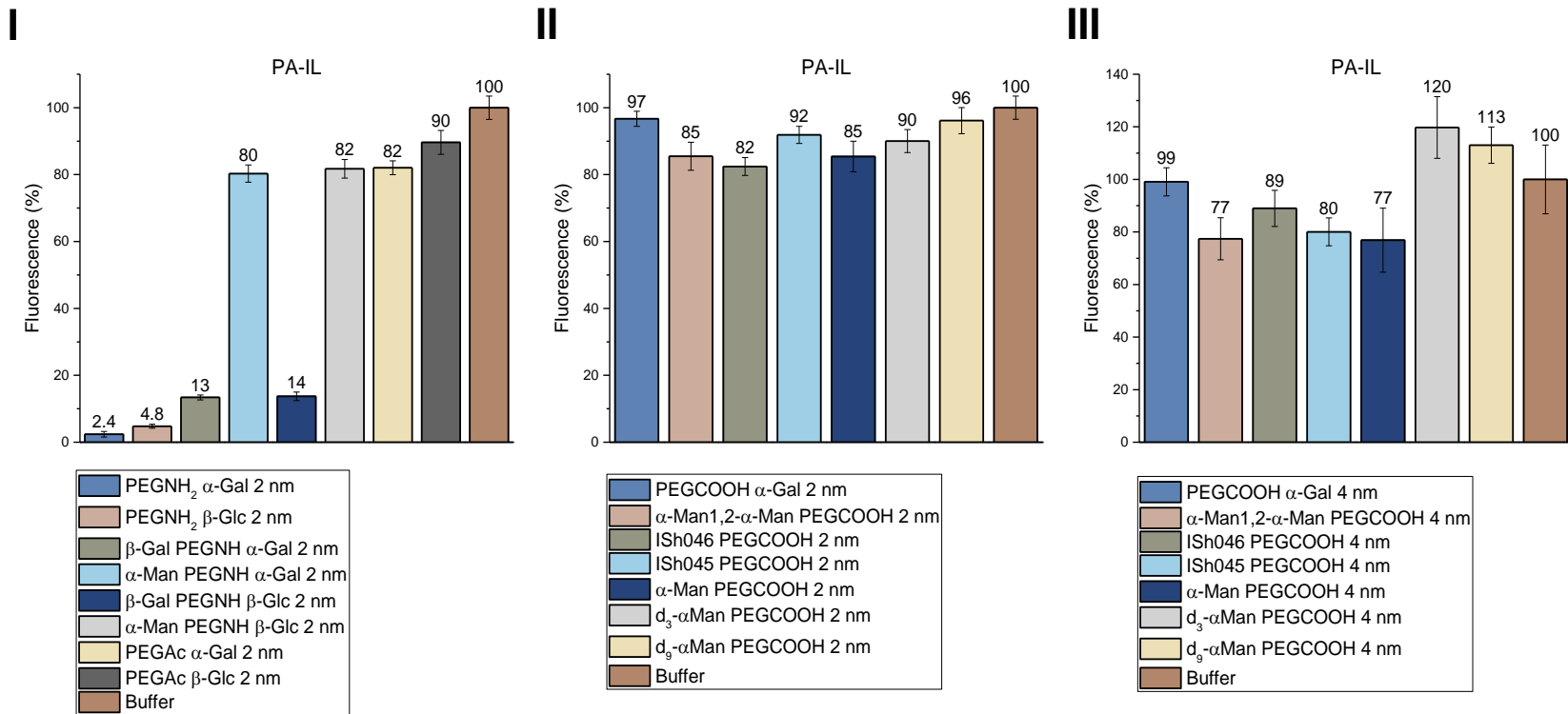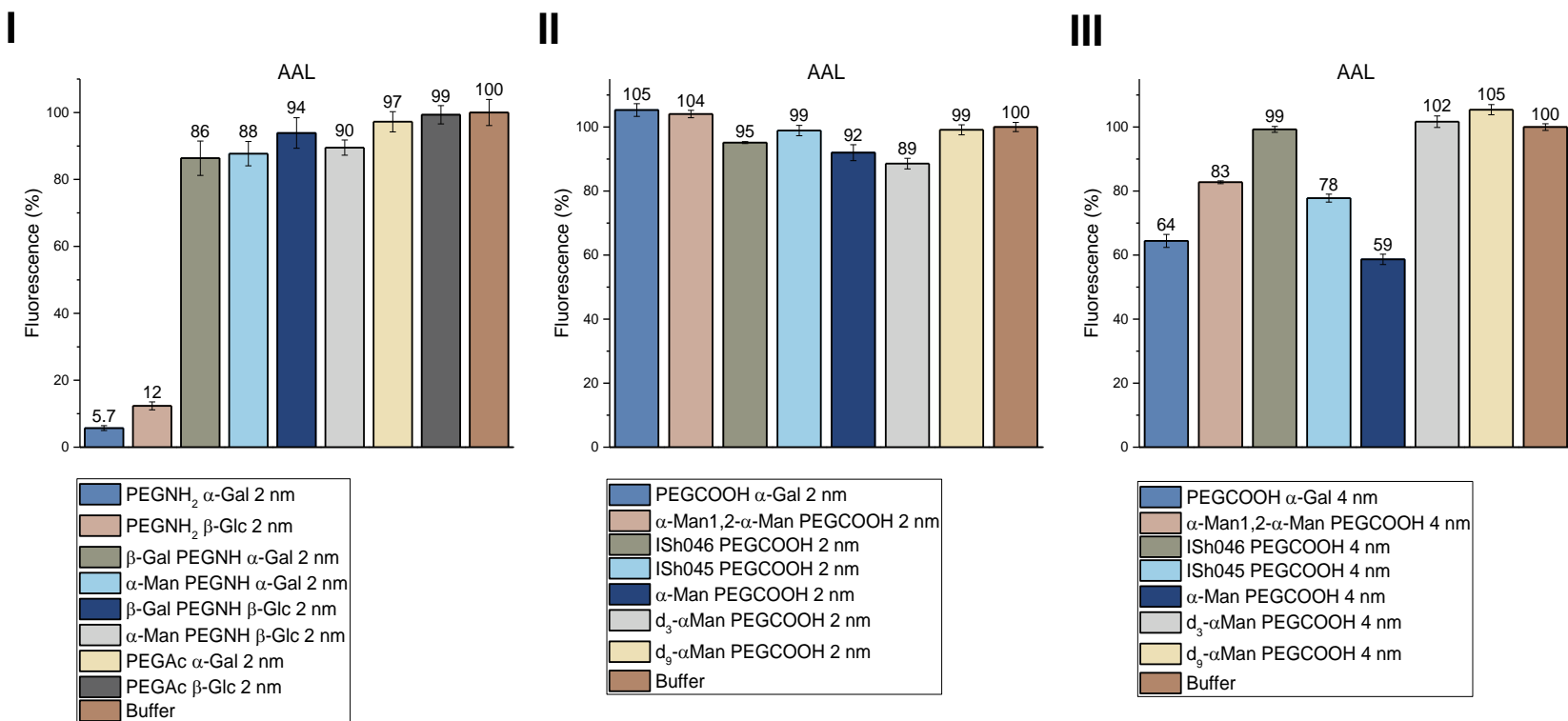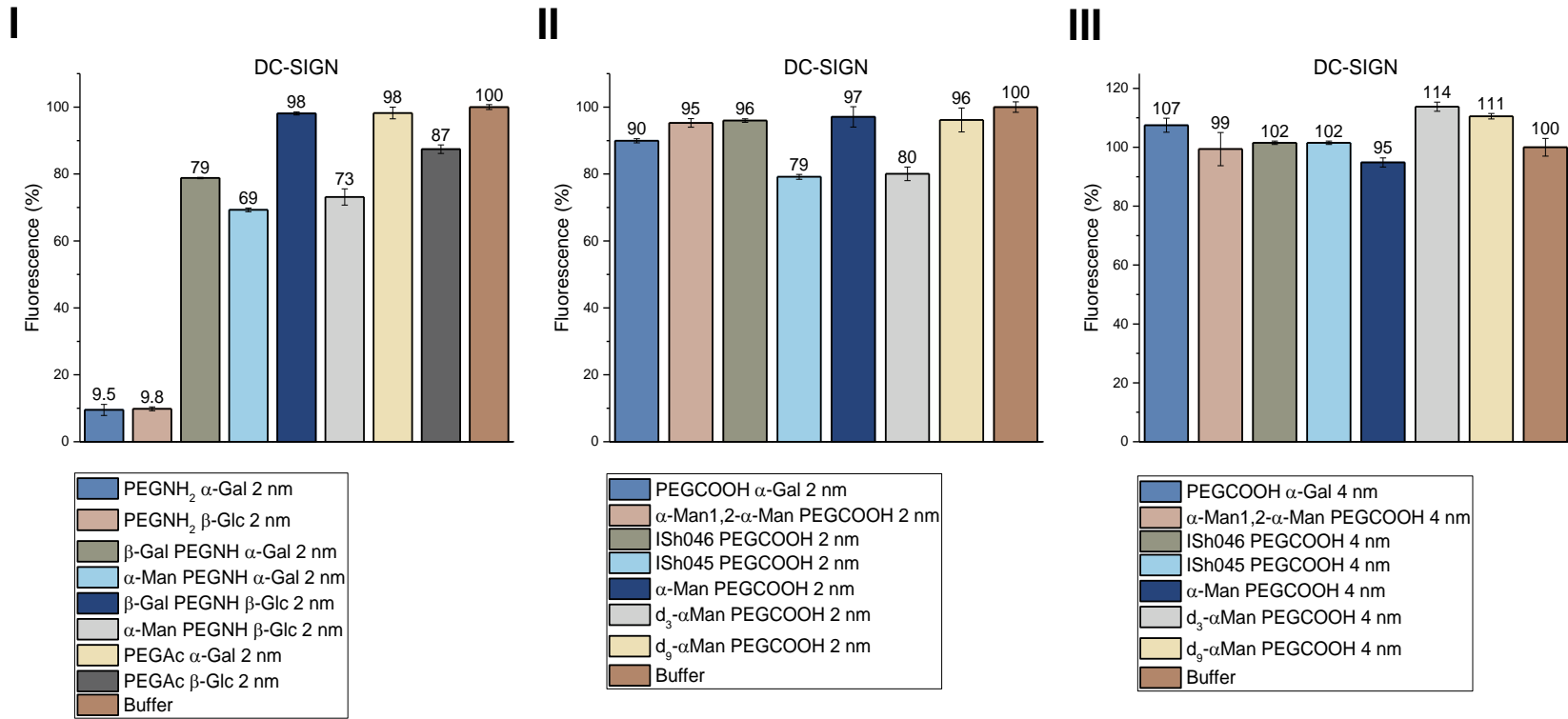
*Figure 16: Relative fluorescence of (I) 2 nm PEG(5)NH₂, (II) 2 nm PEG(8)COOH and (III) 4 nm PEG(8)COOH GNP derivatives incubated on a chip printed with DC-SIGN.*

Among the lectins screened against the **2 nm core GNP**, only two showed a significant and selective binding (quenching of fluorescence): ConA and PA-IL (*Figure 11 and Figure 14*).

ConA is a tetrameric lectin with a 72 Å distance between its CRD and has been shown to interact with various nanoparticle models[62]. It bound to α-mannose and its derivatives, causing a significant quenching of fluorescence. The strongest quenching was obtained with α-mannose1,2α-mannose GNP, followed by the glycomimetics and α-mannose. Interestingly, α-mannose showed higher quenching without the dendrons.

PA-IL is also tetrameric and was demonstrated to bind to ultrasmall GNP bearing β-galactose[63]. PA-IL was able to discriminate between α-galactose (present on the inner part of the GNP with a $C_2$ side chain) and β-galactose GNP.

**4 nm core GNP**, on the other hand, showed a specific quenching of fluorescence for the three L-type α-mannose specific lectins screened. ConA quenching was improved compared to the 2 nm GNP (*Figure 11*), and strong quenching was obtained with HHL and NPL (*Figure 12 and Figure 13*). Again, α-mannose1,2α-mannose and its pseudo-mannoside derivatives were superior to α-mannose, except for ConA, for which both the monomer and the dimer caused a very strong quenching. α-Mannose dendrons underperformed when compared to the unbranched structure, for all the lectins. The downside of the 4 nm GNP is a limited non-specific quenching observed with PA-IL and AAL (*Figure 14 and Figure 15*). The non-specific binding was less intense for the constructs with the highest steric hindrance (ISh046 and the dendrons).

The differences between 2 and 4 nm GNP could be explained by the accessibility of the binding pocket or the distance between the CRD. 4 nm GNP have a flatter surface curvature and a lower ligand density but present more copies of the ligands per particle. Pegamine and PEG carboxylic platforms, with a 2 nm core and five and eight PEG units respectively, gave similar results, although both the ligand chain length and the proximity of the amide (linking point) have been shown to influence the binding properties[64].

DC-SIGN, although known to bind α-mannose derivatives, did not show significant specific quenching of fluorescence for any of the particles (*Figure 16*). This could be explained by the requirement of this receptor for the "perfect" fitting regarding density, valency, linker length and particle core size[33,34,65], or by an assay related issue, such as the orientation of the lectin on the chip or the fluorophore type (DC-SIGN was tagged with Cy3).

Finally, it is interesting to note the strong non-specific binding of PEG(5)NH$_2$ GNP, overcome by protecting residual amine groups (acetamide GNP, negative controls), which led to an almost complete quenching of fluorescence for all the lectins tested (even DC-SIGN). These GNP can therefore be considered as positive controls.

## 3. Biolayer Interferometry with DC-SIGN

The Biolayer interferometry (BLI) experiment was performed using the FortéBio Octet$^{RED}$96 device. DC-SIGN was tested against 2 nm and 4 nm PEG(8)COOH GNP functionalized with α-mannose derivatives.

Biolayer interferometry is a real-time label-free analytical technique employed to detect and quantify the interaction between a ligand and an analyte. The specificity, affinity and kinetics of binding can be determined in a high-throughput automated manner, allowing compound screening. BLI is cost effective, rapid, sensitive, accurate and requires low maintenance compared to similar techniques. It can operate within a broad dynamic range and, the absence of labeling avoids potential alteration of both the ligand and the analyte (e.g. steric blocking of binding sites)[66]. The technique is based on fiber optic biosensors with tips coated with a matrix designed to immobilize a ligand (e.g. streptavidin SA/SAX/SSA, amine reactive AR2G). The analysis relies on interference patterns between light waves. The greater the thickness on the surface of the biosensor, the larger the spectral shift of the reflected light.

The research was conducted in three steps. First, the loading of DC-SIGN was optimized, to avoid both overcrowding and too rapid binding, which can cause uneven loading. Then, the GNP went through a triage process to assess the binding and to compare the constructs. Finally, K$_D$ values of the GNP selected by triage were obtained.

The experiment consisted in streptavidin coated tips that were moved sequentially into different wells. Briefly, after wetting-equilibration in the first well, biosensor tips moved to a second well containing the lectin for loading: biotinylated DC-SIGN. Then, the excess of unbound DC-SIGN was washed away, and the baseline signal was measured. The tips were then moved into the GNP solutions to perform the association step (time-dependent binding of the GNP to the receptor). Finally, in the last well (with buffer), the dissociation step occurred (time-dependent release of the GNP from the receptor) (*Figure 17*).

Association and dissociation were monitored in real time, providing association and dissociation curves, respectively.

For GNP with effective binding, $K_D$ values were obtained. The GNP concentrations were expressed using the gold concentrations and the 2000 gold atoms (4 nm) or 102 gold atoms (2 nm) per GNP models.
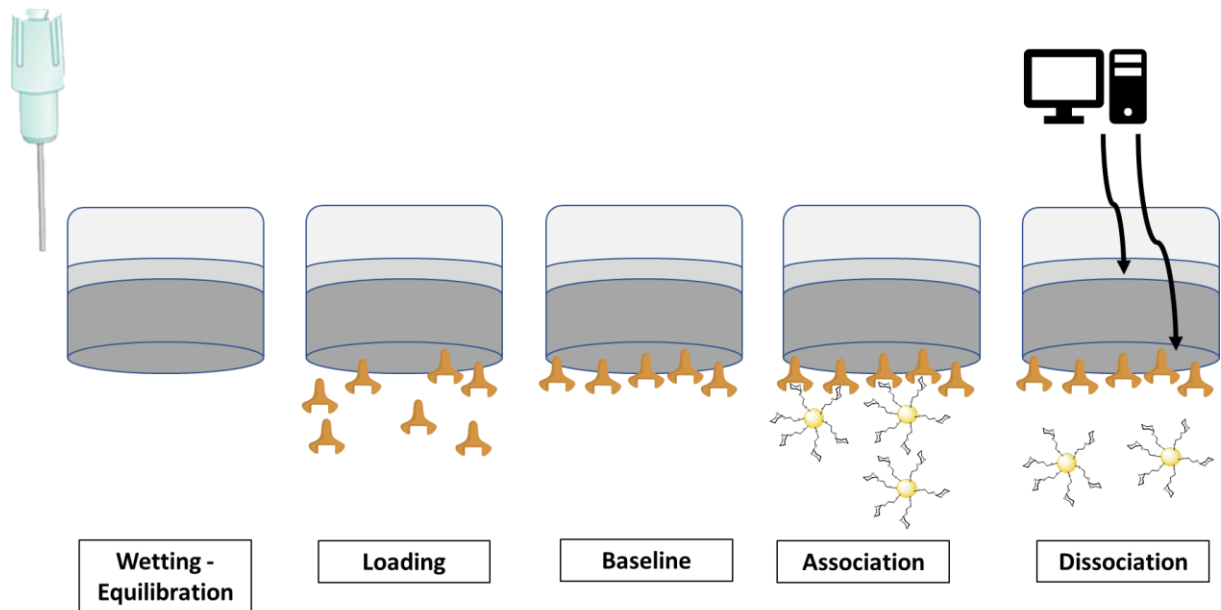


*Figure 17: General principle of BLI and application to GNP interaction with a lectin.*
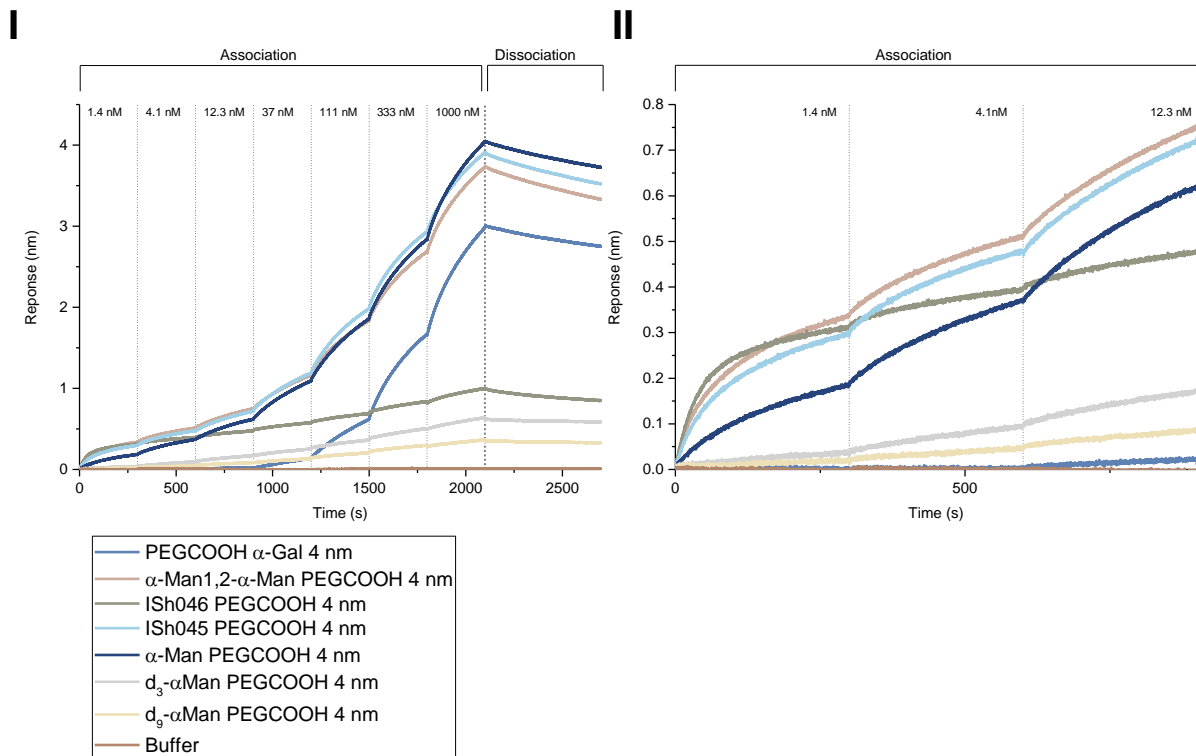


*Figure 18: Association and dissociation of DC-SIGN loaded probe with 4 nm GNP in function of concentration (I) full graph and (II) magnification of the lowest concentrations.*
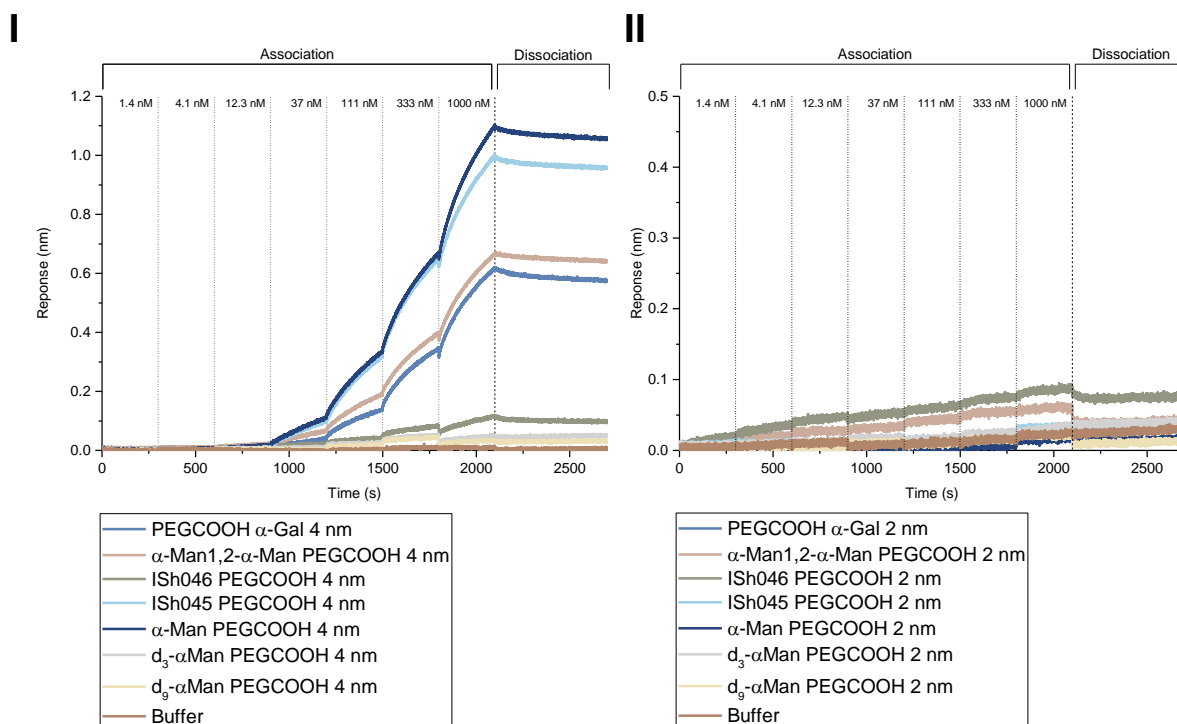
*Figure 19: (I) Association and dissociation of Unloaded probes with 4 nm GNP in function of concentration. (II) DC-SIGN loaded probes association and dissociation with 2 nm GNP in function of concentration.*

Signal was detected for **4 nm core GNP** bearing α-mannose1,2α-mannose and its mimetics ISh045 and ISh046 at the lowest GNP concentration (1.4 nM). α-Mannose GNP also showed binding, but to a lesser extent (*Figure 18 II*). When increasing the concentration of GNP to > 37 nM, α-mannose1,2α-mannose, the mimetic ISh045, α-mannose, and the unfunctionalized GNP (PEGCOOH α-Gal 4 nm) showed continuous increase of binding, while ISh046 reached a plateau. The α-mannose-dendron (d$_3$-αMan and d$_9$-αMan) GNP showed a lower increase of binding at high concentration (*Figure 18 I*). The increase of binding at > 37 nM was also observed for unloaded probes, which indicates non-specific binding (*Figure 19 I*). The fact that ISh046 and dendrons d$_3$-αMan and d$_9$-αMan GNP showed lower non-specific binding could be explained by the high steric hindrance of their ligands (ISh046 contains two benzene groups, dendrons are ramified).

Dissociation was very limited for all constructs, as expected, due to significant analyte rebinding, a feature of multivalent constructs[67].

**2 nm core GNP** showed no significant binding, except for α-mannose1,2α-mannose and ISh046, but the response was low and only appeared at high concentrations (*Figure 19 II*).

Among the constructs screened, 4 nm GNP functionalized with α-mannose1,2α-mannose, the mimetics ISh045 and ISh046 and α-mannose were chosen to obtain $K_D$ data.



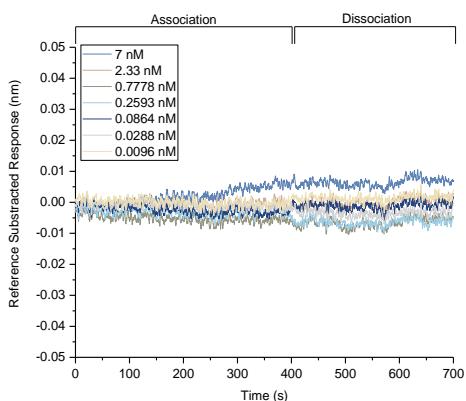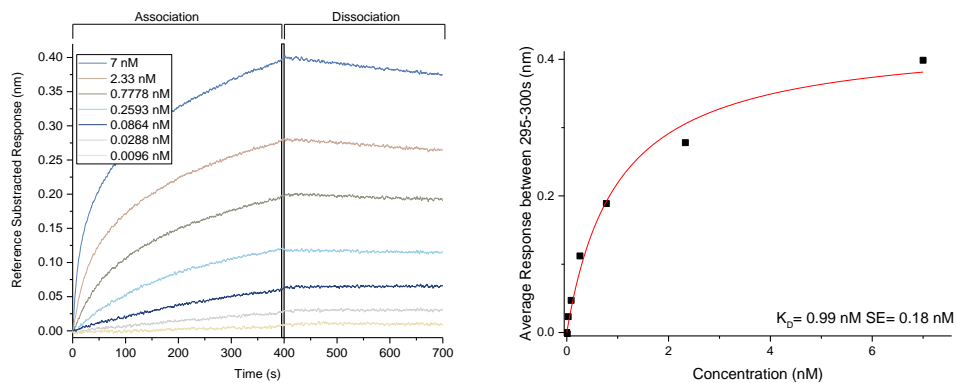*Figure 20: Binding of 4 nm unfunctionalized GNP to DC-SIGN in function of concentration.*



*Figure 21: Binding of 4 nm α-Mannose1,2α-Mannose functionalized GNP to DC-SIGN in function of concentration and $K_D$ determination using Michaelis Menten fit.*
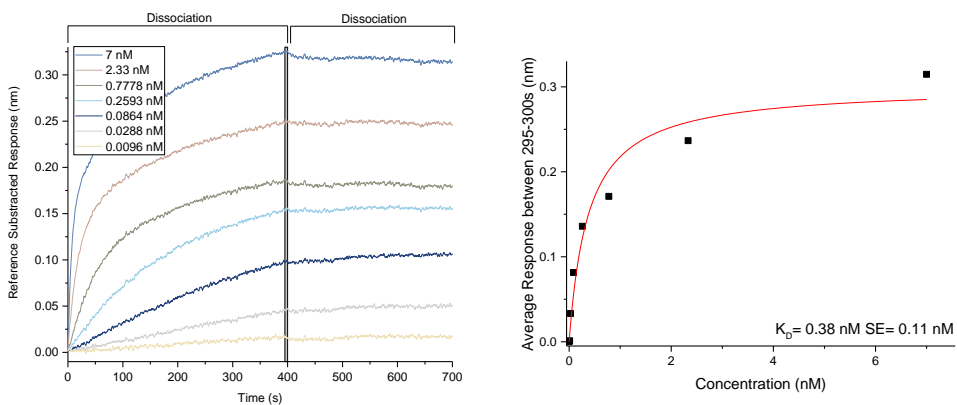


*Figure 22: Binding of 4 nm ISh046 functionalized GNP to DC-SIGN in function of concentration and $K_D$ determination using Michaelis Menten fit.*
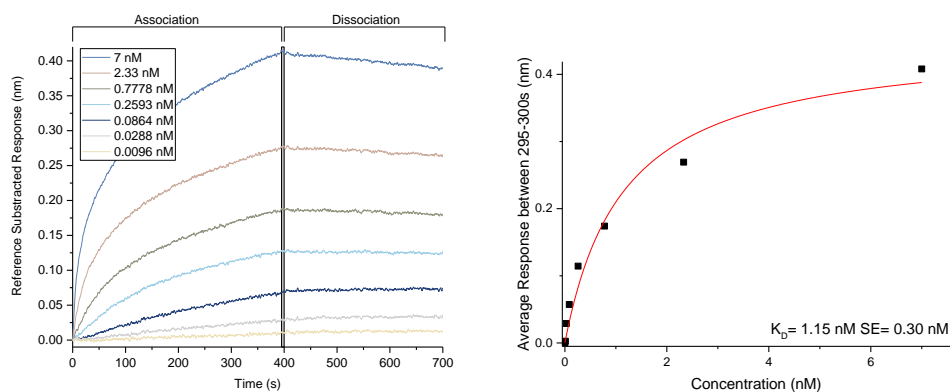
*Figure 23: Binding of 4 nm ISh045 functionalized GNP to DC-SIGN in function of concentration and $K_D$ determination using Michaelis Menten fit.*
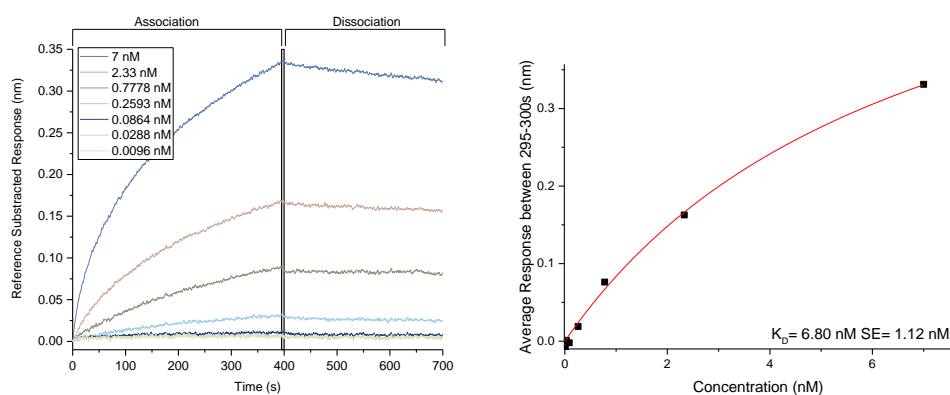


*Figure 24: Binding of 4 nm α-Mannose functionalized GNP to DC-SIGN in function of concentration and $K_D$ determination using Michaelis Menten fit.*

*Table 5: Summary of $K_D$.*

| Sample | $K_D$ (nM) | Standard Error (nM) |
|---|---|---|
| PEGCOOH α-Gal 4 nm | - | - |
| α-Mannose1,2-α-Mannose PEGCOOH 4 nm | 0.99 | 0.18 |
| ISh046 PEGCOOH 4 nm | 0.38 | 0.11 |
| ISh045 PEGCOOH 4 nm | 1.15 | 0.30 |
| α-Mannose PEGCOOH 4 nm GNP | 6.80 | 1.12 |

As expected, α-mannose1,2α-mannose and its mimetics presented a similar $K_D$, while α-mannose gave a higher $K_D$ (*Table 5*). The standard error (SE) was low, demonstrating that a correct dilution range was applied.

## 4. DC-SIGN Mediated Cell Uptake

2 nm and 4 nm GNP functionalized with α-mannose and derivatives were used in an *in vitro* assay with THP-1 cells, a cell line capable of expressing DC-SIGN on the cell surface after stimulation.

From immature THP-1 cells, two models were obtained. By stimulating with IL-4 and PMA, mature THP-1 cells with high levels of DC-SIGN expression were obtained, whereas stimulating with only PMA gave mature THP-1 cells with low levels of DC-SIGN expression.

These two models were incubated with the GNP to assess if DC-SIGN could improve the uptake compared to a non-specific, passive uptake mechanism. Non-DC-SIGN expressing cells and non-α-mannose derivative GNP were used as controls for the non-specific uptake. Cells were recovered after media removal and extensive washing to remove GNP on the cell surface (*Figure 25*).

The gold concentration of the pellet was measured, and values were expressed in percentage of the gold seeded.
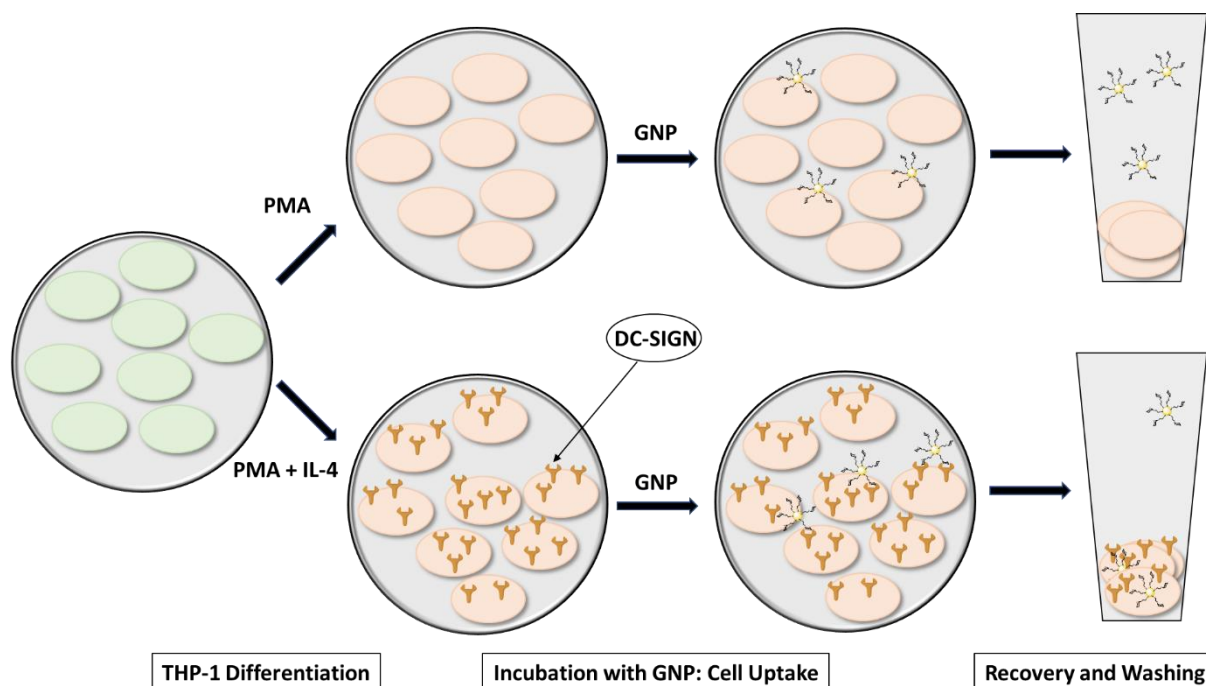


*Figure 25: (I) THP-1 cell differentiation using PMA +/- IL-4. Only IL-4 treated cells express DC-SIGN on their surface. (II) Incubation with GNP. (III) Recovery and washing of the pellets to remove the GNP that did not enter the cells.*
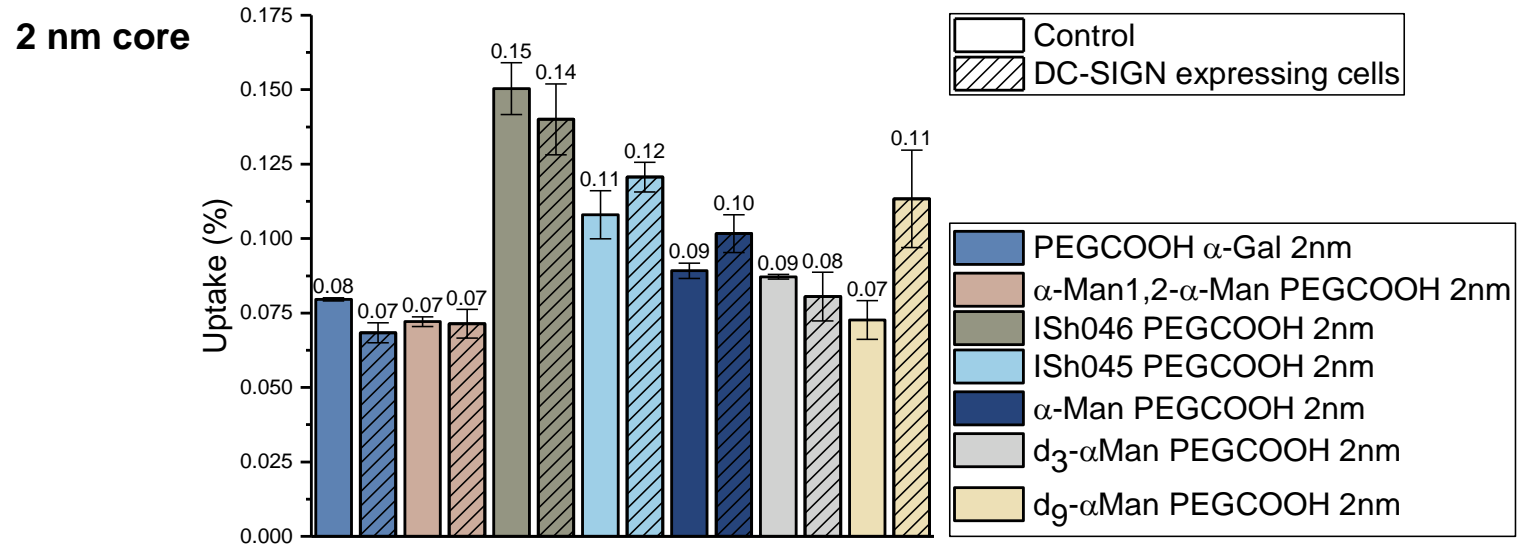
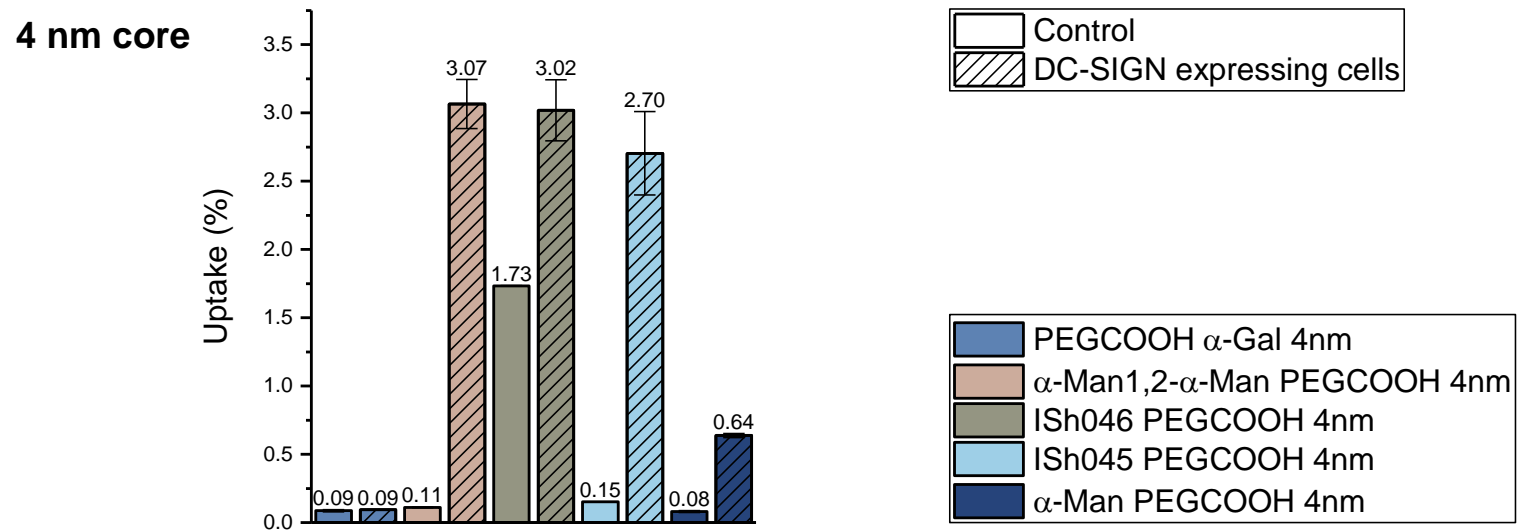*Figure 26: 2 nm GNP cell uptake of gold in THP-1 cells.*

*Figure 27: 4 nm GNP cell uptake of gold in THP-1 cells.*

Among the **2 nm core GNP** incubated with THP-1, no significant differences of cell uptake were observed (*Figure 26*). Functionalization with DC-SIGN targeting molecules (α-mannose and derivatives) had no effect on the uptake. Moreover, the basal uptake was very low, with roughly 0.1 % gold uptake. This is in line with the BLI experiment that showed no significant DC-SIGN binding with 2 nm GNP.

In contrast, the **4 nm core GNP** showed a significant improvement in uptake with the DC-SIGN targeting molecules (*Figure 27*). The uptake was specific for α-mannose, α-mannose1,2α-mannose and ISh045. It was partially specific for ISh046 (it should be noted that the particles functionalized with ISh046 were more adsorbed to plastic surfaces than the rest of the selected GNP).

α-Mannose1,2α-mannose 4 nm GNP showed the highest improvement of uptake, 30-fold. In fact, the active uptake was able to increase total uptake from 0.1 % to 3 % when compared to both the non-functionalized particle with DC-SIGN expressing cells and to itself with the control cells. The glycomimetics showed almost the same level of uptake for DC-SIGN expressing cells. α-Mannose 4 nm GNP resulted in only a 6-fold improvement of uptake. The 4 nm GNP with α-mannose dendrons were not tested.

## 5. Biodistribution of α-Mannose-GNP

To determine the *in vivo* fate of particles coated with α-mannose, a biodistribution assay in rats was performed. The two constructs tested were both obtained through the post-functionalization of PEGCOOH α-Gal **2 nm core GNP**.

One GNP was partially functionalized with α-mannose, leaving a majority of free PEG(8)COOH while the other was completely functionalized with α-mannose. The complete functionalization, apart from increasing the amount of α-mannose per GNP, removes the negative charge brought by the PEG(8)COOH.

The GNP were administered to the rats by tail vein injection. After 24 hours, the animals were sacrificed and different organs and compartments were recovered for the analysis of gold to determine the biodistribution of the GNP (*Figure 28*).
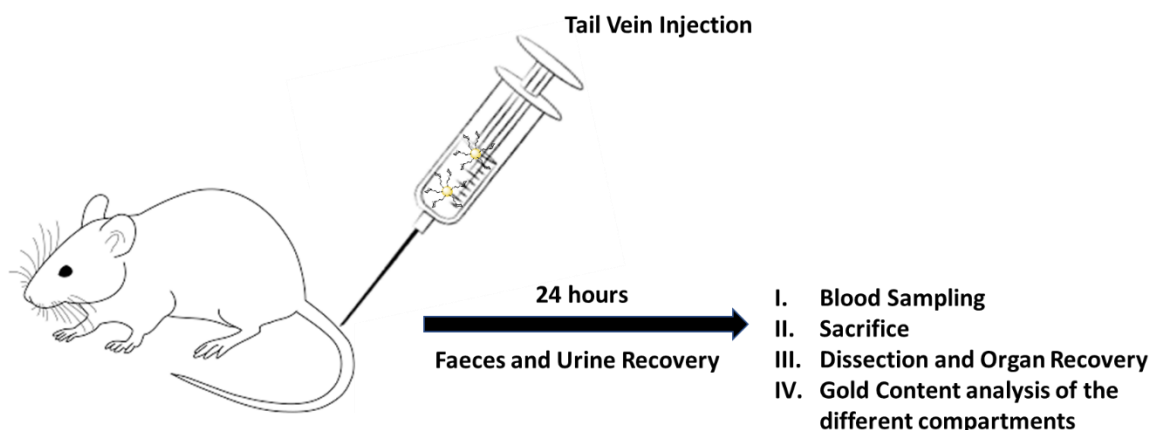
*Figure 28: Biodistribution of GNP with male Wistar rats.*
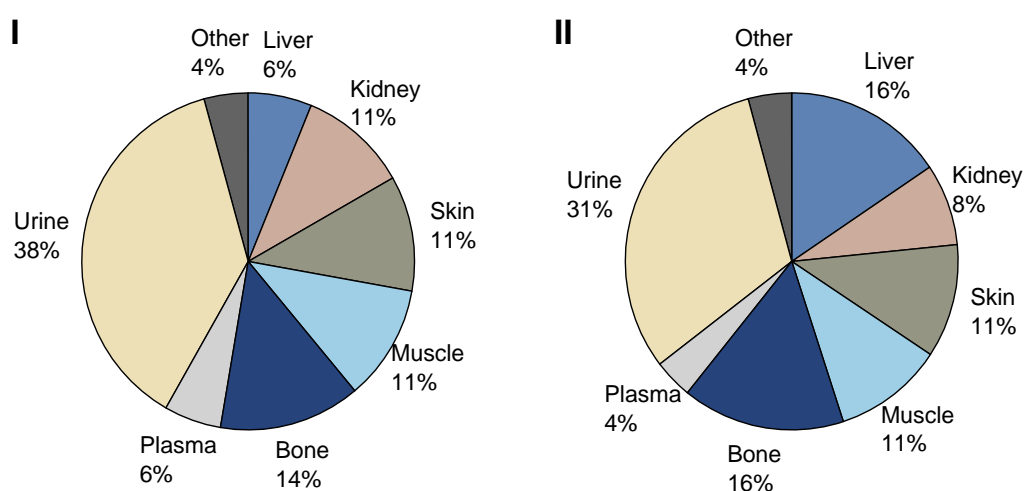


*Figure 29: Biodistribution of 2 nm GNP (I) Partially Loaded with α-Mannose and (II) Fully Decorated with α-Mannose. Other: heart, lungs, spleen, brain, testes, stomach, small intestine, large intestine, eyes, faeces and blood cells.*

From a safety perspective, no acute toxicity symptoms were observed.

The biodistribution of the 2 nm GNP partially and fully loaded with α-mannose was similar. The bulk of the gold distributed to urine, with above 30 % of the administered gold recovered. Gold was also detectable in liver and kidney, which would be expected for the main organs of metabolization and excretion. Also, around 5 % gold after 24 hours was located in plasma (*Figure 29*).

Three other compartments showed a significant amount of gold: skin and muscles (above 10 %) and bones (around 15 %).

On the other hand, gold was low in other organs and compartments: heart, lungs, spleen, brain, testes, stomach, small intestine, large intestine, eyes, faeces and blood cells.

# IV.   Conclusions and Further Work

These experiments have demonstrated the biological versatility and utility of ultrasmall GNP constructs with appropriate carbohydrate ligands.

Lectin microarray experiments successfully validated the capacity of both 2 and 4 nm GNP bearing oligo-PEG to quench fluorescence. Different fluorescently labeled lectins were printed on a chip and incubated with the GNP. After washing, the relative quenching of fluorescence was measured. The experiment established the importance of the core size: 2 nm GNP with α-mannose derivatives only significantly bound to one (ConA) of the three High Mannose specific L-type lectins studied, while 4 nm GNP bound to ConA, HHL and NPL. Sugar specificity was demonstrated, since only β-galactose GNP were able to specifically bind to PA-IL. This confirms the capacity of GNP to potentially be used to treat or prevent infections by targeting *Pseudomonas aeruginosa*. Although they showed more non-specific binding, 4 nm GNP were clearly superior compared to their 2 nm counterparts. The dimer α-mannose1,2α-mannose and its mimetics outperformed the monomer α-mannose, even when presented as a dendron. Interestingly, looking at the binding to High Mannose specific L-type lectins, α-mannose dendrons had worse results compared to the non-ramified structure. The results described above are nevertheless puzzling because of the absence of specific quenching with DC-SIGN. Further investigations should be carried out to understand the absence of binding, especially regarding the BLI and THP-1 cell uptake assay data (*see below*).

The lectin microarray opens wide perspectives for the screening of glycans and Glyco-GNP interactions. Control of fluorescence intensity and visualization of the printing quality since the first step, the printing of the fluorescent lectins, are significant advantages of the GNP quenching assay. Further lectins and GNP could be tested to understand the mechanisms of binding. GNP could also be tuned to obtain the maximum interaction with defined lectins of clinical interest by modulating the loading or adjusting the presentation (e.g. variation of the PEG length, use of rigid alkyl chains).

Biolayer interferometry with DC-SIGN confirmed the differences between the 2 nm and 4 nm platforms. Only 4 nm core GNP bound to DC-SIGN. It should be noted that 4 nm core GNP showed non-specific binding to the biosensor tips at high concentrations. As for the microarray experiment, α-mannose1,2α-mannose and its mimetics were better than the monomer α-mannose, which had better binding affinity as a non-ramified construct than when presented as a dendron.

Using the four best constructs selected by triage, $K_D$ values were generated. 4 nm GNP functionalized with α-Mannose1,2α-mannose, the mimetics ISh046 and ISh045, with $K_D$ of 0.99, 0.38 and 1.15 nM respectively, demonstrated themselves as good candidates for further development. α-Mannose 4 nm GNP, while having a higher $K_D$ (6.80 nM) has the advantage of being a simpler structure. The set of experiments performed with DC-SIGN could be completed by competition assays (with α-mannose in solution) to obtain a significant dissociation, or by blocking the interaction between the lectin and its ligand (e.g. using EDTA to chelate calcium).

The success of the BLI assay with DC-SIGN, and the fact that it is a relatively user friendly technique, opens the path for the screening of different transmembrane human mrCLR: DC-SIGNR, Langerin and the Mannose Receptor (MMR) but also soluble mrCLR, such as mannose-binding lectin (MBL), that, upon attachment to pathogens, increases the uptake by macrophages[15]. Pathogen-lectin such as *Pseudomonas aeruginosa* PA-IL or *Escherichia coli* FimH could also be screened[61]. The screening of different lectins would allow a better understanding of binding models, and hopefully, the discovery of constructs specific for one receptor to overcome the potential off-target effects of non-specificity. Moreover, keeping DC-SIGN as the main focus, GNP could be optimized to improve the $K_D$ and prevent non-specific binding. This could be done, for instance, by modifying the oligo-PEG length or removing the α-Galactose-$C_2$.

Cell uptake with THP-1 cells expressing DC-SIGN correlated with the BLI DC-SIGN assay. Only 4 nm GNP functionalized with α-mannose derivatives showed a significant increase in uptake. Gold uptake was improved by α-mannose1,2α-mannose and the mimetics (ISh046 and ISh045) by around 30-fold, and by α-mannose, although in this case, only by 6-fold.

2 nm and non-functionalized 4 nm GNP showed a very low basal uptake of the GNP. No significant uptake was observed with non-DC-SIGN expressing THP-1 cells (except for ISh046 4 nm GNP, but most likely due to plastic adsorption).

The low non-specific and the high specific uptake of the 4 nm GNP functionalized with α-mannose derivatives make them excellent candidates for specific active cell targeting of APC. If the strategy were to carry on with 2 nm GNP, the length of the ligand should probably be increased (e.g. longer PEG) or the ligand itself should be more rigid (e.g. alkyl chain) to create a construct that would achieve active targeting.

Once uptake had been demonstrated, the effect on the cell metabolism should next be investigated. In fact, cell maturation must be achieved upon GNP uptake to elicit an immune response. Looking forward, the co-delivery of an antigen (pathogen or cancer related peptide) to DC through DC-SIGN mediated uptake should trigger phenotypical changes with the presentation of the antigen on the cell surface and the activation of co-stimulatory signals.

Using THP-1 cells as a DC model, cytokines and co-receptor expression upon GNP uptake could be measured using techniques such as ELISA (enzyme-linked immunosorbent assay), FACS (fluorescence-activated cell sorting) or PCR (polymerase chain reaction)[68]. The GNP platform could also be optimized to improve the uptake or tailor the polarization of the immune adaptive response (inflammation/tolerance). For instance, using α-fucose instead of α-mannose derivatives could lead to a tolerance effect, rather than a pro-inflammatory one[18]. Finally, the success of a construct also relies on its physicochemical characteristics, such as the tissue penetration/retention and the half-life. Maintaining or improving highly specific uptake, while enhancing the rest of the GNP platform characteristics, is critical for the GNP to have an *in vivo* utility. For instance, longer half-life can be attained using longer length PEG providing better shielding from plasma proteins, but it should not be achieved at the expense of cell uptake[69].

The biodistribution assay, showed interesting results about the *in vivo* fate of α-mannose GNP. Systemically injected, 2 nm GNP coated with α-mannose were present after 24 hours in both blood and skin and no acute toxicity was detected. The high distribution within the skin was of particular interest, since most DC are present in peripheral tissues (skin and mucosa), where they can encounter pathogens[9]. Moreover, having a significant amount remaining after 24 hours implies good tissue retention, increasing the chance of contact and interaction between DC and GNP.

With regard to future *in vivo* experiments, several pathways can be taken. Firstly, testing with the same systemic model the 4 nm GNP that gave promising results in the biochemical and *in vitro* assays, PKBD and toxicity data will then, shed some light on the direction to take for future developments. Secondly, using the 4 nm GNP candidates with a vaccination model, administration by a sub-cutaneous route, and assessing the evolution of the adaptive immunity markers (e.g. DC migration to lymph nodes[70]). Co-delivery of an antigen and challenge with a pathogen or a tumor may also be studied[71].

The combination of biochemical and biological assays showed that ultrasmall GNP are a promising model for immune cell targeting through CLR. DC-SIGN was efficiently targeted using α-mannose derivatives, particularly the natural α-mannose1,2α-mannose on PEG(8)COOH/α-Galactose-C$_2$ 4 nm GNP. Apart from DC-SIGN, other lectins have the potential to generate data that will improve the understanding of the mechanisms binding (microarrays, BLI) and the reactions triggered (*in vitro*), hopefully leading to the creation of a clinically relevant product in the field of vaccination[29,72].

# V. Materials and Methods

## 1. Synthesis of gold nanoparticles

Examples of the typical analytical results obtained for 2 nm GNP are available in *Chapter I*. GNP-4 (4 nm core) analytical data is available in *the annex*.

The S/Au obtained by XPS and ICP-AES was higher than the theoretical (0.43) for 2 nm particles, and lower for 4 nm ones (0.145). This means that the formulas used for 2 nm GNP underestimate the number of ligands per particle, while the opposite, an overestimation, occurs for 4 nm GNP (*Table 6*).

*Table 6: S/Au molar ratio calculated from XPS and ICP-AES measurements for 2 nm and 4 nm GNP.*

| Batch | Core Size (nm) | Theoretical S/Au | S/Au XPS | S/Au ICP-AES |
|-------|----------------|------------------|----------|--------------|
| GNP-1 | 2 | 0.43 | 0.51 | 0.52 |
| GNP-2 | 2 | 0.43 | 0.51 | 0.52 |
| GNP-3 | 2 | 0.43 | 0.54 | 0.52 |
| GNP-4 | 4 | 0.145 | 0.11 | 0.08 |

### a. One-Pot ultrasmall GNP

**2 nm core** GNP.

- **GNP-1** = *GNP-12 Chap II* $(PEG(5)NH_2)_{22}(\alpha\text{-Galactose-}C_2)_{22}@Au_{102\text{-}}$
- **GNP-2** = *GNP-13 Chap II* $(PEG(5)NH_2)_{26}(\beta\text{-Glucose-}C_2)_{18}@Au_{102}$
- **GNP-3** = *GNP-10 Chap II* $(PEG(8)COOH)_{22\text{-}26}(\alpha\text{-Galactose-}C_2)_{22\text{-}18}@Au_{102}$.

**4 nm core** GNP were synthesized with a modified Brust-Schiffrin method, using a Syrris Atlas Potassium reactor with a 2 L jacketed torispherical vessel and a 500-50 mm blade propeller stirrer without baffles. The GNP can be represented by the following formula **GNP-4** $(PEG(8)COOH)_{130}(\alpha\text{-Galactose-}C_2)_{160}@Au_{2000}$.

The reaction was carried out at 18 °C with fast stirring (750 rpm). Time, pH, and temperature were continuously monitored. $H_2O$ (Ultrapure, MilliQ) was the solvent used for both synthesis and purification. The different reagents were added from the top of the vessel within minutes (~ 15 min) using a 150-80-8 mm funnel.

HAuCl$_4$•3H$_2$O (1 equivalent, 400 mg, 1.016 mmol, 25 mL, Sigma-Aldrich) was put in presence of a minute amount of disulfide "nucleating" ligands PEG(8)COOH (0.0042 equivalent, 4 mg, 0.004 mmol, 800 mL, Acadechem) and α-Galactose-C$_2$ (0.0018 equivalent, 1 mg, 0.002 mmol, 800 mL, Galchimia) 70:30 molar ratio. Aqueous NaOH solution (~ 2.5-3 mL 2 M NaOH) was used to modulate the pH to ~ 10.5-11. Freshly prepared NaBH$_4$ in excess (0.2 M in 0.01 M NaOH, 5 equivalents, 192 mg, 5.078 mmol, 25 mL Appli Chem) was quickly added to form the particles. After nucleation, "capping" disulfide ligands were added: PEG(8)COOH (0.129 equivalent, 118 mg, 0.129 mmol, 10 mL, Acadechem) and α-Galactose-C$_2$ (0.023 equivalent, 11 mg, 0.023 mmol, 10 mL, Galchimia) 85:15 molar ratio. Extra aqueous NaOH solution (~ 7 mL 2 M NaOH) was used to adjust the pH to ~ 12. After all reagents were added, the gold concentration was 0.6 mM and the final volume of the reaction corresponded to 85 % of the reactor capacity. After 30 minutes, the purification was performed with a Repligen KR2i TFF system with D06-E010-05-N hollow fibers (10 kDa pore size). The final product was filtered with a 0.22 μm membrane, resuspended in H$_2$O and stored in an amber glass vial at 4 °C.

**GNP-4**: ^{1}H NMR (500 MHz, D$_2$O) α-Galactose-C$_2$ δ 4.91 (d, 1H, H-1, area: 1) and PEG(8)COOH δ 2.42 (t, 2H, -CH$_2$-COOH, area: 1.65). Ratio: α-Galactose-C$_2$/PEG(8)COOH 55:45. LC-CAD-MS: α-Galactose-C$_2$ (RT: 1.271 min; area: 0.235) and PEG(8)COOH (RT: 5.783 min; area: 0.547; m/z: 459, 476). Ratio: α-Galactose-C$_2$/PEG(8)COOH 45:55.

### b. Post-Functionalization

Post-functionalization reactions were performed as described in the *previous chapters*.

- ▪ 2 nm PEG(5)NH$_2$ GNP functionalization: **GNP-5**, **GNP-6, GNP-7 GNP-8**, **GNP-9** and **GNP-10**

The reactions were performed under the same conditions as in *Chapter II*. **GNP-8** = *GNP-19 Chap II*, **GNP-9** = *GNP-18 Chap II* and **GNP-10** = *GNP-17 Chap II*.

**GNP-5**: ^{1}H NMR (500 MHz, D$_2$O) α-Galactose-C$_2$ δ 4.99 (d, 1H, H-1, area: 1), PEG(5)NH$_2$ δ 2.80 (t, 2H, -CH$_2$-NH$_2$, area: 0.07), β-Galactose-C$_4$H$_8$-CO-R δ 4.40 (d, 1H, H-1, area: 0.95) and PEG(5)-NH-Ac δ 2.02 (s, 3H, area: 0.27). Ratio: α-Galactose-C$_2$/PEG(5)NH$_2$/β-Galactose-C$_4$H$_8$-CO-R/PEG(5)-NH-Ac 48:2:46:4.

**GNP-6**: ^{1}H NMR (500 MHz, $D_2O$) α-Galactose-$C_2$ δ 4.99 (d, 1H, H-1, area: 1), PEG(5)$NH_2$ δ 2.80 (t, 2H, -$CH_2$-$NH_2$, area: 0.16), α-Mannose-$C_2H_4$-CO-R δ 4.86 (d, 1H, H-1, area: 0.80) and PEG(5)-NH-Ac δ 2.02 (s, 3H, area: 0.52). Ratio: α-Galactose-$C_2$/PEG(5)$NH_2$/α-Mannose-$C_2H_4$-CO-R/PEG(5)-NH-Ac 49:4:39:8.

**GNP-7**: ^{1}H NMR (500 MHz, $D_2O$) α-Galactose-$C_2$ δ 4.99 (d, 1H, H-1, area: 1), PEG(5)$NH_2$ δ 2.80 (t, 2H, -$CH_2$-$NH_2$, area: 0.10) and PEG(5)-NH-Ac δ 2.02 (s, 3H, area: 2.99). Ratio: α-Galactose-$C_2$/PEG(5)$NH_2$/PEG(5)-NH-Ac 49:2:49.

- ▪ 2 nm PEG(8)COOH GNP functionalization: **GNP-11, GNP-12**, **GNP-13**, **GNP-14**, **GNP-15**, **GNP-16** and **GNP-17**

The reactions were performed under the same conditions as in *Chapter II and III*. The glycomimetics, ISh046 and ISh045, and the dendrons, $d_3$-α-Mannose and $d_9$-α-Mannose, were kindly supplied by Laura Medve and Dr. Anna Bernard from Università degli Studi di Milano, and, Antonio Di Maio and Dr. Francisco Javier Rojo from CSIC Sevilla, respectively.

**GNP-11** = *GNP-22 Chap III*, **GNP-12** = *GNP-26 Chap II and* **GNP-13** = *GNP-27 Chap II.*

**GNP-14**: ^{1}H NMR (500 MHz, $D_2O$) α-Galactose-$C_2$ δ 4.99 (d, 1H, H-1, area: 1), PEG(8)COOH δ 2.49 (t, 2H, -$CH_2$-COOH, area: 1.77) and ISh046-NH-R δ 7.35 (d, 4H); 7.25 (dd, 4H); 5.03 (d, 1H, area: 0.47); 4.61 (s, 4H); 4.31 (d, 4H). Ratio: α-Galactose-$C_2$/PEG(8)COOH/ISh046-NH-R 42:38:20.

**GNP-15**: ^{1}H NMR (500 MHz, $D_2O$) α-Galactose-$C_2$ δ 5.00 (d, 1H, H-1, area: 1), PEG(8)COOH δ 2.49 (t, 2H, -$CH_2$-COOH, area: 1.78) and ISh045-NH-R δ 5.05 (d, 1H, area: 0.44); 3.37 (s, 6H). Ratio: α-Galactose-$C_2$/PEG(8)COOH/ISh045-NH-R 43:38:19.

**GNP-16**: ^{1}H NMR (500 MHz, $D_2O$) α-Galactose-$C_2$ δ 5.00 (d, 1H, H-1, area: 1), PEG(8)COOH δ 2.50 (t, 2H, -$CH_2$-COOH, area: 0.93) and α-Mannose-$d_3$-NH-R δ 8.08 (s, 3H, area: 0.83). Ratio: α-Galactose-$C_2$/PEG(8)COOH/α-Mannose-$d_3$-NH-R 57:27:16.

**GNP-17**: ^{1}H NMR (500 MHz, $D_2O$) α-Galactose-$C_2$ δ 5.00 (d, 1H, H-1, area: 1), PEG(8)COOH δ 2.49 (t, 2H, -$CH_2$-COOH, area: 1.03) and α-Mannose-$d_9$-NH-R δ 8.05 (s, 9H); 8.01 (s, 3H, area: 0.81). Ratio: α-Galactose-$C_2$/PEG(8)COOH/α-Mannose-$d_9$-NH-R 56:29:15.

- 4 nm PEG(8)COOH GNP functionalization: **GNP-18**, **GNP-19**, **GNP-20**, **GNP-21**, **GNP-22** and **GNP-23**

The reactions were performed under the same conditions as with their 2 nm counterparts using GNP-4 ([Au] = 2 mg/mL during the reactions).

**GNP-18**: ^{1}H NMR (500 MHz, D$_2$O) α-Galactose-C$_2$ δ 5.00 (d, 1H, H-1, area: 1) and PEG(8)COOH δ 2.51 (t, 2H, -CH$_2$-COOH, area: 0.25). The PEG(8)COOH area of the base particle was subtracted to the PEG(8)COOH area of the functionalized particle (1.65 - 0.25 = 1.40) to obtain the area of the newly formed ligand α-Mannose-C$_2$H$_4$-NH-R δ 4.89 (d, 1H, H-1). Ratio: α-Galactose-C$_2$/PEG(8)COOH/α-Mannose-C$_2$H$_4$-NH-R 55:7:38.

**GNP-19**: ^{1}H NMR (500 MHz, D$_2$O) α-Galactose-C$_2$ δ 5.00 (d, 1H, H-1, area: 1) and PEG(8)COOH δ 2.51 (t, 2H, -CH$_2$-COOH, area: 0.27). The PEG(8)COOH area of the base particle was subtracted to the PEG(8)COOH area of the functionalized particle (1.65 - 0.27 = 1.38) to obtain the area of the newly formed ligand α-Mannose1,2α-Mannose-C$_2$H$_4$-NH-R δ 5.11 (d, 1H); 5.05 (d, 1H).
Ratio: α-Galactose-C$_2$/PEG(8)COOH/α-Mannose1,2α-Mannose-C$_2$H$_4$-NH-R 55:7:38.

**GNP-20**: ^{1}H NMR (500 MHz, D$_2$O) α-Galactose-C$_2$ δ 5.00 (d, 1H, H-1, area: 1) and PEG(8)COOH δ 2.51 (t, 2H, -CH$_2$-COOH, area: 0.28). The PEG(8)COOH area of the base particle was subtracted to the PEG(8)COOH area of the functionalized particle (1.65 - 0.28 = 1.37) to obtain the area of the newly formed ligand and ISh046-NH-R.
Ratio: α-Galactose-C$_2$/PEG(8)COOH/ISh046-NH-R 55:7:38.

**GNP-21**: ^{1}H NMR (500 MHz, D$_2$O) α-Galactose-C$_2$ δ 5.00 (d, 1H, H-1, area: 1) and PEG(8)COOH δ 2.51 (t, 2H, -CH$_2$-COOH, area: 0.34). The PEG(8)COOH area of the base particle was subtracted to the PEG(8)COOH area of the functionalized particle (1.65 - 0.34 = 1.31) to obtain the area of the newly formed ligand and ISh045-NH-R δ 5.05 (d, 1H).
Ratio: α-Galactose-C$_2$/PEG(8)COOH/ISh045-NH-R 55:9:36.

**GNP-22**: ^{1}H NMR (500 MHz, D$_2$O) α-Galactose-C$_2$ δ 5.00 (d, 1H, H-1, area: 1) and PEG(8)COOH δ 2.51 (t, 2H, -CH$_2$-COOH, area: 0.72). The PEG(8)COOH area of the base particle was subtracted to the PEG(8)COOH area of the functionalized particle (1.65 - 0.72 = 0.93) to obtain the area of the newly formed ligand α-Mannose-d$_3$-NH-R.
Ratio: α-Galactose-C$_2$/PEG(8)COOH/α-Mannose-d$_3$-NH-R 55:20:25.

**GNP-23**: $^1$H NMR (500 MHz, D$_2$O) $\alpha$-Galactose-C$_2$ $\delta$ 5.00 (d, 1H, H-1, area: 1) and PEG(8)COOH $\delta$ 2.51 (t, 2H, -CH$_2$-COOH, area: 0.98). The PEG(8)COOH area of the base particle was subtracted to the PEG(8)COOH area of the functionalized particle (1.65 - 0.98 = 0.67) to obtain the area of the newly formed ligand $\alpha$-Mannose-d$_9$-NH-R.

Ratio: $\alpha$-Galactose-C$_2$/PEG(8)COOH/$\alpha$-Mannose-d$_9$-NH-R 55:27:18.

## 2. Lectin Microarray

The microarray experiments were performed within the premises of the Glycotechnology laboratory of CIC biomaGUNE (San Sebastian, Spain) under the supervision of Dr. Niels Reichardt and Dr. Sonia Serna.

Legume, bacterial and fungal lectins are commercially available (Sigma-Aldrich, Vector Labs, EY Laboratories) and were labeled with Alexa Fluor 555 Dye (Thermo-Fisher). DC-SIGN extra cellular domain (ECD) was generously provided by partners of the Immunoshape network (Univ. Grenoble Alpes, CEA, CNRS, Institut de Biologie Structurale, F-38000). It was expressed using *Escherichia coli*, purified and tagged with Cy3. Degree of labeling (DOL) was quantified and optimized.

Lectins were diluted to 0.5 mg/mL (or as close as possible) in a printing buffer (10 mM PBS, 0.01 % Tween 20, 25 µM of the carbohydrate monomer of theoretical highest affinity: $\alpha$-methyl-mannose, galactose or fucose). The solutions were spotted on NHS functionalized glass slides Nexterion® Slide H (Schott AG) using a non-contact piezoelectric printer sciFLEXARRAYER S11 (Scienion) to form covalent bonds with amine moieties of the lectins. The volume printed was 1.25 nL, 5 drops of 250 pL. The slides were divided into 14 sub-arrays, in which the lectins were spotted in 6 replicates. The printed slides were incubated for 2 hours in a 75 % humidity chamber (saturated NaCl solution) at room temperature. Unreacted NHS groups were quenched using a 50 mM ethanolamine solution in a 50 mM borate buffer, pH 8.5, for 1 hour at room temperature.

GNP were diluted to a gold concentration of 0.1 mg mg/mL (optimized concentration) in an incubation buffer (Tris-buffered saline (TBS): 150 mM NaCl, 25 mM Tris 7.5, 4 mM CaCl$_2$, 0.005 % Tween). 16 well ProPlate™ slide modules were adapted on the slides to divide them into 14 wells corresponding to the 14 sub-arrays printed. 100 µL of the GNP solutions were incubated with the printed lectins for 1 hour in the dark at room temperature under mild stirring (300 rpm). The slides were then washed with water and dried.

Fluorescence was measured using a G265BA Microarray Scanner System (Agilent). Data was processed using ProScanArray® Express software (Perkin Elmer). The mean/median of the 6 spots for each lectin was used. Spots presenting an abnormal shape or leakage were manually removed. The fluorescence quenching with the GNP solutions was expressed as a percentage of fluorescence in comparison to a sub-array incubated with the incubation buffer.

## 3. Biolayer Interferometry

An Octet$^{RED}$96 (FortéBio) system was used to perform the BLI assay. Reactions were performed using a sterile-filtered Kinetic Buffer made of 1 % Bovine Serum Albumin (BSA), 0.5 % Tween 20 in Dulbecco's Phosphate Buffered Saline (with $MgCl_2$ and $CaCl_2$).

DC-SIGN (R&D Systems, 9136-DC-05) was biotinylated using "EZ-Link" NHS-PEG4-Biotin (Thermo-Fisher, A39259) in a stoichiometric reaction. Biotinylated DC-SIGN was purified using Zeba™ Spin Desalting Columns, 7 kDa MWCO (Fisher Scientific, 10341164)

The experiments were performed in a flat black 96-well plate, using the kinetic mode, at 30 °C and 1000 rpm. High Precision Streptavidin (SAX) Dip and Read Biosensors (ForteBio, 18-0037) were hydrated for at least 10 minutes and loaded with biotinylated DC-SIGN. The optimal conditions of loading were found to be a DC-SIGN concentration of 10 nM and a loading time of 700 seconds. Residual streptavidin was blocked using 300 μM biocytin (Fisher Scientific, 11594157). To calculate the molarity of the GNP, models of 2000 Au atoms for 4 nm and 102 Au atoms for 2 nm were used.

Data analysis was done using Data Analysis HT 10.0 software. Data processing was made of alignment to the baseline step and Savitzky-Golay filtering.

For triage experiments, biosensors loaded with DC-SIGN (10 nM for 700 seconds) were subsequently immersed in wells with an increasing concentration of GNP ranging from 1.4 nM to 1 μM (cascade 1/3 dilutions) during 300 seconds each for association, followed by 600 seconds for dissociation.

For $K_D$ determination experiments, biosensors loaded with DC-SIGN (10 nM for 700 seconds) were immersed in different wells with a GNP concentration ranging from 0.01 nM to 7 nM (cascade 1/3 dilutions) during 400 seconds for association, followed by 300 seconds for dissociation. To obtain the $K_D$, steady state analysis during the five last seconds of association (395-400 seconds) was used. Data analysis was done using 1:1 binding model and local partial fitting was applied. Data were fitted to the Michaelis Menten equation.

## 4. Cell Uptake

THP-1 cells (Sigma, 88081201, expanded by Sal Scientific) were seeded in 6 well plates at a density of $5x10^5$ cells/ml in complete media (RPMI 1640 + 10 % FBS) and incubated overnight at 37 °C, 5 % $CO_2$. Cells were then treated with either PMA (10 ng/mL) and IL-4 (1000 U/mL) to differentiate and express DC-SIGN, or with PMA (10 ng/mL) alone, to be differentiated but without the expression of DC-SIGN, and later incubated during 72 hours at 37 °C, 5 % $CO_2$. Media were removed and a solution of $1x10^9$ GNP per cell, for 2 nm core, and $1x10^7$ GNP per cell, for 4 nm core, were added (in 400 μL low serum solution: DMEM + 2 % FBS). Samples were prepared and run in duplicate. Cells were incubated for 1-2 hours with the GNP at 37 °C, 5 % $CO_2$. After incubation, cells were scraped and underwent several centrifugation/resuspension cycles, using 10 mM PBS and acid wash (0.2 M acetic acid, 0.5 M NaCl pH 2.8) to remove GNP both in the medium and bound to the cell surface. Supernatant was removed and pellets were frozen.

Pellets were treated using tetramethylammonium hydroxide (TMAH) and Triton X100. Gold was measured by ICP-MS (NexION 300X, Perkin Elmer, software version 1.4).

## 5. Biodistribution

Male Wistar rats in groups of 4 were dosed with 300 μg/kg Au of GNP solutions through intravenous injection. Urine and faeces were recovered for 24 hours. After 24 hours, a blood sample was taken, and the rats were sacrificed. The following organs were then dissected: femur (bone), heart, lungs, liver, kidney, spleen, brain, testes, stomach, small intestine, large intestine, eyes, skin from the nape and skeletal muscles. From the blood samples, plasma and blood cells were separated. All the experiments were performed by experienced operators following standard procedures and ethical guidelines.

Samples were treated using TMAH and Triton X100, followed by a microwave digestion in the case of solid samples. Gold was measured by ICP-MS (NexION 300X, Perkin Elmer, software version 1.4).

Data processing and application of scaling factors provided a picture of the gold distribution after 24 hours.

# VI.   Annex

## 1. Fluorescence Assay

The fluorescence of the particles functionalized with a fluorophore was measured using a LS55 Fluorescence Spectrometer (Perkin Elmer). The assay concentration was optimized to obtain signals intense enough but without saturation of the detector (20-50 μg/mL Au). The excitation was performed according to the manufacturer's instructions and the emission read from 450 to 700 nm (*Table 7*).

*Table 7: Different fluorophores and corresponding GNP.*

| Fluorescent Molecule | λ Excitation (nm) | λ Emission (nm) | GNP Batch | Simplified GNP Name |
|---|---|---|---|---|
| Rhodamine Red X Succinimidyl Ester | 570 | 590 | 24 | Rhodamine PEGNH$_2$ 2 nm |
| Fluorescein isothiocyanate (FITC) | 490 | 525 | 25 | Fluorescein PEGNH$_2$ 2 nm |
| SulfoRhodamine 101 Cadaverine | 583 | 603 | 26 | SulfoRhodamine PEGCOOH 2 nm |
| Fluorescein Cadaverine | 493 | 517 | 27 | Fluorescein PEGCOOH  2 nm |

GNP were tested in two different conditions: diluted in DMSO and diluted in DMSO with TCEP for 2 hours, 950 rpm, 40 °C. TCEP completely etched the GNP and released the ligands.

In both cases, a strong fluorescence quenching was observed for the gold nanoparticles. For GNP-25, GNP-26 and GNP-27 the quenching was complete. GNP-24 still showed a slight fluorescence, possibly due to free dye, as a result of an uncomplete purification (*Figure 30*).

Once the gold core was completely etched and the ligands released, a strong emission signal was observed. This demonstrates the capacity of 2 nm core particles with PEG(5)NH$_2$ and PEG(8)COOH to strongly quench fluorescence.
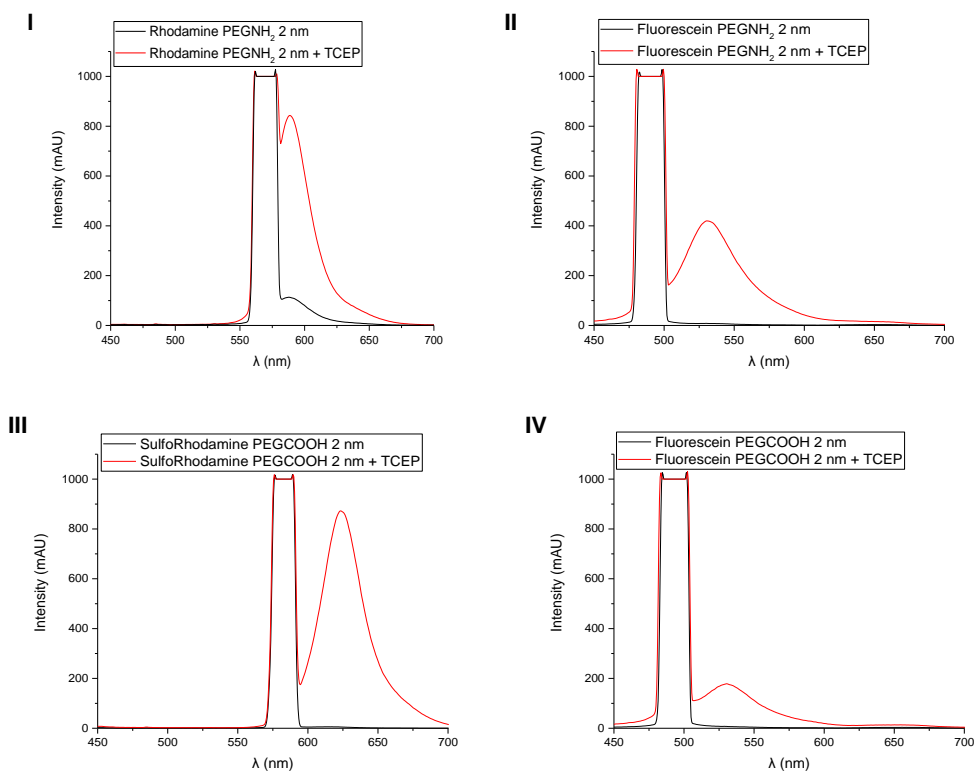
*Figure 30: Florescence spectra of fluorophore bearing GNP (quenching of emission) and etched GNP with TCEP (recovery of fluorescence). (I) GNP-24, (II) GNP-25, (III) GNP-26 and (IV) GNP-27.*

## 2. 4 nm core GNP characterization
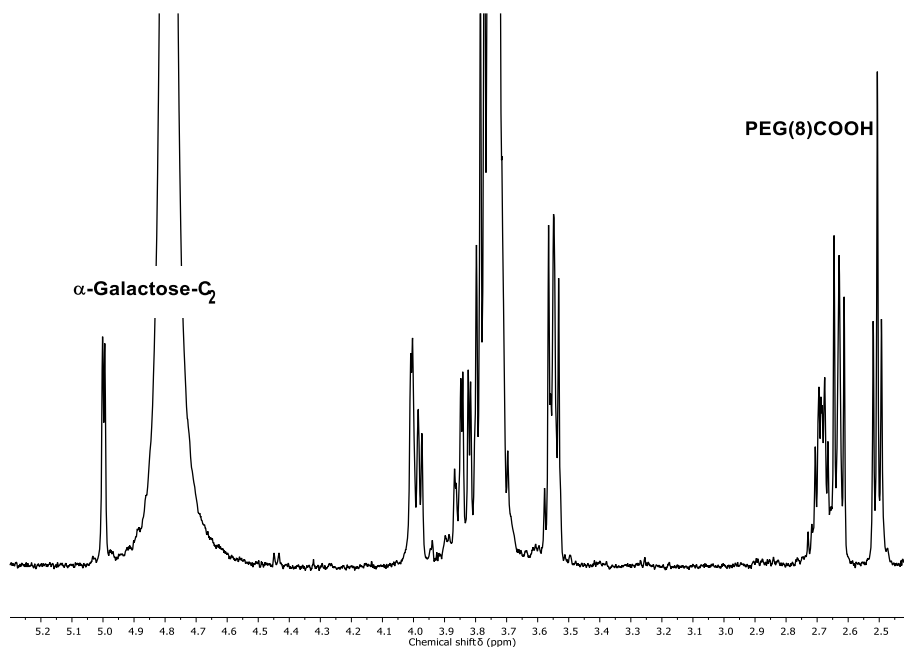


*Figure 31: $^{1}H$ NMR (500 MHz, $D_2O$, KCN/KOH treatment) of a 4 nm core GNP (PEG(8)COOH)($\alpha$-Galactose-$C_2$)@$Au_{2000}$. $\alpha$-Galactose-$C_2$ $\delta$ 5.00 (d, 1H, H-1). PEG(8)COOH $\delta$ 2.51 (t, 2H, -$CH_2$-COOH).*

*Figure 32: LC-CAD chromatogram with MS assignation of a 4 nm core GNP (PEG(8)COOH)(α-Galactose-C$_2$)@Au$_{2000}$ after hybrid KCN/KOH and TCEP etching treatment. α-Galactose-C$_2$ and PEG(8)COOH (m/z: 459, 476).*



*Figure 33: (I) UV-Vis spectrum (λ 350-700 nm), (II) TEM picture and core size distribution, (III) DLS hydrodynamic size distribution by volume, (IV) DCS diameter distribution of a 4 nm core GNP.*

# VII. References

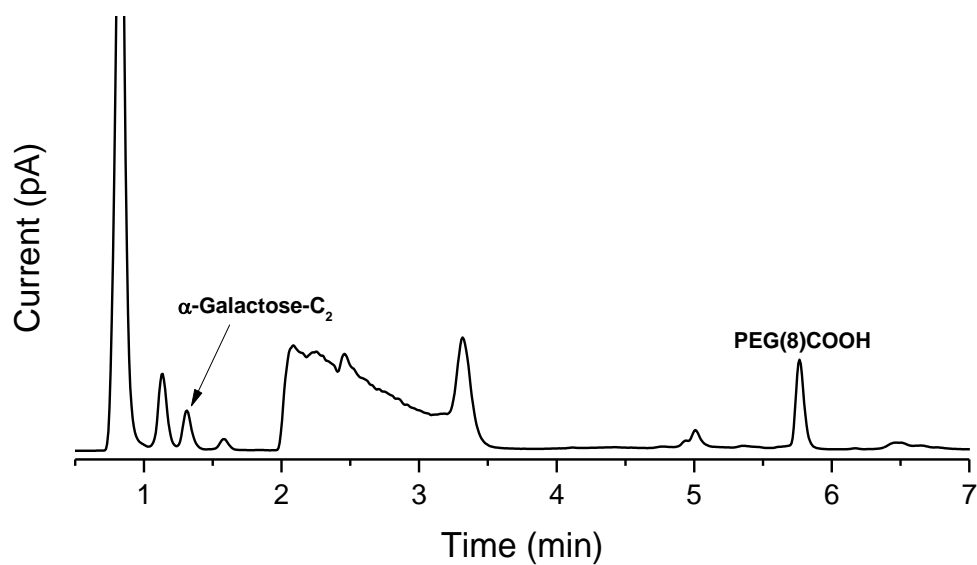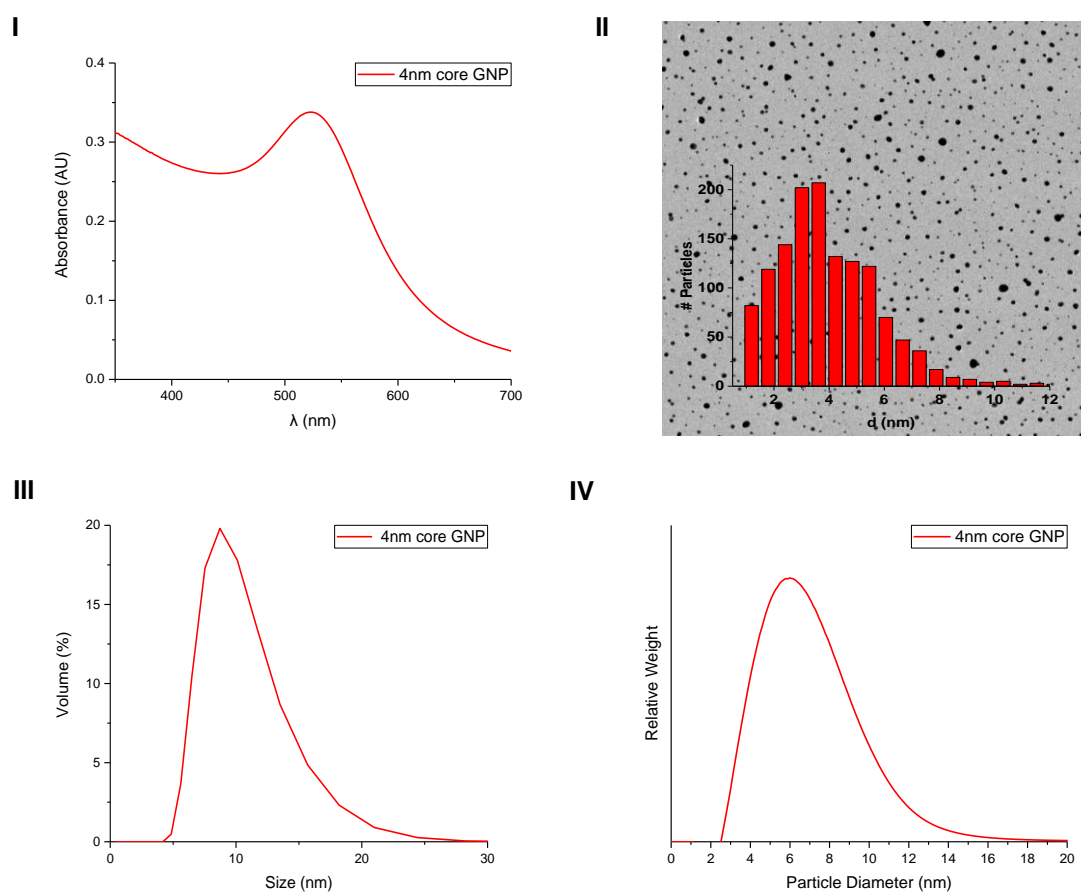1.      Varki, A. & Lowe, J. B. Biological Roles of Glycans. in *Essentials of Glycobiology* (Cold Spring Harbor Laboratory Press, 2009).

2.      Bertozzi, C. R. & Rabuka, D. Structural Basis of Glycan Diversity. in *Essentials of Glycobiology* (Cold Spring Harbor Laboratory Press, 2009).

3.      Cecioni, S., Imberty, A. & Vidal, S. Glycomimetics versus Multivalent Glycoconjugates for the Design of High Affinity Lectin Ligands. *Chem. Rev.* **115**, 525–561 (2015).

4.      Cummings, R. D. & McEver, R. P. C-type Lectins. in *Essentials of Glycobiology* (Cold Spring Harbor Laboratory Press, 2009).

5.      Brown, G. D., Willment, J. A. & Whitehead, L. C-type lectins in immunity and homeostasis. *Nat. Rev. Immunol.* **18**, 374–389 (2018).

6.      Human CTLD database. https://www.imperial.ac.uk/research/animallectins/ctld/mammals/humandata%20updated.html.

7.      Bonnardel, F. *et al.* UniLectin3D, a database of carbohydrate binding proteins with curated information on 3D structures and interacting ligands. *Nucleic Acids Res.* **47**, 1236–1244 (2018).

8.      Monteiro, J. T. & Lepenies, B. Multivalent Lectin–Glycan Interactions in the Immune System. in *Multivalency* 325–344 (John Wiley & Sons, Ltd, 2017).

9.      Banchereau, J. & Steinman, R. M. Dendritic cells and the control of immunity. *Nature* **392**, 245–252 (1998).

10.     Mellman, I. & Steinman, R. M. Dendritic Cells: Specialized and Regulated Antigen Processing Machines. *Cell* **106**, 255–258 (2001).

11.     Robinson, J. A. & Moehle, K. Structural aspects of molecular recognition in the immune system. Part II: Pattern recognition receptors (IUPAC Technical Report). *Pure Appl. Chem.* **86**, 1483–1538 (2014).

12.     Geijtenbeek, T. B. H. & Gringhuis, S. I. Signalling through C-type lectin receptors: shaping immune responses. *Nat. Rev. Immunol.* **9**, 465–479 (2009).

13.     Yan, H., Kamiya, T., Suabjakyong, P. & Tsuji, N. M. Targeting C-Type Lectin Receptors for Cancer Immunity. *Front. Immunol.* **6**, (2015).

14.     Lepenies, B., Lee, J. & Sonkaria, S. Targeting C-type lectin receptors with multivalent carbohydrate ligands. *Adv. Drug Deliv. Rev.* **65**, 1271–1281 (2013).

15.     Figdor, C. G., van Kooyk, Y. & Adema, G. J. C-type lectin receptors on dendritic cells and langerhans cells. *Nat. Rev. Immunol.* **2**, 77–84 (2002).

16.     Loke, I., Kolarich, D., Packer, N. H. & Thaysen-Andersen, M. Emerging roles of protein mannosylation in inflammation and infection. *Mol. Aspects Med.* **51**, 31–55 (2016).

17.     Lee, R. T. *et al.* Survey of immune-related, mannose/fucose-binding C-type lectin receptors reveals widely divergent sugar-binding specificities. *Glycobiology* **21**, 512–520 (2011).

18.     Li, R. E., van Vliet, S. J. & van Kooyk, Y. Using the glycan toolbox for pathogenic interventions and glycan immunotherapy. *Curr. Opin. Biotechnol.* **51**, 24–31 (2018).

19.     Sattin, S., Fieschi, F. & Bernardi, A. DC-SIGN as a Target for Drug Development Based on Carbohydrates. in *Carbohydrate Chemistry: State of the Art and Challenges for Drug Development: An Overview on Structure, Biological Roles, Synthetic Methods and Application as Therapeutics* 379–394 (World Scientific, 2016).

20.     van Liempt, E. *et al.* Specificity of DC-SIGN for mannose- and fucose-containing glycans. *FEBS Lett.* **580**, 6123–6131 (2006).

21.     Porkolab, V. *et al.* Rational-Differential Design of Highly Specific Glycomimetic Ligands: Targeting DC-SIGN and Excluding Langerin Recognition. *ACS Chem. Biol.* **13**, 600–608 (2018).

22.     Feinberg, H. *et al.* Structural Basis for Langerin Recognition of Diverse Pathogen and Mammalian Glycans through a Single Binding Site. *J. Mol. Biol.* **405**, 1027–1039 (2011).

23.     Ordanini, S. *et al.* Designing nanomolar antagonists of DC-SIGN-mediated HIV infection: ligand presentation using molecular rods. *Chem. Commun.* **51**, 3816–3819 (2015).

24.     Neumann, A. K., Thompson, N. L. & Jacobson, K. Distribution and lateral mobility of DC-SIGN on immature dendritic cells–implications for pathogen uptake. *J. Cell Sci.* **121**, 634–643 (2008).

25.     Lot de Witte & Yvette van Kooyk and  Teunis B.H. Geijtenbeek. Pathogen Interactions with DC-SIGN Modulate Immune Responses: A Toll Tale? *Curr. Immunol. Rev.* **1**, 157–163 (2005).

26.     Rodríguez, E. *et al.* Fasciola hepatica glycoconjugates immuneregulate dendritic cells through the Dendritic Cell-Specific Intercellular adhesion molecule-3-Grabbing Non-integrin inducing T cell anergy. *Sci. Rep.* **7**, 46748 (2017).

27.     Geijtenbeek, T. B. H. & van Kooyk, Y. DC-SIGN: A Novel HIV Receptor on DCs That Mediates HIV-1 Transmission. in *Dendritic Cells and Virus Infection* 31–54 (Springer, 2003).

28.     Dings, R. P. M., Cannon, M. & Vang, K. B. Design of Gold Nanoparticles in Dendritic Cell-Based Vaccines. *Part. Part. Syst. Charact.* **35**, 1800109 (2018).

29.     Santos, P. M. & Butterfield, L. H. Dendritic Cell–Based Cancer Vaccines. *J. Immunol.* **200**, 443–449 (2018).

30.     Lee, Y. C. & Lee, R. T. Carbohydrate-Protein Interactions: Basis of Glycobiology. *Acc. Chem. Res.* **28**, 321–327 (1995).

31.     Lundquist, J. J. & Toone, E. J. The Cluster Glycoside Effect. *Chem. Rev.* **102**, 555–578 (2002).

32.     Dam, T. K. & Brewer, C. F. Lectins as pattern recognition molecules: The effects of epitope density in innate immunity. *Glycobiology* **20**, 270–279 (2010).

33.     Yilmaz, G. *et al.* Glyconanoparticles with controlled morphologies and their interactions with a dendritic cell lectin. *Polym. Chem.* **7**, 6293–6296 (2016).

34.     Wang, X., Ramström, O. & Yan, M. Quantitative Analysis of Multivalent Ligand Presentation on Gold Glyconanoparticles and the Impact on Lectin Binding. *Anal. Chem.* **82**, 9082–9089 (2010).

35.     Ahmad, S. *et al.* Targeting dendritic cells through gold nanoparticles: A review on the cellular uptake and subsequent immunological properties. *Mol. Immunol.* **91**, 123–133 (2017).

36.     Singh, P. *et al.* Gold Nanoparticles in Diagnostics and Therapeutics for Human Cancer. *Int. J. Mol. Sci.* **19**, 1979 (2018).

37.     A. Dykman, L. & G. Khlebtsov, N. Immunological properties of gold nanoparticles. *Chem. Sci.* **8**, 1719–1735 (2017).

38.     Arosio, D. *et al.* Effective Targeting of DC-SIGN by α-Fucosylamide Functionalized Gold Nanoparticles. *Bioconjug. Chem.* **25**, 2244–2251 (2014).

39.     Chiodo, F. *et al.* Galactofuranose-Coated Gold Nanoparticles Elicit a Pro-inflammatory Response in Human Monocyte-Derived Dendritic Cells and Are Recognized by DC-SIGN. *ACS Chem. Biol.* **9**, 383–389 (2014).

40.     Martínez-Ávila, O. *et al.* Gold Manno-Glyconanoparticles: Multivalent Systems to Block HIV-1 gp120 Binding to the Lectin DC-SIGN. *Chem. – Eur. J.* **15**, 9874–9888 (2018).

41.     Arnáiz, B., Martínez-Ávila, O., Falcon-Perez, J. M. & Penadés, S. Cellular Uptake of Gold Nanoparticles Bearing HIV gp120 Oligomannosides. *Bioconjug. Chem.* **23**, 814–825 (2012).

42.     Climent, N. *et al.* Loading dendritic cells with gold nanoparticles (GNPs) bearing HIV-peptides and mannosides enhance HIV-specific T cell responses. *Nanomedicine Nanotechnol. Biol. Med.* **14**, 339–351 (2018).

43.     Bertolotti, B. *et al.* Polyvalent C-glycomimetics based on L-fucose or D-mannose as potent DC-SIGN antagonists. *Org. Biomol. Chem.* **15**, 3995–4004 (2017).

44.     Reina, J. J. *et al.* 1,2-Mannobioside Mimic: Synthesis, DC-SIGN Interaction by NMR and Docking, and Antiviral Activity. *ChemMedChem* **2**, 1030–1036 (2007).

45.     Medve, L. *et al.* On-Chip screening of a glycomimetic library with C-Type lectins reveals structural features responsible for preferential binding of dectin-2 over DC-SIGN/R and langerin. *Chem. Eur. J.* **24**, 14448–14460 (2018).

46.     Carvalho, S. B. *et al.* A detection and quantification label-free tool to speed up downstream processing of model mucins. *Plos One* **13**, 0190974 (2018).

47.     Laigre, E., Goyard, D., Tiertant, C., Dejeu, J. & Renaudet, O. The study of multivalent carbohydrate–protein interactions by bio-layer interferometry. *Org. Biomol. Chem.* **16**, 8899–8903 (2018).

48.     Puig-Kröger, A. *et al.* Regulated Expression of the Pathogen Receptor Dendritic Cell-specific Intercellular Adhesion Molecule 3 (ICAM-3)-grabbing Nonintegrin in THP-1 Human Leukemic Cells, Monocytes, and Macrophages. *J. Biol. Chem.* **279**, 25680–25688 (2004).

49.     Brust, M., Walker, M., Bethell, D., Schiffrin, D. J. & Whyman, R. Synthesis of thiol-derivatised gold nanoparticles in a two-phase Liquid–Liquid system. *J. Chem. Soc. Chem. Commun.* 801–802 (1994).

50.     Jadzinsky, P. D., Calero, G., Ackerson, C. J., Bushnell, D. A. & Kornberg, R. D. Structure of a Thiol Monolayer-Protected Gold Nanoparticle at 1.1 Å Resolution. *Science* **318**, 430–433 (2007).

51.     Vergara, S. *et al.* Synthesis, Mass Spectrometry, and Atomic Structural Analysis of Au~2000(SR)~290 Nanoparticles. *J. Phys. Chem. C* **122**, 26733–26738 (2018).

52.     Dass, A. Nano-scaling law: geometric foundation of thiolated gold nanomolecules. *Nanoscale* **4**, 2260–2263 (2012).

53.     Sahoo, H. Fluorescent labeling techniques in biomolecules: a flashback. *RSC Adv.* **2**, 7017–7029 (2012).

54.     Gu, Y.-J. *et al.* Nuclear penetration of surface functionalized gold nanoparticles. *Toxicol. Appl. Pharmacol.* **237**, 196–204 (2009).

55.     Xue, C., Xue, Y., Dai, L., Urbas, A. & Li, Q. Size- and Shape-Dependent Fluorescence Quenching of Gold Nanoparticles on Perylene Dye. *Adv. Opt. Mater.* **1**, 581–587 (2013).

56.     Kang, K. A., Wang, J., Jasinski, J. B. & Achilefu, S. Fluorescence Manipulation by Gold Nanoparticles: From Complete Quenching to Extensive Enhancement. *J. Nanobiotechnology* **9**, 16 (2011).

57.     Raikar, U. S., Tangod, V. B., Mastiholi, B. M. & Fulari, V. J. Fluorescence quenching using plasmonic gold nanoparticles. *Opt. Commun.* **284**, 4761–4765 (2011).

58.     Hirabayashi, J., Yamada, M., Kuno, A. & Tateno, H. Lectin microarrays: concept, principle and applications. *Chem. Soc. Rev.* **42**, 4443–4458 (2013).

59.     Li, H., Wei, L., Fang, P. & Yang, P. Recent advances in the fabrication and detection of lectin microarrays and their application in glycobiology analysis. *Anal. Methods* **6**, 2003–2014 (2014).

60.     Wellhausen, R. & Seitz, H. Facing Current Quantification Challenges in Protein Microarrays. *BioMed Res. Int.* **2012**, 831347 (2012).

61.     Richards, S.-J., Fullam, E., Besra, G. S. & Gibson, M. I. Discrimination between bacterial phenotypes using glyco-nanoparticles and the impact of polymer coating on detection readouts. *J. Mater. Chem. B* **2**, 1490–1498 (2014).

62.     Yilmaz, G. & Becer, C. R. Glyconanoparticles and their interactions with lectins. *Polym. Chem.* **6**, 5503–5514 (2015).

63.     Reynolds, M., Marradi, M., Imberty, A., Penadés, S. & Pérez, S. Multivalent Gold Glycoclusters: High Affinity Molecular Recognition by Bacterial Lectin PA-IL. *Chem. – Eur. J.* **18**, 4264–4273 (2012).

64.     Roskamp, M. *et al.* Multivalent interaction and selectivities in selectin binding of functionalized gold colloids decorated with carbohydrate mimetics. *Org. Biomol. Chem.* **9**, 7448–7456 (2011).

65.     Guo, Y. *et al.* Compact, Polyvalent Mannose Quantum Dots as Sensitive, Ratiometric FRET Probes for Multivalent Protein–Ligand Interactions. *Angew. Chem. Int. Ed.* **55**, 4738–4742 (2016).

66.     Tobias, R. & Kumaraswamy, S. Biomolecular binding kinetics assays on the octet platform. *Forte Bio Appl Note* **14**, 1–21 (2014).

67.     Ji, Y. & Woods, R. J. Quantifying Weak Glycan-Protein Interactions Using a Biolayer Interferometry Competition Assay: Applications to ECL Lectin and X-31 Influenza Hemagglutinin. in *Glycobiophysics* 259–273 (Springer Singapore, 2018).

68.     Han, T. H. *et al.* Evaluation of 3 clinical dendritic cell maturation protocols containing lipopolysaccharide and interferon-gamma. *J. Immunother. Hagerstown Md 1997* **32**, 399–407 (2009).

69.     Cruje, C. & Chithrani, D. B. Polyethylene Glycol Density and Length Affects Nanoparticle Uptake by Cancer Cells. *J. Nanomedicine Res.* **1**, (2014).

70.     Adema, G. J., de Vries, I. J. M., Punt, C. J. & Figdor, C. G. Migration of dendritic cell based cancer vaccines: in vivo veritas? *Curr. Opin. Immunol.* **17**, 170–174 (2005).

71.     Huber, A., Dammeijer, F., Aerts, J. G. J. V. & Vroman, H. Current State of Dendritic Cell-Based Immunotherapy: Opportunities for in vitro Antigen Loading of Different DC Subsets? *Front. Immunol.* **9**, (2018).

72.     Ludewig, B. Dendritic Cell Vaccination and Viral Infection — Animal Models. in *Dendritic Cells and Virus Infection* 199–214 (Springer, 2003).